

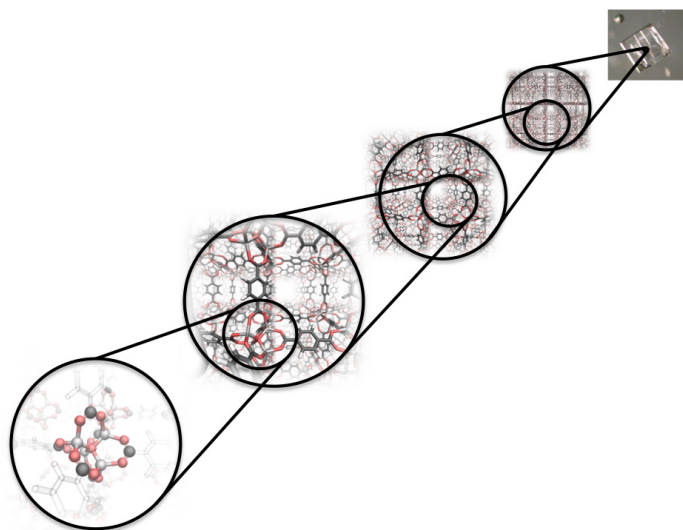
Lehrstuhl für anorganische Chemie II
Organometallics & Materials

RUHR
UNIVERSITÄT
BOCHUM

RUB

DISSERTATION

Investigation of Structural and Dynamic Properties of Metal-Organic Frameworks



Saeed Amirjalayer

January, 2011

For my parents and Masoud

“....von (Popper) lernte ich, was für mich heute das Wesen wissenschaftlicher Forschung ausmacht - dass man bei der Entwicklung von Hypothesen spekulativ und phantasievoll vorgehen kann, um sie anschließend mit größtmöglicher Strenge zu überprüfen, indem man alle vorhandenen Kenntnisse zu Rate zieht und beim (experimentellen) Test möglichst gründlich verfährt. Er lehrte mich sogar, mich über die Wiederlegung einer lieb gewonnenen Hypothese zu freuen, weil auch das ein wissenschaftlicher Fortschritt sei und weil sich aus der Wiederlegung viel lernen lasse. Poppers Einfluss empfand ich als sehr befreiend, löste ich mich doch von den starren Konventionen, welche die wissenschaftliche Forschung in der Regel einengen....Wenn man sich von diesen restriktiven Dogmen befreit, wird die wissenschaftliche Forschung zu einem aufregenden Abenteuer, das einem ganz neue Perspektiven eröffnet;....”

(aus “Auf der Suche nach dem Gedächtnis” von Eric Kandel)

I am very grateful to my supervisor and mentor

PD Dr. Rochus Schmid

for giving me scientific freedom in my work. Rochus did not just support me with his scientific knowledge but also with taking his time for answering all my *short* questions and concerns. I really feel honored to be his first Ph.D. student.

Further I would like to thank Prof. Dr. Roland A. Fischer for his direct and indirect support. Although we had only few scientific discussions, he had a large impact on my work: starting from my Bachelor study until now.

My special thanks go to my (former) colleague Dr. Maxim Tafipolsky for continuously and patiently explaining different scientific issues. His kind support remained although he has moved over to the University of Würzburg. I would also like to thank him for checking my thesis up on consistency.

Further I want to thank the new members of Rochus group, who indeed joined very recently but supported me during the last month and weeks: Dr. Sareeya Bureekaew and Dr. Christian Spickermann.

Furthermore I would like to thank my cooperation partners:

Dr. habil. Frank Stallmach and Markus Wehring (University of Leipzig) for supporting my experimental excursion by measuring my samples.

Prof. Randall Q. Snurr and his group for an exciting stay at Northwestern University. It was a real pleasure to work with you all on simulation.

I want to thank Prof. Dr. Ferdi Schüth for agreeing to be the second referee of my Ph.D. thesis.

A very warm thanks goes to Sabine Pankau, Heike Gronau-Schmid and Jacinta Essling for helping me solving everyday problems at the university. I want to further thank Jacinta for improving my English skills.

Of course, I want to thank the "Harrys": Daniel Esken, Markus Halbherr, Mikhail Meilikhov, Tobias Thiede. The last 8 years with you all was awesome. Our "scientific" discussions help me to figure out the import things in life. Thank you for the Dublin trip!

Special thank goes to Dr. Stephan Hermes, who first introduced me to the experimental world of porous materials and later allowed me to have a look into the “real world” during my time at BASF.

I want to thank some of my “travel partners” for scientific and non-scientific discussions:

Maike Müller and Sebastian Henke for an enjoyable trip to the MOFCAT and for visting *all* the museums in Oslo.

Denise Zacher for an unsual trip to New York and to the ECS conference in Chicago.

The whole MOF-crew for an interesting trip to Marseille.

Dr. Thomas Cadenbach for joining me on a really “scientific” journey to Mexico and the USA, which led to a lot of fruitful discussions up to now.

I am also very grateful to members of the ACII family, who show me every day that chemistry is more than just playing with the computer:

Dr. Anjana Devi, Dr. Christian Gemel, Dr. Radim Beránek, Dr. Harish Parala, Manuela Winter, Uschi Herrmann, Malte Hellwig, Michael Krasnopolski, Mahmoud Sliem, Ke Xu, Mariusz Molon, Timo Bollermann, Vanessa Gwildies, Adinarayana Doddi, Daniela Bekermann, Angélique Bétard, Olesia Vreshch, Sun Ja Kim, Nagen-dra Babu Srinivasan, Manish Banerjee, Arik Puls, Kerstin Freitag, Stefan Cwik

I have to thank the ‘*Fond der chemischen Industrie*’ and the ‘*Sonderforschungsbereich 558 Graduiertenkolleg*’ for granting me PhD fellowships. In addition, I want to thank the Ruhr-University Research School for financial support and the possibility to join interesting seminars.

I also would like to thank Jasmin Söte for her continous motivation and her patience, especially during the last weeks.

Finally, I want to thank my parents and my brother for simply everything they have done for me. They are always by my side - day and night - and do everything to support me. Without them nothing would work!

Contents

1	Introduction and Motivation	10
1.1	Motivation	10
1.2	Bridging the gap	11
1.3	Possible Applications of MOFs	19
I	Theoretical Methods	25
2	Quantum Mechanical	29
2.1	Wavefunction based methods	29
2.2	Density Functional Theory	31
3	Classical Mechanical	35
3.1	Force Fields	35
3.1.1	The basic concept	35
3.1.2	Force Field Development using a Genetic Algorithm Technique	37
3.2	Molecular Dynamic Simulation	39
3.2.1	Self-diffusion constant and probability density	40
II	Understanding the structure of MOFs	42
	Complexity of matter	43
	Reverse Topological Approach	47
4	Copper Paddle Wheel MOFs	55
4.1	<i>Ab-initio</i> Parametrization of a Copper Paddle Wheel Force Field . .	57
4.1.1	Reference Systems	57
4.1.2	Parametrization	60
4.1.3	Validation	61
4.2	Investigation of the Network topology	65
4.2.1	Interpenetration	69
4.2.2	Tuning Network Topology	73

<i>CONTENTS</i>	8
4.3 Summary	75
5 Covalent Organic Frameworks	77
5.1 Reference Systems	80
5.2 Parametrization and Validation	83
5.3 Network Topologies	85
5.4 Prediction of Structural and Dynamic Properties	90
5.5 Summary	92
6 Beyond Network Topology	94
6.1 Validation of the force field	98
6.2 Strategy for the global minimum search: Genetic Algorithm Technique	101
6.3 Conformational Isomers of IRMOF-7 and 993	103
6.4 Strain energy of isorecticular isomers	106
6.5 Summary	109
7 Surface Structure and Energies of HKUST-1	110
7.1 Surface termination	112
7.2 Slicing reaction and Slab model	112
7.3 Surface energies	114
7.4 Summary	118
III Host-Guest Systems	119
8 Interaction between benzene and MOF-5	122
8.1 Evaluation of quantum mechanical methods	125
8.1.1 Adsorption of the benzene molecule in the α -site	125
8.1.2 Adsorption of the benzene molecule in the β -site	133
8.1.3 Different arrangement of the benzene molecule in the α -site .	135
8.2 Evaluation of classical force fields	137
8.3 Summary	142
9 Soft-Modifications	144
9.1 Elongation of the linker	145
9.1.1 Structure and mobility of the benzene molecules within the pores	146
9.1.2 Benzene diffusion mechanism	150
9.1.3 Monte-Carlo Hopping Model	154
9.1.4 Influence of higher loadings on the host-guest interaction . .	159
9.2 Isoreticular Isomers	161

9.2.1	Structure and mobility of benzene in regular and twisted IRMOF-1	161
9.2.2	Defects in the network	165
9.2.3	Diffusion in twisted and regular IRMOF-7	166
9.3	Conclusion	167
10	Conclusion	169
11	Appendix	173
	List of Papers, Talks and Posters	198

Chapter 1

Introduction and Motivation

1.1 Motivation

“What would happen if we would arrange the atoms one by one the way we want them?” This famous quote by Richard P. Feynman addresses the ultimate goal of materials science. To reach it, chemists have studied intensively the structures and interactions of atoms and molecules in solids, liquids and gases. A partial success would be if the question could be answered which effects are important for the arrangement and rearrangement of atoms and molecules. This work deals with these kinds of issues in terms of porous materials, where the arrangement of the atoms generates voids within the structure. In case of crystalline porous materials, which are considered in this work, these pores offer a high degree of regularity. Projecting Feynman’s question on these compounds, would mean that the cavities could be defined on a molecular level, since by modifying the structure the pore system changes. In this regard one part of this work deals with the structure of porous materials and in particular with the question of how the exchange of single units influences the overall system. Accurate theoretical methods will be developed to enable the investigation of structural and dynamic properties of different compounds. Furthermore, an approach is derived, which allows the classification of porous materials in general and helps to understand fundamental aspects of these systems.

However, since the cavities within a porous material are often accessible for molecules, a further questions arises: “If we could define the pore system, can the confinement be used to control the properties of the guest species?” and “How do the molecules interact with the inner surface of these materials?”. To shed light on these issues, the second part of the work focuses on host-guest systems based on

porous materials. After reliable tools are derived, the influence of pore modifications is studied in terms of the interaction between guest molecules and the matrix.

1.2 Bridging the gap

For a long time porous compounds have been known only from mineralogy. In the 18th century, Cronstedt, a Swedish mineralogist and chemist, investigated a so-called hydrous mineral - the mineral stilbite, which release steam when heated [1]. In this context he also coined the term zeolite, which nowadays describes a large class of porous aluminosilicates. His work points out two crucial properties of porous compounds in general: the ability to incorporate guest molecules reversibly and the possibility to control this process by an external stimulus. Despite these fascinating properties, it took until the 1940s, about 300 years, until Barrer, Milton and Breck could synthesize the first artificial zeolite [2, 3], which paved the way for the breakthrough of porous materials in the field of functional materials. The scaffolding of zeolites is assembled (mainly) by aluminium oxide and silicon oxide tetrahedrons, which are usually called **primary building units (PBUs)**. Flanigan et al. extended the class of inorganic porous materials by three-dimensionally connected aluminium phosphate compounds [4]. Later, other PBUs, consisting of metal phosphates, sulfates or cyanides were used to obtain similar structures [5]. Nowadays, their unique properties such as high surface area and size selective adsorption, influence many processes in industry as well as everyday life. Zeolites, for instance, are used as water softeners or as heterogeneous catalyst in the crack processing of crude oil [6]. In this context other porous compounds based on silicate networks, introduced in the 90s of the last century, are also used [7]. Although investigated for a long time and used on large scale, the synthesis of new porous materials is still very challenging and a systematic approach to obtain novel structures has not yet, been developed.

Coordination Polymers

Almost parallel to the progress of these inorganic materials in both academia and industry, an further research area, which is known for its structural diversity, was developed in the middle of the last century. Bailar coined the term “coordination polymer”, which describes well the nature of the investigated compounds [8]. Researchers in this field deal with polymeric forms of Werner type coordination complexes, which contain a metal core surrounded by organic linkers. Correspondingly coordination polymers are constructed by linking metal centers or clusters with multidentate organic linkers. In contrast to their monomeric relatives, coordination polymers form either one, two or even three dimensional networks (Fig. 1.1).

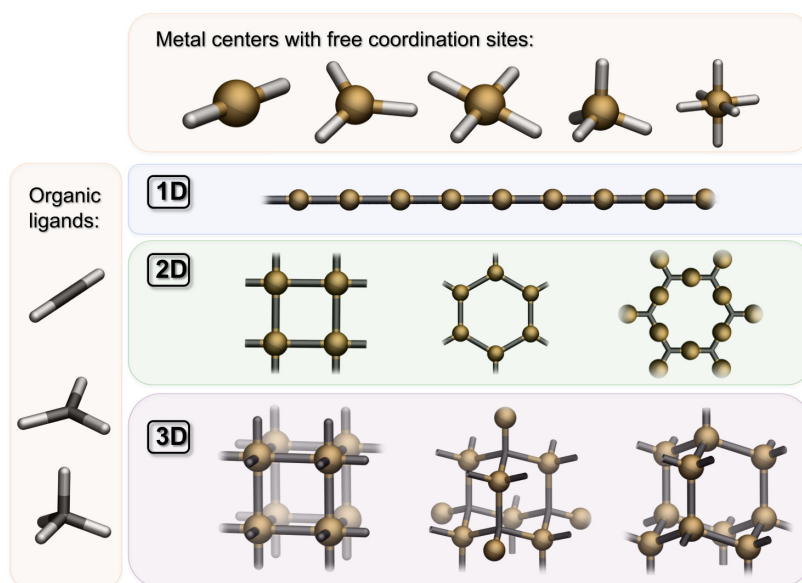


Figure 1.1: Schematic representation of the assembling of coordination polymers.

Being able to vary both the metal center as well as the ligand, a high structural diversity can be achieved. The modular assembling allows the tuning of different physical properties (e.g. magnetism or optical features) [9]. However, compared to zeolites they show no permanent porosity and are structurally less stable. Nevertheless, even in the case of the monomeric coordination complexes the inclusion of organic solvent molecules during the crystallization is known, which is commonly referred to as *clathration* [10]. In 1957 Schaeffer et al. pointed out the potential of these molecular solids to selectively incorporate guest species [11]:

“This (new) class of clathrate formers exhibits a sharp selectivity for forming crystals containing certain organic molecules, the selectivity being based, apparently on the shape rather than the molecular volume occupied by the organic moiety.”

The authors even described the possibility to tune the properties of these compounds in order to accommodate molecules:

“The (three) constituents of these complexes...all contribute to the ability of the complex to form clathrates as well as determine the type of types of organic molecules that will be clathrated”

Interestingly, already at the end of the 19th century Hofmann showed the first example of such a *soft material*¹ - the nickel complex $Ni(NH_3)(CN)_2$ [12]. This

¹The term *soft* is used to stress the lower stiffness of these materials compared to purely inorganic compounds.

complex forms a molecular solid in the presence of certain organic molecules such as thiophene, benzene, phenol or aniline. Even this early work points out that the investigated systems, although without permanent porosity, have the ability to selectively incorporate guest molecules. In this tradition, the investigation of coordination polymers with respect to their ability to accommodate guest molecules is reasonable.

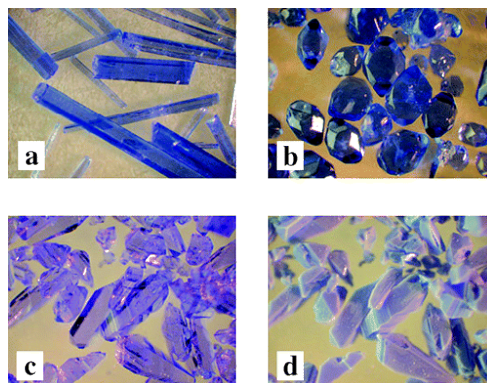


Figure 1.2: Crystalline samples formed by different $Ni(4 - methylpyridine)_4(NCS)_2$ phases[13]: a) α -polymorph and guest free; b) β -polymorph, guest-free phase left after benzene release from 1:1 inclusion compound; c) γ -phase, 1:2 host-to-benzene ratio; d) sample c) after 30 min. in air.

An important feature of these soft materials is that the main part of the incorporated molecules should just interact with the polymeric backbone by non-bonded interactions like $\pi - \pi$ stacking or hydrogen bonding, so that the exchange and removal of the guest molecules is feasible. By using different guest molecules during the assembling process the packing between the different constituents may alter. The change of the host-guest interaction can even be observed macroscopically by different crystal shapes (Fig.1.2)². In addition the incorporated molecules can be exchanged in some cases post-synthetically. Nevertheless, the complete removal of the guest molecules leads either to a loss of the long range ordering of the compound, literally the structure collapses, or results in a non-porous material.

Porous Coordination Polymers

Motivated by the structural diversity and the ability to include molecules, the research of coordination polymers was further pushed, aiming to bridge the gap to the permanent porous - mainly inorganic - materials and enabling the synthesis of new open structures. Robson, who introduced the concept of linking inorganic

²Interestingly, a long time after the work of Schaeffer [11] on $Ni(4-methylpyridine)_4(NCS)_2$ a microporous phase of the compound was obtained [13, 14].

units with a certain coordination number to achieve networks, resembling known inorganic structures [15], wrote in a paper in 1990 [16]:

“Despite Nature’s abhorrence of a vacuum it may be possible to devise rods with sufficient rigidity to support the existence of solids with relatively huge empty cavities. Materials combining good or even high thermal, chemical, and mechanical stability with unusually low density may thereby be afforded.”

In an earlier work probably the first example for an open three dimensional coordination polymer was presented by Robson and co-workers [17]. The framework is built up by $Cu(I)$, which is coordinated in a tetrahedral fashion by 4,4′,4′′,4′′′ – *tertracyanotetraphenylmethane*. The charged network exhibits two different adamantane like pores which are filled with both BF_4 and $C_6H_5NO_2$. Although the authors did not report the complete removal of the solvent molecules, they claim that approximately one-third of the whole crystal volume is the coordination polymer itself and the remaining part is “*effectively liquid*” [16, 17]. Based on this work, coordination polymers with open structures were studied with respect to the selective binding of guest molecules [18, 19]. Kitagawa and co-workers, for instance, could show the reversible adsorption of gases at ambient temperature in coordination polymers [20].

The first example of a coordination polymer with solvent-free permanent porosity was MOF-5 (**m**etal-**o**rganic **f**ramework-5) [21]. The cubic pore system of MOF-5 is constructed by linking Zn_4O -tetrahedrons with terephthalic acid (Fig.1.3).

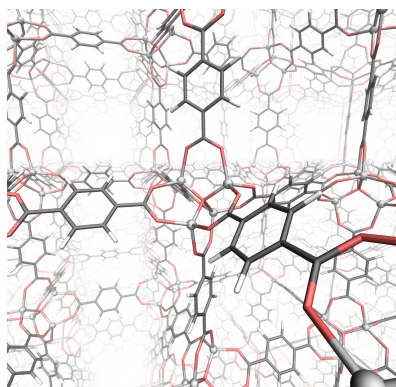


Figure 1.3: Molecular structure of MOF-5 (silver: zinc; red: oxygen; black: carbon; white: hydrogen atoms).

The specific linking of the inorganic and organic fragments, which are usually called **secondary building units (SBUs)**³, causes the high structural stability. Until now MOF-5 is the most investigated representative of the class of *hybrid* porous materials⁴.

However, even pioneers like Robson did not estimate the whole range of structural possibilities of the new class of porous materials [16]:

“We propose that a new and potentially extensive class of solid polymeric materials with unprecedented and possibly useful properties may be afforded by linking together centers with either **a tetrahedral or an octahedral array** of valencies by rod-like connecting units.”

And during the past two decades an enormous number of new coordination polymers with various topologies (Fig.1.4) and permanent porosity are synthesized. Some of them even show high thermal and chemical stability [22]. The nomenclature of these materials is by far not uniform. Beside the expression metal-organic framework, Kitagawa, among others, coined the term **porous coordination polymers (PCPs)**, which describes literally the nature of the compounds. Other groups connect the obtained compound with the location, in which it was synthesized first, like for instance the abbreviation MIL used by the group of Ferey, which stands for **Matériaux de l’Institut Lavoisier** [23]. Within this work MOF and PCP are used as umbrella terms even though the nomenclature of individual compounds may differ in the literature.

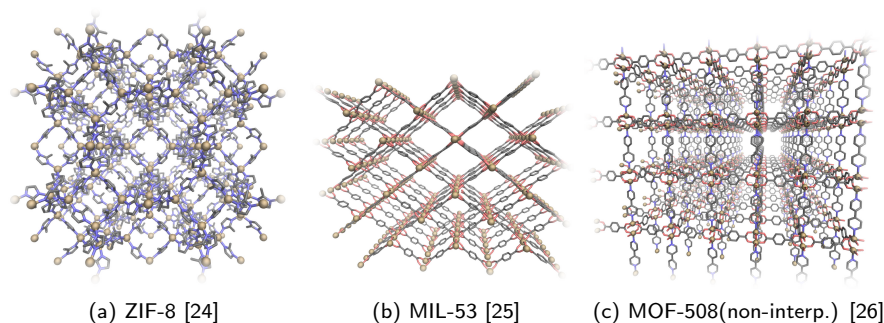


Figure 1.4: Example of metal organic frameworks with different pore structures.

To point out the development of the PCPs, Kitagawa introduced a classification hierarchy [27]. It discriminates between coordination polymers in terms of their structural change due to solvent removal (Fig.1.5).

³Note, that in case of zeolites the term SBU is used to describe repeating motives in a system obtained by the assembling of PBUs. In case of MOFs the inorganic and organic fragments are tagged by this term due to their complexity.

⁴The term *hybrid* shall emphasize that the materials are build up by both inorganic and organic units.

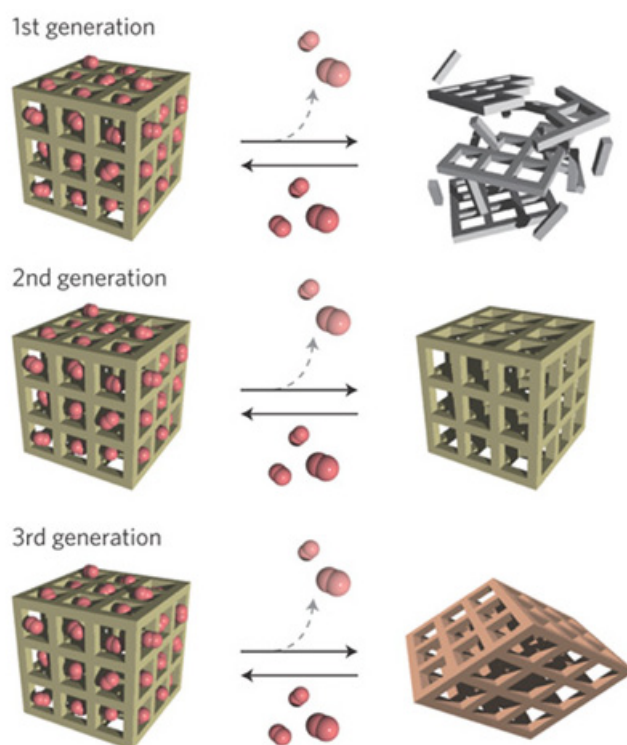


Figure 1.5: Classification of coordination polymers according to Kitagawa et al. [28].

Compounds of the first generation, which one could call the *classical* coordination polymers, break down if the guest molecules are removed. The scaffold is stable only in the presence of guest molecules. The second generation covers those structures which show porosity when the included species are removed. These networks stay intact although the structure has pores without any solvent molecules. These pore systems can be further sub-divided into classes featuring one, two or three dimensional porosity, with various shapes and sizes. In this case reversible adsorption and desorption of different molecules is possible. Furthermore, some MOFs show structural dynamics. These hybrid materials are referred to as the third generation. The dynamics can be induced by external stimuli. For instance, the exchange of solvent molecules can lead to an expansion or contraction of the network. The three generations show the development of coordination polymers from non-porous materials with high structural potential to materials with permanent porosity and dynamic features.

From inorganic over hybrid to organic porous materials

A brief comparison between zeolites and the hybrid compounds shows that MOFs extend the features of porous materials (Tab. 1.1).

Table 1.1: Comparison between zeolites and metal organic frameworks

Zeolites	Metal organic frameworks
purely inorganic	hybrid: inorganic nodes and organic linkers
limited number of elements (Si, O, Al)	wide variety of elements in the inorganic part (Cu, Zn, Fe, Cr, V, Ni, Al, Ga, Co, ...)
tetrahedral coordination in EO_4 (E=Si, Al)	wide variety of coordination numbers and modes (including clusters)
thermodynamically strong $E - O$ bonds	weaker coordination bonds, linkers mostly stable; but decomposition reactions (e.g. decarboxylation of carboxylates) are possible.
only $E - O - E$ bridge, porous network because of network topology	different (tunable) linkers, length of linkers defines pore size and structure
network topology defined by template molecules (structure directing agents [29])	network topology can to some extent be controlled by the structure and conformation of the linker
difficult to functionalize	functionalize either by linkers with functional groups or by post-synthetic modifications
very rigid framework	can be both very flexible ("soft", because of conformational changes in the linkers and bending at the coordination centers) and rigid due to the assembling (In the case of MOF-5, for instance, the rigid character is due to the specific arrangement of the linkers around the inorganic node.)
high thermal stability	limited thermal stability (but exceptions are known[22])
high chemical stability already used in large-scale	limited chemical stability still in the explorative stage

The comparison shows advantages and disadvantages on both sides, thus one can assume that none of the subclasses of porous materials will cover all demands in the various application fields alone. In addition to this very strict classification between zeolites and MOFs, it should be mentioned that the smooth transition from

hybrid materials to purely inorganic ones is promoted by networks with different dimensionality of the inorganic unit (Fig. 1.6). The variation of the organic and inorganic fraction leads to different network properties (e.g. stiffness or dynamics).

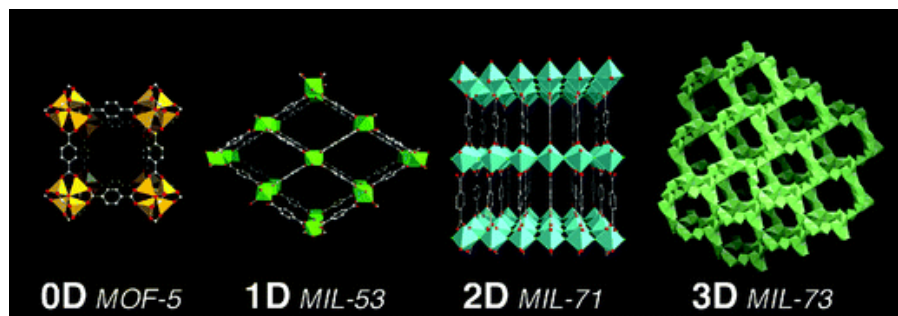


Figure 1.6: Different dimensionality of the inorganic unit in porous materials [30].

Within the scope of the presented porous coordination polymers, materials were developed which cover the other side of the spectrum. These networks are built up by purely organic fragments. One class of these crystalline porous materials is called **covalent organic frameworks (COFs)** [31]. Due to their metal free composition they exhibit interesting properties such as low densities. A detailed overview of these crystalline compounds is given in Part II ⁵.

Apart from the discussed range from organic over hybrid to purely inorganic materials, the new compounds complete also the class of porous materials in the sense of chemical bonding. Three main kinds of chemical bonding can be distinguished. While the zeolites are rather ionic type materials, COFs are built up by covalent bonds. These two extreme cases are bridged by MOFs. In this case coordination bonds are present in the framework, which have both ionic and orbital directing properties.

Finally, it should be emphasized that both the MOFs and COFs are still in the explorative stage. None of them is used, yet, in an industrial process, which poses different challenges⁶. Nevertheless, the discovery of new porous materials enables one to address more specifically the requests in various application fields.

⁵Possible applications, which are described in the next paragraph, are also ones which can be accomplished by COFs.

⁶The transfer of a material from the small-scale to the large-scale leads to further requirements such as mechanical ones; the industrial used materials are in most cases post-treated after synthesizing to obtained specific forms for example pellets to enable industrial applications. In addition the chemical stability of the materials towards impurities of reactant have to be considered. However, it should be mentioned that some effort have been done to use MOFs and related materials beyond academia [32, 33].

1.3 Possible Applications of MOFs

Metal-organic frameworks represent the fusion of properties known from different fields making them promising candidates for a variety of applications. Due to their crystalline nature, they allow to develop, materials with stiffness and long-range order comparable to inorganic porous compounds. In addition, they offer through their hybrid framework the possibility to introduce different functional groups using techniques known from the field of organic chemistry. Their modularity, which is certainly inherited from classical coordination chemistry, enables the combination of inorganic and organic units to synthesize materials with desired pore structures. Combining all features, the long-term goal is to obtain unique porous materials with various functionality, which can be addressed very selectively. A comparison with the macro-molecules known from nature (e.g. proteins), which show high selectivity and efficiency, may be adventurous but not completely absurd, since the specific tuning of active centers in a confined environment allows to control different processes (e.g. reactions [34]) with respect to time and space. In this regard, terms such as “design” of materials [35] are used and the results of recent years are very promising. Nevertheless, very fundamental issues, for instance the growth mechanism, remain almost unexplored, which are essential to derive a rational approach for the development of new functional materials. Concerning this matter the current work focuses on some fundamental issues: Why do we get a particular structure - network topology - for a certain MOF system? Why is one structure preferred? Furthermore, due to the high porosity, the incorporation of guest molecules is obvious. Thus the understanding of different aspects of host-guest interaction in porous coordination polymers is another fundamental issue, which is also an objective of the current work. Dealing with these constitutional questions, is, beside scientific curiosity, beneficial for almost all potential applications of these functional materials. Thus in order to motivate the investigations shown later, some potential applications are presented below. Note, that the aim is not to give a complete overview, but rather to expose *snapshots* of former studies inspiring later investigations.

Storage and Separation

One of the primary research fields of MOFs was, and still is, gas storage [36, 37]. Both the high porosity and their enormous specific surface area make these materials promising candidates in this particular application. In this context the storage of hydrogen in MOFs, as an efficient energy carrier for the future, is probably the most investigated system. These studies are further encouraged by the targets defined by the Department of Energy (DOE) [36]. However, detailed investigations put into perspective the initial hope to achieve these targets primarily by the physisorption

of hydrogen on the high surface areas of MOFs. One important result of the mostly theoretical studies [38], is that for an efficient storage at room temperature an adsorption energy of about 20 kJ/mol [36] is needed, which is in the intermediate range between physisorption and chemisorption. The current materials allow the fulfillment of the target by the DOE only at very low temperature (77K). To increase the binding energy, several possibilities such as the use of unsaturated metal sites in the MOF backbone [39–42] or the doping of the matrix with metal atoms [38, 43–45], were developed. Besides the storage of hydrogen other molecules like methane (as an energy carrier) or carbon dioxide (as a green house gas) were studied [37].

Although the focus is currently on the adsorption of gases, which weakly interact with the network, the high porosity and the often large pores allow the uptake of molecules like dyes [46, 47], too⁷. One interesting point is the use of porous materials in pharmaceutical applications e.g. as vessels for drug delivery [48]. MOFs allow the storage and release of them in a controlled manner (Fig. 1.7) [49]. Being often large molecules with aromatic groups, they interact strongly with the backbone of the MOFs in contrast to small molecules like hydrogen or methane.

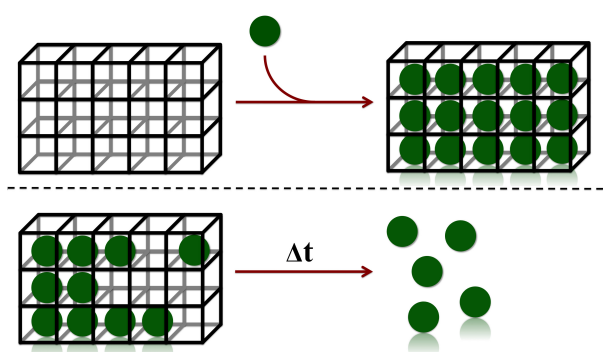


Figure 1.7: Controlled storage and released of guest molecules by MOFs.

So far, very few systematic studies have been carried out to understand the interaction of larger guest molecules within the pore system [50–52]. In fact, the results would help to optimize the compound as a storage media as well as for the separation of liquid mixtures. Their tunability is ideal for the use as membranes or columns in chromatography. Studies on the separation of gas mixtures (like CO_2/N_2) are well-known from the literature [37, 53–59], but detailed investigations on the adsorption of, for instance, aromatic guest molecules in MOFs are still rare [60–62].

One advantage of MOFs, compared to inorganic porous materials, is the possibil-

⁷Note, that the potential for the uptake of molecules strongly correlates with the ratio between molecule size and pore opening, if the framework is rigid. In addition, the interaction between the host and the guest molecules influence the adsorption process.

ity to introduce systematically functional groups into the framework, which influence the pore character (e.g. exchange of a hydrophobic group by a hydrophilic one). Therefore adsorption and separation properties of the porous media can be tuned, not only by the change of pore shape and size, which is the approach usually used in zeolite chemistry, but by the specific tailoring of the host-guest interaction. Using the building block approach (Fig. 1.1) the *communication* between the adsorbate and the matrix can be optimized, so that, for example, mixtures with tiny differences (e.g. chiral molecules) can be separated. Thus for the rational application of MOFs as storage or separation media, an understanding of the host-guest interactions with respect to the ordering and the mobility of the guest molecules within the pores, is essential.

Catalysis

The tunable porosity and the hybrid nature of MOFs allow to use the matrix either as a support or as an active partner in reactions (Fig. 1.8). The latter is observed in MOFs with unsaturated metal sites⁸, but also when appropriate functional groups (like amine groups) are embedded in the framework. These reactive centers can either undergo reactions (e.g. post-synthetic modification of the network [63]), which enable the modification of pore features (e.g. polarity) [64], or act as catalysts [65]. Embedding the catalytic site in a molecular environment allows to tune its performance as in the case of homogeneous catalysis by introducing, for instance, a chiral group near the reactive center [66]. However, in contrast to non-periodic homogeneous catalysis, the arrangement of the active sites in MOFs is well ordered. Both their distance as well as their orientation can be controlled, making synergetic effects possible. Furthermore the pore shape and size allow to influence the selectivity toward desired products.

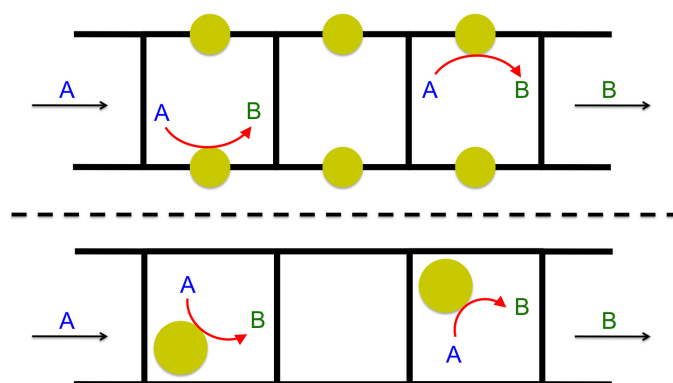


Figure 1.8: Schematic representation of MOF based catalysts.

⁸The vacant site is obtained after complete removal of the solvent molecules from the pores.

The porous materials can be *activated* as well by introducing active guest species, which are stabilized by the matrix via non-covalent interactions. One example for these kinds of MOF-based catalysts are the so-called *Metal@MOF* systems [67–69]. In this case the pores are loaded with metal nanoparticles. To obtain these composite materials two strategies are possible. One is the physical vapor deposition of metal atoms. The second one is the chemical infiltration using metal precursors [70], which are decomposed within the pores of the MOF by either photo-, thermal or chemical techniques [67, 69]. Using systems which are not completely saturated by the nanoparticles the porosity is maintained to some extent, so that molecules can reach the active centers on the surface of the metal particles and undergo reactions. Further the confinement by the pores and the host-guest interaction can be used to encapsulate reactive species (e.g. metalloporphyrins) within the matrix [52, 71].

To enhance systematically the performance of MOF-based catalysis, a detailed knowledge of the reaction mechanism at the active center is needed, but at the same time the mobility and the alignment of all reactants within the pores have to be studied.

Dynamic molecular vessel

MOFs having both a well-ordered framework and structural flexibility are sometimes termed **soft porous crystals** (SPCs) [28]. As mentioned in the previous section, the exchange or removal of guest molecules can significantly influence the structure of coordination polymers (Fig. 1.5). In the case of SPCs, the system has two or more stable phases, where at least one of them has crystalline properties. By external stimuli like electric fields or adsorption of guest molecules the phase transition of the network occurs (Fig. 1.9a).

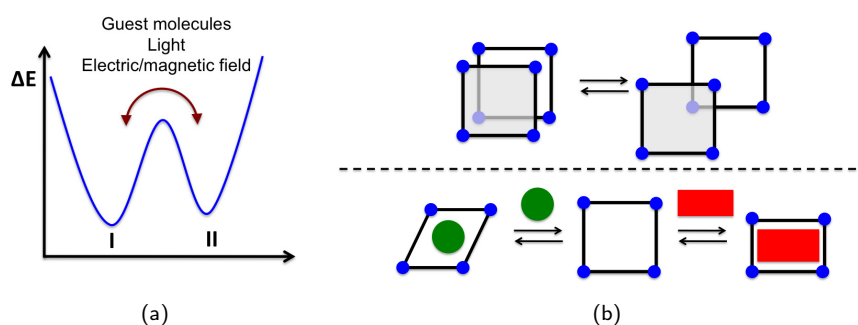


Figure 1.9: (a) Schematic representation of the energy landscape of soft porous crystals. (b) Different types of structural flexibility.

Different kinds of reversible structural dynamics are possible. One example may

be observed if two or more networks are interpenetrated (Fig. 1.9b). Since there is no strong bonding between the frameworks, the individual parts can be displaced against each other. Due to non-bonding interactions the movement is inhibited, so that phenomena like hysteresis can be observed, which can be used for selective adsorption [26]. Similar properties can be observed, if the framework can expand or shrink (Fig. 1.9b) depending on conditions like temperature or adsorbed molecules [72, 73].

In some cases the structural transformation is less pronounced, but its consequences are farreaching. In a recent example the group of Kitagawa showed how apparently little flexibility can influence the polymerization reaction of *p* – *divinylbenzene* [74]. Just by changing the metal center (*M*) in the porous coordination polymer $[M_2(1,4\text{-benzenedicarboxylate})_2(1,4\text{-diazabicyclooctane})]_n$, from copper to zinc, the framework gains some degree of flexibility in the inorganic unit. As a result the polymerization is topotactic in the flexible system, whereas in the other stiff network the reaction is not selective. Note, that the MOF itself does not take part in the reaction. It is only the ability of the flexible framework to influence the arrangement of the guest molecules in a favorable manner, which controls the reaction.

Another example for structural flexibility is the rotation of unit, which are part of the network [75–78]. These groups are well-ordered within the periodic scaffold but their motion does not influence the overall network topology. However physical properties can change by this structural transformation. On the one hand the rotation, which is often an activated process, can be influenced the adsorption and diffusion of guest molecules. On the other hand external stimuli such as electric or magnetic fields can have an impact on the rotation, which can cause, for example, the modification of the dielectric properties of the MOF.

To control the dynamic features of SPCs a detailed knowledge of the structural properties and the host-guest interactions is crucial, since the flexibility of the MOF matrix can influence the performace of these materials in different areas such as mixture separation.

MOF-Surface and Sensing

So far the porous coordination polymers were considered as infinite materials. This is for sure not the case in a real material, but since in most applications like gas storage the surface of the materials can be neglected, the focus is on the understanding of bulk properties. Nevertheless, in some potential applications such as sensing the surface has a significant fraction of the whole material. The possibility to tune the pore size, shape and functionality of MOFs enables the development of devices, which respond selectively. In addition, specific detection is possible since

the properties of some MOFs change by external conditions (see above). In general three different approaches are possible to synthesize thin films of MOFs on substrates [79]: (a) simultaneous growth and deposition of the MOF within e.g. a solvothermal synthesis, (b) assembling of preformed MOF units and (c) the growth by a layer-by-layer technique⁹. The latter can also be an important tool to explore the nucleation and growth mechanism. In this context it should be kept in mind, that although the MOFs are solid compounds, they have distinct molecular properties, which dominate possible surface terminations and thus differ significantly from metallic or ionic surfaces.

Probably the first example of a sensor based on MOF thin films has been developed by Allendorf et al. [80].

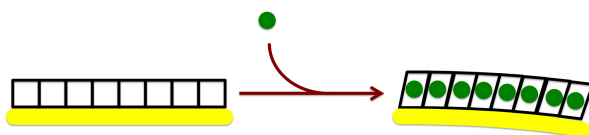


Figure 1.10: Structural change of a MOF thin film, which is grown on a substrate, by adsorption of molecules.

They deposited a thin film of $[Cu_3(\text{benzene} - 1,3,5 - \text{tricarboxylate})_2]_n$, formally known as HKUST-1, on a cantilever. The resultant device is able to selectively detect alcohols or water molecules due to the fact that their adsorption causes a very small, but for the underlying cantilever sufficiently large, structural transformation (Fig. 1.10).

⁹By stepwise and alternating addition of each reactant, the MOF is grown.

Part I

Theoretical Methods

Scientists often deal with processes, which take place on different time and length scales. In atmospheric chemistry, for example, reactions occur on an atomic level, however the resulting weather phenomena spread out over countries or even continents. In addition, the latter takes place in hours or years in contrast to the elementary reactions, which occur in picoseconds. In the case of MOFs similar multi-scaling phenomena are observed. During the often solvothermal synthesis single crystals or powder samples are obtained, which can be examined with the naked eye. Nevertheless, the overall structure and the macroscopic properties of the compounds are governed by local and molecular features (Fig.1.11). To get an overall picture of these kinds of problems and to bridge the gap between the macroscopic observations and the elementary reactions, investigations of different time and size regimes are crucial (Fig.1.11).

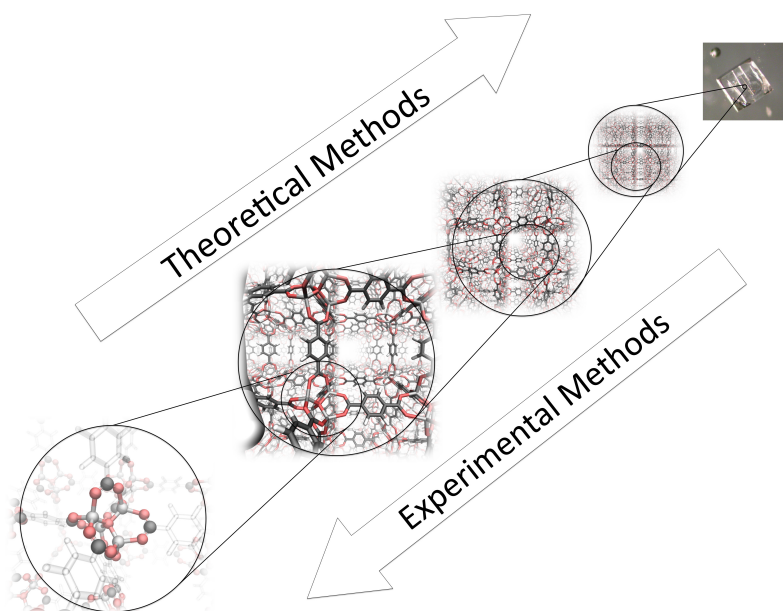


Figure 1.11: Illustration of different length scales using the example of MOF-5 (silver: zinc; red: oxygen; black: carbon; white: hydrogen atoms).

A wide range of diverse possibilities to study different aspects of a (chemical) system are known experimentally. The starting point of these studies is usually the synthesis of the material. Based on the obtained compound, which can be analyzed macroscopically (e.g. color change), different spectroscopical or diffraction methods are used to increase the time and size resolution to allow an insight into the system (Fig.1.11). In addition to these post-synthetic techniques, *in-situ* measurements are gaining more attraction, but are still rare due to their technical difficulties.

Beside experimental research, theoretical approaches are crucial in almost every scientific field. One example is the simulation of car crash tests, which enables fast and cost efficient studies. Dealing with atoms or molecules, quantum-mechanical (QM) simulations allow the investigation of their structure and reactivity in detail, which is sometimes difficult or not even possible to perform in an experimental set-up. Unfortunately, highly accurate QM methods are due to their complexity limited to systems with few atoms and degrees of freedom. Therefore to enable theoretical investigations of large systems on a reasonable time scale, different approximations or coarsening steps are needed. With the advancement of computer resources different simulation tools have been developed to study various subjects using appropriate approximations. Regarding the simulation of crash tests, the car is of course not treated with respect to the atoms but rather with a so-called finite element method, which has adjustable parameters to describe the considered system properly. Since the developed methods often skip or treat certain phenomena (e.g. correlation effects) merely in an effective way, choosing the proper methods before performing a simulation is important; especially if one tool is not able to handle the desired phenomena at all (e.g. the finite element method cannot treat chemical reactions). Note that a appropriate decision is also important in the area of experimental studies¹⁰.

Since approximations within the used theoretical method are needed for the simulation of almost all chemically relevant processes, often the confidence in experimental observations is stronger compared to the results from theoretical studies. A *good* theoretical method thus seems to be the one, which is able to reproduce the obtained data from measurements. Based on this assumption experimental data are often used as references to adjust theoretical tools. However, as chemistry is a multi-scaling discipline, besides the question of which method is appropriate in order to obtain reasonable results, one has to define the present system as accurately as possible. For an elementary discussion, the composition of the system, the basic structure or arrangement of units and relevant boundary conditions (e.g. time scale) must be known. For instance, the presence of defects or impurities can influence the performance of a compound. Experimentally, the tailoring and detection of these features is often not straightforward and a systematic study of small impurities is difficult. In contrast to this, theoretical models allow the investigation of well defined systems. Thus one basic question should always be addressed when comparing experimental and theoretical results: Are both systems equal? One simple example, which might lead to disagreements, is, if the time scale chosen for the simulation is too short allow the desired questions to be answered (e.g. formation of nanoparticle). In this case the error is not due to the used methods.

Experimental studies can have the drawback that the resolution is not high

¹⁰For example, the use of X-ray diffraction methods to study local properties is not appropriate.

enough to define all boundary conditions, making comparison difficult. One example concerning MOFs is the evaluation of adsorption studies. Impurities (e.g. remaining solvent molecules) or defects (e.g. partial decomposition) can significantly influence the amount of adsorbed molecules. Since simulations usually do not include these features, discrepancies are almost inevitable. Therefore one has to doubt whether a *good* theoretical method *always* reproduce experimental findings and one should be careful to use experimental data to fit theoretical models. In addition one should keep in mind, that for the interpretation of measured data often theoretical concepts (e.g. Brunauer-Emmett-Teller theory [81]) are used to obtain the desired properties (e.g. surface area). However these models are only valid within their assumptions, which might not be fulfilled by the considered system.

To overcome the gap between theoretical and experimental results both fields have to improve their methods to allow a consistent picture of the system over different time and length scales. In the current work on MOFs, the focus is to start stringently from high level theoretical methods, which are known with respect to their accuracy, and to use the obtained data to *teach* a less expensive, lower level of theory, so that large systems can be treated. In the sense of length and time scale bridging multi-scale simulations [82], it is decided to use a coarse grained model, which ignores the actual electronic structure of the system. In all of the considered systems the connectivity between the atoms is conserved, so that a bonded and classical model is used.

Further, defined structures, which are either known or not yet observed experimentally, are investigated using the developed methods. To approximate the macroscopic crystal structure periodic boundary conditions are used [83]. The obtained results are in a second step compared with experimental observations. Similarities as well as differences between the results allow a detailed understanding the properties of MOFs. Moreover, due to the complexity of the porous coordination polymers, experimental studies of, for instance, mechanic or thermal properties of these materials are difficult with respect to well defined boundary conditions (e.g. crystal quality). In this regard allow the theoretical investigations, although limited in size and time scales, the analysis and to pre-screen some characteristic features of the compounds.

In the following, the theoretical methods used in this work are presented. Since a large number of textbooks and reviews are available describing the tools in detail, only a brief overview is provided, here.

Chapter 2

Quantum Mechanical

2.1 Wavefunction based methods

To describe a chemical system on a quantum mechanical level wavefunction based methods can be used. In this case often the stationary Schrödinger-equation is solved:

$$\hat{H}\Psi = E\Psi, \quad (2.1)$$

with the Hamiltonian \hat{H} in atomic units [84]:

$$\hat{H} = -\frac{1}{2} \sum_{i=1}^N \vec{\nabla}_i^2 - \sum_{\alpha=1}^P \frac{1}{2M_\alpha} \vec{\nabla}_\alpha^2 + \sum_{\alpha>\beta}^P \frac{Z_\alpha Z_\beta}{R_{\alpha\beta}} - \sum_{\alpha,i}^{P,N} \frac{Z_\alpha}{r_{\alpha i}} + \sum_{i>j}^N \frac{1}{r_{ij}}, \quad (2.2)$$

(∇ = Laplace Operator, P = Number of nuclei; N = Number of electrons; M_α = ratio of the mass of the nucleus α to the mass of a electron).

The first and second term is the kinetic energy of the electron and nuclei, respectively. The third term describes the nuclei-nuclei interaction. The potential of the nuclei acting on the electron is represented by the fourth term and the final term covers the electron-electron interaction. Based on the Born-Oppenheimer approximation, the motion of the nuclei and electrons can be decoupled due to the large difference in their mass. Thus the wavefunction can be separated:

$$\Psi(\vec{r}; \vec{R}) = \Phi(\vec{R}) \cdot \chi(\vec{r}; \vec{R}). \quad (2.3)$$

The electronic wavefunction χ depends in this case parametrically on the position of the nuclei. \vec{r} and \vec{R} are general coordinates. Since the nuclei are frozen within the Born-Oppenheimer picture, the second term of the Hamiltonian vanishes. The nuclei-nuclei interaction can be reduced to a constant term (V_{NN}). Using this approximation the electronic Schrödinger equation can be written as

$$\hat{H}_{el}(\vec{r}; \vec{R}) \chi(\vec{r}) = E_{el}(\vec{R}) \chi \quad (2.4)$$

with the Hamiltonian \hat{H}_{el}

$$\hat{H}_{el} = -\frac{1}{2} \sum_{i=1}^N \nabla_i^2 - \sum_{\alpha,i}^{P,N} \frac{Z_\alpha}{\vec{r}_{\alpha i}} + \sum_{i>j}^N \frac{1}{\vec{r}_{ij}}. \quad (2.5)$$

Thus the total energy can be expressed as

$$\left[\hat{H}_{el}(\vec{r}; \vec{R}) + V_{NN}(\vec{R}) \right] \Psi(\vec{r}; \vec{R}) = \left[E_{el}(\vec{R}) + V_{NN}(\vec{R}) \right] \Psi(\vec{r}; \vec{R}). \quad (2.6)$$

The simplest solution of this eigenvalue problem and simultaneously taking care of the Pauli-principle, which is crucial to cover the nature of the electrons, is the single-determinant approach (Hartree-Fock (HF)). Since in this case the variational principle can be used systematic improvements of the wavefunction are possible. Based on the Hartree-Fock method more sophisticated so-called post-Hartree-Fock methods are developed. One, which is also used in this work, is based on the Rayleigh Schrödinger perturbation theory [84]. Within the perturbation theory, which is not variational, the total Hamiltonian of the system is separated into parts. The so-called zeroth-order Hamiltonian \hat{H}_o has known eigenfunctions and eigenvalues, but does not cover the whole nature of the system. The remaining contributions are treated by a perturbation \hat{V} . The total Hamiltonian is thus

$$\hat{H} = \hat{H}_o + \lambda \cdot \hat{V}, \quad (2.7)$$

and the eigenvalue problem, which has to be solved is

$$\hat{H}\Psi = [\hat{H}_o + \lambda \cdot \hat{V}] \Psi = E\Psi, \quad (2.8)$$

where λ is an ordering parameter. The exact eigenvalue and eigenfunction of the ground state can be expanded in terms of the perturbation in a Taylor series as

$$E_0 = E_0^{(0)} + \lambda \cdot E_0^{(1)} + \lambda^2 \cdot E_0^{(2)} + \dots \quad (2.9)$$

$$\Psi_0 = \Psi_0^{(0)} + \lambda \cdot \Psi_0^{(1)} + \lambda^2 \cdot \Psi_0^{(2)} + \dots \quad (2.10)$$

The values in bracket are called the order of perturbation. If these expressions are inserted into the eigenvalue problem and ordered according to the λ^n a hierarchy of energy expressions can be obtained. Since it is assumed that in the zeroth-order part the major contributions are considered the relevance of higher order perturbation energies should decrease. In the case of the Møller-Plesset (MP) perturbation theory, the one-electron HF energy is taken as the zeroth-order energy. The full HF approach represents the first order perturbation. At MP2 level the interaction of the HF ground state with excited wavefunction is considered [84, 85]. However, in this *standard* MP2 the description of the dynamic and static electronic correlation effects is not balanced, since Fermi correlation is already included in the HF theory. To compensate this effect to some degree the **spin-component scaled** (SCS) MP2 approach is developed, in which the second-order parallel ($\alpha\alpha + \beta\beta$) and anti-parallel-spin ($\alpha\beta$) pair correlation energies are scaled separately [86]. The SCS-MP2 energy is obtained by adding the HF energy to

$$E_{SCS}^{(2)} = p_T \left(\sum e_{\alpha\alpha}^{(2)} + \sum e_{\beta\beta}^{(2)} \right) + p_s \sum e_{\alpha\beta}^{(2)}, \quad (2.11)$$

where p_T and p_s are empirical parameters.

2.2 Density Functional Theory

The basic of the Kohn-Sham Density Functional Theory (DFT) are the two theorems of Hohenberg and Kohn. The first theorem proves, that the electron density ρ of a system defines the Hamiltonian. The second one deals with the variational principle

in the DFT. The energy of the electronic ground state E_0 can be expressed as a functional of the density ρ :

$$E_0 [\rho_0] = T [\rho_0] + E_{Ne} [\rho_0] + E_{ee} [\rho_0]. \quad (2.12)$$

This functional would reveal an exact solution of the energy, if all terms were known. The expression of E_{Ne} , which describes the interaction between nuclei and electrons, is the only one, which is known exactly. The functional for the kinetic energy T and the term for electron-electron interaction E_{ee} are not known. The latter can be divided into two contributions

$$E_{ee} [\rho_0] = \frac{1}{2} \iint \frac{\rho(\vec{r}_1) \rho(\vec{r}_2)}{|\vec{r}_1 - \vec{r}_2|} d\vec{r}_1 d\vec{r}_2 + E_{ncl} [\rho_0] = J [\rho_0] + E_{ncl} [\rho_0], \quad (2.13)$$

the first term is the classic Coulomb interaction J_0 , the second term E_{ncl} covers the non-classic contributions, which are purely of quantum mechanical nature. The functional form for the kinetic energy of a non-homogeneous electron density, which is present in a chemical system, is so far unknown. To circumvent this problem Kohn and Sham developed an approximation, which lays the grounding for the breakthrough of DFT methods in chemistry [87, 88]. They introduced for the calculation of the kinetic energy a reference system of non-interacting electrons. It should cover the major part of the kinetic energy. The electron density of this reference system ρ_0^{KS} , which must be equal to the one of the real systems, is expressed in one electron wavefunctions φ

$$\rho_0^{KS}(\vec{r}) = \sum_i^N (\varphi_i)^2 \quad (2.14)$$

and the kinetic energy T_{KS} is given as

$$T_{KS}(\vec{r}) = -\frac{1}{2} \sum_i^N (\varphi_i | \nabla^2 | \varphi_i) \quad (2.15)$$

Using this approximation the total energy can be written as

$$E [\rho_0] = T_{KS} [\rho_0] + J [\rho_0] + E_{XC} [\rho_0]. \quad (2.16)$$

The last term E_{XC} , which is called exchange-correlation functional, contains all unknown contributions (e.g. differences in the kinetic energy between real and reference system) and is assumed to be minor compared to the known part. Using the Kohn-Sham operator \hat{H}_{KS}

$$\hat{H}_{KS} = \frac{1}{2}\nabla^2 + \int \frac{\rho_0}{r_{12}^2} d\vec{r}_2 + V_{xc}(\vec{r}_1) + \sum_{\alpha}^P \frac{Z_{\alpha}}{r_{1\alpha}}, \quad (2.17)$$

in which

$$\hat{V}_{KS} = \frac{\partial E_{XC}}{\partial \rho}, \quad (2.18)$$

the wavefunctions φ (Kohn-Sham orbital) can be derived by

$$\hat{H}_{KS}\varphi_i = \epsilon_i\varphi_i. \quad (2.19)$$

A number of different exchange-correlation functionals are developed. Beside localized density approximations (LDA) and gradient corrected ones (GGA; e.g. BLYP [89, 90]), hybrid functionals are often used in chemistry [87, 88]. The B3LYP functional [91] is one of the famous one, which is based on an empirical combination of an LDA (VWN [90]) and GGA (Becke88 [89], LYP[92]) functional with the exact exchange integral of Hartree-Fock. The hybridization schemata for the exchange-correlation functional of is given by

$$E_{xc}^{B3LYP} = E_{xc}^{LDA} + a_0(E_x^{HF} - E_x^{LDA}) + a_x(E_x^{GGA} - E_x^{LDA}) + a_c(E_c^{GGA} - E_c^{LDA}), \quad (2.20)$$

where a_0 , a_x , a_c are empirical parameters fitted to experimental data.¹

But the presented functionals are not able to describe dispersion interactions, thus often empirical corrections or sophisticated functionals like double-hybrid functionals are used. The B2PLYP [95] is one type of double-hybrid functionals, in which the orbital information from a DFT calculation is used for a second-order Møller-Plesset perturbation theory calculation (PT2). The B2PLYP exchange-correlation energy is defined as

¹Note, that the parameters of the B3LYP functional are different in the TURBOMOLE [93] and gaussian03 code [94].

$$E_{xc}^{B2PLYP} = (1 - a_x)E_x^{GGA} + a_x E_x^{HF} + bE_c^{GGA} + cE_c^{PT2}. \quad (2.21)$$

with the empirical parameters a_x , b , c .

Chapter 3

Classical Mechanical

3.1 Force Fields

3.1.1 The basic concept

The basic of classical methods is the assumption, that the total energy of a system can be separated into additive parts. All interactions are composed of one, two, three or many body-contributions. The types of interaction, which are present in a chemical system, can be roughly divided into two categories: bonding and non-bonding ones. The total potential energy is the sum of them

$$E_{pot} = E_{bonding} + E_{non-bonding}. \quad (3.1)$$

Further each interaction of the two main categories is described by a single analytic function and corresponding adjustable parameters. This approach of describing the potential energy is usually termed **force field (FF)**. In this study an extended MM3 [96] force field expression is used. Thus the bonding interaction is subdivided according to

$$E_{MM} = \sum_b E_b^{stretch} + \sum_a (E_a^{bend} + E_a^{str-str} + E_a^{str-bnd}) + \sum_o E_o^{opb} + \sum_t E_t^{tors}, \quad (3.2)$$

where b runs over all bonds, a over all bond angles, o over all out-of-plane bends on trigonal centers and t over all torsions.

For the bond stretch terms, a cubic term

$$E_b^{stretch} = \frac{1}{2}k_b(r_b - r_b^{ref})^2 \left[1 - 2.55(r_b - r_b^{ref}) + \frac{7}{12} \left(2.55(r_b - r_b^{ref}) \right)^2 \right], \quad (3.3)$$

is used, where r_b is the bond distance, k_b the force constant and r_b^{ref} the corresponding reference distance.

For bond stretches a six order polynomial is used

$$E_a^{bend} = \frac{1}{2}k_a(\theta_a - \theta_a^{ref})^2 [1 - 0.14(\theta_a - \theta_a^{ref}) + 5.6 \times 10^{-5}(\theta_a - \theta_a^{ref})^2 - 7 \times 10^{-7}(\theta_a - \theta_a^{ref})^3 + 2.2 \times 10^{-8}(\theta_a - \theta_a^{ref})^4], \quad (3.4)$$

where θ_a is the bond angle, k_a the force constant and θ_a^{ref} the reference angle.

Again, according to the MM3 scheme, for trigonal centers the bond angle θ_a is actually taken as the projection into the trigonal plane. Correspondingly, for these sites an additional out-of-plane bending term, using the Wilson-Decius definition for the out-of-plane angle θ_o is employed. The out-of-plane energy term E^{opb} is identical to the six order polynomial for the in-plane bending (Eq. 3.4) with the difference that θ_o^{ref} is always zero.

Cross terms, which describe the coupling of different degrees of freedom, are only included for adjacent bonds and bond angles. For three connected atoms A-B-C of a bond angle a the distance r_{a1} refers to the distance A-B, and r_{a2} to the distance B-C. Note, that the reference distances r_{a1}^{ref} and r_{a2}^{ref} are the same as r_b^{ref} for the same bond type

$$E_a^{str-str} = k_{ss}(r_{a1} - r_{a1}^{ref})(r_{a2} - r_{a2}^{ref}) \quad (3.5)$$

$$E_a^{str-bend} = [k_{sb1}(r_{a1} - r_{a1}^{ref}) + k_{sb2}(r_{a2} - r_{a2}^{ref})](\theta_a - \theta_a^{ref}). \quad (3.6)$$

Torsions are computed using the usual Fourier term

$$E_t^{tors} = \sum_n \frac{V_t^n}{2} [1 + \cos(n\tau_t + \tau_t^n)], \quad (3.7)$$

where V_t^n and τ_t^n are the energy barrier and the phase shift, respectively, for the n -fold term with τ_t being the torsion angle of torsion t . In some simple cases only the two-fold torsion term was needed.

The non-bonding term is constructed by two terms

$$E_{non-bonding} = \sum_n (E_n^{vdw} + E_n^{coul}). \quad (3.8)$$

The first summand describes the **van der Waals** (vdW) interaction and the second one the Coulomb interaction. The sum in the equation runs over all non-bonded pair interactions n , with the bonded 1-2 and 1-3 interactions excluded. Following MM3 in case of hydrogen, the center of the vdW interaction is moved along the X-H bond by a factor of 0.923 towards X. For the Coulomb interactions point charges are used¹ and for the vdW interactions the MM3 type Buckingham potential is employed.

$$E_n^{coul} = \frac{1}{4\pi\epsilon} q_1 q_2 \frac{1}{d_n} \quad (3.9)$$

$$E_n^{vdw} = \epsilon_n \left[1.84 \times 10^5 e^{-12 \frac{d_n}{d_n^0}} - 2.25 \left(\frac{d_n}{d_n^0} \right)^6 \right] \quad (3.10)$$

Here d_n is the distance of the two atoms of interaction n , q_1 and q_2 are the atomic charges and ϵ_n and d_n^0 the well depth and minimum distance, respectively. For heteroatomic vdW-interactions the standard Lorenz-Bethelot mixing rules are adopted (arithmetic average of d_n^0 and geometric average of ϵ_n). A cutoff of 12.0 Å is used for the vdW and short ranged electrostatic interactions. The long range electrostatic interaction is computed by a smooth particle mesh Ewald summations [97].

3.1.2 Force Field Development using a Genetic Algorithm Technique

As already pointed out, the force field parameters are derived from quantum mechanical reference data according to 98. In this context, the focus is to *teach* the classical model both the geometry and the normal modes. The latter is of particular interest, since the investigated MOFs have, in contrast to the inorganic porous materials (e.g. zeolites) structural flexibilities. These dynamic properties of the framework are covered mainly by the Hessian matrix, which describes the curvature at a point on the energy hypersurface (second derivative with respect to the atomic coordinates). In some works [99] the values from the Hessian matrix are directly converted to obtain the force constants. But the drawback in these approaches is

¹Except in the case of the study on isorecticular isomer of IRMOFs, where bond dipoles were used, according to the MM3 force field.

the difficulty of extracting the relevant information from the matrix. Using quantum mechanical results within a fitting procedure allows to get force field parameters without the problem of selecting specific elements of the Hessian. In this case either a systematic search or stochastic method is needed to parametrize the force field. Genetic algorithms (GAs), which are the most popular class of evolutionary algorithms, are an example of the latter [100]. These heuristic search techniques are motivated by biological processes. Thus operations like selection, crossover or mutation of a *gen* are done in a computational setting to deal with the search problem. The crucial point is the definition of a quality criterion of a *individual* - the fitness. Thus a objective function (OF) is introduced, which includes the relevant data of the considered problem. An example for an OF would be to use the deviation of a bond length obtained from the force field with the corresponding quantum mechanical counterpart. The Hessian matrix can be treated in the same manner within the OF. However the use of the cartesian matrix is unsuitable, since relevant data for the fitting procedure are buried under many off-diagonal elements. Using the Hessian matrix in a complete (redundant) internal set allows to assign the information from the second-derivative matrix to specific force field terms (e.g. bond term). In the current work both structural as well as curvature data are projected into this basis, which is defined by the connectivity used in the force field, and included into the OF. This approach allows to extract relevant data from the reference considering the form of the molecular mechanic model.

The projection of the Hessian matrix in cartesian coordinates (F_x) into the set of internal coordinates (F_R) is done by

$$F_R = (B^T)^{-1} F_x B^{-1} \quad (3.11)$$

(matrix notation) [101], where B is the Wilson's rectangular matrix ($3N \times M; M > 3N; N = \text{Number of atoms}, M = \text{Number of internal coordinates}$) [102], which transfers the rectilinear Cartesian coordinates to a redundant set of curvilinear internal coordinates. Note, that the transformation is unique for a given set of internal coordinates, if the B-matrix has full rank ($=\min(3N, M)$) and the translational and rotational degrees of freedom are projected out.

Based on this, the calculation of the fitness can be divided into five steps. First, the geometry of the considered model system is optimized using the functional form of the force field and a trial set of parameters. Second, the Hessian matrix is calculated in cartesian coordinates, which is in the third step transformed together with the cartesian coordinates into the principal axes system. Both are then convert from cartesian data into a predefined set of redundant internal coordinates. The last step is the calculation of the sum of mean square deviations (MSDs) between

the trial solution and the reference data:

$$\begin{aligned}
 \chi^2 = & \frac{w_{bonds}}{N_{ref}^{bonds}} \sum_{i=1}^{N_{ref}^{bonds}} (r_i^{MM} - r_i^{ref})^2 + \frac{w_{bends}}{N_{ref}^{bends}} \sum_{j=1}^{N_{ref}^{bends}} (\alpha_j^{MM} - \alpha_j^{ref})^2 \\
 & + \frac{w_{wags}}{N_{ref}^{wags}} \sum_{k=1}^{N_{ref}^{wags}} (\theta_k^{MM} - \theta_k^{ref})^2 + \frac{w_{tors}}{N_{ref}^{tors}} \sum_{l=1}^{N_{ref}^{tors}} (\phi_l^{MM} - \phi_l^{ref})^2 \\
 & + \frac{w_{diag}}{N_{ref}^{diag}} \sum_{m=1}^{N_{ref}^{diag}} (F_m^{MM} - F_m^{ref})^2 + \frac{w_{cross}}{N_{ref}^{cross}} \sum_{n=1}^{N_{ref}^{cross}} (F_n^{MM} - F_n^{ref})^2. \quad (3.12)
 \end{aligned}$$

This procedure is embedded in the genetic algorithm, which is performed in a loop mode (Fig. 3.1). The stopping criteria for the GA is either based on thresholds for the single sums of the MSDs or by defining a fixed number of generations.

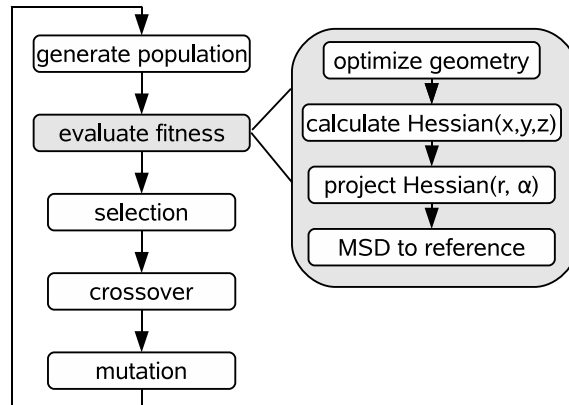


Figure 3.1: Flowchart for the force field parametrization

3.2 Molecular Dynamic Simulation

The equation of motion describes the time evolution of a system. The oldest formalism, in the framework of classical mechanics, is the Newton equation of motion from 1687 and uses the force $\vec{F}(\vec{r}, t)$ to describe the system

$$m \frac{\partial^2 \vec{r}}{\partial t^2} = \vec{F}(\vec{r}, t). \quad (3.13)$$

By integrating this equation in time the motion of the systems is obtained as a trajectory defining the system at each time. The force \vec{F} is defined as the derivative of the potential energy with respect to the position

$$\vec{F} = -\frac{\partial E_{pot}}{\partial \vec{r}}. \quad (3.14)$$

To calculate the forces different methods can be used e.g. quantum mechanical ones. Within the current work classical methods are used to derive the forces. They are further applied as the input for the numeric integration of the discredited equation of motion. By continuously integrating the equation of motion the dynamic of the system for the time $t = n \cdot \Delta t$ (n = number of steps; Δt = time interval) can be obtained. In this regard a modified Beeman propagator is used in this work [103] as implemented in the *tinker* code [104] with a timestep of 1.0 fs, which was checked to yield energy conserving microcanonic dynamics.

Note that in addition to the potential energy the kinetic energy must be considered in simulations at $T > 0^\circ C$. The selected temperature defines the kinetic energy of the system by

$$E_{kin} = \frac{1}{2}k_B T, \quad (3.15)$$

where k_B is the Boltzmann factor. Based on this the velocity v_i of each atom i is derived using a Boltzmann distribution. The average kinetic energy is

$$\frac{1}{2}mv_i^2 = \frac{1}{2}k_B T. \quad (3.16)$$

The total energy of the system results as the sum of potential energy and kinetic energy

$$E_{total} = E_{pot} + E_{kin}. \quad (3.17)$$

3.2.1 Self-diffusion constant and probability density

Molecular dynamic (MD) simulations were performed in order to investigate the host-guest interactions in various systems. Generally, the values obtained from a

preliminary lattice optimization of each system were kept fixed during the simulations, since a constant pressure dynamics run (NPT ensemble) considered systems showed only small oscillations of the lattice parameters. All MD simulations were performed in a NVE ensemble, whereas for every loading and temperature 10 independent trajectories were started from different configuration, generated from a high temperature simulation at 1000 K in each case, in order to avoid any correlations. The final analysis has been performed on the averaged data from all trajectories, whereas statistical errors have been calculated from the standard error of the 10 individual runs. The initial velocities were randomly generated according to a Boltzmann distribution at the given temperature. The first 500 ps were discarded as an equilibration period. From the 3 ns trajectories the last 2.5 ns were used for the analysis, with a configuration stored every 0.1 ps (every 100 timesteps). Thus, per trajectory a total of 25,000 configurations were stored and used for the further analysis.

The self-diffusion constant was computed according to the Einstein relation

$$D_{self} = \frac{1}{6} \lim_{t \rightarrow \infty} d/dt \langle |r(t) - r(0)|^2 \rangle, \quad (3.18)$$

by analysing the mean-squared displacement (MSD) curve using multiple time origins and time intervals from 0.1 ps up to 2500 ps, and by averaging over all values for a given time interval Δt and all particles. The jitter in the corresponding curves increases for larger Δt , because of the decreasing quality in the statistics as less datapoints are available. Thus, the slope of the MSD curves have been determined from a linear fit to the curves just in the range of time intervalls from $\Delta t = 250$ to 1000 ps, which is above the onset of the diffusive regime as verifying by a double logarithmic plot. The final values and the corresponding error bars have been calculated from the average over the uncorrelated trajectories. Note that the error is just an approximation, since the error in the self-diffusion is harder to sample than the value itself [?]. Therefore twice the standard error (standard deviation of the mean value) is considered as a good measure for the statistical accuracy.

The probability density was generated from the center-of-mass (COM) trajectories (with the COM positions folded back into the simulation domain) in a 803 point mesh and was analyzed and rendered with the program VMD [105]. To improve the statistics of the calculations the symmetry of the loaded framework was to symmetrize the probability densities if possible.

Part II

Understanding the structure of MOFs

Complexity of matter

Being able to think abstractly allows human beings to contemplate and discuss about very non-pictorial and complex topics. The visualization of convoluted topics is often possible by condensing a subject to its essential. This, of course, leads to the loss of information, but simultaneously, if the simplification is appropriate, it can lead to the attainment of knowledge and comprehension. Especially in science this form of abstraction is important, since the subjects are in most cases way beyond imaginable. By using different concepts, scientists are consistently able to discuss illustratively, new and elaborated research areas. Lewis structure formula [106], which enable the visualization of molecules, is one famous example in the field of chemistry. In this case, atoms are described by simple letters and chemical bonds by lines. This concept allows to gather the nuclei and the electrons, which are not easy to treat due to their quantum mechanical nature. Surprisingly, within the framework of Lewis structures it is even possible to describe chemical reactions in a qualitative manner by “flipping the lines”. But this ability also points out an intrinsic property of these kinds of techniques: obviously, an electron transfer reaction is a non-trivial process like the movement of lines. Thus the concept is just a caricature of the real system. This fact should be kept in mind when using these kind of tools in order to avoid overinterpretation. However, in science there are numerous examples how rather simple concepts (compared to the complexity of the system) enable the understanding of certain aspect of a topic, which would not be otherwise obvious, due to the intricacy of the overall subject. Based on the Lewis structure formula other tools are developed like the Valence Shell Electron Pair Repulsion (VSEPR) theory [107]. It allows to describe and understand the structure of chemical compounds by considering the repulsion of atoms and electrons pairs. Even general statements can be derived from the VSEPR theory like the tendency how the arrangement within a molecule is influenced by the exchange of an atom or group.

Going from discrete molecules to high dimensional macromolecules the complexity increases dramatically. In biochemistry, for example, proteins or the DNA (Deoxyribonucleic acid) are molecules, which consist of millions of atoms. In this

case the use of Lewis structures not reasonable to gain an insight. Thus, alternative methods are needed. By uniting atoms, which are either spatially or chemically close, groups can be determined, which allow to texture the large molecule. In the case of proteins, a basic approach is to allude the sequences of the repeating units - the nucleic acids. This type of coarsening allows the characterization and comparison of different proteins. In addition it also enables the systematical investigation of this class of molecules by studying the effect of specific variations. In this context, general concepts such as Ramachandran plots could be derived [108] to predict to some extent, the three dimensional shape of a protein by using solely the ordering of the nucleic acids within the chain (Fig. 3.2).

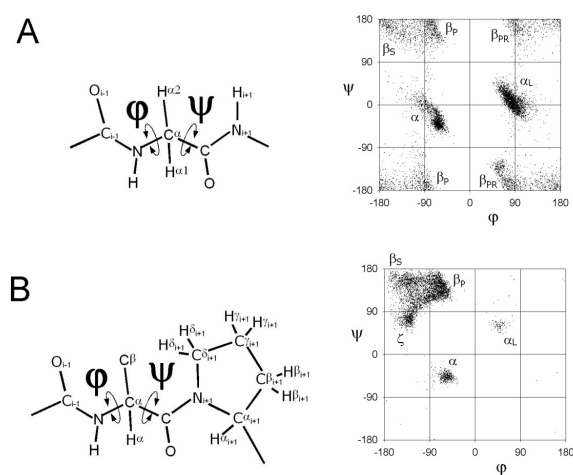


Figure 3.2: Ramachandran plot of (A) glycine and (B) pre-prolineHo and Brasseur [109]

Considering porous materials like zeolites and MOFs, the complexity of their structure is not minor, thus similar tools are desirable to understand these compounds. Deriving an overall concept in this field is very ambitious, due to the diversity of these materials. The starting point is to characterize the structure in a way, which points out the essential part of the structure. Finding repeating units, which are representative for the topology of the network, is one possible strategy. It allows to characterize and to enumerate the structure of these materials and consequently to compare different systems. The developed concepts are mainly motivated by Wells [110, 111], who laid by his pioneering studies dealing with both abstract networks and experimental results the foundation for further works. Since one feature of the porous materials is their open structure, the ring size of the pore opening is one common criterion used to describe the structure of zeolites. In this case Vertex or Schläfi symbols, for instance, are used to describe the ring sizes [112].

Regarding the hybrid porous materials exceptional complexity is usually present in the obtained structures. Extracting the essential information is thus often not obvious. Similar to the proteins, the approach is to skip the atomic resolution. In this case the molecular framework is lead back to a geometric graph. This concept, which is sometimes called topological approach (Fig. 3.3), is the state of the art in the enumeration of porous coordination polymers [112, 113]. In the first step the porous coordination polymer is simplified in the sense that all atoms not needed to keep the periodicity of the framework are removed. Secondly, repeating fragments of the network are determined, which are usually called **secondary building units (SBUs)**. The individual SBUs are afterwards analyzed with respect to their geometrical shape. Based on these results a topological investigation of the whole framework is performed.

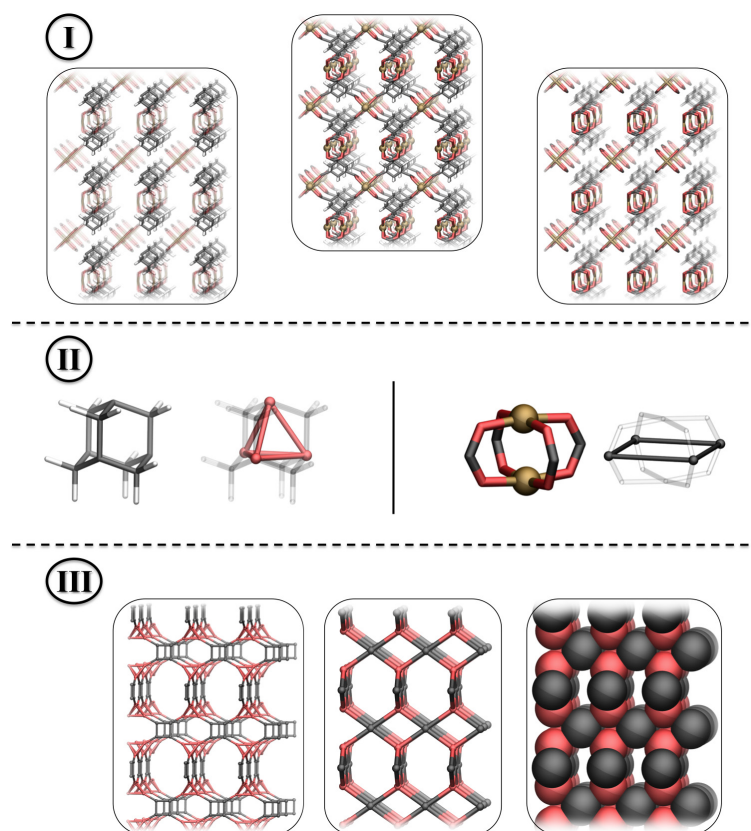


Figure 3.3: Topological approach

The derived network (or graph) can be seen as a blue print of the MOF ². It

²Note, the similarity to Lewis structure formula. The SBUs are similar to the atoms represented only by a node and linked by lines, which are called linkers in this context.

can be enumerated and characterized with respect to other known solids - either porous or non-porous. The nomenclature of the topology is based on a three letter code. In contrast to the zeolite community lower case letters are used (e.g. **pcu** for a primitive cubic network). The MOFs investigated in this work have all equal edge in their networks. In this case the net is *edge-transitive*, but other networks with different kinds of edges are also known [114]. Furthermore the underlying network topology is described according to the connectivity of the vertices. In a N,M-connected net, two kinds of nodes are present (binodal network). One kind is connected to N and the other to M neighbors.

A Reverse Topological Approach

Due to the size and insolubility of the products, the synthesis of extended structures like MOFs has to be performed in a self-assembling fashion. The use of discrete or well-defined building units, which are either part of the starting materials or obtained *in-situ* during the assembling reaction, has in this regard some advantages. The control of their size, shape and functionality can be used to modify the assembling process or maybe force the development of specific periodic systems. In the framework of a target-based approach the answer to the question “Which periodic structures can be obtained by using individual units?” is pivotal. Thus the enumeration of known materials with respect to their basic topology, which can be done routinely by the topological approach, is in this regard, as pointed out by Thomas et al., more than just a “*Fleißarbeit*” [115]. Detailed structural investigations rather allow the development of synthetic concepts, which support the idea of *engineering* new materials. In principle the knowledge about the possibilities to link simple geometrical object like octahedrons or squares to form periodic networks, allows to work out recipes for the synthesis of frameworks with targeted topologies, if reasonable *bricks* are available. Unfortunately, the number of combinations of connecting even just one kind of geometrical object is infinite [116]. But the analysis of a wide range of known MOF structures pointed out that in most cases high symmetric topologies are obtained [116], which motivates the idea of constructing new MOFs using rigid molecular SBUs with well-defined shapes. Although a number of examples are known where the apparent “*combinatorial symmetry*” [116] constrains the system to one or very few high symmetric topologies, porous coordination polymers are known with quite low network symmetries. For example, owns MOF-177 [47], which is built up by octahedral and trigonal SBUs, the **qom**-topology. This network graph has three different kinds of three-coordinating and two different kinds of six-coordinating nodes. Since the number of *known* MOFs structures is still few compared to the enormous quantity of thinkable systems and is continuously growing in the last years, the thesis of McCrone that the “*number of forms known*

for a given compound is proportional to the time and money spent in research of that compound" [117] might also be applicable to the field of porous coordination polymers. Indeed Caskey et al. [118] could show how the SBUs of the MOF-177 framework can lead to different topologies. The possibility of synthesizing frameworks with different periodic structure by the same bricks hampers the development of rational synthetic concepts. Note, that the structural diversity known from the zeolites, which are constructed mainly by Si_4O -tetrahedrons, is due to different connecting of this single unit. The recently developed class of ZIFs (zeolitic imidazolate frameworks), which is a subclass of the porous coordination polymers, shows similar structural features [24].

In addition to these topological considerations, molecular solids include other challenges. In the case of discrete molecules the possibility of *isomers* is known. Within this umbrella term, which describes the phenomena that compounds of the same molecular formula can occur in different structural forms, a number of isomeric types are defined to classify molecules and related compounds. One example in this case is the presence of *structural* (or constitutional) isomers. In this case the same atoms are assembled in different orders. In the field of macro-molecules like MOFs the term *supramolecular isomers* [119] is often used to describe similar structural features. In this regard Zaworotko and co-workers introduced four different categories [120]. According to the non-periodic systems the first class, which is termed *structural isomers*, describes the assembly of the same units, in this case SBUs, in different manners to obtain various networks. Further *catenated*³ and non-catenated networks were discriminated. The third category deals with the possibility of chiral networks and is paraphrased by the word *optical isomers*. Considering the molecular nature of the coordination polymers, *conformational isomers* are defined as periodic systems, which are built up by the same SBUs but these units occur in different conformeric forms (e.g. *gauche* and *anti* form of bis(4-pyridyl)ethane [119]) leading to different network topologies. Besides this heuristic approach, Schröder et al. [121] classified supramolecular isomers more generally with respect to the interactions present within the periodic system. First, using the same molecular units equal binding motives (e.g. metal-ligand coordination bond) can give rise to different networks. Second, in some cases the SBUs can interact via different functional groups, which cause the assembling of various topologies. Third, the influence of the packing of guest-molecules on the structure is considered.

Both concepts point out the need to classify the structure of porous coordination polymers systematically and motivate the idea to develop a general concept. In addition to topological descriptions, the concept should deal with the molecular nature of the system and should not be based on current experimental observations like the approach of Zaworotko. To elaborate the complexity of molecular solids a

³Catenation is just another term used to describe interpenetrated systems.

thought experiment can be performed to reveal stepwise the structural features of the periodic system. Based on this a **hierarchy of structural complexity** can be derived. The basic assumption is that molecular solids is constructed using building blocks, which have well-defined shapes and allow directional bondings. Note, that the word *construction* does not mean that these fragments are involved in the actual growth mechanism. Rather they are introduced to understand the structure as in the topological approach. Since these SBUs may usually be represented by simple geometrical objects like octahedrons or squares the concept of describing MOFs by graphs is evident, as pointed out before. Using combinatorial methods, the possibilities to link these abstract units to periodic networks can be explored. Figure 3.4 shows some example for different assembling of octahedral and trigonal units. Due to the different assembling of the units significant differences in the pore size and shape are expected. Further note that the isomers are build up by the same SBUs but the ratio between the used SBUs differs.

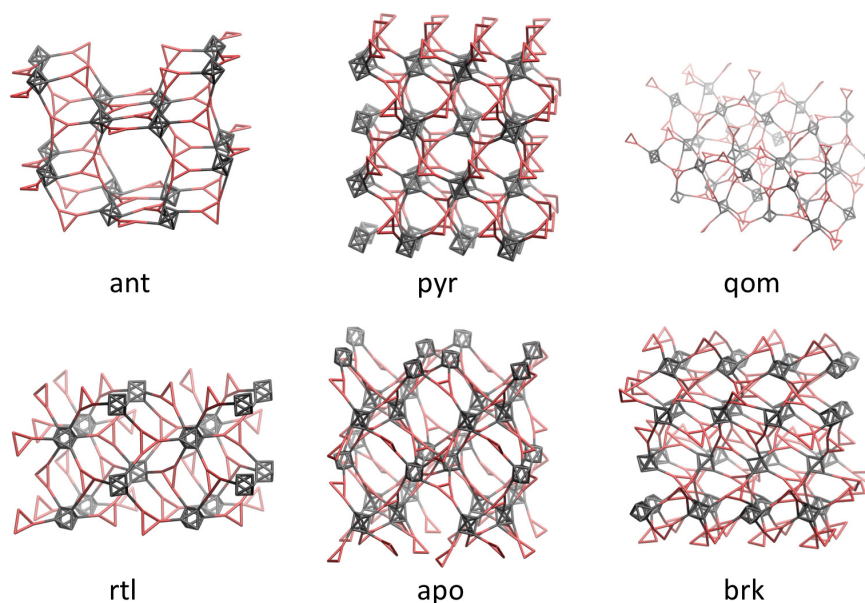


Figure 3.4: Different topologies constructed by alternating linking of three and six coordinating nodes. Using these networks as blueprints for MOFs and introducing the same SBUs *topological isomers* are obtained. For visualization reasons the augmented form of the network is depicted.

In principle, all these generated networks should be potential topologies for a particular MOF with appropriate units. As pointed out by Zaworotko these MOFs are supramolecular isomers. But to emphasize the structural differences these isomers will be called *topological isomers*⁴. The polymers can be distinguished solely by the

⁴The term "topological isomers" was used before by Blake et al. [122] with the same meaning.

underlying network topology. In agreement with the definition of Blake et al. [122], the systems termed as conformational isomers in the classification of Zaworotko [120] are isomers, which should also be called topological isomers, since the different shapes of the SBUs lead to constitutional different graphs. Within the structural classification, topological isomers are the first level of structural complexity.

If the network topology is appropriate, networks of the same type may be put into each other (Fig.3.5). The system is called to be *interpenetrated* or *catenated* (second level of complexity). The free pore volume is in this case decreased since the pores are filled with another network. If the pore size is suitable many fold interpenetration is possible. But note, that in some cases the molecular network might not be able to interpenetrate due to the size of the SBUs, even though interpenetration is possible for the underlying *blue print*. The interpenetrated and non-interpenetrated system are isomers, since the composition of the MOFs is maintained.

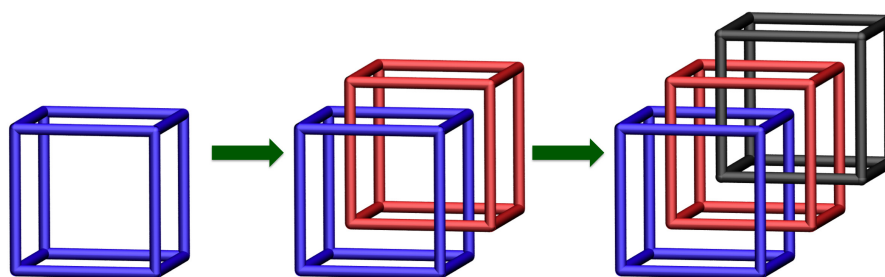


Figure 3.5: Interpenetration of a cubic network. Left is the non-interpenetrated network shown. In the center and on the right side are the one-fold or two-fold interpenetrated system illustrated, respectively.

So far the building blocks are just considered as geometric objects, but nevertheless a large number of different isomers can be generated within the thought experiment on these two levels. But once, one topology is chosen and the degree of the interpenetration is defined, the SBUs, which are not purely abstract objects have to be embedded. In the previous classifications the molecular structure of the SBUs within the network was not considered but in the following it is shown how the embedding of the SBUs influences the molecular structure of the MOF and can lead to further isomeric forms.

First, the SBU has to be investigated with respect to the degrees of freedom, which remain if the fragment is built into the periodic system. If a rigid framework is assumed all translational degrees of freedom are lost once the unit is embedded. A special case, where a translational contribution is maintained, is if the whole MOF has a dynamic feature like in the case of an “breathing” framework [123]. Here, a set of SBUs are able to translate together, although the overall motion is restricted.

Different stable forms can be distinguished, which will be referred to as *dynamical isomers* (Fig. 3.6). Their interconversion is dominated by non-bonding interactions and thus reversible and tunable by external stimuli (like guest molecules).

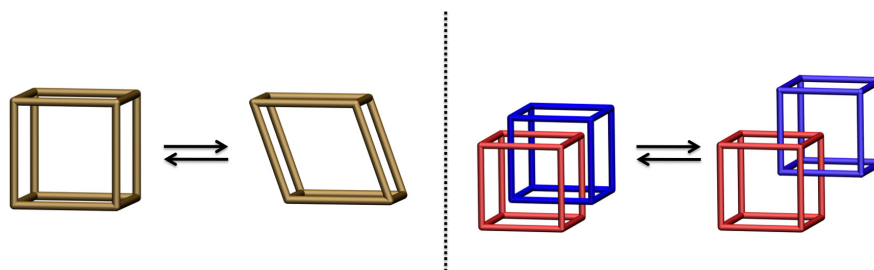


Figure 3.6: Two examples of dynamic isomerism

Considering rigid frameworks, the SBUs can keep some rotational degrees of freedom or be completely spatially invariant within the matrix. In the latter case the symmetry and metric of the SBUs has to be analyzed. If both are in agreement with the parameters of the vertex in the network graph, just one possibility is thinkable to build in the unit into the MOF. But SBUs with a lower symmetry compared to the node are conceivable. One example is the $(Zn_4O)(COO)_6$ -SBU. It has an octahedral shape but the symmetry of the unit is lower (just T_d) due to the presence of the zinc tetrahedral core (Fig. 3.7). Thus this unit can be embedded in two different manners into the same network topology. It is important to note, that once they are built in, no rearrangement into a different orientation is possible without bond breaking. Furthermore it should be kept in mind, that the different *forms* of the SBUs occur due to the hindrance of their movements by strong bondings within the framework. MOFs, which differ in the arrangement of their low-symmetrical SBUs are termed *isorecticular isomers*, since the topology is maintained comparing these networks just the local environment varies with respect to the orientation of the SBUs.

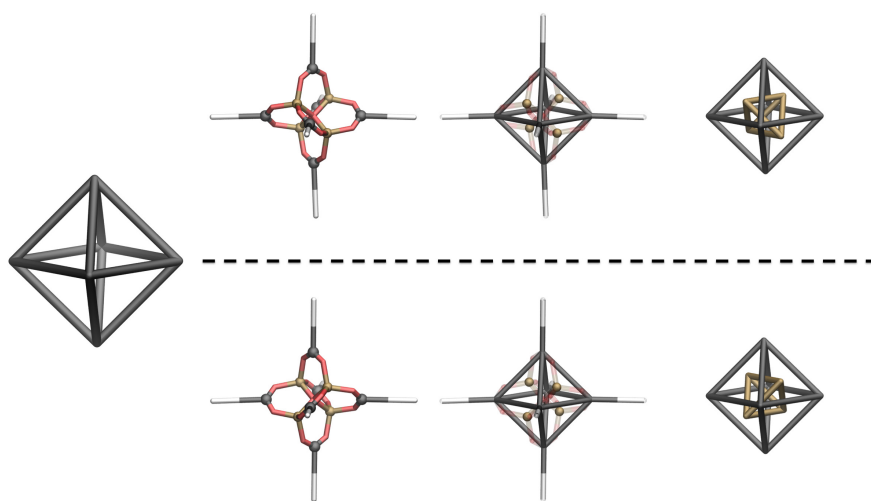


Figure 3.7: Example of a SBU with a lower symmetry compared to the vertex of the network. In this case the molecular SBU has a tetrahedral symmetry in contrast to the octahedral symmetry of the node and consequently the SBU can be embedded in two orientations without influencing the network topology.

Another type of isorecticular isomers can occur if the SBU has a different metric compared to the blue print. Changing the orientation of these units changes the local metric. An example for this type of isorecticular isomers was shown recently by the synthesis of a MOF, which has the **nbo**-topology but due to the asymmetric shape of one SBU two different *phases* were observed [124].

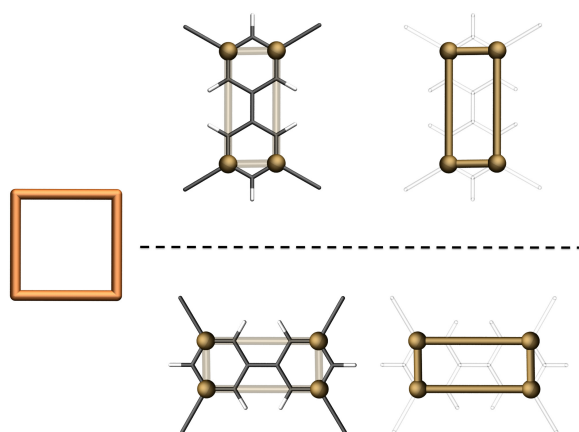


Figure 3.8: Example of isorecticular isomerism, which occurs due to a difference in the metric of the molecular SBU and the vertex in the blueprint.

But the change of the metric can also lead to the change of the chemical nature of the connecting points between the SBUs. For instance, if a triangular unit is modified by shortening one edge, the three connecting points are no longer equivalent (Fig. 3.9). One vertex has two neighbours, which are equally apart, and the other two points have one short and one long edge. Schnobrich et al. demonstrated the possibility to obtain these kind of isorecticular isomers by modifying the metric of three and four coordinating organic SBUs [125]. Note, that if the metric of the SBU and the chemical nature of the connecting points is changed, the possibility to obtain a network topology is also influenced. The last class of isorecticular isomers can be generated if chiral groups are present in the SBU, since the topology does not change by modifying the chiral information.

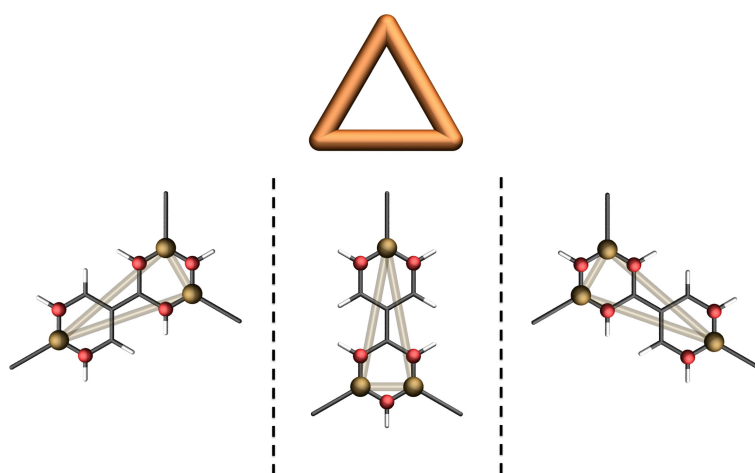


Figure 3.9: Illustration of a SBU with asymmetric shape compared to the vertex. The red balls indicate the different atoms next to the connecting points (yellow). By rotation of the unit the ordering changes.

After this fourth level of complexity, the rotational degrees of freedom of the SBUs have to be considered. The rotation can lead to different arrangements of this flexible group, which are energetically probably equal. But the local environment changes, since, for example, functional groups point into the pore center in one arrangement and not if the SBU rotates. This structural phenomena, which is reversible, will be termed *conformational isomerism*. In contrast to the isorecticular isomers, these isomers can be interconverted by external stimuli (like temperature) without influencing the overall topology, even when the whole MOF is built up. Due to bonding and non-bonding interactions within the matrix the rearrangement of the rotatable SBUs has multiple local minima and thus the interconversion of the conformational isomers is an activated process.

Based on this hierarchy of different structures phenomena, MOFs can be on the

one hand systematically classified but on the other hand the approach to start with a topological consideration and to elaborate stepwise the molecular nature allows the investigation of MOFs in more detail with respect to their structure. The difference in the basic idea of this approach compared to the topological approach, which starts from the experimental data, should be kept in mind. The presented **reverse topological approach (RTA)** can be further combined with theoretical methods to study quantitatively MOFs with respect to possible isomers, which all influence the performance of the final compound. In addition, detailed studies of the isomerism of MOFs are crucial to enable the development of rational synthetic strategies.

In this regard the influence of modifications or exchanges of the SBUs, on the preferred structure can be investigated systematically. Thus even network not, yet, synthesized can be generated and features like different types of isomerisms can be studied, so that the initially asked question: *Which periodic structures can be obtained by using individual units?* can be answered in the long-run.

In the following two chapters different MOF systems are investigated to illustrate the ability of the **RTA** in order to explain the structure of porous coordination polymers, which are experimentally known. In addition the approach is used to tune the network to a desired topology. In the last chapter of this part the focus lays on the isorecticular and conformational isomers. To get reliable quantitative data by the theoretical studies, ab-initio force field for the different MOFs are explicitly parametrized.

Chapter 4

Copper Paddle Wheel MOFs

The self-assembling process of MOFs include the formation of different fragments, which are linked in a specific fashion to construct the final network. The question how the individual units are obtained during the reaction is complex and depends on the particular system. Usually the organic part is provided as one of the starting materials (e.g. terephthalic acid). The inorganic unit is often formed *in-situ* during the synthesis, like the Zn_4O -cluster in MOF-5. Thus it is obvious, that the synthetic conditions of the MOF (e.g. pH-value or concentration) have to match with the ones for the formation of the inorganic unit. However based on one inorganic SBU various MOFs can be generated by changing the organic unit. These MOFs can have either related network (e.g. topological isomers), if the organic linkers have the same shape, or substantially different topologies, if the shape of the organic SBUs change (e.g. going from a linear to a trigonal unit).

In this regard the class of “paddle wheel” SBUs have to be mentioned, since a wide range of MOFs could be synthesized based on them. These inorganic units consist of a metal dimer core, surrounded by four bridging carboxylate ligands in the *syn-syn* mode (Fig. 4.1), with the general formula of $M_2(CO_2)_4$. In the most cases the metals are either copper or zinc atoms. Using the carboxylate carbons as connecting points a square planar SBU is formed with the characteristic paddle wheel shape.

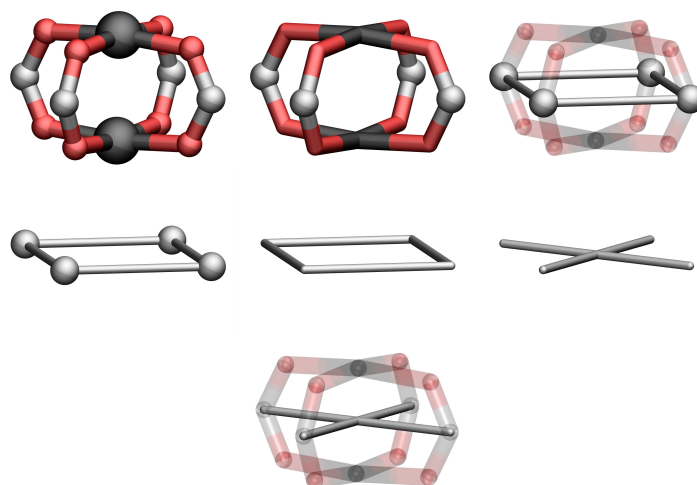


Figure 4.1: Different representation of the paddle wheel unit

One of the first and most studied MOF systems is the **copper paddle wheel** (CPW) based HKUST-1 ($[Cu_3(btc)_2]_n$, $btc = 1,3,5 - \text{benzenetricarboxylate}$) [126]. The 3,4-connected binodal network forms the cubic **tbo** topology [127]. By changing the organic unit, other MOFs with different topologies (e.g. 4,4-connected network [128]) are possible. Even chiral networks could be realized by using a homochiral linker together with the CPW-SBU [129]. It should be mentioned, that in the as-synthesized samples of these materials the axial position of the copper atoms is occupied with solvent molecules. By adequate post-synthetic treatments (e.g. heating of the sample) the axial ligand can be removed. The remaining unsaturated metal site may be used as a reactive center [130] or as strong binding site within the pores, improving the adsorption properties [131]. In addition, porous coordination polymers are known, which are build up by the paddle-wheel unit, but do not form a four coordinated vertex rather use the axial position as an additional connecting point of the network. In this case the SBU is a six coordinating node and indeed the zinc derivative of the CPW-SBU appears only in this motive in a MOF [132]. In the current topological investigation the copper paddle wheel unit occurs just in the square planar form representing a four-coordinating vertex.

In advance to these structural studies a force field based on quantum mechanical reference data is derived to enable quantitative simulations. Currently, no force field is known describing accurately the flexible nature of the unit, presumably due to the difficulty to describe the coordination environment in the deformed square planar Cu(II) system. Up to now, theoretical investigations concentrate on the HKUST-1 system, with a particular focus on guest molecule adsorption and transport within the pores [133–142]. In all these molecular simulations the framework was kept

rigid. To overcome this limitation one aim of this chapter is to derive a force field, which is able to describe both the structure and the internal dynamics of the MOF. Combining this *ab-initio* derived force field with the reverse topological approach, structural phenomena of CPW-MOFs are discussed in the second part. In particular 3,4 connected networks, build up by square planar and trigonal nodes, are considered. The aim is to understand topological isomers of the copper paddle wheel MOFs and to answer the question how the exchange of the organic unit influences the network topology. Based on the obtained results it will be demonstrated how a linker can be designed to achieve a designated network topology rationally.

4.1 *Ab-initio* Parametrization of a Copper Paddle Wheel Force Field

4.1.1 Reference Systems

Dinuclear paddle wheel carboxylates are ubiquitous in metal-organic chemistry [143]. A number of second-row transition metal containing compounds have been studied both experimentally and theoretically, with a special emphasis on the metal-metal interactions. For example, a DFT investigation of molecular structures and vibrational spectra of dinuclear tetracarboxylates (formate and acetate) of molybdenum and rhodium confirms the reliability of the DFT method [144]. Much less attention has been devoted to the theoretical investigation of the first-row transition metal carboxylates (excluding chromium), such as copper and zinc compounds, with the general belief that no metal-metal bond is formed in their dinuclear carboxylates. However the unusual magnetic properties of the dicopper tetraacetate hydrate complex are known for a long time. The antiferromagnetic character of the two d^9 -centers was explained by its dimeric structure [145], which was predicted [146] before it could be confirmed [147]. The theoretical studies could show that the triplet excited state is very close to the open-shell singlet ground state, and the energetic splitting is a very sensitive probe to judge the performance of different levels of theory [148–151].

For the parametrization of the CPW-SBU a multi-scaling approach was applied, with *ab-initio* reference data on the DFT level. To chose adequate model systems, which are reasonable for high level quantum mechanic calculations a building block technique was adopted. Thus the dicopper paddle wheel system was modelled using the most simple molecular system, namely the dicopper tetraformate shown in Figure 4.2. The geometry of $Cu_2(O_2CH)_4$ was optimized using the spin-unrestricted hybrid DFT method (UB3LYP) and applying the so-called broken-spatial-symmetry (BS) approach [152, 153]. Due to the antiferromagnetic exchange coupling, the

high-spin (triplet) excited state of the acetate is only 292.2 cm^{-1} above the open-shell singlet ground state (C_i symmetry) [154]. The calculations (UB3LYP with the aug-cc-pVDZ-PP basis set [155–157]) gave a value of 372 cm^{-1} for the acetate $\text{Cu}_2(\text{O}_2\text{CCH}_3)_4(\text{H}_2\text{O})_2$, taken as two times the (geometry optimized) energy difference between the high spin (HS) and the BS states, $2 \cdot (E_{HS} - E_{BS})$ (see also ref. 148). Since both the geometry and the vibrational frequencies for these two states are nearly indistinguishable for the purpose of the force field parametrization, the triplet state was used as the reference, because it is more straightforward to calculate. In addition, the triplet state is appreciably populated at room temperature. Note, that the closed-shell singlet state was calculated to lay energetically far above the triplet state (12860 cm^{-1}) and should not be used as a reference. In Figure 4.2 the optimized structure with relevant geometrical data is shown.

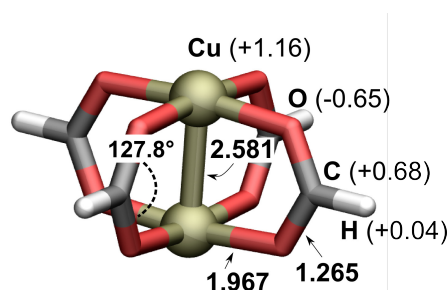


Figure 4.2: Model system used for the force field parametrization. Important bond length and angle are given in Angstrom and degrees. Computed atomic charges for each atom type are shown in parentheses.

In order to assess the quality of the DFT reference structure, a comparison with experimental data is performed (Tab. 4.1). To facilitate this, the computed results for the water coordinated formate and acetate complex are also given (Tab. 4.2). However, an important point when comparing the experimental data and results obtained from the simulation in vacuum for the hydrate complex, are the hydrogen bonding interactions between the axial water ligand and the carboxylate oxygens. For the theoretically optimized structures with axial water, the $\text{Cu} - \text{Cu} - \text{O}_{\text{water}}$ angle is significantly bent in order to allow an intramolecular interaction with the carboxylate oxygens. This structural feature is not observed in the neutron diffraction study of the dicopper acetate [158], pointing out the difficulty in comparing experimental results with theoretical data. The orientation of the water is purely an artifact of the isolated molecule calculation, where the presence of other surrounding molecules is ignored. This leads to the reduction of the symmetry and two different $\text{Cu} - \text{O}_{\text{carb}}$ bond lengths. Further, the different intermolecular hydrogen bonding interactions in the experimental structures also result in a scatter

of the observed $Cu - O_{carb}$ bond distances, making it hard to compare properly. Moreover, in the as-synthesized HKUST-1 material [126] no bending of the $Cu - Cu - O_{water}$ is seen, and all $Cu - O_{carb}$ distances are of the same length (within the experimental error). Obviously, an extensive hydrogen bonded network with some additional water molecules is formed. As observed in a previous study [98], the metal-oxygen bond lengths are somewhat overestimated on the DFT level as compared to the corresponding MP2 results (UMP2/aug-cc-pVDZ-PP). The most noticeable change on axial coordination with water is the fact that both the $Cu - Cu$ distance and the $Cu - O_{carb}$ distances are elongated by ca. 0.08 Å and 0.01-0.03 Å, respectively. This effect has recently been observed for the HKUST-1 network [159]. The preformed calculations on the paddle wheel unit without axial water give the $Cu - Cu$ distance in good agreement with that found in the fully desolvated HKUST-1 framework (2.50 Å [159, 160]). Note, that the $Cu - O_{carb}$ bonds in solid copper acetate monohydrate, which are not perturbed by hydrogen bonds, are similar in length (1.942(1) and 1.952(1) Å [158]) to those found in the HKUST-1 framework (1.952(3) Å [126]).

From this comparison it was concluded that effects like the systematic error of the given level of theory, the simplified formate model system, or additional hydrogen bonding on the structural parameters are small. Thus, the formate model computed on the DFT level can serve well as a reference for the force field parametrization, as the minimum structure and curvature of an “unbiased” potential energy surface is sought. The deficiencies of the DFT method were intentionally not correct, but fit to reproduce this higher level method in the sense of a multi-scale simulation approach. Accordingly, the calculated Hessian matrix elements were taken unscaled for the parameter fit.

Table 4.1: Selected structural data for dinuclear copper tetracarboxylates without the coordination of water.

Method	Formate: $Cu_2(O_2CH)_4$		
	B3LYP ^a	MP2 ^b	FF
$r(Cu - Cu)$, Å	2.518	2.504	2.519
$r(Cu - O_{carb})$, Å	1.967	1.935	1.967
$r(C - O)$, Å	1.265	1.274	1.265
$\angle O - C - O$, deg	127.8	127.7	127.8

^a Triplet state; UB3LYP/aug-cc-pVDZ-PP. ^b UMP2/aug-cc-pVDZ-PP.

The effective atomic charges were obtained from the fitting of the electrostatic potential (ESP) based on the Merz-Kollman sampling scheme [161] using ca. 2000 grid points per atom¹. The van der Waals exclusion radius of 2.26 Å for the Cu atom was taken from ref. 163. The resulting atomic charges are given in parentheses

¹A critical comparison of methods for charge derivation is given in ref. 162.

Table 4.2: Selected structural data for dinuclear copper tetracarboxylates with the coordination of water.

Method	Formate:	Acetate:	
	$Cu_2(O_2CH)_4(H_2O)_2$	$Cu_2(O_2CCH_3)_4(H_2O)_2$	
	B3LYP ^a	B3LYP ^a	Exp. (XRD) ^c
$r(Cu - Cu)$, Å	2.604	2.564	2.613
$r(Cu - O_{carb})$, Å	1.980, 2.001	1.974, 1.998	1.947 ^d , 1.990
$r(Cu - O_w)$, Å	2.270	2.302	2.161
$r(C - O)$, Å	1.262, 1.265	1.268, 1.272	1.260 ^d
$\angle O - C - O$, deg	127.7	125.4	125 ^d

^a Triplet state; UB3LYP/aug-cc-pVDZ-PP. ^b UMP2/aug-cc-pVDZ-PP. ^c Experimental values from ref. [158]. ^d Averaged values.

in Fig. 4.2. The calculated charges are in good agreement with those obtained in previous studies with slightly different basis sets and fitting protocols [136, 142]. In order to describe the HKUST-1 system additional parameters, missing in the standard MM3 parameter set, were derived from a sodium benzoate model, which was optimized on the same B3LYP/aug-cc-pVDZ level of theory, following a previous study on carboxylate force fields [164].

4.1.2 Parametrization

The parametrization strategy focuses on accuracy in reproducing the reference data at the expense of transferability. The primary step is the choice of the nonbonded parameters. Van der Waals (vdW) interactions are described by the MM3 specific Buckingham potential [96] and the usual Lorentz-Berthelot mixing rules, with all parameters taken unadjusted from ref. 163 (for a listing see Tab. 11.1 in the appendix). Note that these generic vdW parameters, available for the full periodic table, are the only values extrapolated from few high accurate, experimental data. All other parameters have been derived from the corresponding first principle calculations. In contrast to the MM3 energy expression, where bond dipoles are used to describe electrostatic interactions, atomic point charges are used in the force field (with interactions between 1-4 connected atoms scaled by a factor of 0.5). In order to arrive at a charge neutral $Cu_2(O_2C)_4$ fragment, the small charge on the formate hydrogen was added to the Cu and O_{carb} , leading to the following charges used in the force field calculations: Cu +1.2, O_{carb} -0.64, and C_{carb} +0.68. For the remaining atoms of the organic linkers, the following atomic charges were used: C_{ph} -0.12 and H +0.12 for all $C_{ph} - H$ groups and a zero charge for all other C_{ph} . A general issue in modeling coordination compounds are large partial charges needed to represent the electrostatic potential in the surrounding. In particular, in the copper dimer the charge of +1.2 on the two metal atoms in close proximity of only about 2.5 Å leads to a strong electrostatic repulsion, which is an artifact of

the atomic point charge model [165]. This leads to too stiff carboxylate bending potentials in order to compensate this repulsion and to maintain the structure. To avoid this problem an explicit $Cu - Cu$ bond was introduced to exclude this 1,2-interaction. Note that this is only for modeling the system properly and has nothing to do with the true presence of a chemical bond between the metal atoms.

The functional form of the energy expression for the bonded interactions is a modified form of the MM3(2000) force field of Allinger [96]. The original MM3 stretch-bend cross-term was modified by introducing two different force constants for the two bonds that comprise a bond angle and implemented a new stretch-stretch cross-term [98]. The weaker $Cu - O_{carb}$ coordination bonds are described by a Morse potential

$$E_{stretch}^{Morse} = \frac{k_{stretch}}{2\alpha^2} \left[1 - e^{-\alpha(r-r_0)} \right]^2$$

(where $k_{stretch}$ is the force constant, r_0 the reference distance, and $\alpha = 2.5 \text{ \AA}^{-1}$), which was found to be superior to the standard MM3 quartic term used for all other bonds [162]. For the square coordination environment of Cu(II) with angular minima at 90° and 180° , an improved Fourier type angle bending potential is used

$$E_{bend}(\theta) = \frac{1}{2} k_{bend} [1 + \cos(\theta)] [1 + \cos(2\theta)],$$

where θ is the $O_{carb} - Cu - O_{carb}$ angle and only k_{bend} needs to be adjusted [166, 167].

As explained in the theoretical part of this work the DFT optimized geometries of the reference systems and the cartesian Hessian matrices were projected into a redundant set of internal coordinates, defined by the force field connectivity, and used as input for the genetic algorithm to parametrize the force field. The linker model system was used to parametrize the $C_{carb} - C_{ph}$ interaction including stretch, bend, out-of-plane bend, torsion and cross-terms. For torsional barriers, in addition to the curvature at the energy minimum, also rotational energy barriers were included in the fitting procedure. Following the MM3 scheme for aromatic systems, the parameters for the $C_{ph} - C_{ph}$ bond stretch force constant and the two-fold torsion potential were adjusted by performing a self-consistent field molecular orbital calculation for the π -system using a modified Pariser-Parr-Pople method [168]. However, this was not done “on-the-fly” but the parameters were kept fixed. The final parameter set is given in Tab. 11.1 (appendix).

4.1.3 Validation

At first, the results of the dicopper formate model (Fig. 4.2) were directly compared with the DFT reference. As expected, the structure is reproduced very well as shown

in Tab. 4.1. The low vibrational frequencies below 300 cm^{-1} are compared in Tab. 4.3. The largest relative deviations are observed for the two lowest modes, which can be described as a twist around the $\text{Cu}\cdots\text{Cu}$ axis and a D_{4h} to D_{2d} symmetry distortion from a square planar to a tetrahedral copper coordination environment, respectively. These discrepancies in the normal modes persist, despite the low deviations between elements of the redundant internal coordinate Hessian, included in the fitting, from the force field and the DFT reference, respectively. However, a close inspection of the off-diagonal terms of the reference Hessian matrix shows for example a strong coupling between the $\text{Cu}-\text{Cu}$ and the $\text{O}_{\text{carb}}-\text{C}_{\text{carb}}$ stretch with a force constant above $1\text{ mdy}/\text{\AA}$. This reveals the peculiar electronic interactions in a coordination complex, which can not fully be captured by a force field without a stretch-stretch cross-term for non-adjacent bonds. In addition, it can be presumed that the large electrostatic interactions between highly charged atomic sites in close proximity might also lead to a too stiff potential [165]. However, the overall agreement is gratifying in view of the fact that only limited number of cross-terms are included. In particular, the frequency of the normal mode best described as the $\text{Cu}\cdots\text{Cu}$ stretching ($222/219\text{ cm}^{-1}$) and the soft “in-plane” deformations of the square SBU ($154/161\text{ cm}^{-1}$ and $164/164\text{ cm}^{-1}$, bending of $\text{O}_{\text{carb}}-\text{Cu}-\text{O}_{\text{carb}}$), which are most relevant for the flexibility of the MOFs, are very well reproduced by the force field.

Table 4.3: Vibrational modes (in cm^{-1}) below 300 cm^{-1} for dicopper tetraformate model system

UB3LYP/aug-cc-pVDZ-PP	Force Field	deviation	mode degeneracy
58	91	-33	1
67	124	-58	1
106	118	-13	2
154	161	-8	2
164	164	0	1
222	219	+4	1
225	179	+45	1
232	229	+3	2
251	229	+22	1
274	290	-16	1

In the next step the FF was used to investigate the experimentally well characterized periodic HKUST-1 (Fig.4.3) [126]. The optimized lattice size of 26.3833 \AA (corresponding to the zero Kelvin limit) is in good agreement with the value of $26.3046(2)$ [169] for a fully desolvated HKUST-1 measured at low temperature ($T = 77\text{ K}$). The results suggest that the lattice constant is particularly sensitive to the $\text{Cu}-\text{O}$ length. The discrepancy can be explained by the overestimation of this distance by the B3LYP functional (1.97 \AA) as compared to the experimental

value (1.92 Å) [169]. A similar observation has been made before in a study on MOF-5 [98]. Intentionally, this slight deviation is accepted, which is due to the first principles reference, and a manual “tuning” of the parameters after the automated GA fitting procedure is refrained.

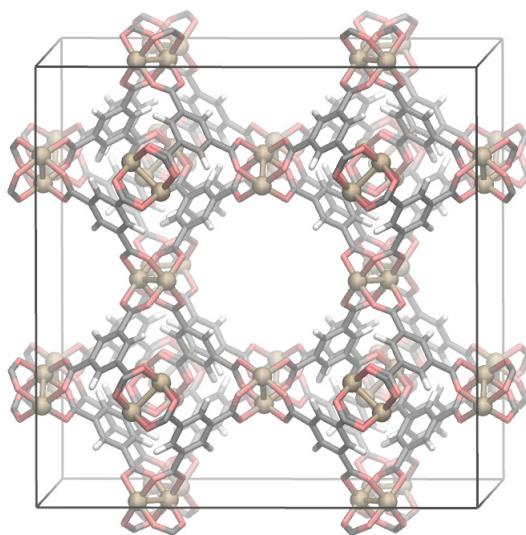


Figure 4.3: HKUST-1

In the network, the trigonal vertex has a threefold symmetry axis, whereas the four coordinated vertex has a reduced local D_{2d} symmetry with two different angles of 109.5° and 70.5° . As a consequence a deformation is needed to accommodate the square planar copper paddle-wheel SBU, leading to the typical bowing of the linker as shown on the right in Fig. 4.4. In contrast to the 19.5° deviation in the parent network, the $C_{carb} - X_{Cu_2} - C_{carb}$ (where X_{Cu_2} is the centroid of the two Cu atoms) deviate only by 2.4° from orthogonality. The remaining deformation is transferred to an out-of-plane bending of the carboxylate “hinge” and a bending of the carboxylate out of the phenyl ring plane. However, relaxing a cut out paddle wheel unit with the adjacent phenyl rings (shown on the left in Fig. 4.4) reveals that a strain energy of only 1.1 kcal/mol is stored in this fragment, well accessible by thermal fluctuations. A comparison of the $C_{carb} - X_{Cu_2} - C_{carb}$ and the $X_{Cu_2} - C_{carb} - C_{ph}$ angles with the corresponding experimental data (in parentheses in Fig. 4.4) from ref. 169 demonstrate the accuracy of the FF.

In order to test the validity of the flexible force field for dynamic properties the thermal expansion coefficient of desolvated Cu-btc was computed. In Fig. 4.5 the temperature dependence of the lattice constant is shown, obtained from a series of NPT ensemble simulations between 200 and 500 K at a pressure of 1 atm. At each

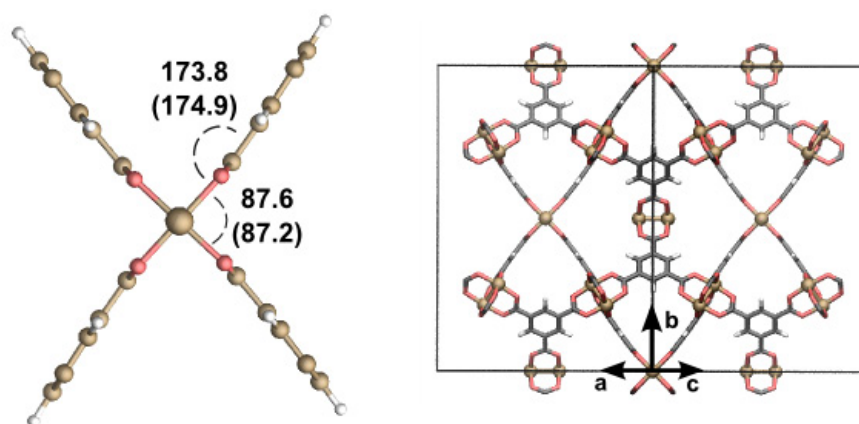


Figure 4.4: **tbo** network topology. $C_{carb}-X_{Cu_2}-C_{carb}$ and the $X_{Cu_2}-C_{carb}-C_{ph}$ angles in deg, experimental data in parentheses from ref. 169.

temperature, the system was subjected to 100 ps of temperature equilibration at a constant volume (NVT) followed by a 100 ps equilibration in the NPT ensemble and a 400 ps sampling run (NPT). Despite the above discussed offset in the lattice parameter, the simulations give a volumetric thermal-expansion coefficient of $-1.07 \times 10^{-5} K^{-1}$ and reproduce quantitatively ² the negative thermal expansion (NTE) behavior of the desolvated HKUST-1 material as measured recently in experimental studies [160, 169] (see Fig. 4.5). However, it is significantly smaller than that found for MOF-5 [170]. This result is a clear indication for the accuracy of the first principles derived FF, which is able to reproduce such a complex global framework motion without the use of experimental data in the parametrization.

In addition the elastic constants were computed, which can be important for technical applications. The bulk modulus B is calculated to be 25 GPa (for computational details see ref. 98) in excellent agreement with the experimental value of about 30 GPa for the non-desolvated HKUST-1 [171]. In accordance with the lower NTE, the predicted bulk modulus is appreciably larger than that found in MOF-5 with 14 GPa [98], indicating its higher stiffness. Note that in contrast to the discrepancy between experimental results, determined by nanoindentation, and theoretical results in the case of MOF-5 [172], here a good agreement between measured and computed bulk modulus is found. The shear modulus ($C_{11} - C_{12}$) of HKUST-1 is computed with 3.5 GPa and the strain modulus C_{44} with 13 GPa.

Due to the presented results the parametrized force field can be seen as reliable for further investigations.

²The S-PXRD values plotted in Fig. 4.5 are taken from Tab. S1 of the Supporting Informations of ref. 169. From this data a averaged linear volumetric expansion coefficient of $-1.06 \times 10^{-5} K^{-1}$ can be derived by linear regression.

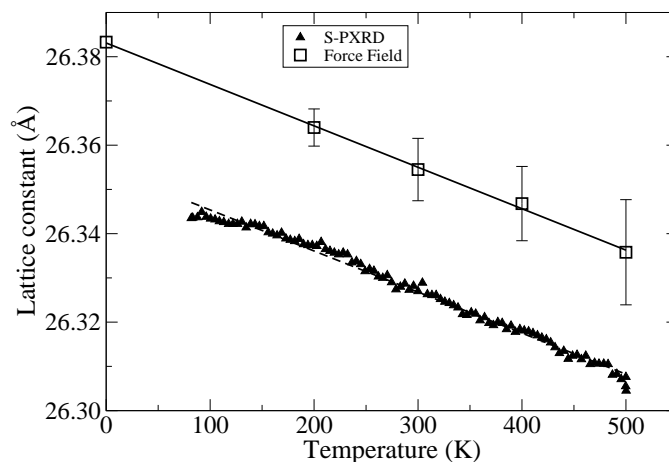


Figure 4.5: Temperature-dependent variation in the simulated lattice constant of Cu-btc with standard deviations (open squares). The value at $T = 0$ K results from the full optimization of Cu-btc. Experimental data are from synchrotron powder X-ray diffraction measurements (triangles).[160]

4.2 Investigation of the Network topology

Two high symmetry network topologies are possible for 3,4-connected networks with a square and trigonal unit [127]. In Fig. 4.6 the augmented form of these edge transitive networks: **tbo** and **pto** [127, 173] are depicted.

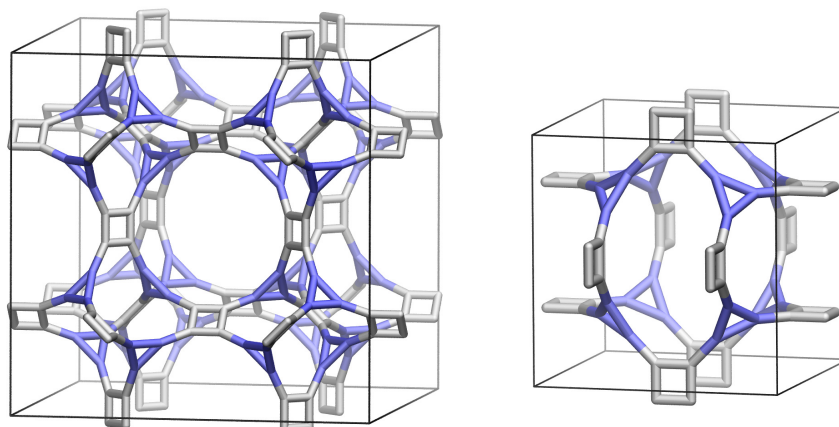


Figure 4.6: Augmented network of a) tbo and b) pto

According to the reverse topological approach a molecular network can be constructed by replacing the (augmented) vertices in the blue print by molecular SBUs as schematically shown in Fig. 4.7. If the trigonal vertex is replaced by a C_6H_3 unit, MOFs of the formula $Cu_3(BTC)_2$ are formed, which will be abbreviated in

the following as Cu-BTC. The experimentally known HKUST-1 [126], represents Cu-BTC in the **tbo** topology (Cu-BTC-tbo).

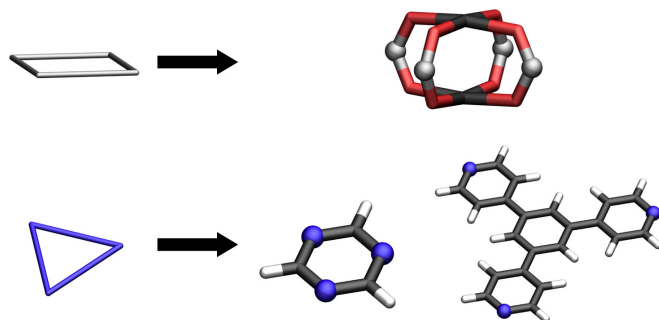


Figure 4.7: Correspondence of vertices and real building blocks.

An isorecticular network, in analogy to the linker extension in the IRMOF series [174], can be formed by adding three phenylene groups (see Fig. 4.7), resulting in the *btb* linker (*btb* = *benzene*–1,3,5–*tribenzoate*). The corresponding MOFs will be referred to as Cu-BTB-X (X= **tbo** or **pto**). Interestingly, the only known copper paddle-wheel MOF with a *btb* linker is MOF-14, which represents Cu-BTB in a peculiar interwoven **pto** network [175]. Using the *ab-initio* parametrized force field topological isomers of these networks can be investigated. Since also experimentally unknown system can be studied, reasons for the energetical preferences of one topology can be derived, which helps to understand the structure of the system in more detail. With respect to the experimental results the following questions arise: Why does the MOF forms the **tbo** structure in the case of HKUST-1 but the **pto** topology is obtained in MOF-14? Can the topology be influenced by the choice of the SBUs? It is important to stress again, that the two networks - **tbo** and **pto** - represent isomers with the same connectivity and therefore are located both on the same molecular mechanics energy surface, even though bond breaking would be needed to interconvert them. Thus, relative strain energies can be computed.

Therefore, the Cu-BTC MOF was optimized in both topologies without any symmetry constraint (space group P_1). The **pto** network consists of two formula units S_3T_4 (where S represents the square and T the trigonal building block) per unit cell, whereas the **tbo** cell is formed from eight such minimal units. For comparison, all energies are given per formula unit S_3T_4 in the following. In Tab. 4.4 relative steric energies of all investigated systems are summarized.

Table 4.4: Relative Energies (per formula unit S_3T_4 and in [kcal/mol]), lattice size in [\AA] and solvent accessible surfaces (SAS, per formula unit and in [\AA^2]) for all investigated network topologies.

Cu-BTC	tbo	pto	tbo (int)^a	pto (int)^b
ΔE_{strain}	0.0	11.9	-40.1	179.2
lattice size	26.383	15.281	26.362	15.063
SAS	457	214	44.4	28.3

Cu-BTB	tbo	pto	tbo (int)^a	pto (int)^b
ΔE_{strain}	15.3	0.0	-7.6	-31.8
lattice size	47.409 ^c	27.463	47.344 ^c	26.994
SAS	1913	2024	1367	976

^a interpenetrated (see Fig. 4.10a). ^b interwoven (see Fig. 4.10b). ^c averaged (for strained systems multiple local minima were observed close in energy with a small orthorhombic symmetry breaking).

The Cu-BTC-tbo network is by 11.9 kcal/mol per formula unit more stable than the alternative **pto** topology. Thus, the experimentally obtained structure of HKUST-1 [126] is due to a thermodynamic preference reducing the steric strain. A closer analysis of the **tbo** case reveals a non-planar deformation of the trimesic acid linker in order to maintain the square coordination at the paddle-wheel unit (Fig. 4.8a). However, apart from this slight bending, the linker is planar in contrast to the situation in the **pto** topology, where the carboxylate planes are rotated by 33.4° with respect to the C_6H_3 aromatic plane (Fig. 4.8b). As observed previously in experiment [77] as well as theoretical works [164], the phenyl carboxylate bond has a sizable rotational barrier due to conjugation. The energetic penalty for the carboxylate rotation in **pto** outweighs the linker deformation in the **tbo** net. This observation demonstrates the necessity for an accurate parametrization of the force field, since a delicate balance between different small deviations from the individual equilibrium geometries of the building blocks needs to be accurately captured.

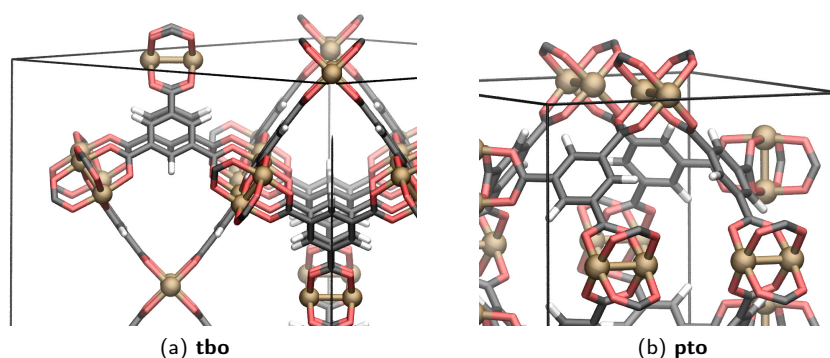


Figure 4.8: Close-up views of the Cu-BTC systems (Cu: copper, C: dark grey, H: white, O: red).

From the above analysis it can be concluded that an additional “joint” in the linker backbone, allowing a rotation of the carboxylate group out off the trigonal plane should lead to a preference for the alternative **pto** topology. This can be realized by exchanging the btc with the btb linker (Fig. 4.7), where the biphenyl bond has a much lower rotational barrier. The corresponding networks were constructed and optimized in both topologies (Cu-BTB-tbo/-pto). The relative lattice energies (Tab. 4.4) reveal now a preference of the **pto** structure by 15.3 kcal/mol. The closeup of the linker structure in Fig. 4.9a shows clearly that in the **tbo** topology the non-planar btb core does not fit to the constraint of carboxylate units in the trigonal plane. Both the $C_{ph} - C_{carb}$ and the $C_{biph} - C_{biph}$ bonds are twisted, leading to numerous minima close in energy, all of them breaking the cubic symmetry, an effect observed for other systems before [176]. In contrast to that the **pto** topology matches perfectly to the linker equilibrium geometry (Fig. 4.9b): the $C_{biph} - C_{biph}$ bond is rotated by 38.1° , close to the biphenyl equilibrium torsion, whereas the carboxylate groups are not rotated.

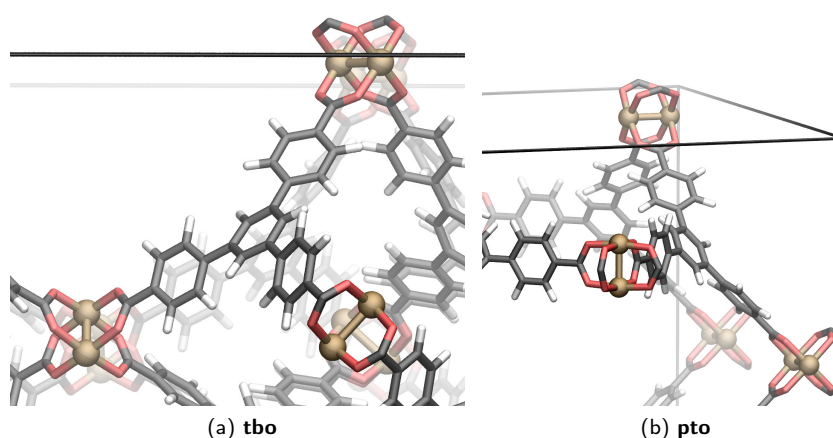


Figure 4.9: Close-up views of the Cu-BTB systems (Cu: copper, C: dark grey, H: white, O: red)

4.2.1 Interpenetration

Both Cu-BTB networks are unknown experimentally, but the very intriguing MOF-14 represents the interpenetrated variant of Cu-BTB-ptb [175]. This system is particularly interesting, since the interpenetration of the second network follows the P-minimal periodic surface and - in contrast to usual interpenetration - the pore volume is only slightly reduced. This behaviour is referred to as interweaving³ and for the following discussion it is necessary to analyse the different interpenetration modes of the **tbo** and **pto** networks in general. The interpenetrated **tbo** can be generated by shifting the second net by $[\frac{1}{4}, \frac{1}{4}, \frac{1}{4}]$ (fractional coordinates) with respect to the primary, thus filling its pore space. In Fig. 4.10 the interpenetrated networks are shown in augmented form. In case of **pto**, shifting an identical copy of the primary network by $[\frac{1}{2}, \frac{1}{2}, \frac{1}{2}]$ leads to a situation, where the trigonal vertices of both networks coincide. Only by a distortion of the networks via a displacement of the trigonal vertices away from each other, two non-intersecting interwoven networks can be formed as shown in Fig. 4.10b. Note that if one connects the neighboring trigonal vertices of the two networks, which are rotated by 180 deg with respect to each other, an octahedral six coordinated vertex is formed and the resulting non-interpenetrated net is now 4,6-connected (referred to as **pto-d** in the RCSR database [173]). Since in the resulting interwoven **pto** net (Fig. 4.10b) only the square vertices occupy pore space of the other network, the resulting structure is very rigid, but still porous.

³Sometimes the term "minimal displaced" is used to describe interweaving networks. However the latter is used here, since it is more descriptive.

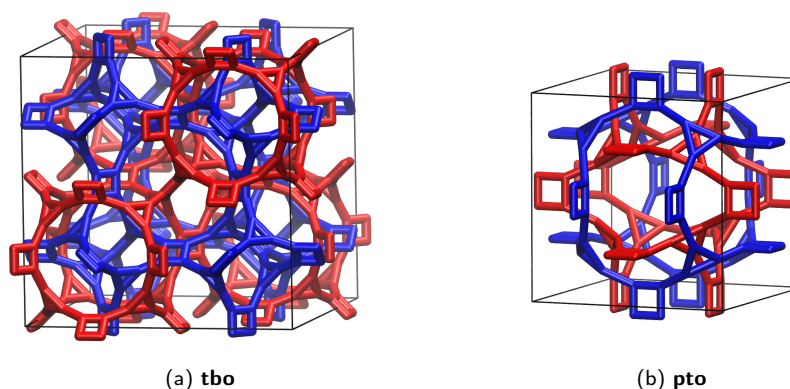


Figure 4.10: Interpenetrated (a) **tbo** and (b) **pto** networks in augmented form.

However, the structure of the interwoven MOF-14, determined experimentally, poses an additional challenge, due to the steric deformation of each individual net. In order to address this problem, all possible interpenetrated systems of Cu-BTC and Cu-BTB in both topologies **tbo** and **pto** were investigated. In the following discussion the terms “interpenetrated” and “interwoven” are used as synonymous, since the latter is just a special variant. In principle, steric energies of interpenetrated nets can be compared with non-interpenetrated ones in the same way as different topologies, since all structures reside on the same molecular mechanics potential energy surface. Nevertheless, in this case it is more difficult to assess the preference of the real system. Due to the additional close contacts between the nets a mainly dispersive stabilization in the gas phase is usually observed. In real systems, this stabilization could be compensated by differences in the free energy of solvation. In case of an attractive interaction between solvent and network, interpenetration leads to a destabilizing reduction of the solvent accessible surface (SAS). The entropic contributions to the free energy of solvation in the microporous framework are not easy to assess and depend also on the type and size of the solvent. In particular, open metal site frameworks can coordinate donor solvents and a delicate hydrogen bonding network can be formed. But the current used model is not capable to describe these interactions. Further the changes in solvent free energy when going from one topology to another or changing the interpenetration mode should be determined to get an overall picture. Note that this problem is closely related to the solvation of biomolecules. The native state of a protein structure can often only be described by including the free energy of solvation considering “nanoscaled” cavities or pores [177]. However, such a treatment including a sampling of the solvent configurational space is beyond the scope of this work. Thus, a simple and qualitative measure was used for the possibility of solvent stabilization, namely the determination of the SAS with a probe diameter of 3 Å. This is a typical value for

water, often applied for the evaluation of solvation energies of biomolecules [178]. Interestingly, the same approach is used to determine the inner surface of porous hybrid materials [179].

The computed SAS values summarized in Tab. 4.4 are given per formula unit, since they were considered to be roughly proportional to the solvent stabilization energy per formula unit. For the Cu-BTC systems the **pto** topology has about half the accessible surface, as compared to **tbo**, even though it is only by a factor of 1.3 more dense. Interestingly, in case of the larger Cu-BTB systems both topologies are nearly equal in surface size, with **pto** having a slightly larger SAS. In case of the Cu-BTC, interpenetration reduces the accessible surfaces by an order of magnitude. These systems are essentially non-porous and a sufficient solvent framework interaction will lead to a large energy penalty for interpenetration. In contrast to that, for the Cu-BTB systems, the reduction is about a factor of two. This is what can be expected for very large pores, where - in analogy to two infinite planes - maximizing the contact would halve the accessible surface per formula unit.

From an energetic point of view, interpenetration does not change the tendency to form a **tbo** structure for the BTC linker, nor for **pto** in case of the larger BTB (Tab. 4.4). As mentioned above, however, interpenetration in the gas phase is always stabilizing. Thus, from the bare gas phase steric energies the non-porous interpenetrated Cu-BTC in **tbo** structure appears to be most stable. This stabilization will largely be reduced by the loss in solvation free energy. A close inspection of the structure of this system even reveals, that it might be impossible to be formed at all under real growth conditions: a hydrogen atom of one net is situated just 3.22 Å away from a copper site of the other net, exactly in the direction of the Cu-dimer axis. Thus, under growth conditions, where a solvent molecule like water or ethanol will be strongly bonded to this copper atom, a large steric repulsion to the second network will result. Thus, the formation of an interpenetrated Cu-BTC can be ruled out, despite the stability of the “activated” system in the absence of such an axial ligand. Correspondingly, no indication for interpenetrated Cu-BTC is reported in the literature. The situation is different for Cu-BTB. Again, the interwoven **pto** structure is the most stable in the gas phase. However, such close contacts for the axial position of the Cu-dimer are absent here and the loss in SAS is much smaller. Thus, the interwoven Cu-BTB can be expected to be formed, which is indeed the case. The parametrized force field allow to determine the energy contributions necessary to generate the interwoven Cu-BTB-ptb (MOF-14), which is depicted in Fig. 4.11. Starting from the relaxed non-interwoven Cu-BTB-ptb net, the bowing of the trigonal BTB backbone leads to a deformed structure shown in the center of Fig. 4.11. An energy of 16.3 kcal/mol is necessary for this deformation. As a result, half of the paddle-wheel SBUs are shifted apart, whereas the other half gets closer to each other. Consequently, alternating enlarged and shrinked pores are gener-

ated. Now, by combining two such deformed nets, the final interwoven structure is generated. The stabilization in the gas phase is with -48.0 kcal/mol rather large, compensating the deformation energy.

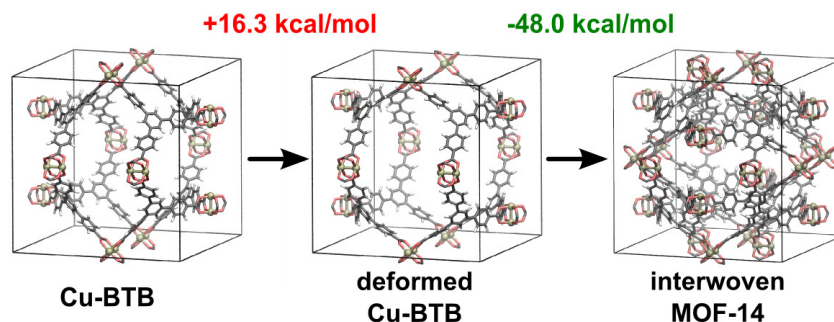


Figure 4.11: Stepwise formation of MOF-14 starting from a single Cu-BTB network in **pto** topology. The energies for deformation and interweaving are given per formula unit.

A detailed comparison of the theoretical structure, computed by a first principle derived force field without any recourse to experimental data, shows the accuracy of the theoretical model ⁴. In Fig. 4.12 a graphical overlay is shown. Note that due to the small difference in the cell parameters (XRD: 29.948 Å; FF: 29.994 Å) a slight overall shift of the atoms is observed. The largest deviation is because of the shorter Cu-Cu distance in the theoretical structure, due to the fit to the “gas phase” paddle-wheel without axial ligands [159]. Apart from that the overall network structure coincides perfectly. Also the typical bending of the carboxylate with respect to the square coordination at the metal atom is well reproduced. The non-bonding $C_{ph} - C_{ph}$ distances of the π -stacked central aromatic rings of the two networks are very similar with 3.742 Å and 3.697 Å, for the experimental and theoretical network, respectively. The most important measure for the deformation of the **pto** network are the distances between the Cu-dimer centroids. In the non-interwoven and unperturbed structure they are both exactly half the cell parameter. In the deformed structure, two centroids have to approach each other whereas the other two are pushed apart in order to allow the interweaving of the networks. Again, the sum of both distances is equal to the cell spacing. In Fig. 4.12 these two critical distances are indicated by arrows. The deviation from experiment is within about 0.2 Å in the same order as the deviation in the cell parameter. These results indicate that the force field is able to model the distortion in the interwoven MOF-14 accurately.

⁴Here, the experimental structure with all coordinating ligands and solvent atoms removed is compared [175]. Two structural analyses are given here, which differ only slightly. The as synthesized structure with the slightly better R-value was used.

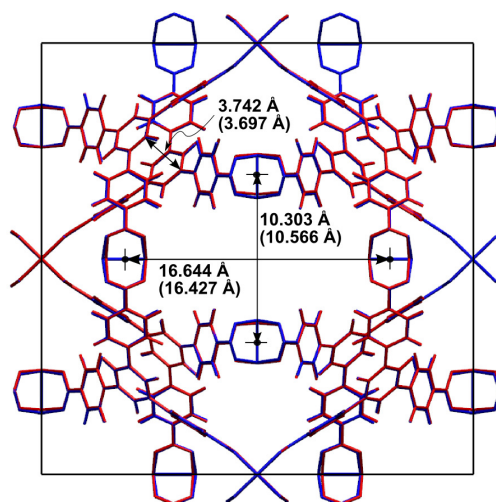
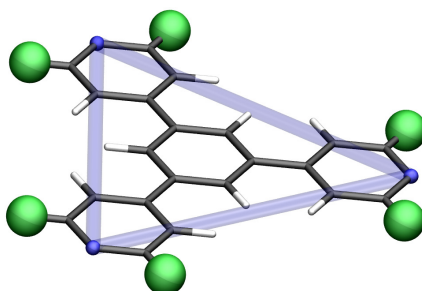


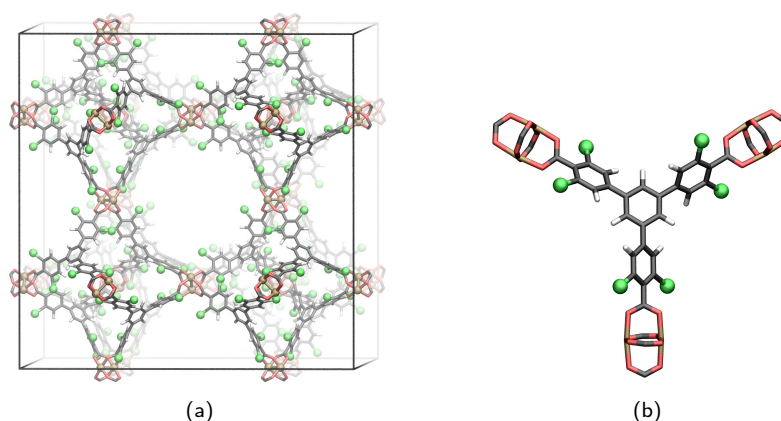
Figure 4.12: Superposition of fully relaxed calculated (red) and experimental (blue, from ref. 175) structure. The two different Cu-dimer centroid and the linker-linker π -stacking distances are given for comparison, with the FF computed values in parentheses.

4.2.2 Tuning Network Topology

From the analysis of the non-interpenetrated Cu-BTC and Cu-BTB systems it becomes clear that the **tbo** topology is sterically preferred when the three carboxylate groups remain in the plane of the trigonal vertex, as in case of the BTC linker. Because of the twisted biphenyl bond and the $C_{carb} - C_{ph}$ conjugation this is unfavorable for btb and the **pto** net is formed. Using the advantage of a theoretical method, the force field was applied to design a btb-type linker where the more open **tbo** topology is preferred. To achieve this a steric strain was introduced to avoid the coplanar conformation of the peripheral phenylene and the carboxylate group. It was shown previously that bromium ortho-substitution can induce enough strain to overcome the $C_{carb} - C_{ph}$ conjugation and rotate the carboxylate group out of the phenyl ring plane. For example, the benzenedicarboxylate (bdc) linked copper paddle-wheel system forms a 2D periodic square grid, whereas the 2-bromo substituted BTC derivative is a 3D periodic network of **nbo** topology [180]. In order to minimize positional disorder a *btb* derivative, substituted with six bromium atoms in all ortho-positions with respect to the carboxylate, was tested. This *btb* - Br6 linker is shown in Fig. 4.13.

Figure 4.13: Molecular representation of the *btb* – *Br*6 linker.

In the **tbo** topology each peripheral bromo substituted phenyl ring can rotate out of the trigonal vertex plane in two directions leading to a large number of local energy minima structures. In Fig. 4.14a the lowest minimum, which would be located by an extensive simulated annealing is shown. The cutout linker structure in Fig. 4.14b does not maintain the three fold symmetry axis of the vertex. In contrast to that, the **pto** network of Cu-BTB-Br₆ (Fig. 4.15) is sterically locked into a single configuration, which is indeed 7.0 kcal/mol higher in energy as the **tbo** network. It must be kept in mind that these is just the intrinsic steric preference of the network itself, which might be compensated by solvent or kinetic effects. In addition, the very open structure might lead to the formation of a less porous interpenetrated system. However, one can conclude that by introducing steric strain in ortho-position of the carboxylates, leading to a rotation out of the aromatic plane, can trigger the formation of the more porous **tbo** network topology for extended btb-type linkers. In particular, the sixfold bromium substituted btb-Br₆ ligand is proposed as candidate for this behavior.

Figure 4.14: Cu-BTB-Br₆ network in the sterically preferred **tbo** topology (a). Cutout of a linker with the adjacent copper paddle-wheel units (b). (Cu: copper, C: dark grey, H: white, O: red, Br: green).

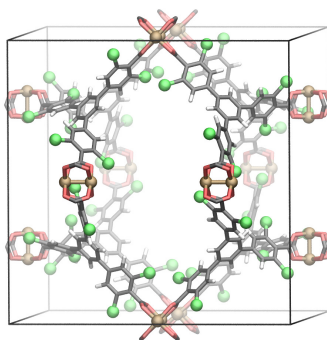


Figure 4.15: Cu-BTB-Br6 network in the unfavorable **pto** topology. (Cu: copper, C: dark grey, H: white, O: red, Br: green)

4.3 Summary

The first *ab-initio* derived fully flexible force field for copper paddle wheel based MOFs was developed. The MM3 energy expression was extended with specific cross terms, bond stretch and angle terms, suited to model the pseudo square planar copper coordination environment. In this context, a genetic algorithm parameter fitting method was used. Both structure and Hessian matrix reference data of non-periodic models were calculated on the B3LYP/aug-cc-pVDZ level, which was verified to be sufficiently accurate in comparison to experimental data and higher level theory. For validation, the resulting force field was employed to compute structure, elastic constants and thermal expansion of the well known HKUST-1. An indication for the accuracy of the force field is the fact that the measured NTE is quantitatively reproduced. The origin of this effect is a delicate global motion of the framework and shows that in particular low normal modes, responsible for the network deformation, are well parametrized. In addition, the bulk modulus calculated by the force field is in good agreement with the measured value.

Based on this, the network structures of different copper paddle wheel MOFs were studied in terms of topological isomerism. Considering MOFs, constructed by this inorganic unit and tritopic carboxylate linkers, two high symmetric network can be generated: **tbo** or **pto**. Using the first principles derived force field, corresponding structures and strain energies for networks obtained by the *btc* linker and its extended variant *btb* were computed. In addition interpenetrated system were investigated. As observed experimentally in HKUST-1, for *btc* the **tbo** topology is preferred, since the bowing of the linker means less strain than a rotation of the carboxylate groups out of the aromatic plane, necessary in the **pto** case. The contrary is true for the extended *btb* linker, where the **pto** topology is energetically favored because of the additional flexibility in the biphenyl bond. This tendency is maintained

also in case of interpenetration. From an estimate of the solvation contribution via the solvent accessible surface, the interwoven **pto** network appears to be the energetically preferred system, which is known indeed experimentally as MOF-14. Most noteworthy, the structural deformation for this interweaving is accurately predicted by the force field and the corresponding strain energy can be quantified. By ortho-substitution with a sterically demanding bromium the carboxylate is rotated out of the aromatic plane. On the basis of the force field calculations it is proposed that a sixfold brominated BTB-Br₆ should again prefer the more open **tbo** network topology.

Chapter 5

Covalent Organic Frameworks

Covalent organic frameworks (COFs) have recently been introduced as a further new class of functional porous materials [31, 181, 182]. Similar to the inorganic (e.g. zeolite) and hybrid (e.g. MOFs) porous compounds, they are crystalline compounds. They are assembled from molecular building blocks and maintain their long-range ordering and porosity even after the removal of guest molecules. Although this part of the work is entitled with the term “MOF”, the COFs are treated in the same scope, due to the close chronological development of them and because of the possibility to use the reverse topological approach to study them. As mentioned in the introductory part of this work, COFs are built from light main group elements such as carbon and oxygen. Thus the network is, in contrast to MOFs, constructed by purely covalent bonds. The two- and three-dimensional COFs are obtained by polycondensation reactions of mostly boronic acids.

From the perspective of the potential applications like gas storage, COFs are interesting due to their high porosity and their low densities. In fact one representative (COF-108) has the lowest density known for a crystalline material [31]. In this regard, theoretical studies of COFs dealt mainly with adsorption of light gases like hydrogen or methane [38, 183–185]. These investigations allow a deeper insight into the host-guest interactions and would, in principle, also help to modify and optimize the framework systematically by a computational pre-screening of properties. For example, the possibility to improve the hydrogen uptake by “doping” of COFs with Lithium atoms has been studied [186–189]. However, in the majority of cases the network structure was taken from experimental data and was kept fixed, which limits the predictive capability of the theoretical method. In addition, as pointed out before, using experimental results as input for theoretical investigations might

lead to wrong conclusions. Considering COFs the discrepancy might be more severe compared to the copper paddle wheel MOFs, since so far they are just obtained as polycrystalline powders [31, 181, 182], which makes experimental characterization difficult. To evaluate the X-ray diffraction data, theoretical models are needed as a starting point for the Rietveld refinement procedure. In practice, considering the boron containing 3D networked COFs the formation of high symmetry, edge transitive networks has been assumed. For these 3,4-networks with trigonal and tetrahedral building blocks two high-symmetric topologies are in principle possible [127, 173], namely **tbo** and **ctn**, shown in Fig. 5.1. The topology of all 3D-COFs was deduced by a comparison of the measured and simulated PXRD data for these options.

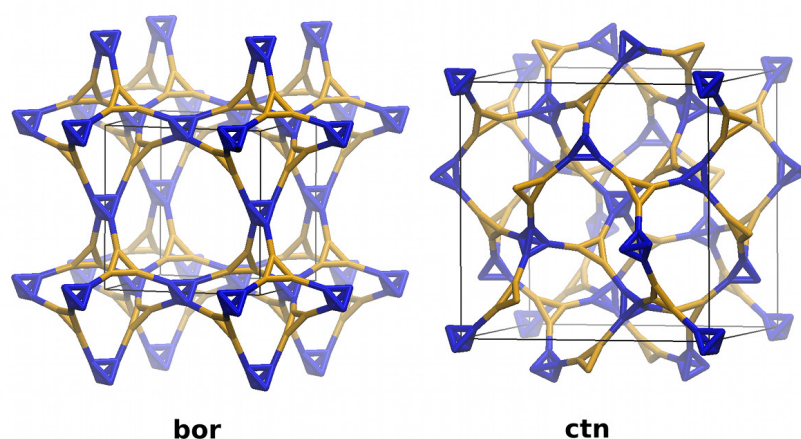


Figure 5.1: Network Topologies of the two high symmetric (edge transitive) 3,4-heteroconnected networks with a tetrahedral and trigonal building unit. The augmented networks are shown, respectively.

To allow theoretical investigation without the use of any experimental data, one aim of this chapter is to present an accurate force field for all currently known boron based 3D-COFs, covering the building blocks shown in Fig. 5.2. Although for purely organic systems parametrization like for example the MM3 and MM4 force fields [96, 168, 190] or MMFF94 [191] are available the accuracy for the particular systems is neither known nor can it systematically be improved. To get an explicit force field for the COFs a parametrization strategy is applied similar to the one used in the case of the copper paddle wheel based MOFs. Thus the parameters are obtained in a strictly bottom-up fashion without recourse to any experimental data. Importantly, the convergence of the quantum mechanical reference calculations is carefully controlled, and thus the resulting force field accuracy is known, in sharp contrast to “black-box” generic force fields (e.g. UFF [192]). This allows structural predictions of yet not-synthesized systems for a computational pre-screening of properties like gas

adsorption [189], lifting the constraint to experimental known structural data. In addition, dynamic effects like for example elastic constants or thermal expansion can be computed.

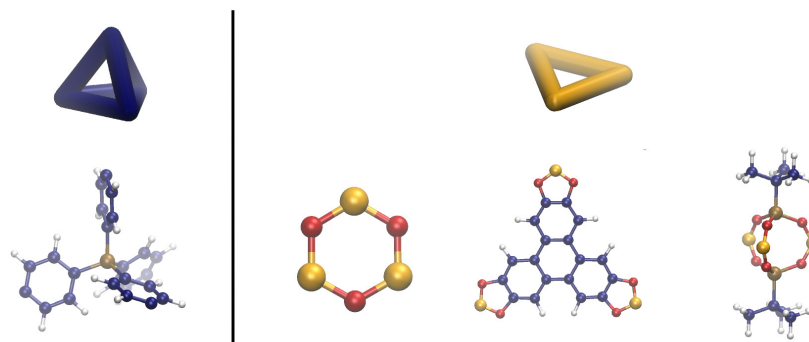


Figure 5.2: SBUs considered in this work together with the augmented vertex figures. Note that the central atom in the tetrahedral SBU (left) is either carbon or silicon.

Further within the framework of the reverse topological approach the structure of all boron based 3D-COFs are investigated to understand experimental results. Surprisingly, all but one are found to form the **ctn** topology, and for unknown reasons only COF-108 crystallizes in the **bor** topology. This observation is obviously in contrast to the basic assumption of concepts like the *reticular chemistry* [116, 193]. In the latter case it is presumed, that the linking of SBUs with a well-defined conformation and shape leads to a specific topology, and in case of “shape-conserving” variations this results in a family of isorecticular materials [174].

In order to understand and control the formation of certain framework topologies, it remains to be clarified which factors govern the solvothermal growth process. In principle, due to seeding and kinetic effects specific topologies could prevail over others. However, because of the slow solvothermal growth process of COFs it is plausible that thermodynamic factors will dominate. Thus, the framework topology with the lowest free energy under synthesis conditions of the overall system, including the solvent, will be formed. Two major factors, determining this free energy, can be discriminated: First, there are “extrinsic” effects, governed by the synthesis conditions like for example the nature of the solvent, the temperature or the concentrations of the building blocks. These effects are crucial in the case of zeolites, where primarily templating allows to obtain specific topologies with the same tetrahedral SiO_4 -unit [29, 194]. In fact, the synthesis conditions of the COFs differ to some extent substantially. In contrast to that, “intrinsic” contributions depend only on the steric preference for a topology of the framework itself and are tightly connected to the conformational freedom of the building blocks. It is an important aspect of

porous materials like MOFs and COFs that these “intrinsic” effects can dominate, which allows to alter the topology by substituting the organic linker [195]. Such a tuning of the framework topology has only rarely been achieved in a true rational way, since detailed understanding of the subtle balance between strain effects in different topologies is needed. As mentioned before, experimentally, in a few cases different topologies have been achieved by varying the synthesis conditions, but it is difficult to discriminate between intrinsic and extrinsic effects. Theoretical methods, on the other hand, allow to investigate also hypothetical systems to clearly separate and analyse the relative strain in different topologies. Therefore, the second aim is to gain an understanding of the “intrinsic” factors determining the formation of a specific topology, which is only possible with the computation of reliable steric energies also for large systems in a sequential multi-scale fashion. In particular, the question shall be reconsidered, whether the outlier in the 3D-COF series, namely the less dense **bor** topology of COF-108 is due to the specific nature of the building blocks or just because of the “extrinsic” synthesis conditions. Therefore the first challenge in this context is to model the respective systems with sufficient accuracy in order to assess the strain energy and its origin with sufficient precision.

5.1 Reference Systems

According to the approach used for the copper paddle wheel systems and motivated by experimental concepts [173, 193, 196, 197], a building block approach was used to generate appropriate reference systems. Thus the necessary parameters for the currently known boron based 3D COFs 102, 103, 105, 108 [31] and 202 [182] have been derived from six non-periodic model systems shown in Fig. 5.4 and 5.3. These fragments are derived from the SBUs of the real systems by just cutting carbon-carbon bonds. In the case of the trigonal SBUs the boron atoms are always saturated with benzyl groups. Due to the size of the trigonal unit in COF-105 and 108 it was further divided into two subunits (B1 and B2; see Fig. 5.3).

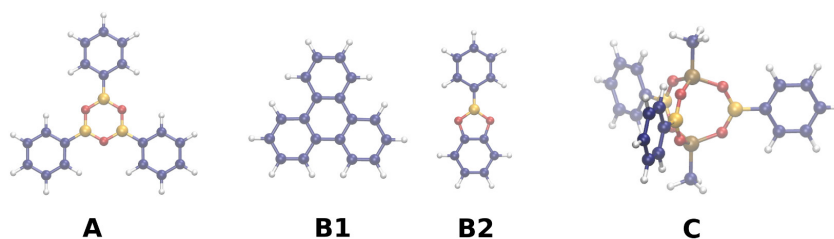


Figure 5.3: Non-periodic reference system used for the force field parametrization of the trigonal units.

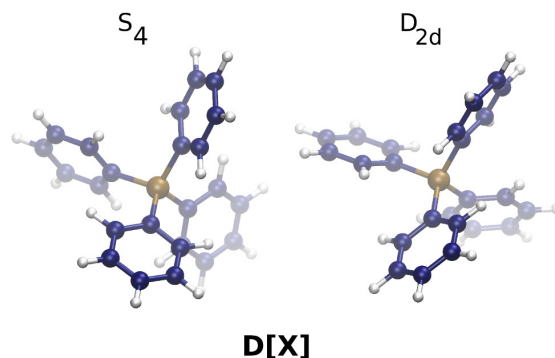


Figure 5.4: Non-periodic reference system used for the force field parametrization of the tetrahedral units D[X] (X=C, Si).

It should be emphasized once more that both the minimum structures and the corresponding second derivatives are fundamental for the force field parameter fitting approach, since they allow a proper extrapolation of the potential energy surface (PES) in the accessible energy range around the reference structures. Thus, convergence with respect to the theoretical level needs to be monitored. All structures were optimized on the B3LYP level, which is known to yield accurate structural data for organic molecules. A comparison of relevant structural parameters like bond lengths and angles showed good convergence already with the cc-pVTZ basis set. The Hessian matrix for all models was also calculated on the B3LYP level with the cc-pVTZ basis set [155–157]. This was verified by a normal mode analysis for **D[C]** on the cc-pVTZ which showed negligible changes. However, a crucial point in the parametrization is the fact that in the two topologies (Fig. 5.1) different local symmetries of the tetrahedral units are present: In the **ctn** net the four coordinate vertex has a local S_4 symmetry, whereas in **bor** it has a D_{2d} symmetry. In the real network this is realized by two different conformations of **D** (Fig. 5.3). Already in a previous work the need to refit the standard MM3 parameter set in order to properly model the molecule was pointed out [198]. Thus to accurately describe the PES for the conformational freedom with respect to single bond rotations, the rotational transition states of the reference systems was considered. In this context dispersion effects have to be included, which are not covered by standard DFT functionals. The importance of non-covalent intramolecular interactions was shown before [199, 200]. In the modeling of porous hybrid materials, dispersion contributions were just considered in the context of weak host-guest interactions like for instance in the case of hydrogen physisorption. Consequently, mostly wave function

based correlated methods were used to parametrize these intermolecular potentials [38, 162, 185, 201, 202]. However, so far these effect were not considered with respect to their influence on intramolecular steric interactions in porous materials. Using the structures obtained on the B3LYP level, improved relative energies were computed by single point calculations using the double hybrid functional B2PLYP. In addition, for the tetrahedral SBUs the MP2 method was used for a full geometry optimization.

In case of the models for the trigonal SBUs a rotation around one of the carbon-boron single bonds was investigated. For the tetrahedral models **D[X]** the concerted X-C bond rotation from S_4 to D_{2d} symmetry was computed. In Tab. 5.1 the calculated rotational barriers for the non-periodic fragments **A**, **B2**, **C** and **D[Si]** are given. Enlarging the basis set slightly decreases the rotational barrier of all conjugated carbon-boron bonds in **A-C**, since by a larger basis set the less conjugated transition state structure is stabilized. This was also observed previously for the linker rotation in carboxylate MOFs [164]. The inclusion of dispersion effects leads to a decrease of the rotational barrier for **B2** but to an increase for **A** and **C**. For the tetraphenylsilane **D[Si]** the influence of basis set and theoretical level is not significant.

Table 5.1: Energy barrier different conformers ΔE in [kcal/mol]

		A	B2	C	D[Si]
		$\Delta E(0^\circ - 90^\circ)$			$\Delta E(S_4 - D_{2d})$
B3LYP	cc-pVDZ	6.74	6.01	6.46	1.84
	cc-pVTZ	6.42	5.51	6.15	1.83
B2PLYP	cc-pVDZ	6.88	5.84	6.64	1.91
	cc-pVTZ	6.57	5.44	6.26	1.87
MP2	cc-pVDZ	-	-	-	1.85
Force Field		6.64	5.63	6.39	1.90

On the other hand, the most difficult reference system was found to be the tetraphenylmethane **D[C]**. Replacing the central silicon by a carbon atom causes a decrease of the rotational barrier by about 1 kcal/mol to only 0.69 kcal/mol on the B3LYP/cc-pVDZ level, despite the shorter C-C versus Si-C bond lengths, showing the different nature of the **D[C]** and **D[Si]** units. In addition, an increase of the rotational energy barrier is observed when enlarging the basis set, converging at a value of 0.84 kcal/mol for B3LYP. Furthermore, dispersion effects are very important for an accurate description of the conformational energies of **D[C]**. Since the MP2 values show a very slow convergence, the cc-pVDZ, cc-pVTZ and cc-pVQZ

[155–157] results were exponentially extrapolated to the complete basis set (CBS) limit. The MP2/CBS value of 1.45 kcal/mol is about 0.6 kcal/mol higher than the B3LYP result. However, the use of the double hybrid functional B2PLYP, gives an intermediate value of about 1.1 kcal/mol for the barrier and converges much more quickly with the basis set size, as mentioned before [95]. Due to the known overestimation of MP2 for aromatic interactions [203] and the good description of the B2PLYP functional for the isomerization energy of organic molecules [204], the double hybrid DFT method seems to be a reasonable choice for the particular system.

Table 5.2: Energy difference between the S_4 and D_{2d} conformer of tetraphenylmethan **D[C]** [*kcal/mol*].

	B3LYP	B2PLYP	MP2
cc-pVDZ	0.69	1.13	1.76
cc-pVTZ	0.82	1.11	1.56
cc-pVQZ	0.84	1.09	1.49
CBS	0.85	1.06	1.45
Force-Field		1.10	

Thus the B3LYP/cc-pVDZ level are used for computing the structural and curvature reference data. However, the corresponding value for the rotational energy barriers between conformers are taken from calculated data on the B2PLYP/cc-pVTZ level (or B2PLYP/CBS where available).

5.2 Parametrization and Validation

Appart from the van der Waals parameters, taken unaltered from the standard MM3 set [163], also some parameters for bonded interactions, mainly for the phenylene units, could be maintained. However, for all boron containing fragments, different boron atom types were introduced, because of the significant differences in their chemical environment, which had all to be parametrized. In the same manner, new parameters for the central atoms of the **D[X]** units were fitted. In addition, in order to properly describe the annealated system in **B1** a new atom type was introduced for the carbon atoms of the central aromatic ring. Note that all bonded terms, where new atom types are involved, were parametrized from scratch. The atomic point charges were derived from the electrostatic potential (ESP) fitted charges (Merz-Kollman sampling scheme [161]) of the model systems, by using a group-neutrality concept to enable transferability to the periodic system. Therefore just some linking carbon atoms were slightly adjusted in order to maintain charge neutrality of the fragments. The final charges are listed in Tab. 11.8 (appendix).

In the case of **A**, **B1**, **B2** and **C**, the minimum structure and the Hessian matrix were used to fit the parameters by the genetic algorithm optimization. In addition, to be able to reproduce the rotational profile around the carbon boron bond, it is sufficient to adjust the corresponding torsion parameter manually to reproduce the B2PLYP/cc-pVTZ energy barrier afterwards, since this term couples only very weakly. A very good correspondence between the final force field and the reference first principles data for both structure (mean deviation: bond: < 1.5%; angle: < 0.7%) and vibrational normal modes (high overlap of the normal mode vectors and similar vibrational frequencies) is found (Tab. 11.9).

Again for the **D[C]** unit some problems occur, when determining the atomic charges by ESP fitting. For such highly symmetric systems it is difficult to assign a proper charge for the central atom, which is usually referred to as the “buried atom” problem. Here a physically not meaningful high charge of about -1.83 was obtained for the central carbon atom together with a compensating charge for the adjacent carbon atoms of +0.64. A similar problem was observed for the central oxygen in the Zn_4O unit occurring in various MOFs [162, 205]. Note that Manz et al. recently suggested a new charge fitting scheme to overcome this problem [206]. In the present system it was decided to keep both the central carbon and the four directly linked carbon atoms at zero charge, since the high symmetry leads to negligible effects on the electrostatic potential in the periphery of the system, but the fitting of the conformational degrees of freedom became more stable.

In order to describe the delicate PES for the symmetry breaking motion of the tetrahedral **D[X]** units, a new fitting approach was used within the GA method: the relative energy between the S_4 symmetric minimum and the D_{2d} symmetric transition state was explicitly included into the objective function, with the reference values taken from the B2PLYP level calculations. This strategy was found to be crucial in order to obtain a good agreements for the tetraphenyl units with respect to both second derivatives and the rotational barrier, since the transition between the S_4 and D_{2d} conformers is governed by a coupling of multiple force field terms.

As a validation of the building block approach the transferability to larger systems was tested. The larger model system **B** (Fig.5.5), which represents the trigonal vertex in COF-105 and 108, is formally built from **B1** and three connected **B2** fragments. The results for the complete molecule **B**, using the combined force field fitted to **B1** and **B2**, are compared with the corresponding reference data computed on the B3LYP/cc-pVDZ level. The geometry is perfectly reproduced (Tab. 5.3). More importantly, also the normal modes below 400 cm^{-1} , which are mainly collective motions of the whole system, like the out of plane deformation or twisting of the **B2** fragments with respect to the **B1** unit, compare very well (Tab. 5.4). For the normal mode describing the buckling of the system excellent agreement between

DFT reference (17 cm^{-1}) and force field (18 cm^{-1}) are obtained. The overlap of the normal mode vectors is 1.0. This confirms the decision to partition the periodic system into non-periodic subunits for the parametrization. A similar accuracy of our force field was found for the butyl-substituted **C** as in COF-202 (Tab. 11.10).

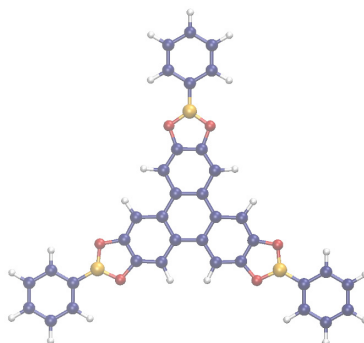


Figure 5.5: Non-periodic model system **B** used for the force field validation

Table 5.3: Comparison of the geometry of the system **B** in [\AA]

bond	B3-LYP/cc-pVDZ	Force Field
$C_{ph(center)} - C_{ph(center)}$	1.466	1.467
$C_{Ph(center)} - C_{Ph}$	1.424	1.439
$C_{Ph} - C_{Ph}$	1.373	1.379
$C_{Ph} - O$	1.372	1.378
$O - B$	1.399	1.394
$B - C_{Ph}$	1.542	1.543

5.3 Network Topologies

It is striking that four of the five known boron containing 3D-COFs are experimentally obtained in the **ctn** topology. This holds also for the later published COF-202, which is unique in the sense that the phenylene units stand perpendicular to the trigonal vertex plane (see also model **C** in Fig. 5.3), whereas in all other COFs they are parallel to this plane (Fig. 5.6)

Table 5.4: Normal modes in [cm^{-1}] below 400 cm^{-1} of the model system **B**

B3-LYP/cc-pVDZ	Force Field	deviation	overlap ^a	mode degeneracy
17	18	+1	1.00	1
23	21	-2	0.85	2
34	31	-3	0.99	1
34	35	-1	1.00	2
39	41	+2	0.87	2
63	59	-4	0.90	2
62	68	+6	1.00	1
100	77	-23	0.99	1
82	86	+4	0.98	1
120	123	+3	0.99	2
160	145	-15	1.00	1
141	175	+34	0.79	2
221	205	-16	0.99	2
186	215	+29	0.97	1
250	230	-20	0.99	1
232	240	+8	0.68	2
316	293	-23	0.99	2
284	333	+49	0.97	2
404	367	-37	0.99	2
391	368	-23	1.00	1
323	370	-47	0.99	1
358	373	+15	0.91	1
410	390	-20	0.76	3
376	399	-23	0.71	2

^a Scalar product of the respective normalized eigenvectors of the Hessian matrix.

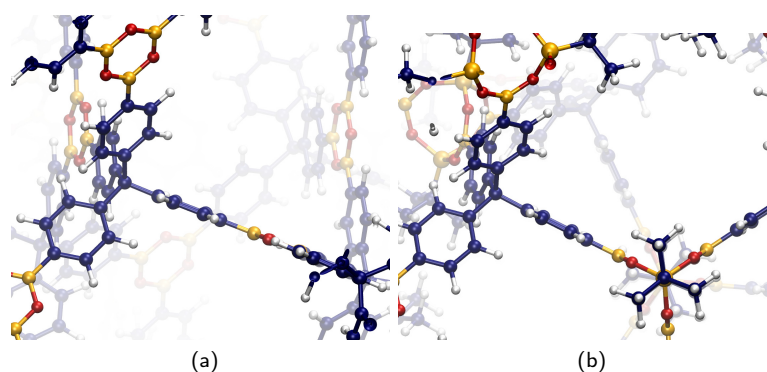


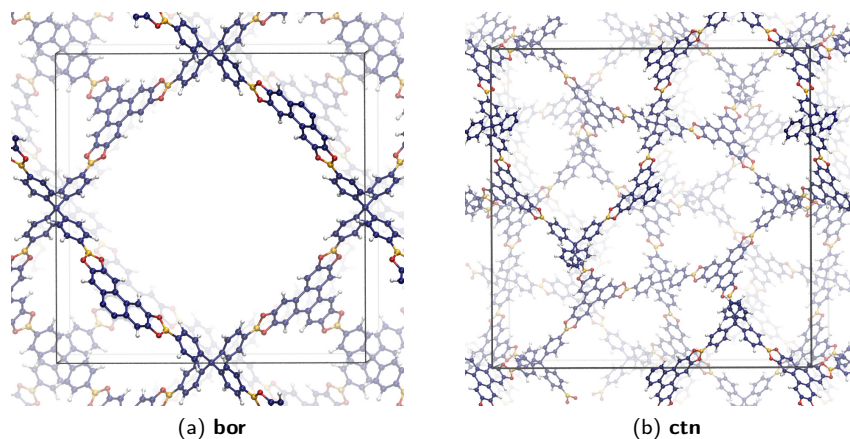
Figure 5.6: Comparison of the orientation of the phenylene units in (a) COF-102 and (b) COF-202

Only COF-108 shows the less dense **bor** topology, which differs from COF-105 only by substituting silicon with carbon in the center of the tetrahedral unit. However, the first principles calculations of the reference systems already pointed out

that this substitution leads to noticeable differences in the conformational behavior and the model **D[C]** was the hardest to parametrize accurately. Thus, it might indeed be possible that COF-108 is special in its conformational flexibility. On the other hand, the synthesis conditions for the preparation of COF-108 are substantially different from COF-105 (e.g. different solvent mixtures and variation of the synthesis time, temperature and ratio of the starting materials [31]), so that the observed structure could also be due to “extrinsic” factors. In order to shed light on this question, the parametrized force field was used to investigate the structure and strain energy for the ideal crystalline frameworks in both the **bor** and the **ctn** topology and in the absence of any solvent molecules (in other words perfectly activated). However, it should be pointed out that not all compounds could be obtained fully activated like for instance COF-108 [31]. Nevertheless, all systems were generated and fully optimized in both topologies. As an example, in Fig. 5.7 the unit cells of COF-108 in both topologies is shown. A comparison of the computed cell parameters obtained with the corresponding experimental values shows excellent agreement (Tab.5.5). As already mentioned, the different networks are topological isomers and reside on the same potential energy surface. The relative strain energies are given in Tab. 5.5 per formula unit (three tetrahedral and four trigonal SBUs). The results clearly show that for all COFs the **ctn** topology is sterically preferred. The difference is less pronounced for the COFs 102 and 108 with the tetraphenylmethane SBU, and also the larger trigonal linkers in 105 and 108 lead to a reduced preference, making COF-108 to the system with the lowest energy difference. However, with 8.1 kcal/mol energetic preference for the **ctn** topology it is clear that the experimental outlier is due to the synthesis conditions in this case. At this point it can just be speculate on the origin of these “extrinsic” effects, but the theoretical results allow to conclude that under specific conditions, e.g. with appropriate templating molecules, also for the other COFs the **bor** topology should be accessible in principle and vice versa it might be possible to construct COF-108 in the **ctn** topology .

Table 5.5: Relative Energies (per formula unit in [kcal/mol]) and lattice size in [Å] for all investigated COFs.

	$\Delta E(bor - ctn)$	lattice		
		bor	ctn	exp.[31, 182]
COF-102	8.75	17.660	27.144	27.1771(13)
COF-103	12.89	18.395	28.353	28.2477(21)
COF-105	11.88	29.060	44.596	44.886(5)
COF-108	8.09	28.345	43.387	28.401(5)
COF-202	17.58	17.953/19.539/17.945	30.331	30.1051

Figure 5.7: Structure of COF-108 in the **bor** and **ctn** topology

A detailed inspection of the final structures explains the clear preference. In the **ctn** topology the tetrahedral SBUs are all locked in a conformation similar to the S_4 symmetric minimum. In contrast to this a distorted form, close to the D_{2d} transition state structure of the SBU model, is present in the **bor** case. This is shown on the example of COF-108 in Fig. 5.8. There is not even a local minimum for the **bor** network, since an optimization starting from the S_4 symmetric conformation in the tetrahedral SBUs relaxes back to D_{2d} .

In order to verify the force field in this point, which is crucial for the steric preference of COF-108, one of the tetrahedral units of the two COF-108 networks were cut out. The dangling bonds were saturated by hydrogen atoms (with only these hydrogen positions optimized), leading to a nonperiodic system similar to the reference system **D[C]**. Afterwards the energy difference between these distorted fragments was computed, which are different from the relaxed minima used in the parametrization, both on B2PLYP/cc-pVTZ and force field level. The quantum mechanical energy difference of 1.27 kcal/mol is in good agreement with the 1.54 kcal/mole computed by the force field, corroborating the accuracy of the force field for such subtle strain effects.

Also the structural differences of the trigonal units reveal a further reason for the preference for the **ctn** topology, since in **bor** these units are significantly bended as shown in Fig. 5.9. This bending is obviously energetically unfavorable, which is more pronounced in the smaller and stiffer boroxen units in COF-102 and 103. Note that this bending is very close to the low vibrational buckling mode of the model B, which is reproduced within 1 cm^{-1} by the force field with respect to the DFT

reference.

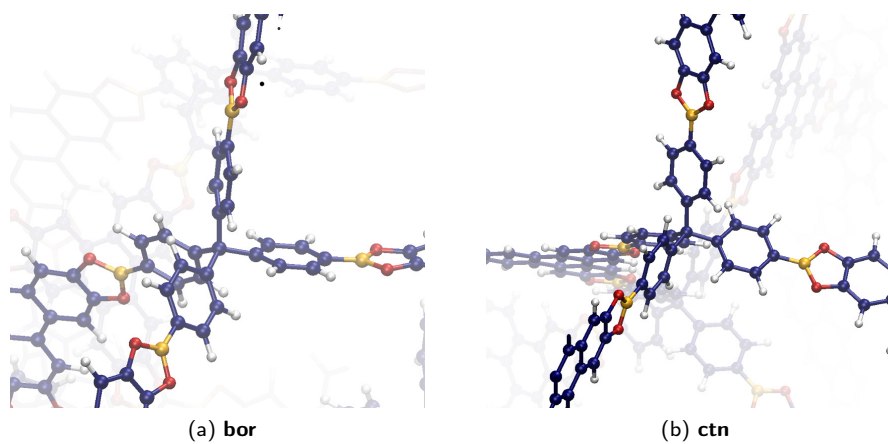


Figure 5.8: A close-up of the Tetraphenylmethane-unit $D[C]$ in COF-108.

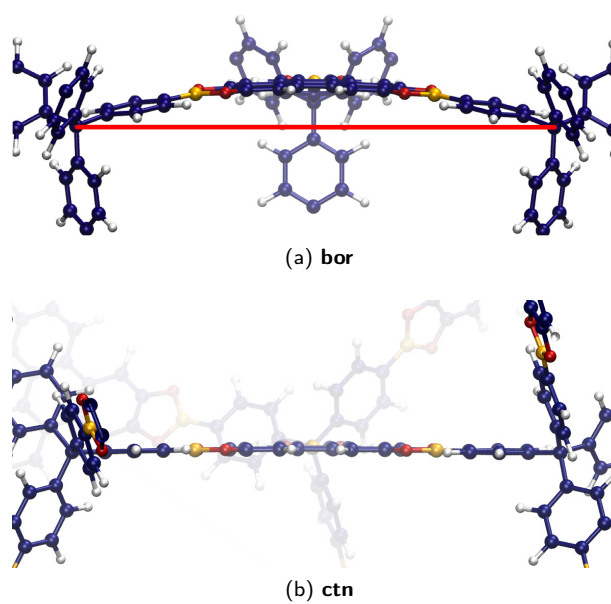


Figure 5.9: Bending of the trigonal unit in the [a] **bor** and [b] **ctn** topology of COF-108

Finally it should be noted that the highest energy difference is obtained for the COF-202, which is due to a strong deformation of the trigonal SBU in the **bor** topology.

5.4 Prediction of Structural and Dynamic Properties

Currently, all theoretical investigations of COFs are mainly focused on gas adsorption studies. Measured data on other properties are rather rare [183, 207]. One reason for this could be the polycrystalline nature of the so far obtained samples and the difficulty to completely remove solvent and monomer molecules. With an accurate theoretical method at hand structural properties can be predicted for the ideal systems, which can serve as a benchmark and reference for the experimental studies. In addition, also the structure of yet unsynthesized systems can be predicted and investigated on the same footing. Some examples of this approach, using one previously developed force field limited to COF-102, have appeared recently [189, 208]. Therefore the new force field, parametrized consistently for all known boron containing 3D-COFs, was used to compute structural and dynamic properties for both possible topologies. Even though the **ctn** topology is preferred for steric reasons, the example of COF-108 shows that this preference can be compensated by proper reaction conditions.

The geometrically determined accessible surface area was computed, which was shown by Düren et al. [179] to be very similar to the experimentally surface area, usually determined via a BET analysis of the nitrogen adsorption isotherm, giving an upper boundary of this property for the ideal, defect free and optimally activated framework. In addition the dynamic properties of thermal expansion and elastic constants are studied. All computed results have been summarized in Tab. 5.6.

In general, the **bor** topology is always less dense than the **ctn** topology [173]. On the other hand, by substituting carbon with silicon when going from COF-102 to 103 or from COF-108 to 105, the larger mass per formula unit is compensated by the larger lattice due to the longer Si-C bond length, which is reflected by a decrease of the density ρ . The accessible surface per formula unit S ($[m^2]$) is very similar for both topologies, since in all cases the pores are large enough so that the exposed surface for each building block remains the same. Thus, the larger S_m ($[\frac{m^2}{g}]$) for the **bor** case is only due to the lower density. A noteworthy exception is COF-202, with its strong deformation in the **bor** topology. Here, the accessible surface area S and S_m are reduced due to the deformed structure.

It is interesting to compare the computed surface areas S_m for the ideal system with the results obtained experimentally via fitting to the adsorption isotherms with the BET model. So far, only the surface areas of COF-102 and 103 in the observed **ctn** topology have been determined with $3472 m^2/g$ and $4210 m^2/g$, respectively [31]. In agreement with the theoretical data, COF-103 has a higher S_m . However, in both cases the calculated values are significantly larger, indicating the presence of included solvent molecules or partial decomposition of the network in the mea-

sured samples. In a more recent paper, Furukawa et al. [207] presented new data for the BET surface areas of COF-102(**ctn**) with $3620\text{ m}^2/\text{g}$ and COF-103(**ctn**) with $3530\text{ m}^2/\text{g}$. Nevertheless, the discrepancy between the experimentally and theoretically determined surface areas remains. In this regard the theoretical ideal surface area of COF-108 in the experimentally obtained **bor** topology has a surface area of $6553\text{ m}^2/\text{g}$, which exceeds all known porous materials, even the recently reported metal-organic frameworks UCM-1[209] and MOF-210[209]. Unfortunately, the solvent molecules present in the pores after the synthesis could not be removed, yet, [31] to enable adsorption studies of COF-108.

An indication for the flexibility of the framework is the thermal expansion coefficient, which was found to be negative for different MOFs [170, 210]. This negative thermal expansion (NTE) effect could be quantitatively predicted by accurate force fields [160, 169, 211]. Using the previous force field for COF-102 [198] Zhao et al. already computed a volumetric expansion coefficient of $\beta = -4.5 \times 10^{-6}\text{ K}^{-1}$ for COF-102 in the **ctn** topology [208]. With the new improved force field the value of β is about two times higher. Most importantly, the values given in Tab. 5.6 allow for a comparison for different systems and topologies on a consistent footing. Interestingly, the less dense **bor** topology shows a smaller NTE in particular for the large systems COF-105 and 108. A substantial exception is again COF-202. Obviously the cage like trigonal SBU is much more flexible than for the other COFs with the largest NTE of all systems. On the other hand, the sterically very unfavorable and deformed **bor** topology is “locked” in its strained position, which leads to a symmetry breaking to an orthorhombic cell and a complete loss of the NTE. Here a positive thermal expansion was found.

In addition, the elastic constants for all 3D-COFs were computed. Noteworthy, the systems with a larger NTE have a smaller bulk modulus. In fact the low density materials COF-105 and 108 show bulk moduli below IRMOF-1 ($B = 14\text{ GPa}$ [98]). In the case of the **bor** topologies, B is smaller despite the smaller NTE, showing that stiffness and elastic constants are not always directly related. Considering other porous materials like ZIF-8, which has a bulk modulus of 6.52 GPa [212], points out the high mechanical stability of these purely organic materials. Especially, the **ctn** networks of COF-102 and 103 show values for B , which are comparable with IRMOF-1 ($B = 14\text{ GPa}$ [98]), emphasizing their structural stiffness.

Table 5.6: Computed structural and dynamic properties of all COFs in both topologies.

COF	102		103		105		108		202	
	bor	ctn	bor	ctn	bor	ctn	bor	ctn	bor	ctn
$\rho[g/cm^3]$	0.38	0.42	0.35	0.38	0.16	0.18	0.17	0.19	0.57	0.51
$S[\text{\AA}^2]^a$	1079	1066	1193	1182	2676	2657	2559	2542	1275	1549
$S_m[m^2/g]^a$	5115	5052	5447	5392	6714	6668	6553	6508	3580	4350
$\beta[10^{-6}K^{-1}]^b$	-7.0	-9.8	-3.1	-10.9	-11.1	-19.1	-10.6	-18.2	+41.5	-38.5
$B[GPa]^c$	8.3	15.4	5.7	11.8	2.1	5.7	2.9	7.0	1.5	11.0
$C_{11}[GPa]^c$	11.7	17.0	8.0	12.9	2.7	6.1	3.9	7.5	2.5	12.3
$C_{12}[GPa]^c$	8.5	14.6	6.1	11.3	2.2	5.5	3.0	6.8	0.6	10.3
$C_{44}[GPa]^c$	5.1	3.6	3.5	2.6	1.4	0.9	2.2	1.3	2.0	2.2

^a Solvent accesible surface area per formular unit. ^b Volumetric thermal expansion coefficients. ^c Elastic constants

5.5 Summary

In this chapter a force field was derived for all currently known three dimensional boron containing covalent organic frameworks. The parametrization was done in a bottom-up fashion using a genetic algorithm. In order to perform correlated quantum mechanical calculations, the periodic systems were represented by non-periodic models of the frameworks. In terms of these reference calculations the accuracy of the theoretical level was extensively analyzed. Indeed the importance of intramolecular dispersion effects was investigated for the first time. Since the aim was to use the force field for the study of network structures of COFs, a focus was set on the energy barrier between different conformers of the embedded units. This aspect is crucial with respect to the high symmetric network topologies possible for the considered systems: **bor** and **ctn**. The largest influence of dispersion effects was observed for the tetraphenylmethane. The energy barrier between the S_4 and D_{2d} conformer changes in this case by about 20 % (B3LYP vs. B2PLYP). Based on the quantum mechanical calculation, a force field was parametrized, which is able to reproduce the structure, Hessian matrix and the energy barrier of the conformers. The quality of the force field was further verified by calculations on non-periodic systems, which were not included in the parametrization scheme.

Further investigations based on the *ab-initio* force field reveal a energetic preference for the **ctn** topology in all COF systems, which is in agreement with the experimental observation except for the COF-108. In this case the **bor** topology is experimentally obtained. The discrepancy can be explained by the fact, that within the theoretical study extrinsic factors such as solvent molecules were not considered. Consequently, due to the high accuracy of the force field in terms intrinsic effects, it can be assumed that by modifying the synthetic conditions COF-108 can also be

obtained in the **ctn** topology.

Finally, surface areas and dynamic properties of the COFs were computed in a pre-screening fashion, since they are only synthesized in polycrystalline form, yet, which makes detailed investigation difficult. The calculated data can be used as benchmarks for further experimental works.

Chapter 6

Beyond Network Topology

In addition, to the topology, which is the main concern, when dealing with the structure of inorganic porous materials (e.g. zeolites), the molecular nature of the matrix has to be considered in the case of MOFs. Thus within the reverse topological approach two forms of isomerism are distinguished: isorecticular and conformational isomers. Both can appear within one topology, if corresponding SBUs are present. Investigations of these structural phenomena are pivotal, since a detailed understanding of the molecular structure would promote the performance of functional materials such as MOFs and COFs. In this regard the RTA enables the systematic exploration of the structural diversity of a MOF system. Using abstract network topologies as blueprints and replacing the vertices and edges of these scaffolds by molecular SBUs allows to generate different MOFs. The obtained molecular matrices are based on the same composition and the identical topology but differ in their local structures. By inserting every individual SBU selectively, this technique allows to analyze the internal molecular features (e.g. rotational degrees of freedom within the framework) systematically. Theoretical methods are valuable tools for these kind of studies, since small deviations from an ideal structure are usually hard to observe experimentally.

Since the focus of this chapter is the study of isorecticular and conformational isomers, a simple network topology is chosen. MOF-5 has a rather simple blueprint. The network can be simplified to a primitive cubic topology (**pcu**). Beside the frugal topology of MOF-5, it is a reasonable choice for detailed investigations, since several derivatives are known both experimentally and theoretically [174, 213–215]. They are usually summarized with the umbrella term **iso-recticular MOF** (IRMOFs)¹ [174, 214], since they own the same network topology and the same inorganic SBU and just differ with respect to their organic linkers. Indeed this family of MOFs

¹The term IRMOF is commonly used in the context of MOF-5 derivatives, although similar variation are possible for other MOFs.

represent the first example, in which systematic variations of the molecular system could be realized. For example, by replacing the terephthalic acid linker in MOF-5 by longer organic units the pore open could be varied [174]. In addition the MOF-5 system was subject of different works, trying to introduce functional groups by either derivatives of the organic linker as starting material [216] or in a post-synthetic fashion [63], but keeping the metric of the parent framework. Note that in all IRMOFs the topology of the framework is maintained just the pore surface is modified (e.g. introducing functional groups or scaling of the matrix). Although there are a large number of studies on these MOF-5 derivatives, which point out the high potential of these materials, detailed investigation on the influence of isorecticular modification on the local structure have not been done, yet.

A detailed examination of the MOF-5 structure points out a characteristic feature of the framework. The system has a **pcu** topology but with two kinds of vertices. The reason for this deviation is the inorganic SBU. The vertices of the **pcu** network have a high symmetry of O_h . The corresponding augmented form is thus build up by perfect octahedrons (Fig. 6.1). The $Zn_4O(O_2C)_6$ SBU has indeed an octahedral shape and represent the corners of the MOF-5 matrix. But due to the Zn_4O -tetrahedron in the core of the fragment the unit has a lower symmetry (T_d), which induce two possible orientations of the SBU within the network. In the case of MOF-5, they are embedded alternating, which is the reason why the MOF-5 topology is usually labeled as **pcu-b** to point out the two kinds of vertices². The arrangement of inverted or mirrored neighbouring tetrahedral nodes is due to the planarity of the terephthalic acid linkers. Thus, neighbouring linker planes are orthogonal to each other, which results in the enormous stability of the pore structure. Thus, the primitive cell of IRMOF-1³ consists of a $2 \times 2 \times 2$ array of cubic cells, which can, however, be separated in two sets of different type. In the A-cell, the faces of the Zn_4O -tetrahedrons and the planes of the linkers face into the pores, whereas in the B-cell the edges of the linkers and a vertex of the nodes tend inwards (see also Fig. 6.1). These two cells can not interconvert by a rotation of the linkers. It should be emphasized, that the present of different types of cells is a consequent of the low symmetry of the inorganic SBU.

However, this type of controlling the embedding of the inorganic unit by its organic environment is only the case for a planar linker (like terephthalic acid), where the planes of the carboxylic acid groups are coplanar. The situation changes if the carboxylic planes are orthogonal to each other, and thus the non planar linker is “twisted” by 90° . This is schematically shown in Fig. 6.2. The “twisted” linkers

²Note, that both vertices of the **pcu-b** topology have according to the RCSR-database[173] a O_h symmetry, which is not the case in MOF-5. The octahedrons of the augmented network should have just the T_d symmetry. Nevertheless, the label **pcu-b** is used to stress the difference between the networks.

³MOF-5 as also called IRMOF-1, since it is the parent structure for the IRMOF-family.

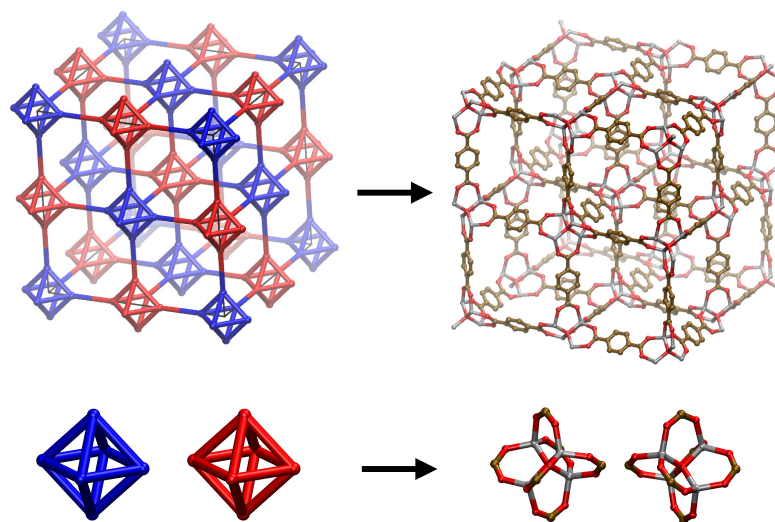


Figure 6.1: Derivation of the IRMOF-1 structure from the augmented **pcu-b** network (left). The two types of vertices correspond to the identical, but inverted lower symmetry tetrahedral SBU. For the unit cell of IRMOF-1 (right) the hydrogen atoms are omitted for clarity (C brown; O red; Zn grey).

promote the assembling of an isorecticular isomer, where the tetrahedral nodes are just translated but not mirrored. This type of matrix can be derived directly from the **pcu** network with $Pm\bar{3}m$ space group symmetry in contrast to $Fm\bar{3}m$ in the **pcu-b** system. The cubic pore structure is maintained, but the primitive cell is no longer a $2 \times 2 \times 2$ array of pores, since all cells are identical now. It should be stressed, that MOFs, which are obtained using the **pcu** and **pcu-b** topology, are isorecticular isomers within the reverse topological approach, since they share the same basic network topology, but just differ in the local orientation of their SBUs. Further one should keep in mind that to interconvert the two isomers rearrangement of strong coordinating bonds are needed.

In case of IRMOF-1 the conjugation between the carboxylic groups and the aromatic system (rotational barrier around the $C_{carbox} - C_{phen}$ bond of about 8 kcal/mol [205]) enforce the planarity of the linker and a twisted isomer has never been observed. However, there is experimental evidence for this type of isomerism. Both IRMOF-9 and 10 are based on a biphenyl linker (see Fig. 6.3), but they differ in the amount of solvent molecules and IRMOF-9 represents an interpenetrated structure. In addition to that, for IRMOF-9 the cubic symmetry is broken due to the fact that the linkers along one axis are twisted (non-coplanar) whereas the others are planar [174]. This is due to the much weaker conjugation of the biphenyl bond $C_{phen} - C_{phen}$ (the rotational barrier in biphenyl is about 2.5 kcal/mol [217]). For

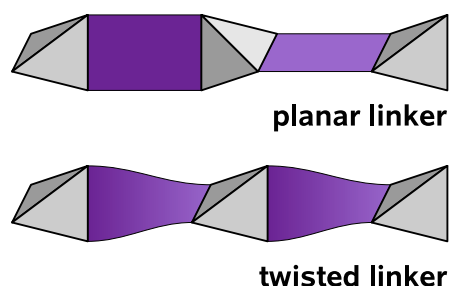


Figure 6.2: Schematic representation of the regular IRMOF structure with a planar linker (top) and the isomeric form with the twisted linker (bottom). The tetrahedrons represent the (Zn_4O) fragment.

the non-interpenetrating IRMOF-10 a single crystal structure could not be determined and the structure was solved from powder diffraction data, showing planar linkers but with a rotational disorder [174]. Thus, for linkers with weakly conjugated (biphenyl) bonds in the backbone a non-planar orientation of the $-COO$ groups is indeed possible. Another reason for a non-planar twisted linker can be steric repulsions as for example in 1,4-*naphthalen*-*dicarboxylic acid* based IRMOF-7 (see Fig. 6.3). Here a repulsion between the carboxylic oxygen and the hydrogen atom of the annealed ring makes a planar structure energetically unfavorable and the $-COO$ planes can either be planar or orthogonal to each other. This is even more pronounced for the symmetric linker in IRMOF-993, which was proposed and theoretically investigated in Ref. [213, 215], but not synthesized, yet.

As a consequence, all the corresponding IRMOFs could potentially form isorecticular isomer. Interestingly, the single crystal structure analysis of IRMOF-7 gives a cell parameter of 12.914 \AA , which is about half of the value of IRMOF-1 and corresponds to a $1 \times 1 \times 1$ cell structure [174]. The naphthalene units are fourfold disordered with respect to a rotation around the axis by 90° but also the Zn_4O tetrahedra are disordered (equal probability for the mirror image). Thus, the twisted isomer⁴ with the same type of disorder would yield an equal solution. It is therefore not clear, whether IRMOF-7 has a regular structure like IRMOF-1 or is actually the twisted isomer (or even a mixture of both).

In order to investigate this type of isomerism in detail and to quantitatively assess the possibility of its formation a classical molecular mechanics forcefield have been used to calculate the relative energies of the isomers for all linkers shown in Fig. 6.3. Note, that just the two high symmetric isorecticular isomers are investigated, but in principle a set of infinite number of isorecticular isomers are possible, if the

⁴Due to the twisting of the organic linker in the pcu-type MOFs this type of isorecticular isomers will be called twisted isomers.

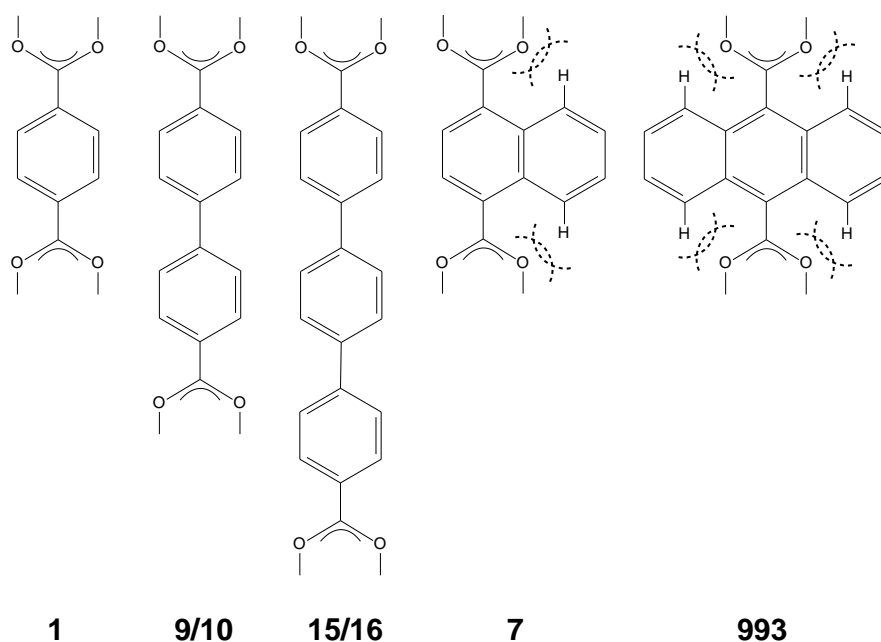


Figure 6.3: Bicarboxylic linkers of IRMOF-1, 9, 10, 15, 16, 7 and 993. Possible steric repulsions in case of IRMOF-7 and 993 are marked by dashed curves.

ordering of the two kinds of octahedron is less systematic and the system size is large enough.

Using a force field, which is explicitly parametrized for MOF-5 [205], it is possible to investigate IRMOF structures, which just differ with respect to their organic linkers and are covered by the standard MM3 parameter set. However, the force field will be validated concerning the barrier of rotation for the naphthalene unit present in IRMOF-7. In addition to possible isorecticular isomers, conformational isomers are possible, since the organic linkers in the IRMOFs have a rotational degree of freedom within the framework. Thus it is necessary to implement an efficient screening strategy to consider all possible conformers of the linkers within the study. Therefore a genetic algorithm (GA) will be used to screen all conformational isomers.

6.1 Validation of the force field

As already noted a force field derived for IRMOF-1 was used without modifications for the other organic linkers shown in Fig. 6.3. However, for the sterically more congested systems like IRMOF-7 and 993 additional electronic and repulsive interactions are in a delicate balance with the conjugation of the $C_{carbox} - C_{phen}$ bond. In order to verify the validity of the approach the rotational barrier around the linker axis for these two systems was determined on the B3LYP level (together

with the Stuttgart relativistic small core ECP [218] for the Zinc atoms and a 6-31G(d,p) basis [94] for the other atoms) for the non periodic model of the edge of the framework. Two Zn_4O units were capped by five formic acid groups and connected by the respective linker. In order to avoid an unreasonable bending of the $[(Zn_4O)(O_2CH)_5]$ fragments, they were constrained to the positions optimized for the unconstrained terephthalic acid case. This restriction was invoked for both the DFT and MM3 optimization. The two transition states of the rotation at 0° and 90° were located by using the corresponding symmetry constraint (IRMOF-7: C_{2v} ; IRMOF-993: D_{2h}). In Tab. 6.1 the results are summarized. Obviously the minimum geometry and the relative barrier heights can be well reproduced by the force field, and also the absolute barrier heights are quite well predicted with a largest deviation of 1.8 kcal/mol for the 90° structure of IRMOF-7. Note that hybrid DFT functionals like B3LYP lack the inclusion of attractive dispersion interactions [219], which is empirically included in the force field. This could lead to higher steric barriers in case of DFT.

Table 6.1: DFT vs. MM3 energy in kcal/mol for the three special points for the rotation around the linker axis. For the minimum the optimized dihedral angle is given in parentheses.

Dihedral	0°	Minimum	90°
IRMOF-7			
DFT	5.6	0.0 (34.3°)	6.9
MM3	4.6	0.0 (35.6°)	5.1
IRMOF-993			
DFT	13.5	0.0 (57.8°)	1.9
MM3	13.0	0.0 (55.3°)	2.1

The energy profile of the torsion can be subdivided into three contributions (Fig. 6.4). First, the π -conjugation of the carboxylic groups with the aromatic system ($C_{carbox} - C_{phen}$) leads to a preference of a planar structure. In contrast to that the steric strain is minimized for a 90° torsion angle. In addition, the attractive electrostatic interaction of the aromatic ring hydrogen (positive partial charge) and the carboxylic oxygen (negative partial charge) is again maximized for a planar configuration. The resulting total energy profile and the individual contributions to the MM3 force field energy are shown in Fig. 6.4. Obviously, due to a more and more pronounced steric strain the potential energy minimum is shifted towards higher and higher torsion angles in the series IRMOF-1, 7, and 993.

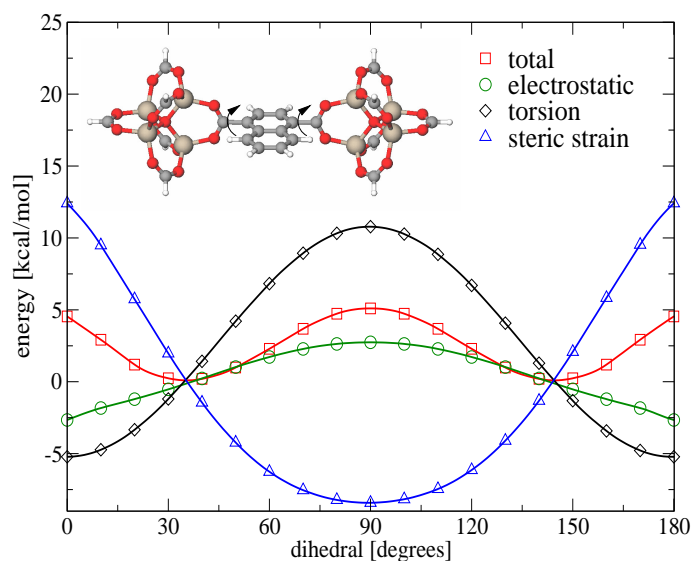


Figure 6.4: Energy contributions to the rotational barrier.

It can be concluded that the approach gives a faithful representation of the energy profile for an individual linker. The possible vast amount of conformational isomers is due to the complex electrostatic and dispersion interactions between different aromatic fragments present in close proximity in the network (Fig. 6.5).

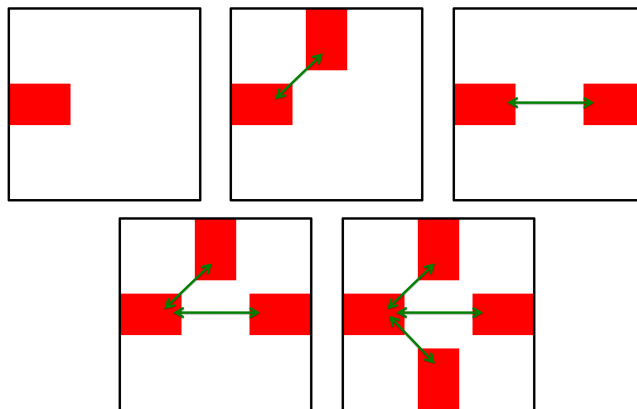


Figure 6.5: Schematic representation of possible conformers of the aromatic linkers (red rectangle) in IRMOF-7, due to the attractive inter-linker interactions (green arrows). Note, that just one pore opening of the cubic framework (black square) is shown. Based on the five different arrangements a large number of different pore system can be obtained.

The ability of MM3 to capture these aromatic interactions has been shown for example on the case of the gas phase structure of the naphthalen trimer [220]. Here, the relative energies calculated by first principle methods was well reproduced by the

MM3 forcefield. In addition, the benzene crystal structure is also well reproduced [221]. Thus, the force field appears to be well suited for the problem at hand.

6.2 Strategy for the global minimum search: Genetic Algorithm Technique

In case of IRMOF-7 and IRMOF-993 the energy of the periodic network depends significantly on the orientation of the linker planes, because of the $\pi - \pi$ -interaction of the aromatic linkers amongst each other, leading to a large variety of conformers for both the “regular” and the “twisted” systems. Different annealing protocols were not found to be able to locate the global minimum structure within a reasonable time. Unfortunately it is not possible to assess the relative stability of the isomeric structures without knowledge about the individual global minima. As a consequence, a Genetic Algorithm strategy was implemented for this purpose, which was found to be very efficient for global optimization problems in various fields [222].

The orientation of the linker plane with respect to the linker axis was used as the “gene” for encoding the structure of a specific conformation. Because of the energy minimum in the rotational profile between 0° and 90° (see Fig. 6.4) there are overall four possible orientations for each linker, encoded by the integers $[0, 1, 2, 3]$ in case of IRMOF-7 (see Fig. 6.6). In IRMOF-993 two conformations are identical due to the symmetry of the anthracene unit, and just a binary gene $([0, 1])$ is needed to encode a single linker.

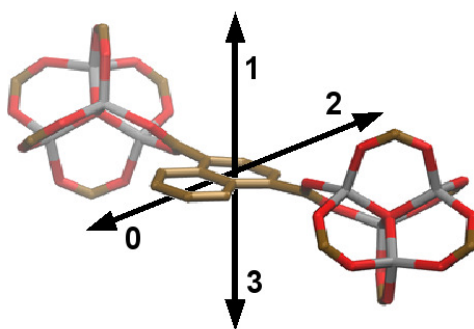


Figure 6.6: Encoding of the four minimum energy orientations of the linker as a gene in the case of regular IRMOF-7.

Since no symmetry constraints were imposed and there are 24 independent linkers in the periodic unit cell, a “chromosome” of 24 genes encodes the full structure. An “individual” is defined by a specific chromosome, which serves as a blue print to generate an idealized initial 3D structure. This is then optimized to obtain a final

potential energy, which serves as a fitness criterion, and determines whether the individual is kept for the next optimization cycle (generation). The data flow for this process is shown schematically in Fig 6.7. In the first generation the chromosomes are initialized randomly, whereas later they are generated by crossing (rate: 0.9) over and mutating (rate: 0.1) chromosomes of the previous generations. It should be noted that, due to the high symmetry of the network, different chromosomes can represent an identical structure. However the redundant chromosomes were not excluded by symmetry constraints since they did not hamper convergence, but helped to maintain diversity in the population. With this approach a much more rapid convergence of the energy compared to any of the annealing schemes was observed. Despite that, the optimization process sometimes stalled because of a depletion of diversity. In this case the GA was restarted, reusing the best candidates and filling the population with randomized individuals. After a number of restarts and about 300 cycles for IRMOF-7 and about 200 for IRMOF-993 this process converged to a relatively high symmetry structure, which is discussed in detail below. It must be pointed out that the approach does of course not guarantee to give the global minimum of the system. However, a number of independent restarts did not result in any further improvement for a large number of generations, and one can be thus confident to have located the global minimum structure. Note also that in principle a larger unit cell with more individual linkers would allow for further conformations, which is not possible in the used periodic model. Because of the symmetry of the global minimum structure for both IRMOF-7 and 993 and the nature of the inter-linker interaction this does, however, not affect the nature of the global minimum.

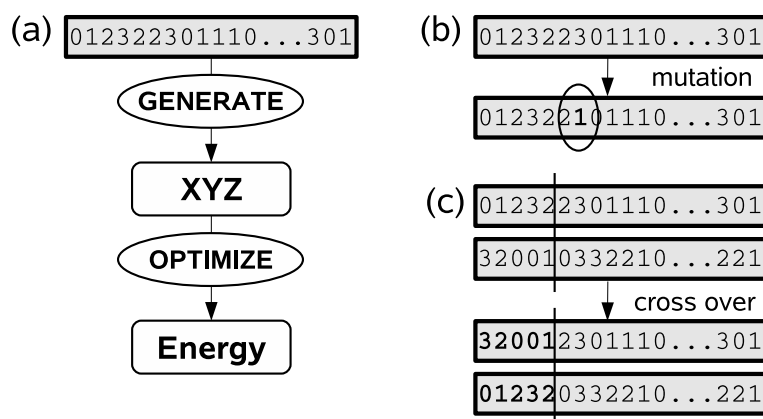


Figure 6.7: Evaluation of Fitness (a), mutation operation (b) and crossing over (c) of chromosomes in the GA approach.

6.3 Conformational Isomers of IRMOF-7 and 993

A careful inspection of the low energy structures of both isostructural isomeric forms of IRMOF-7 and 993 revealed subtle inter-linker interactions, manifesting in a deviation of the rotational dihedral angle compared to the value for the corresponding model systems (see Tab. 6.1). In most cases a pair of linkers, opposite to each other on a face of a cubic cell, tend to bend towards each other, thereby covering the pore. This type of conformational isomers is quite obvious in all global minimum structures shown in Fig. 6.8, 6.9, 6.11, and 6.10. In general, a displaced parallel or "T-shaped" orientation is commonly observed when aromatic systems interact in $\pi-\pi$ interactions. Such an arrangement, optimizing both electrostatic quadrupole interactions and maximizing attractive dispersion forces [223], is also found for aromatic guest molecules like benzene in IRMOF-1 [224, 225]. However, in this case the limited freedom of the linker, which can only rotate around the linker axis at a nearly fixed distance, does not allow for such a structure. Nevertheless, a total attractive inter-fragment interaction energy of about 0.5 kcal/mol is obtained for such a "pair" of two naphthalene units, found in the global minimum structure for the regular IRMOF-7 (Fig. 6.8). Thus, given the energetically accessible range of rotational dihedral angles (see Fig. 6.4) this arrangement of opposite linkers forming a pair and thus generating different conformational isomers is dominating the pore structures. Note that in case of the regular IRMOF-993 structure shown in Fig. 6.11 all four linkers situated at the four edges of a cell face are interacting in this way. In addition to that, these "sheets" of aromatic linker fragments formed in the planes of the network are always stacked. For example in case of regular and twisted IRMOF-7, the checkerboard formed by naphthalene pairs (see Fig. 6.8b and Fig. 6.9) is exactly the same in all planes.

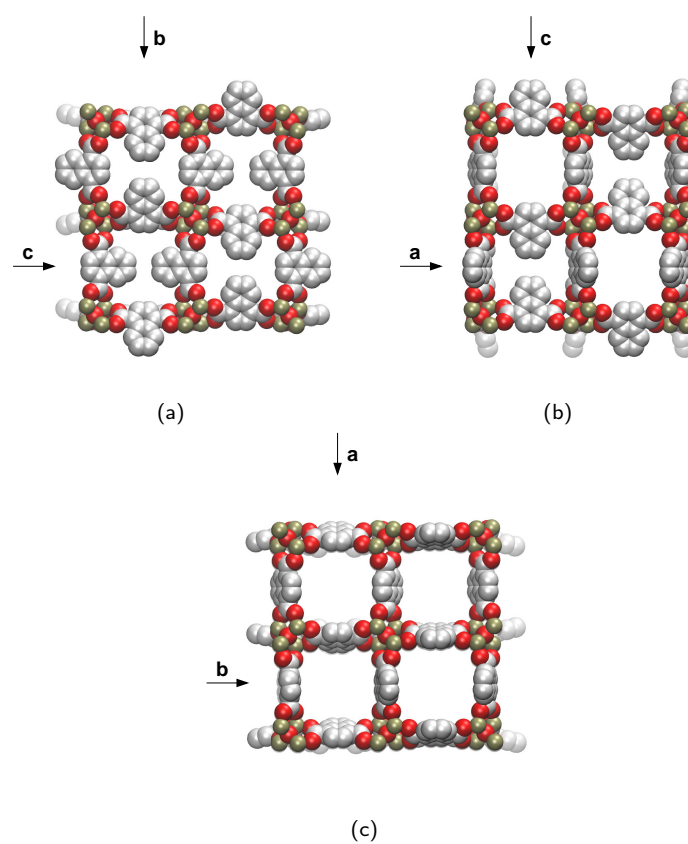


Figure 6.8: Global minimum structure of regular IRMOF-7 (coplanar carboxylic groups). Pictures (a), (b) and (c) show a view along the three different spatial directions.

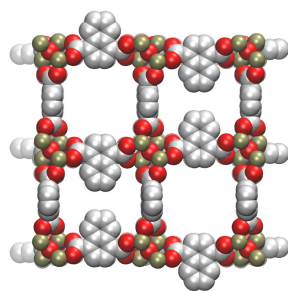


Figure 6.9: Global minimum structure of twisted IRMOF-7 (orthogonal carboxylic groups).

Interestingly, as a consequence of these inter-linker interactions, in both mini-

imum energy conformers of the regular IRMOF-7 and 993 a breaking of the cubic symmetry (Fig. 6.8 and 6.11) is found, which is not occurring for the twisted isomers (Fig. 6.9 and 6.10). For example, in case of IRMOF-7 all cell faces in one plane are completely closed by these pairs (a), whereas in one orthogonal plane (b) only half of the pores are covered. In the last plane (c) all pores are open and accessible as in the case of IRMOF-1. Due to symmetry reasons in case of IRMOF-7, only 3 faces of the total of 6 cell faces can be covered by a linker “pair” and therefore always exactly half of the pores are covered for both the regular and the twisted isomer. For IRMOF-993 all faces can be covered by “pairs” as seen in the global minimum structure for the twisted isomer (Fig. 6.10). For the regular isomer, however, the formation of quadruples in two planes (a) and (b) occurs, leaving the pores in the last plane (c) completely open, similar to IRMOF-7. Note that the difference in the environment of the A and B cells in the regular structures is clearly reflected also by the arrangement of the linkers. The sheets of anthracene units in regular IRMOF-993 (Fig. 6.11 (a) and (b)) are buckled, with the aromatic parts bending into the interior of the A cells but avoiding the B cell. For the twisted isomer of IRMOF-993 all cells are equal, and so is the linker orientation (Fig. 6.10).

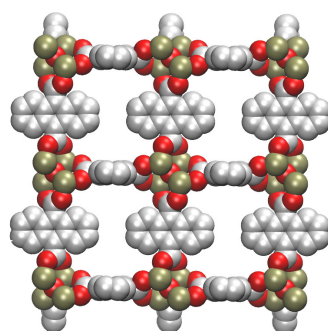


Figure 6.10: Global minimum structure of twisted IRMOF-993 (orthogonal carboxylic groups).

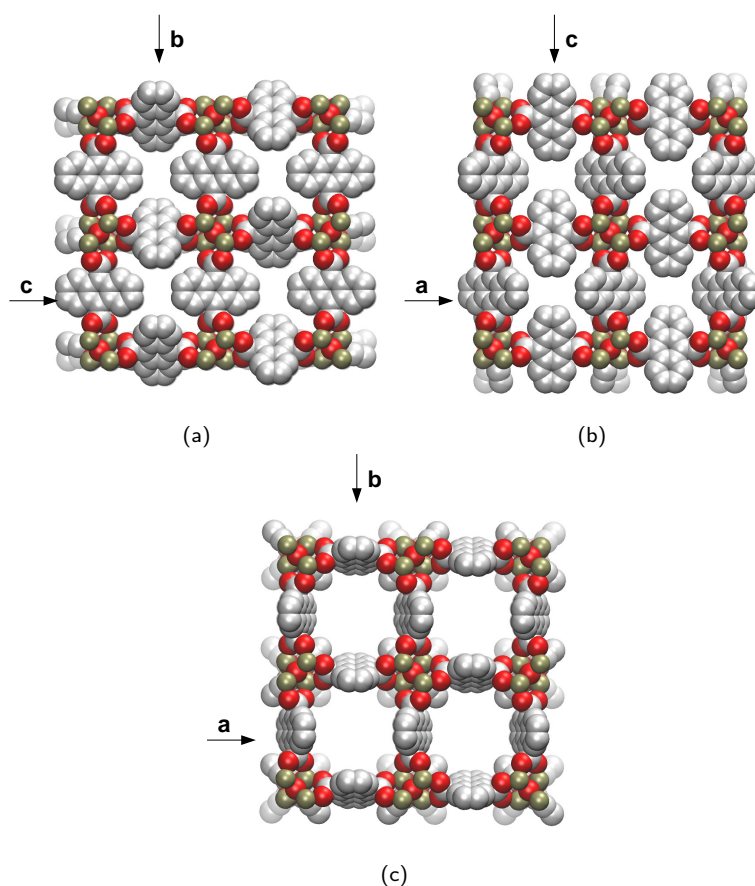


Figure 6.11: Global minimum structure of regular IRMOF-993 (coplanar carboxylic groups). Pictures (a), (b) and (c) show a view along the three spatial directions.

6.4 Strain energy of isorecticular isomers

For the parent system IRMOF-1, the experimentally observed regular structure, with a planar orientation of the linkers, is more stable by 17.9 kcal/mol per formula unit with respect to the twisted isomeric form (Tab. 6.2). This is due to the electronic conjugation of the $C_{Phen} - C_{Carbox}$ bond and the absence of steric repulsions. In strong contrast to that, the corresponding energy difference for IRMOF-7 is with only 2.04 kcal/mol about an order of magnitude smaller. Similar to IRMOF-1 the global minimum structure of the regular form is more stable.

Table 6.2: Optimized cell parameters and relative energies (per formula unit in [kcal/mol]) between the regular and twisted IRMOFs $\Delta E(\text{twist} - \text{regular})$.

	ΔE	regular: a/b/c [Å]	twist: a/b/c [Å]
IRMOF-1	17.9	25.946	25.886 / 25.997 / 25.746
IRMOF-10	2.65	34.588	34.506
IRMOF-16	0.44	43.183	43.158
IRMOF-7	2.04	25.918 / 25.860 / 25.798	25.840
IRMOF-993	5.59	25.912 / 25.912 / 25.699	25.951

However, the plethora of conformers for both isorecticular isomers span a wide and overlapping range of energies above the global minimum (Fig. 6.12), and possibly a free energy difference at a given temperature would be needed for the ultimate answer on the question of the relative stability.

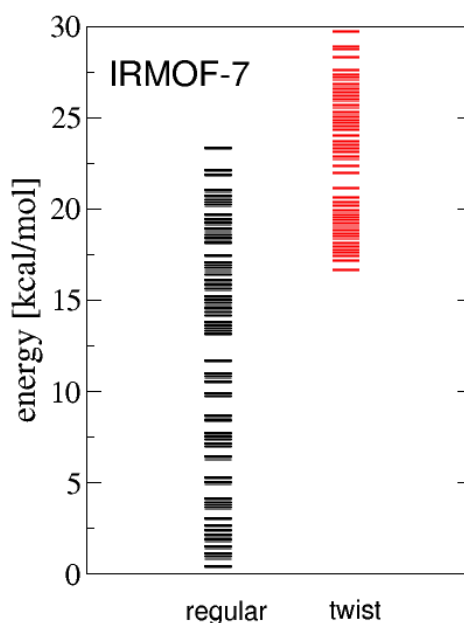


Figure 6.12: Comparison of the potential energies for all lower energy conformers located for regular and twisted IRMOF-7.

Clearly, the energetic penalty for introducing a defect of a single inverted Zn_4O node in the regular structure (which means a total of six twisted linkers) is rather small. Similarly, a plain of twisted linkers, leading to the formation of two mirror symmetric regular domains, could easily be realized during the crystallization of a real system. In principle, the model electron density resulting from the XRD analysis of IRMOF-7 would fit both to the regular and the twisted isomer [174]. Nevertheless, the results corroborate the interpretation that IRMOF-7 prefers the same regular

structure as IRMOF-1, but also explains the amount of disorder. Interestingly, for IRMOF-993 with its more symmetric linker and higher steric repulsion, an energetic preference for the regular structure with 5.59 kcal/mol has been calculated, which lies between the values for IRMOF-1 and IRMOF-7.

In addition the regular and twisted isomers of IRMOF-10 and 16 were calculated (Tab. 6.2; Fig. 6.13,6.14). Here, only a limited amount of rotational isomers are possible and it was not necessary to invoke the GA scheme to find the global minimum energy structures.

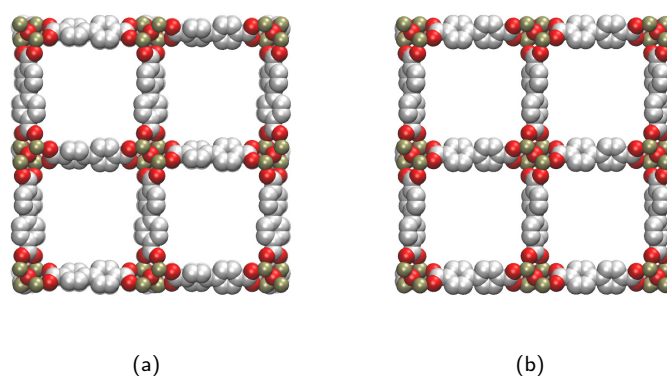


Figure 6.13: Global minimum structure of IRMOF-10. Pictures show the (a) regular and (b) twisted isomer along one spatial directions.

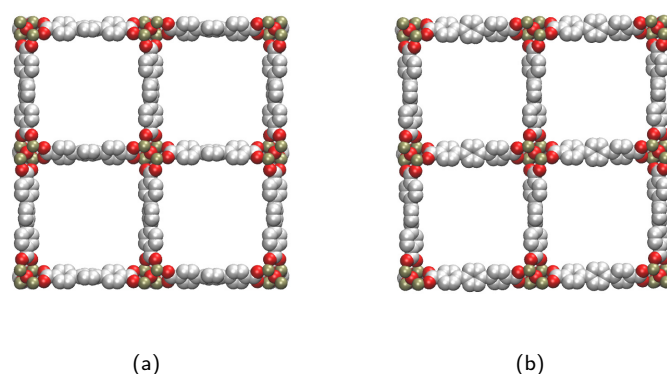


Figure 6.14: Global minimum structure of IRMOF-16. Pictures show the (a) regular and (b) twisted isomer along one spatial directions.

The non-planar biphenyl unit, with its low rotational barrier, allows for a formation of both the regular and the twisted structure with energy differences of 2.65 kcal/mol for IRMOF-10 and 0.44 kcal/mol for IRMOF-16, being even below the

value for IRMOF-7. Nevertheless, in both cases the regular form was found to be slightly more stable. However, the packing of the solvent molecules during synthesis or the interaction with the inter-penetrated counterpart could change the preference here as observed experimentally.

6.5 Summary

In this chapter the isorecticular and conformational isomerism within the IRMOF family was investigated. First, the extended MM3 force field, parametrized for the IRMOF-1, was validated in terms of the sterically more demanding linkers in IRMOF-7 (naphthalene unit) and IRMOF-993 (symmetric anthracene unit). The force field is able to reproduce well the rotation profile of the organic groups compared to B3LYP data. In order to analyse the structure of the periodic systems, a genetic algorithm search strategy was developed, since the inter-linker interaction in the IRMOFs lead to a broad variety of conformational isomers of systems. Using this approach the global energy minimum for each system was successfully located. In case of the regular arrangement of the Zn_4O tetrahedrons the “zero temperature” structure of both IRMOF-7 and IRMOF-993 show an interesting breaking of the cubic symmetry leading to a blocking of the channels connecting the cubic cells in certain directions by the aromatic linkers. This symmetry breaking is not observed for the twisted isomeric form, which was investigated for the first time in this work. The isorecticular isomers, where the carboxylic planes of the linkers are orthogonal and neighboring Zn_4O are not mirror symmetric to each other, are energetically less favorable for all considered MOFs. However, for IRMOF-7 the energy difference is an order of magnitude smaller compared to IRMOF-1. This explains the amount of disorder in the experimental X-ray structure of the naphthalene system. For the biphenylene and triphenylene based IRMOF-10 and 10 the energy differences are even smaller. Consequently the formation of such defects during the crystallization process appears to be very likely. Finally, it should be emphasized that after formation of one isorecticular isomer, the interchange into the isomeric form is only possibly with bond breaking.

Chapter 7

Surface Structure and Energies of HKUST-1

The surface of a crystalline solid is obviously a disruption of the periodicity of the material. Depending on the standpoint it can have two distinct meanings. After the synthesis procedure is finished, it marks the termination of the material in at least one dimension. In contrast to this, it represents the location for further growth during the formation of the compound. Both aspects are essential with respect to the final properties of the material, since on the one hand the surface conditions influences the growth rate and on the other hand it defines the interaction of the compound with its environment. Consequently, a detailed knowledge of the assembling mechanism and surface termination is pivotal to improve the performance of the solid. In terms of MOFs, it is clear that an atomistic understanding of surface (and interface) phenomena will be of prime importance to realize technical applications like for example membranes or sensing devices in the future. In addition, it should be noted, that growth mechanisms are closely related to degradation and thus long term stability of such materials.

Recently, some efforts have been done to tackle different issues of MOF surfaces [226–230]. The in this respect most investigated MOF system is the copper paddle-wheel based $Cu_3(btc)_2$ ($btc = 1,3,5 - \text{benzenetricarboxylate}$; HKUST-1) [126]. Bein et al. observed an oriented growth on gold substrates with functionalized thiol self-assembled monolayers (SAMs) under solvothermal conditions [226]: on OH-functionalized SAMs, $Cu_3(btc)_2$ interfaces preferentially with the [001] surface; together with the general preference for the [111] surface in the bulk synthesis, large octahedrally shaped crystals were achieved on the surface (Fig. 7.1)¹. The alternative layer-by-layer (lbl) growth mode [228] results in contrast in smooth and

¹It was further shown in the work that on a carboxylate terminated surfaces, $Cu_3(btc)_2$ interfaces preferentially with the [001] surface.

thin MOF films. Nevertheless, the same growth orientation on functionalized thiol-SAMs could be documented. Interestingly, in this case, the formation of the MOF is observed already at room temperature, if the acetate precursor $Cu_2(O_2C-CH_3)_4$ was employed, which is already a dimer, whereas the monomeric nitrate precursor $Cu(NO_3)_2$ is active only at higher temperatures in the solvothermal mode. A further experimental observation, made both with *in situ* AFM in solvothermal synthesis [229, 230] and in layer-by-layer mode is that always half a unit cell is grown at once, which means incorporation of two “layers” of copper dimers at once. For further reference to the evolving field of MOF surface chemistry see ref. 79. Despite the substantial advancement in the investigation of the exposed $Cu_3(btc)_2$ surface and growth, an atomistic understanding is still missing and in particular the origin of the oriented growth is completely unclear.

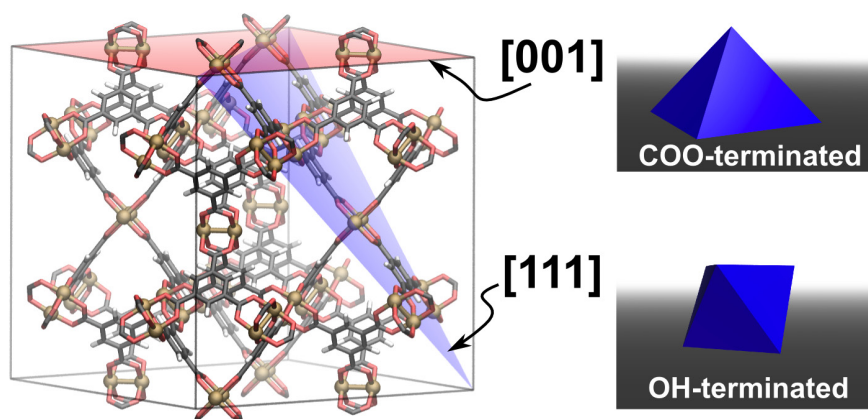
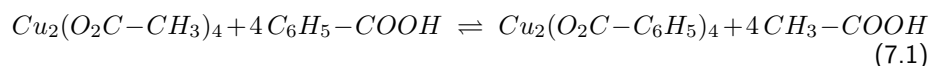


Figure 7.1: The unit cell of $Cu_3(btc)_2$ showing the $[001]$ and $[111]$ crystal planes (left) and the a schematic picture of the corresponding observed crystal morphology on functionalized thiol-SAMs (right).

In Chapter 4, a force field was derived for copper paddle wheel based MOFs, which is, for instance, able to predict the negative thermal expansion of $Cu_3(btc)_2$ or the deformed and “interwoven” structure of $Cu_3(btb)_2$ (MOF-14). Consequently, it enables to make structural predictions beyond experimental knowledge and within the constraint of avoiding bond breaking, relative conformational energies can be computed. In order to shed light on the origins for the preferred surface termination and crystal morphology, the atomistic structures and energies of possible surface terminations of $Cu_3(btc)_2$ is studied based on the well validated force field.

7.1 Surface termination

The formation of $Cu_3(btc)_2$ occurs already at ambient temperatures in the layer-by-layer mode from the dimeric acetate precursor $Cu_2(O_2C-CH_3)_4$. This means, the acetate is replaced (presumably in a proton catalysed exchange reaction) by the aromatic carboxylate *btc*. In order to analyse the thermodynamics of this process, we first computed isodesmic reaction energies for the model reaction replacing ac by benzoate:



With a reaction energy of $\Delta H_R = -0.61 \text{ kcal/mol}$ (including zero point energy, thermal contributions at $T = 298.15 \text{ K}$) the exchange is (almost) energetically neutral. Despite the sensitivity of this reaction energy to the description of free acids, the value slightly changed by including solvation effects ($\Delta H_{R,solv.} = -0.84 \text{ kcal/mol}$; solvation effects were included by using the CPCM method and the parameters for ethanol). Thus, from an enthalpic point of view the formation of $Cu_3(btc)_2$ is not preferred, however, during the formation of one formula unit six acetate molecules are released. It can be concluded that the formation is an entropy driven process, which is actually even less preferred for the even stronger copper binding NO_3^- ligand. In addition, one can expect the surface of $Cu_3(btc)_2$ to be terminated preferentially by not, yet, substituted acetate ligands. In this context it is important to note that for the surface chemistry of hard materials like oxides or semiconductors dangling bonds and a corresponding surface reconstruction is usually observed [231–233]. However, in the case of MOFs grown under solvothermal conditions this will never be the case. Instead, always the weakest coordination bonds will be broken and the resulting free coordination sites will be blocked by donating ligands like acetate or possibly solvent molecules. Recently, an attempt was made to model the surface of the carboxylate based MOF-5 by breaking the C-C bond between the phenyl and the carboxylate groups, which leads to a completely unphysical surface state [234]. The acetate-termination of the exposed surfaces is the basic assumption in the work.

7.2 Slicing reaction and Slab model

For the computation of surface energies the following strategy was employed. From the 3D periodic system a 2D periodic slab was generated by slicing all $Cu-O$ bonds in a specific hkl-plane. As a result two different surfaces are generated, one with Cu_2 -dimers and one with free CO_2 groups exposed. This is schematically represented with blue shaded part in Fig. 7.2 for the [001] surface. In order to

chemically saturate these surfaces and to make them identical, a reservoir of free acetate precursors $Cu_2(ac)_4$ is used (red shaded in Fig. 7.2).

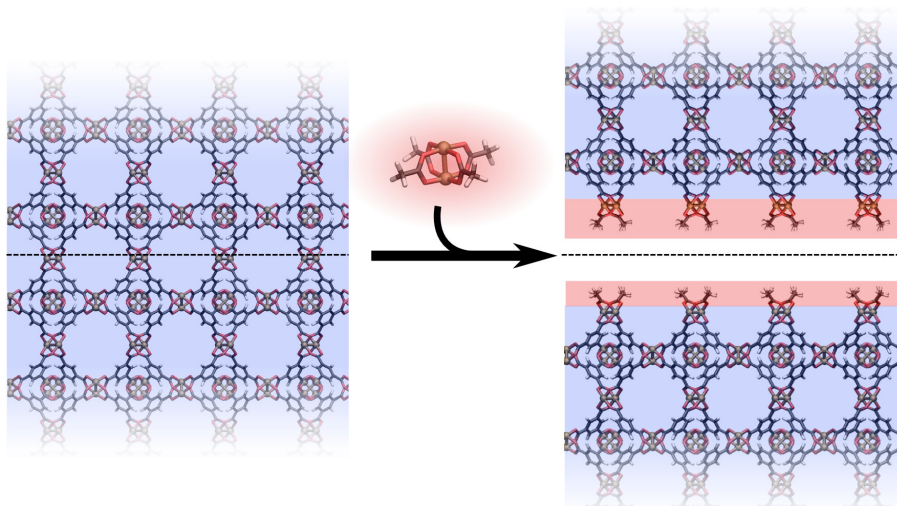
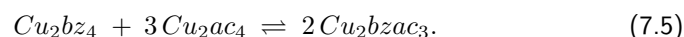
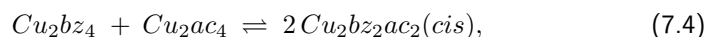
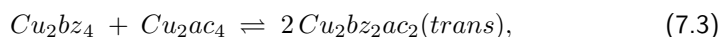
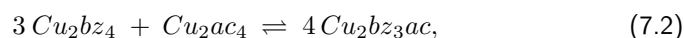


Figure 7.2: Isodesmic slicing reaction: generation of acetate terminated surfaces

Note that depending on the number of surface groups a different number of these free acetate precursor molecules have to be used. This results in two identical and acetate terminated surfaces. The overall reaction is of course fictitious and not related to the growth process. Nevertheless, by assuming that the binding energies of acetate and benzoate are nearly additive and are not significantly affected by the substitution pattern, which is an intrinsic approximation of the classical model with additive terms, this isodesmic reaction can be safely treated by our molecular mechanics force field. However, in order to validate this assumption the different carboxylate scrambling reactions were computed ($ac = O_2C - CH_3$; $bz = O_2C - C_6H_5$)



The obtained reaction energies $\Delta H_{R,solv.}$ and the corresponding free energies $\Delta G_{R,solv.}$ clearly justify the approach ($\Delta H_{R,solv.}$; $\Delta G_{R,solv.}$ in [kcal/mol]: Eq. 7.2: -0.01 ; -0.31 , Eq. 7.2: -0.19 ; -0.10 , Eq. 7.2: -0.13 ; -0.03 , Eq. 7.2: -0.10 ; -0.07).

To cover the periodicity of the truncated MOF systems, a symmetric 2D periodic slab model was used (Fig. 7.3). The periodic boundary conditions in 3D

were retained by replication of the slab perpendicular to the constructed surface. The cell dimensions parallel to the surface were adapted to the fully optimized bulk properties. Adjacent slabs were separated by a layer of vacuum to prohibit interactions between them. This gap is defined by the cell axis perpendicular to the surface. Further, to avoid the interactions of the two surfaces located at one slab, the thickness of the latter has to be adjusted. Therefore, the calculated energies were tested for convergence in terms of the layer separation and the slab thickness.

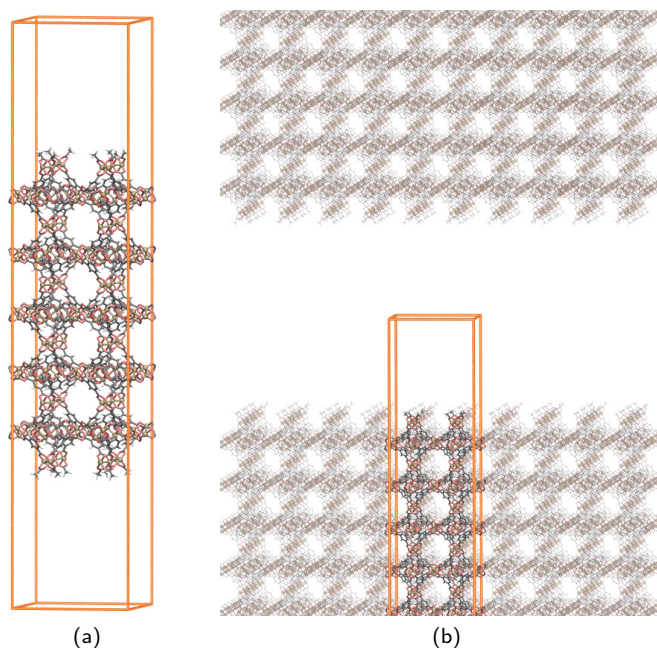


Figure 7.3: Example of (a) a simulation box for the slab calculations (here [001] surface) and (b) the embedding with the periodic boundary conditions.

After generating the respective surface models the structures were fully relaxed in order to compute the strain resulting from the terminating groups as well as the possible release of structural strain on the surface. The surface energy is the reaction energy of this fictitious slicing reaction divided by the exposed surface area.

7.3 Surface energies

It is crucial to realize that for the $Cu_3(btc)_2$ network in its **tbo** topology different surfaces can be constructed in the presented way for certain hkl-planes. In Fig. 7.4 all five systems considered in this work are shown with a line indicating the slicing plane. Both for the [001] and [111] two surfaces are possible, which differ in the number of broken $Cu - O$ bonds and accordingly in the density of acetate

groups. These two possibilities are labeled “a” and “b” in the following. As it is obvious from Fig. 7.4 for the surfaces [111]a and [001]a the least number of bonds have to be broken, and therefore the number of both terminal acetate groups and free acetate molecules needed to saturate the surface, is smallest. In Tab. 7.2 the acetate density in groups per nm^2 is given for all investigated surfaces.

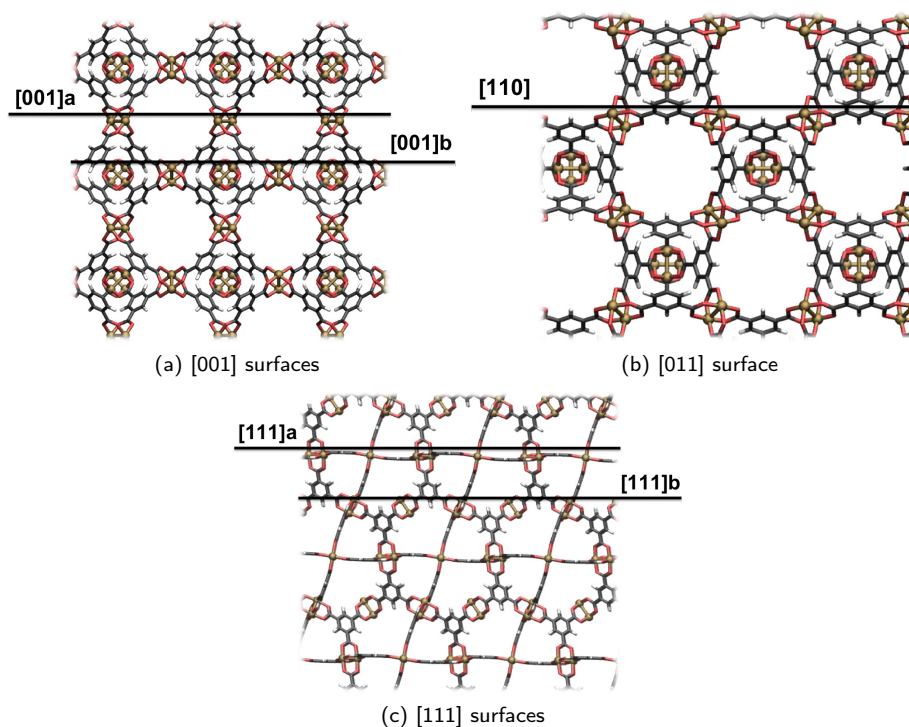


Figure 7.4: Possible surfaces to be generated by slicing through $Cu - O$ bonds. For [001] and [111] two different surfaces denoted **a** and **b** can be generated with a different acetate density on the surface. The figure shows a sideview of the periodic system with a line indicating the slicing plane.

Table 7.1: Calculated surface energies ΔE_{surf} [$kcal\ mol^{-1}\ nm^{-2}$] and acetate density ρ_{ac} [$groups/nm^{-2}$] for all considered surfaces.

surface	$\rho_{ac}[groups/nm^{-2}]$	$\Delta E_{surf} [kcal\ mol^{-1}\ nm^{-2}]$
[001]a	0.57	$4 \cdot 10^{-3}$
[001]b	1.15	-0.17
[011]	0.81	0.33
[111]a	0.50	0.08
[111]b	1.00	0.18

The calculated surface energies ΔE_{surf} , summarized in Tab. 7.2, namely the change in the strain energy when converting the bulk material to the acetate termi-

nated surface, are in all cases almost zero, which indicates that the surfaces are not more strained than the bulk system. A comparison of the two structures indicate that the structure of the MOF does not significantly reconstruct at the surface (Fig. 7.5). This is a differences compared to the other solid materials, where, as already mentioned, the materials relax at the surface. Note that this type of analysis is only possible due to the high quality of the used force field. Nevertheless, it should also be pointed out that the omitting of solvent molecules causes an artificial stabilization by van der Waals interactions between vicinal acetate groups on the surface, which is the reason for the negative surface energies of the $[001]_b$ surface (Fig. 7.6).

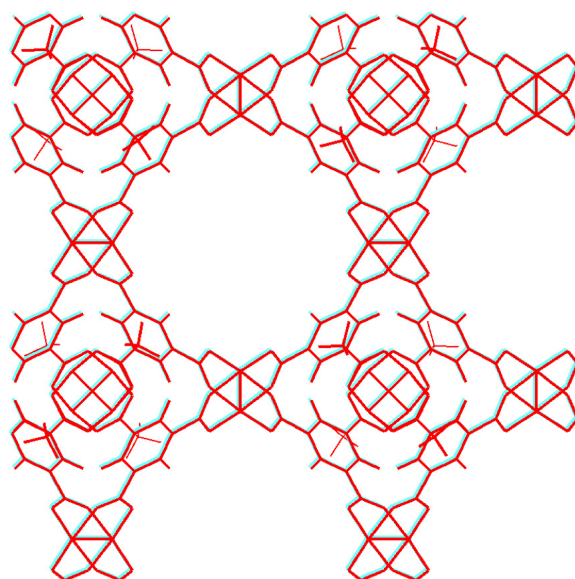


Figure 7.5: A comparison of the bulk (cyan) and surface (red) structure of along the $[001]$ plane.

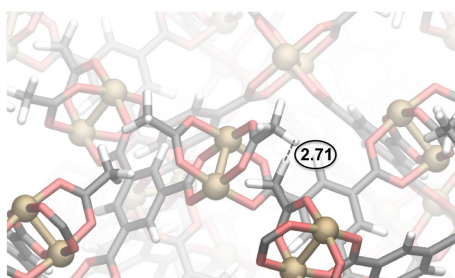


Figure 7.6: Representation of the $[001]_b$ surface. The value gives the distance between the hydrogen atoms of adjacent acetate groups on the surface.

In order to get a more realistic picture of the HKUST-1 surface, it is necessary

to consider the surface free energy. In this regard it is assumed, that vibrational degrees of freedom have a constant phase space volume during the reaction and can safely be ignored. Thus, only the translational entropy of the free acetate are included by means of the Sackur-Tetrode formula

$$S_{trans} = k_B \cdot N \cdot \ln \left\{ \frac{V}{N \cdot \lambda^3} \right\} + \frac{5}{2} k_B \cdot N,$$

with λ as the de-Broglie wavelength

$$\lambda = \frac{h}{\sqrt{2 \cdot \pi \cdot k_B \cdot m \cdot T}}$$

(k_B = Boltzmann factor; m = mass of a single Cu_2ac_4 , N = number of Cu_2ac_4 , V = Volume). The surface free energies ΔG_{surf} are given in Tab. 7.2 at different temperatures and concentrations for the free acetate.

Table 7.2: Calculated surface free energies ΔG_{surf} [$kcal\ mol^{-1}\ nm^{-2}$] at different temperatures and concentration for free $Cu_2(ac)_4$ in $[0.1\ mol/L]$.

surface	ΔG_{surf}		
	$T = 300, c = 0.01$	$T = 300, c = 0.1$	$T = 400, c = 0.1$
[001]a	3.60	3.60	4.90
[001]b	7.03	7.03	9.63
[011]	5.43	5.43	7.26
[111]a	3.20	3.20	4.32
[111]b	24.17	24.17	26.42

In contrast to the growth process, the incorporation of the free acetate precursors $Cu_2(ac)_4$ and the corresponding loss of entropy makes the free surface energy significantly endergonic. However, due to the lowest acetate density along the [111]a plane, the corresponding surface is the most stable one. Thus this preference of the [111]a surface is an entropic effect since the enthalpic strain energy difference between the surfaces is rather small. This is in agreement with the experimental observed crystal morphology. Further the results also explain the experimentally monitored step sizes of half a unit cell, which is exactly the distance between two [111]a surfaces. The corresponding intermediate [111]b surface is less stable. Nevertheless, the Wulff-construction reveals only a truncated octahedral crystal morphology, even at higher temperatures or lower concentration of free $Cu_2(ac)_4$. This discrepancy with the experiment can have different reasons. As already mentioned are solvation effects not included in the current investigation, which might influence the surface stability. Further the restriction to acetate terminated surfaces might not cover all relevant features of the HKUST-1 system. In this regard other slicing of the bulk materials are thinkable like acid terminated surfaces. However, in this case the inclusion of solvation effects is even more important.

7.4 Summary

The surface of soft crystals like MOFs are very different in comparison hard solids like metal oxides. Due to the molecular nature of MOFs, the truncation of the periodic system takes place along the weakest bond of the framework, and the generated unsaturated sites are blocked by donating ligands. In case of the investigated HKUST-1, the acetate termination of the surface is one reasonable assumption, especially if the synthetic conditions are considered (using of $Cu_2(ac)_4$ as starting material). Based on this, the surface of HKUST-1 was investigated by slab calculations using the previously developed force field. In this regard different surfaces were constructed for specific hkl-planes. The calculations provide that the most stable surfaces are not energetically very different compared to the bulk material. By including entropic effects, the experimentally observed preference for the [111] surface could be explained. However, the results pointed out that for a complete picture of the surface termination the presence of solvent molecules has to be taken into account.

Part III

Host-Guest Systems

Non-covalent interactions: Communication between molecules?

By communication people are able to exchange information and tell other people, for instance, whether they agree or disagree with one subject. To transmit these messages human beings use different tools such as verbal or non-verbal ones. Metaphorically speaking, molecules *communicate* in a primitive way by their functional groups. The nucleotides of the DNA (Deoxyribonucleic acid) communicate, for instance, by hydrogen bonding. Based on them, pairs are obtained, which harmonize such as Adenine and Thymine or Guanine and Cytosine. Non-covalent interactions are of course not directly comparable with the human communication, but both are tools relevant for the embedding within an environment. The importance of intramolecular interactions, where no chemical bond is formed or cleaved, strikes out if biochemical processes are considered. The folding of a protein, for example, occurs due to them. The non-covalent interactions between different groups induce the arrangement of the subunits of the protein and guide the folding. Although they are weaker compared to covalent interactions, the structure of the macromolecule and thus the whole biological activity is dominated by them. The relevance of the non-covalent interactions can be illustrated if the mutation of a protein is studied. In this case one or more fragments of the protein are aligned in a different fashion or are replaced by others. Due to this change, the ensemble of non-bonding interactions is (significantly) disturbed; as a result, the structure of the folded protein differs. How serious the effect can be with respect to the resulting activity becomes obvious, if diseases like cancer or BSE (Bovine spongiforme enzephalopathie) are contemplated. However, non-covalent intramolecular interactions are not limited to biological systems and in fact the conformational isomers discussed in the context of IRMOF-7 (Chapter 6) are examples how they can influence the structure of functional porous materials. In the case of IRMOF-7 the pore structure is dominated by

aromatic interactions between the naphthalene units and consequently properties of the network (e.g. permeability) are defined by these non-bonding interactions.

In addition to these *intramolecular* features, a wide range of *intermolecular* phenomena are governed by non-covalent effects. The solvation of salts in water, for example, is based on electrostatic forces between the ions and the water molecules. Considering biochemical systems, again, specific interactions between ligands and proteins allow the selective recognition of molecules, which is important, for instance, in the context of antibodies. Further, the development of new drugs is promoted by the understanding of the interaction between pharmaceuticals and macromolecules within the human body. Since in (almost) all application fields of porous materials like MOFs, the open structure is used to incorporate molecules, similar selective *communication* within the host-guest system, is intended. At the first stage the adsorption of molecules within the framework is dominated by the ratio between the size and dimension of the molecule and the pore opening². If the molecule is larger compared to the opening, steric effects prevent the adsorption or diffusion process. This allows the separation of molecules depending on their sizes and shapes. A geometrical analysis should therefore be the first step to evaluate the host-guest system, since it allows a fast screening of the materials. However, once the molecules are able to enter the pores, the interaction with the inner surface of the MOF gets crucial, which can be either attractive or repulsive. Since, in principle, the inner surface of the matrix can be adjusted systematically, using the building block approach, the interaction of the guest molecules with the framework can be tuned for specific applications. Unfortunately, a evaluation of the interaction between the inner surface and the guest species is often not straightforward due to the diversity of possible kinds: hydrogen molecules interact, for instance, by weak dispersion forces, whereas water molecules form bonds with unsaturated metal sites of MOFs (e.g. in HKUST-1; see also Chapter 4). To improve the performance of MOF based materials, detailed understanding of the host-guest interaction is crucial. In this regard the focus of this part of the work lays on the investigation of MOF systems and in particular on the study of non-covalent interactions between guest molecules and the matrix.

²Note, that, due to the potential structural flexibility of the framework (e.g. rotation of the units or *breathing* of the structure) the pore opening might change significantly. This factor has to be considered if the pore opening is evaluated.

Chapter 8

Interaction between benzene and MOF-5

The physisorption of guest molecules on the inner surface of MOFs is based on the combination of electrostatic and dispersion effects. The fraction of each contribution depends on the particular host-guest system and variation of the framework or the guest molecules can influence significantly the strength of the interaction. To be able to tune the latter, it is thus pivotal to understand elementary issues of the physisorption process. Theoretical methods are indispensable to study these non-covalent phenomena in detail, since experimental tools have, as mentioned before, often not enough resolution to provide reliable data. Grand canonical Monte Carlo or molecular dynamic simulations based on classical force fields are often used in the literature to investigate adsorption and transport properties of MOFs [235]. Nevertheless, it should be noted, that the description of non-bonding effects, which are present in a chemical system, is challenging within the framework of conventional force fields. In general, the construction of these models, which use an additive energy expression, might not reflect the nature of many body forces, in which the non-bonding interactions are non-pairwise additive. Concerning this matter force fields are often deficient in the sense that they are able to reproduce the properties of small clusters like dimers or trimers but fail in describing bulk features or vice versa. In addition, errors might arise due to a number of approximations. For example, electrostatic effects are usually described by the Coulomb law using atomic point charges. The latter is a reasonable choice at large distance between the fragments, but becomes non-physical if the units get closer, so that the electron clouds can overlap. Being aware of these kind of limitations concerning the use of classical force fields, the validation of these tools is always needed to avoid artificial behaviours of the model for the system at hand.

In terms of theoretical works, done on loaded MOF systems, only in the case of hydrogen and methane the non-bonding parameters were verified or explicitly parametrized using quantum mechanical references [38, 183, 202]. For many other guest molecules similar evaluations were not performed [140, 235, 236]. To describe the Coulomb interaction, point charges were occasionally derived from first-principle calculations. It should be emphasized, that the use of parameters obtained from different sources (e.g. deriving vdw-parameters from experiment data and atomic charges from quantum mechanical calculations) might cause an unbalanced description of the system. As a consequence, the force field may, for example, be able to reproduce the macroscopic observable (e.g. adsorption isotherm), but fail describing the elementary interaction of the guest molecule with the MOF. In this case the partial success of the model is due to error cancellation.

In order to evaluate the quality of different force fields, used in the literature to investigate loaded MOFs, results obtained from the classical model will be compared with *ab-initio* data. But it should be emphasized, as mentioned before, that quantum mechanical tools, feasible to treat chemical systems, also imply different approximations. In this regard non-bonding contributions (e.g. $\pi - \pi$ interactions) are still challenging with respect to an efficient and accurate description by theoretical tools. Taking this fact into account, first principle methods are analyzed in advance for the particular system to obtain reasonable reference data.

Since the focus lays on the understanding of *pure* host-guest interactions, the adsorption of a *single* molecule on the inner surface of the MOF is studied to avoid any guest-guest interactions. As a probe molecules for large guests like metal precursors, dyes or pharmaceuticals, a benzene molecule is chosen. The host matrix is MOF-5, which was already introduced in detail in previous Chapters. As a remainder, MOF-5 is composed of Zn_4O clusters linked by 1,4-*benzenedicarboxylates*, forming a cubic framework. To allow high level quantum mechanical calculations of the *benzene@MOF-5* system non-periodic models are used to represent the periodic matrix. In agreement with previous studies [224, 237–240], it is assumed that the primary adsorption sites in MOF-5 are at the inorganic unit. Due to the tetrahedral shape of the Zn_4O cluster two binding sites can be distinguished in general: one over the faces (α -site) and one above the apex of the tetrahedron (β -site) (Fig. 8.1).

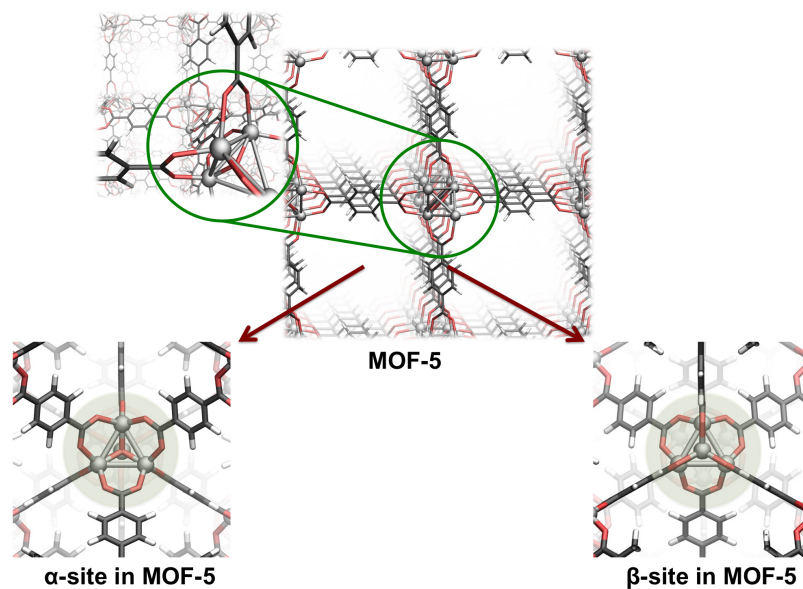


Figure 8.1: Different adsorption sites at the inorganic vertex of the MOF-5 framework.

To represent the inorganic unit of the matrix different charge-neutral model systems are used. The simplest non-periodic derivative is obtained by using formate ligands around the tetranuclear zinc cluster instead of terephthalic acid groups (**F**), resulting in the formula: $(Zn_4O)(O_2C-H)_6$ (Fig. 8.2). In addition mix ligand systems are employed, build up by both formate and benzoate ligands with the general formula $(Zn_4O)(O_2C-H)_3(O_2C-C_6H_5)_3$ (**B-alpha**, **B-beta**) (Fig. 8.3).

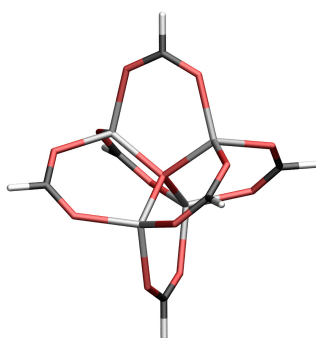


Figure 8.2: Non-periodic model system (**F**) used to represent the inorganic vertex of MOF-5.

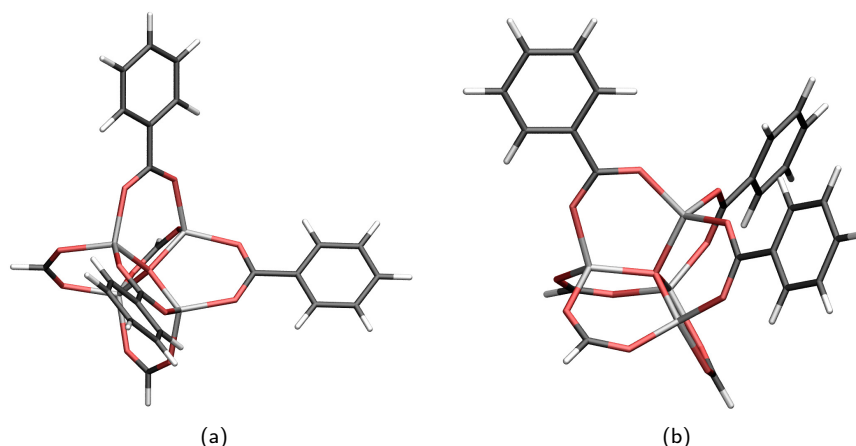


Figure 8.3: Extended model system used to represent the inorganic unit in MOF-5. These mix-ligand complexes consists of three formate and three benzoate ligands, respectively. (a) will be referred to as **B-alpha** and (b) as **B-beta**.

8.1 Evaluation of quantum mechanical methods

8.1.1 Adsorption of the benzene molecule in the α -site

Based on the finite models of the host matrix, the interaction with a benzene molecule is studied. In this regard potential energy curves for the displacement of the units are calculated. The geometry of each molecule was first optimized separately on the B3LYP/cc-pVDZ level according to its point symmetry. Afterwards, the structures were kept rigid and just the interatomic distance was varied, respectively. In order to evaluate the quality of different quantum mechanical methods in terms of their ability to describe the non-covalent interaction between the aromatic molecule and the MOF-5 vertex, first, the adsorption in the α -site along the three-fold axis of the inorganic unit is examined (Fig. 8.4).

The potential energy curves calculated for the *benzene@F*-system with the BLYP and B3LYP functional, show strong basis set dependencies (Fig. 8.5). For example, employing the cc-pVDZ basis set with the BLYP functional a minimum at about 6 Å is observed. However, this small energy well disappears, if the basis set is expanded (Fig. 8.5). Taken into account the basis set superposition error, both functionals offer a repulsive behaviour of the intermolecular potential.

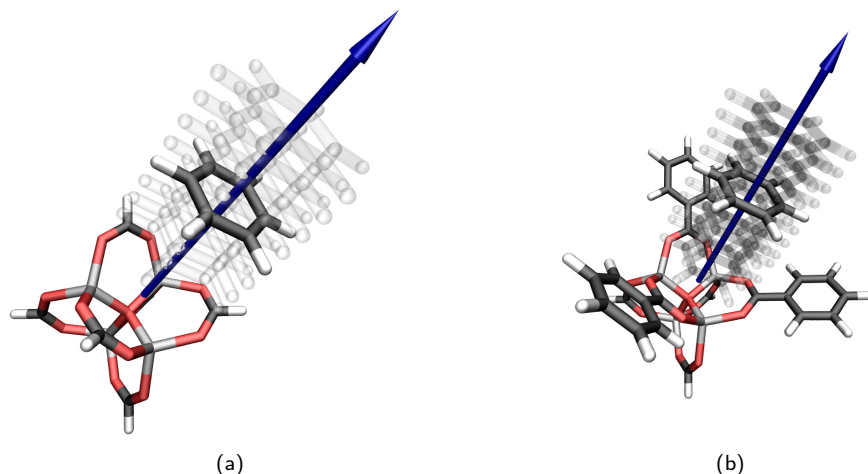


Figure 8.4: Schematic representation of the displacement of the benzene molecule relative to the inorganic complex along the three-fold axis in the α -site for (a) the model **F** and (b) **B-alpha**.

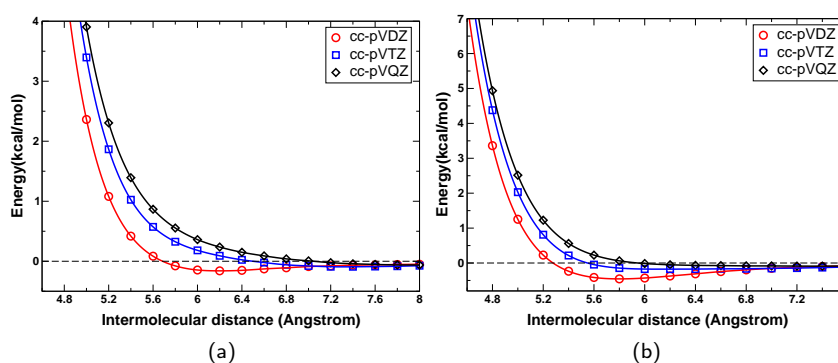


Figure 8.5: Potential energy curve for the displacement of a benzene molecule and model **F** obtained employing the (a) BLYP and (b) B3LYP functional and different basis sets. The intermolecular distance is defined as the distance between the central oxygen atom and the center of the benzene ring. The symbols represent the calculated values; the solid lines are obtained by a cubic spline interpolation.

It is now well established that both DFT methods are not able to describe (non-local) dispersion effects [241, 242], which might be present in the considered complex. The deficiency is due to the construction of these so-called *local* functionals, which are based on the local density, its gradient, and the local kinetic-energy density [241]. In particular correlation contributions present at relatively low electron density regions like in the intermediate region between the molecules are not

covered by these methods. The non-local correlation effects can be separated methodically depending on the electron correlation length [204, 243]. To overcome the effects dominated at medium range, Grimme et al. introduced the double hybrid functional B2PLYP [95]. In this case, the contributions, which are related to the involved orbitals, are treated in a perturbative fashion [95]. Therefore to understand the non-covalent interaction between the benzene molecule and the formate complex in more detail, the B2PLYP functional is used to calculate the potential energy curve of the physisorption process (Fig. 8.6). The double hybrid functional offers an energy well of 2.1 kcal/mol at a distance of 5.3 Å between the central oxygen atom and the center of the benzene ring (Tab. 8.1). The results show (almost) no basis set dependency. Comparing the values obtained by different functionals point out, that dispersion phenomena have to be taken into account to enable an appropriate description of the system (Fig. 8.6).

Table 8.1: Equilibrium distance and corresponding intermolecular interaction energies for the *benzene@F* system obtained by different quantum mechanical methods.

method	basis set	$R_{min}[\text{\AA}]$	$E [\text{kcal/mol}]$
B2PLYP	cc-pVDZ	5.28	-2.10
	cc-pVTZ	5.30	-2.10
B3LYP+D	cc-pVDZ	4.85	-7.47
	cc-pVTZ	4.89	-6.54
	cc-pVQZ	4.90	-6.01
B2PLYP+D	cc-pVDZ	4.92	-6.12
	cc-pVTZ	4.94	-6.00
SCS-MP2	cc-pVDZ	5.10	-4.56
	cc-pVTZ	5.08	-5.07

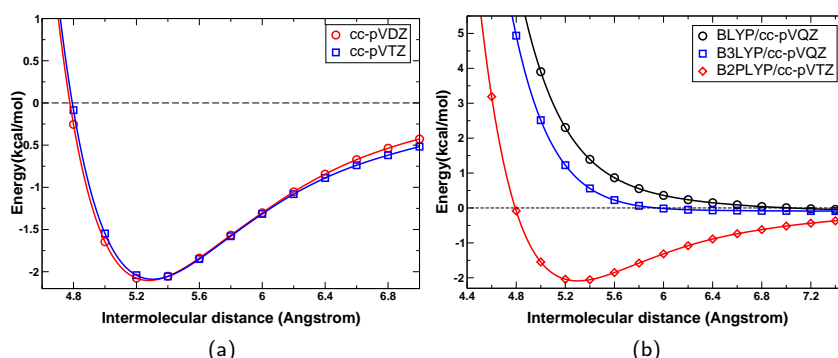


Figure 8.6: (a) Potential energy curve for the displacement of a benzene molecule and model **F** obtained using the B2PLYP functional. (b) Comparison of potential energy curve with respect to different DFT functionals. The intermolecular distance is defined as the distance between the central oxygen atom and the center of the benzene ring. The symbols represent the calculated values; the solid lines are obtained by a cubic spline interpolation.

Nevertheless, since the B2PLYP functional does not cover all correlation effects, an underbinding is usually observed for van der Waals complexes [204, 243]. Coupled cluster calculations are in this regard often seen as benchmarks for the study of these features [242]. For the *benzene@F* system corresponding investigations are not feasible due to the size. To treat correlation effects in the framework of wave-function based methods, often post Hartree-Fock techniques are employed, which use the Møller-Plesset perturbation approach. For instance, in previous works MP2 calculations were performed to analyze the interaction of hydrogen and methane with MOF-5 [38, 183]. However, a number of studies pointed out the deficiency of the *standard* MP2 method to describe e.g. aromatic interactions, which are overestimated by this level of theory [204, 241, 242]. In order to improve the accuracy of the perturbation method, the spin-component-scaled MP2 (SCS-MP2) was developed [86]. In this case antiparallel and parallel spin components are scaled separately to balance dynamic and static correlation effects. Except for some cases, the SCS-MP2 approach indeed improves the agreement with corresponding coupled cluster data in terms of the description of dispersion effects [204, 242]. Motivated by the success of the modified perturbation approach, the potential energy curve for the *benzene@F* system was calculated using the SCS-MP2 method (Fig. 8.7).

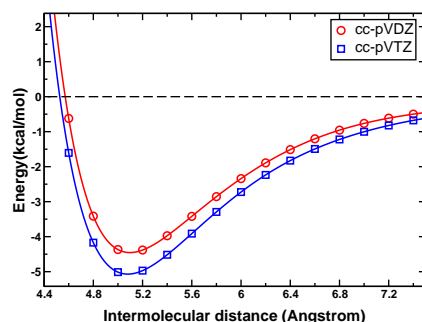


Figure 8.7: Potential energy curves for the displacement of a benzene molecule and **F** calculated at the SCS-MP2 level. The intermolecular distance is defined as the distance between the central oxygen atom and the center of the benzene ring. The symbols represent the calculated values; the solid lines are obtained by a cubic spline interpolation.

In comparison with the B2PLYP results, the SCS-MP2 binding energy is by a factor of approximately 2.5 larger (Tab. 8.1). In contrast to the equilibrium distance, the adsorption energy shows a basis set dependence. Going from the double- ζ to the triple- ζ basis set the interaction increases by 0.49 kcal/mol. Since even the calculation performed, using the cc-pVTZ basis set, are expensive, further expansion of the basis set were not practicable to observe convergence of the data. In spite of the remaining basis set incompleteness error, the results and the trend obtained by the wavefunction based method emphasize that the binding energy is significantly larger than the value computed by the double hybrid functional. Nevertheless the B2PLYP methods is for the particular system a more robust method with respect to the basis set. In this regard an improvement of the DFT method would be beneficial, which would abolish the deficiency of the B2PLYP functional to describe long-range correlation effects [243, 244]. These contributions are with increasing distance less dominated by quantum mechanical effects, so that an effective potential can be used to represent them [204, 243]. Based on this, a r^{-6} potential term (+D) is added to the DFT results to cover the correlation phenomena in an empirical fashion. In principle the correction term can be applied to tune all calculated DFT results. The crucial point is the use of a reasonable damping function for the potential to avoid double counting and singularity at very small distances [242]. Consequently, the potential has to be damped to different degrees depending on the DFT functional. Grimme and co-workers derived corresponding parameters for various functionals [244], which are used in the current investigation.

Adding the classical term (+D) to the results obtained by the B3LYP and B2PLYP functional (Tab. 8.1) reveals a significant increase of the attractive interaction between the benzene molecule and **F** by about 4.0 kcal/mol compared to

the pure DFT results (Fig. 8.8; Tab. 8.1). Further the equilibrium distance of the non-covalent complex is shortened by about 0.4 Å to 4.9 Å. From a technical point of view, it is interesting to see that the potential energy curves obtained by the two dispersion corrected DFT methods match almost perfectly, although applying the B2PLYP functional is due to the perturbation calculation computationally more costly.

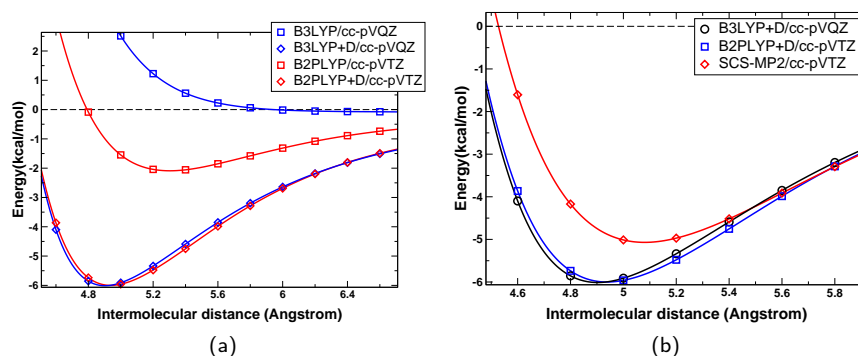


Figure 8.8: Comparison of potential energy curves (a) with respect to different DFT functionals and the use of the dispersion correction (+D) and (b) of SCS-MP2 results with the DFT+D results for the benzene@F-system. The intermolecular distance is defined as the distance between the central oxygen atom and the center of the benzene ring. The symbols represent the calculated values; the solid lines are obtained by a cubic spline interpolation.

In the so far considered model system **F** the phenylene rings connecting adjacent $(Zn_4O)(O_2C)_6$ clusters in MOF-5 are substituted by hydrogen atoms. This simple representation of the network vertex might not cover all properties of the periodic system, which are important to analyse reasonably the host-guest interaction. The neglect of the phenylene rings enclosing an α -site in the MOF-5 matrix should have the largest impact in terms of the truncation. To include the aromatic groups of the MOF-5 matrix in the investigation of the host-guest interaction, model **B-alpha** (Fig. 8.3) is used.

Table 8.2: Equilibrium distance and corresponding intermolecular interaction energies for the *benzene@B – alpha* system obtained by different quantum mechanical methods.

method	basis set	$R_{min}[\text{\AA}]$	$E [\text{kcal/mol}]$
B2PLYP	cc-pVDZ	5.32	-3.92
	cc-pVTZ	5.36	-3.78
B3LYP+D	cc-pVDZ	4.92	-11.80
	cc-pVTZ	4.96	-10.39
B2PLYP+D	cc-pVDZ	4.98	-10.59
	cc-pVTZ	4.99	-10.25
SCS-MP2	cc-pVDZ	5.08	-9.09
	cc-pVTZ	5.09	-9.93

The analysis of the adsorption process (Fig. 8.4) using the extended model provides a repulsive potential energy curve on the BLYP and B3LYP level (Fig. 8.9). Note, that similar to results obtained for the model **F**, both DFT methods show significant basis set dependency. Including dispersion effects in the framework of the B2PYLP functional reveals an attractive character of the intermolecular interaction (Fig. 8.9; Tab. 8.2). The overlap of the conjugated π -system in **B-alpha** with the orbitals of the benzene molecule is (probably) the reason for an increase of the binding energy by 1.68 kcal/mol (B2PYLP/cc-pVTZ: 3.78 kcal/mol) in comparison to the formate model (B2PYLP/cc-pVTZ: 2.10 kcal/mol).

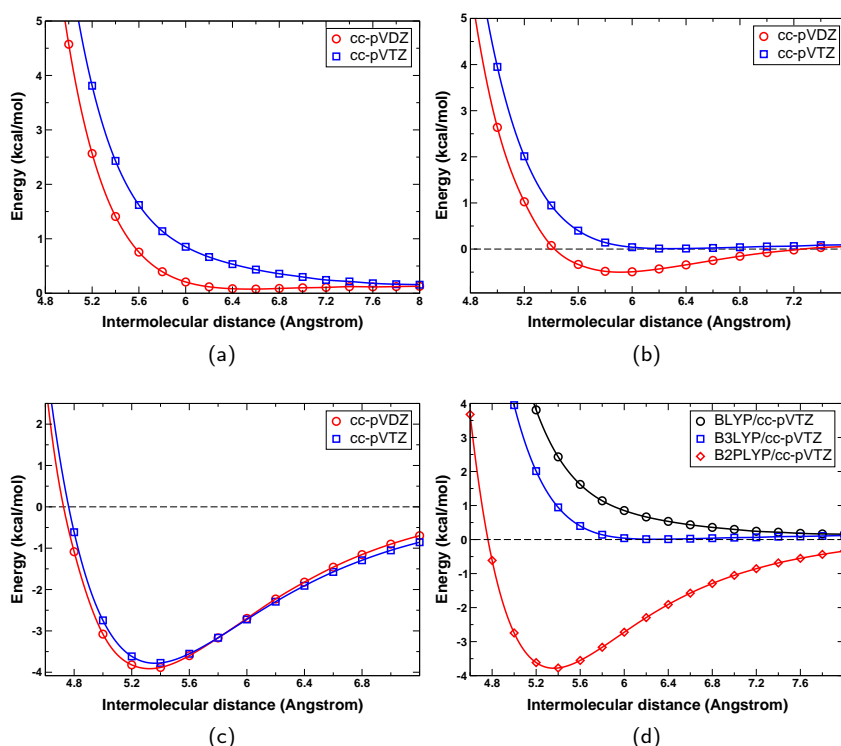


Figure 8.9: Potential energy curve for the displacement of a benzene molecule and model **B- α** obtained employing the (a) BLYP, (b) B3LYP and (c) B2PLYP functional and different basis sets. In (d) the calculated potential energy curves employing the largest basis sets are compared. The intermolecular distance is defined as the distance between the central oxygen atom and the center of the benzene ring. The symbols represent the calculated values; the solid lines are obtained by a cubic spline interpolation.

However, the results for the model **F** indicate that the B2PLYP method is not able to cover all dispersion contributions of this particular system. In fact, performing calculations on the more sophisticated SCS-MP2 level exhibit an intermolecular energy of 9.93 kcal/mol for the adsorption of the benzene molecule in the α -site. Unfortunately, the binding energy obtained by the wavefunction based method do not convergence within the used basis sets (Tab. 8.2).

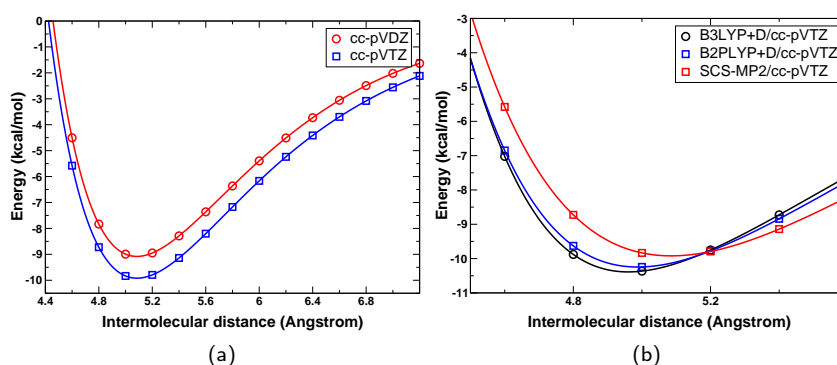


Figure 8.10: (a) Potential energy curve for the displacement of a benzene molecule and **B-alpha** calculated at the SCS-MP2 level. (b) Comparison of SCS-MP2 results with the DFT+D results. The intermolecular distance is defined as the distance between the central oxygen atom and the center of the benzene ring. The symbols represent the calculated values; the solid lines are obtained by a cubic spline interpolation.

Using the more robust DFT+D approach an intermolecular interaction energy of 10.39 kcal/mol and 10.25 kcal/mol for B3LYP+D and B2PYLP+D, respectively, was computed (Tab. 8.2). The significant change of the interaction strength by about 4 kcal/mol depending on the system size, emphasizes the need to include the aromatic groups of the periodic framework into the consideration to get a reasonable picture of the host-guest interaction.

8.1.2 Adsorption of the benzene molecule in the β -site

In addition to the α -site, the benzene molecule can adsorb above the apex of the Zn_4O tetrahedron in the MOF-5 (Fig. 8.11). In this case not only the orientation of the cluster changes rather is the arrangement of the organic linkers different with respect to the guest molecule. Both factors should influence the host-guest interaction. To evaluate the different adsorption sites at the MOF-5 vertex, the potential energy curve for the displacement of the benzene molecule along the C_3 axis in the β -site is investigated using the model **B-beta** (Fig. 8.11; Tab. 8.3)

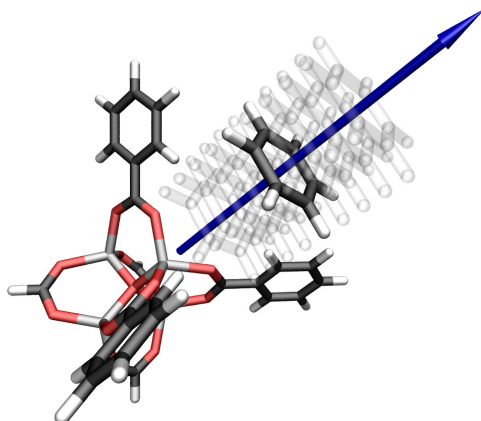


Figure 8.11: Schematic representation of the displacement of the benzene molecule relative to the inorganic complex along the three-fold axis conserving the C_{3v} -point symmetry in the β -site for the model **B-beta**.

All quantum mechanical calculations, which were performed for the *benzen@B-beta* system, indicate (except for the B3LYP results) a weak binding of the guest molecule. The interaction energy on the B2PLYP/cc-pVTZ level is about 30% of the value obtained for the physisorption in the α -site. The B3LYP+D and B2PLYP+D data offer a binding energy of 4.49 and 4.05 kcal/mol, respectively, which is significantly smaller compared to the interaction in the previous arrangement. The SCS-MP2 results, being converged to some extent, differ by about 0.5 kcal/mol from the B2PLYP+D value, which show in contrast to the previous investigation basis set dependency. Due to this it can be assumed that the binding energy is about 4 kcal/mol, which is half the value obtained for the adsorption in the α -pocket.

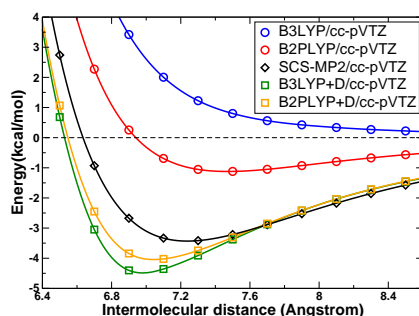


Figure 8.12: Potential energy curves for the displacement of a benzene molecule and **B-beta** calculated using different methods. The intermolecular distance is defined as the distance between the central oxygen atom and the center of the benzene ring. The symbols represent the calculated values; the solid lines are obtained by a cubic spline interpolation.

Table 8.3: Equilibrium distance and corresponding intermolecular interaction energies for the *benzene@B – alpha* system obtained by different quantum mechanical methods.

method	basis set	$R_{min}[\text{\AA}]$	$E [kcal/mol]$
B2PLYP	cc-pVDZ	7.41	-1.51
	cc-pVTZ	7.46	-1.1
B3LYP+D	cc-pVDZ	6.97	-5.33
	cc-pVTZ	6.98	-4.49
B2PLYP+D	cc-pVDZ	7.05	-4.48
	cc-pVTZ	7.04	-4.05
SCS-MP2	cc-pVDZ	7.24	-3.52
	cc-pVTZ	7.24	-3.43

8.1.3 Different arrangement of the benzene molecule in the α -site

In addition to the two different adsorption motives around the inorganic fragment the orientation of the benzene molecule can vary within the different sites. So far the plane of the aromatic ring and one face of the zinc tetrahedron were parallel. To get a broader picture of the host-guest interaction, a different arrangement of the guest molecule in the α -site shall be regarded, where the benzene molecule is perpendicular to the zinc triangle and a hydrogen atom points toward the central oxygen atom of the MOF-5 vertex. The overall performance of the B2PLYP+D

approach to treat the previous cases, encourage the use of this level of theory to study the non-covalent interaction for other arrangements of the benzene molecule.

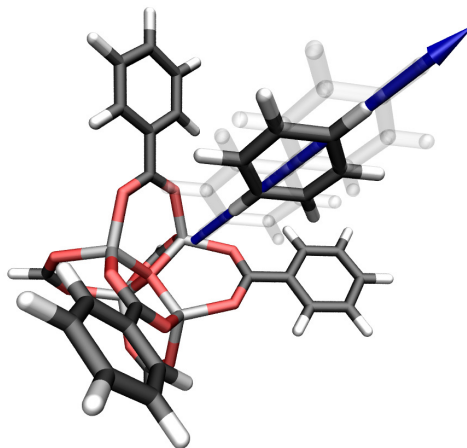


Figure 8.13: Schematic representation of the displacement of the benzene molecule relative to the α -site for the model **B-beta** along the three-fold axis of the inorganic unit. The plane of the benzene ring is perpendicular to one face of the zinc tetrahedron.

The intermolecular energy for the perpendicular adsorption of the benzene molecule is 7.28 kcal/mol (B2PLYP+D/cc-pVTZ), which is less compared to the parallel orientation (B2PLYP+D/cc-pVTZ: 10.25 kcal/mol) but still higher with respect to the interaction in the β -site (B2PLYP+D/cc-pVTZ: 4.05 kcal/mol). Further, the rotation of the benzene molecule within the α -pocket causes an increase of the equilibrium distance by 0.65 Å (parallel: 4.99 Å; perpendicular: 5.64 Å).

Table 8.4: Equilibrium distance and corresponding intermolecular interaction energies for the *benzene@B – alpha* system obtained by different quantum mechanical methods for the perpendicular orientation of the benzene molecular with respect to the face of the Zn_4O tetrahedron.

method	basis set	R_{min} [Å]	E [kcal/mol]
B2PLYP	cc-pVTZ	6.08	-2.46
B3LYP+D	cc-pVTZ	5.61	-8.12
B2PLYP+D	cc-pVTZ	5.64	-7.68

8.2 Evaluation of classical force fields

In terms of a multiscaling approach the carefully calculated quantum mechanical results of the interaction between benzene and MOF-5 can be used for benchmarking *coarse-grain* tools, which enable large scale simulations of the host-guest system. The advantage of this kind of bottom-up strategy was demonstrated in the previous part of this work by the successfully employing of ab-initio derived force fields for the understanding of MOF structures.

In contrast to those cases, investigations dealing with the *benzene@MOF-5* system are known, in which force field are employed [224, 236, 245, 246]. However, concerning the used classical models, some significant differences are present in terms of the representation of the interaction within the host-guest system. In two of the studies [245, 246], the zinc-oxygen environment in the MOF-5 framework was treated in a non-bonding fashion. In these approaches the van der Waals (vdW) interactions were described by a Lennard-Jones (LJ) energy term. In the first case, which will be termed LJ-1, the vdW parameters for the network were adjusted with respect to their ability to reproduce both the experimental measured cell parameters and the adsorption isotherm of methane and carbon dioxide in MOF-5. Using the CHELPG sampling scheme, the atomic charges were derived from DFT calculations (PBE/6-31+G*). For the benzene molecule the TraPPE [245] force field parameters were employed. With respect to the second force field (LJ-2) [246], the vdW parameters from the CVFF and a previously developed force field for zinc oxide minerals were utilized, which were partially modified to match the experimental structure. The electrostatic interactions were described by atomic point charges, as well. The third model (Buck), which was developed in a previous work [162, 205, 224] and already applied to study different isomers in the IRMOF family (Chapter 6), represents the whole framework (including the inorganic unit) by a non-reactive and bonded force field. The vdW interactions are expressed by Buckingham potentials. The corresponding parameters are from the standard MM3 force field [?], in which the individual values are calculated by extra- or interpolation of very few accurate experimental data. Within the Buck force field the atomic charges are derived using a Merz-Kolman sampling method of the electrostatic potential.

In none of the investigations, the performance of the non-bonding parameters was validated in terms of their reliability for the *benzene@MOF-5* system using quantum mechanical data. Thus to evaluate the different models with respect to the host-guest interaction, the potential energy curves for all previously studied non-periodic models were calculated using the force fields and compared to the B2PLYP+D/cc-pVTZ data.

Although the format model **F** is not large enough to represent all properties of

the MOF-5 vertex, the results for this fragment can be used among other as benchmark for the quality of the force fields to describe the interaction between benzene molecules and the inorganic cluster. The LJ-1 value shows an underestimation of the interaction energy by 2.45 kcal/mol. As a consequence the equilibrium distance is large compared to the DFT result. In contrast to this, the binding energy calculated with LJ-2 is strongly overbinding by a factor of two (12.13 kcal/mol; B2PLYP+D/cc-pVTZ: 6.00 kcal/mol). In spite of this large attractive interaction, the intermolecular distance is less in comparison with the B2PLYP+D value. Only the force field Buck is able to reproduce both the interaction energy and the intermolecular distance reasonably. The deviation is about 2 %. To consider the effects of the Coulomb interaction, calculations were performed, in which the atomic charges were omitted. Except for LJ-1 the binding energy decreases in this case. However, the excluding of the electrostatic interaction changes the values by less than 10 %, indicating that the van der Waals contribution is the main part. This is also in agreement with the quantum mechanical investigations, which point out that dispersion effects have to be taken into account for this system.

Table 8.5: Equilibrium distance and corresponding intermolecular interaction energies for the *benzene@F* system calculated using different force fields. For comparison, the values obtained on the B2PLYP/cc-pVTZ level are given. The values in parentheses are calculated binding energies without using atomic point charges.

method	$R_{min}[\text{\AA}]$	$E[\text{kcal/mol}]$
B2PLYP+D/cc-pVTZ	4.94	-6.00
LJ-1	5.31 (5.30)	-4.55 (-4.67)
LJ-2	5.14 (5.15)	-12.13 (-12.61)
Buck	5.06 (5.08)	-6.16 (-5.65)

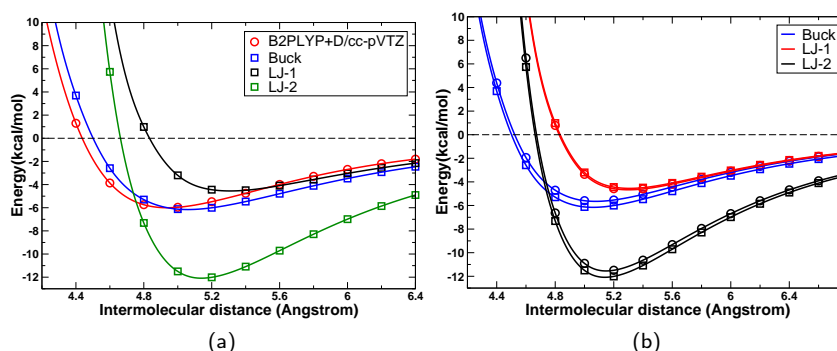


Figure 8.14: Potential energy curves for the displacement of a benzene molecule and **F**: (a) comparison of the force field data and the B2PLYP+D/cc-pVTZ results, (b) force field results calculated with (circles) and without charges (squares). The intermolecular distance is defined as the distance between the central oxygen atom and the center of the benzene ring. The symbols represent the calculated values; the solid lines are obtained by a cubic spline interpolation.

Considering the extended models **B-alpha** and **B-beta**, reveals similar pictures (Tab. 8.6,8.7; Fig. 8.15). Both force fields based on the Lennard-Jones potential show a steep repulsive behavior at small distances (Fig. 8.15). The reason for this can be on the one hand due to the description of the repulsive part, which is represented in these cases by a r^{-12} term in contrast to the exponential expression, which is used in the Buckingham potential. On the other hand the non-bonding force field employed for the inorganic part of the framework might cause this deviation of the potential energy curve, since to reproduce the structure of the framework the van der Waals parameters have to be adjusted to compensate the large Coulomb interactions present around the zinc atoms. But due to the used vdW mixing rules these parameters also describe the host-guest interaction.

Note, that at large intermolecular distances the potential energy curve for Buck and LJ-1 are almost identical. The higher quality of LJ-1 compared to LJ-2 is probably because of the strategy used to derive the vdW parameter, where both structural as well as adsorption properties are simultaneously fitted.

Table 8.6: Equilibrium distance and corresponding intermolecular interaction energies for the *benzene@B – alpha* system calculated using different force fields. For comparison the values obtained on the B2PLYP/cc-pVTZ level are given. The values in parentheses are calculated binding energies without using atomic point charges.

method	$R_{min}[\text{\AA}]$	$E [\text{kcal/mol}]$
B2PLYP+D/cc-pVTZ	4.99	-10.25
LJ-1	5.35 (5.36)	-8.73 (-8.46)
LJ-2	5.22 (5.22)	-18.89 (-18.13)
Buck	5.15 (5.17)	-9.43 (-8.61)

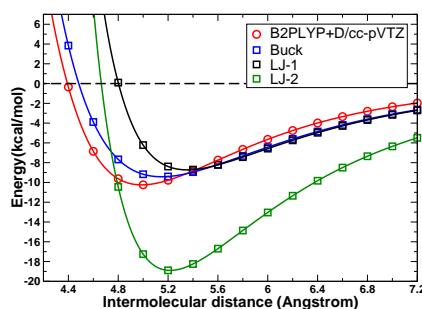


Figure 8.15: Potential energy curves for the displacement of a benzene molecule and **B-alpha**: comparison of the force field data and the B2PLYP+D/cc-pVTZ results. The intermolecular distance is defined as the distance between the central oxygen atom and the center of the benzene ring. The symbols represent the calculated values; the solid lines are obtained by a cubic spline interpolation.

Table 8.7: Equilibrium distance and corresponding intermolecular interaction energies for the *benzene@B – beta* system calculated using different force fields. For comparison the values obtained on the B2PLYP/cc-pVTZ level are given. The values in parentheses are calculated binding energies without using atomic point charges.

method	$R_{min}[\text{\AA}]$	$E [\text{kcal/mol}]$
B2PLYP+D/cc.pVTZ	7.04	-4.05
LJ-1	7.36 (7.33)	-3.53 (-3.99)
LJ-2	7.03 (7.01)	-8.59 (-9.21)
Buck	7.33 (7.31)	-3.38 (-3.70)

For the adsorption process of the rearranged benzene molecule in the α -site, the agreement between the force field and B2PLYP+D results is poorer. The deviation is about 2 kcal/mol for Buck and 1.52 kcal/mol for LJ-1 (Tab. 8.8). However, it should be kept in mind, that none of the force fields were tuned for the particular

system. Further the relevance of this arrangement is probably less, since the parallel orientation is energetically more favourable.

Table 8.8: Equilibrium distance and corresponding intermolecular interaction energies for the *benzene@B – alpha* system obtained by different quantum mechanical methods for the perpendicular orientation of the benzene molecular with respect to the face of the Zn_4O tetrahedron. The values in brackets are calculated binding energies without using atomic point charges.

method	$R_{min}[\text{\AA}]$	$E[kcal/mol]$
B2PLYP+D/cc-pVTZ	5.64	-7.68
LJ-1	6.10 (6.14)	-6.16 (-5.80)
LJ-2	5.86 (5.84)	-14.28 (-14.85)
Buck	6.06 (5.81)	-5.70 (-6.23)

The comparison of the force field and quantum mechanical results reveal that the force field Buck is able to reproduce the interaction of benzene with the vertex of MOF-5 to a high degree. The non-bonding LJ force fields show poorer performance in this regard, whereas LJ-2 has severe errors for the host-guest system. LJ-1 gives a reasonable description at larger intermolecular distances.

Interestingly, the observations obtained for the non-periodic models are in coincidence with the simulations performed for the periodic system. All three force fields were used to simulate the self diffusion constant (D_{self}) of benzene in MOF-5 at low loading. Fortunately, experimental data are available for this particular system ($D_{self} = 2.0 \cdot 10^{-9} m^2/s$) [247], which allows to evaluate the quality of the force fields. Considering the results obtained by LJ-2, the mobility of the benzene molecules is by an order of magnitude smaller compared to the measured results ($D_{self} = 0.2 \cdot 10^{-9} m^2/s$ [246]). The deviation becomes clear by the detailed investigation of the finite model system. Due to the strong attractive interaction between the benzene molecule and the matrix, the diffusion process is suppressed. Therefore the presumption [245] that the short simulation time is the reason for the wrong value can be disproved (to some extent). Both LJ-1 and Buck are able to reproduce the transport properties of benzene in MOF-5 ($D_{self}(LJ-1) = 2.9 \cdot 10^{-9} m^2/s$ [245]; this work: $D_{self}(Buck) = 2.5 \cdot 10^{-9} m^2/s$). However, two points should be stressed. First, the force field Buck describes different length scale with a high accuracy, which is, as already mentioned, often challenging with respect to a simple classical model. Second, the force field is obtained using no experimental data. It should be also noted that the model is able to reproduce both the structure and the internal dynamics of the framework itself [98, 205]. Hence this force field Buck is superior compared to the other currently known ones. Finally, it allows further detailed investigations of host-guest systems based on MOF-5 type networks and

aromatic guest molecules. For instance, allows the additive energy expression of the force field the decomposition of the van der Waals energy according to the atom types. In this regard the potential energy curves of the *benzene@B-alpha* system were calculated switching off the vdW parameters for the central oxygen atom, the zinc atoms, the carbonyl oxygen atoms and carbonyl carbon atoms, respectively. This kind of analysis suggest that the central oxygen atoms has almost no contribution to the vdW interaction (about 0.1 kcal/mol). In contrast to this the vdW interaction between the benzene molecule and the zinc atoms is about 20 % (about 2 kcal/mol). A similar situation is observed with the oxygen atoms of the carbonyl group. The carbon atoms of the acid group contribute about 1 kcal/mol (10%) to the total intermolecular vdW energy. The remaining part is the interaction between the benzene molecule and the phenyl rings of **B-alpha**. As a proof of concept the aromatic groups were cut off the model and was saturated by hydrogen atoms. Calculating the interaction of the benzene molecule and this system using the force field and the B2PLYP+D/cc-pVTZ method offers reasonable agreement (B2PLYP+D/cc-pVTZ: 5.51 kcal/mol; FF-Buck: 4.36 kcal/mol), which validates the quality of the force field Buck.

8.3 Summary

In conclusion, the quantum mechanical benchmark calculations on the finite model systems expose different aspects of the host-guest system. The aromatic guest molecule interacts more strongly with the vertex of the MOF-5 framework (about 10 kcal/mol) compared to other molecules like hydrogen, where the binding energies is in the range of 1 - 2 kcal/mol [38]. Although the physisorption process is stronger, similar theoretical methods are needed, which include dispersion effects, to describe the interaction accurately. The B2PLYP+D method emerges as an accurate and robust tool for the investigation of these non-bonding phenomena in MOF based host-guest systems. In addition, the analysis points out the importance of appropriate model systems, since the calculated binding energies depend on the truncation of the periodic matrix. To include all aspects, which are important for the binding of the benzene molecule to the vertex of the network, the phenylene rings of the organic linkers have to be taken into account. By comparing the quantum mechanical data with force fields, used to study the *benzene@MOF-5* system, reveals that currently only the (previously) derived force field based on MM3 is able to describe accurately the interaction of the benzene molecule and the MOF-5 vertex. The other force fields either deviate significantly in this point or offer artificial behaviours at short distances. In addition the force field with a Buckingham potential is able to reproduce the measured self-diffusivity of benzene in MOF-5. The ability to describe both length scales encourage further investigations based on this force

field.

Chapter 9

Soft-Modifications

Due to their construction, porous coordination polymers offer the possibility to obtain new networks systematically. The secondary building units, which build up the structure, have well-defined geometrical shapes and due to their functional groups their linking is directed. Thus, various networks can be achieved, which have either different topologies or vary in their pore features. The latter is of particular interest, since the selective tuning of a network offers the possibility to develop materials with desired functionality. To use this unique property of these materials, systematic investigations are needed in order to understand the influence of pore modifications on the host-guest interaction.

Starting from one MOF, different kinds of framework modifications are possible. On the one hand the local chemical environment can be changed. Examples are the variation of the metal center in the SBUs or the introduction of active groups like replacing a hydrogen atoms of an aromatic ring by an amine-group. On the other hand the matrix can be modified by changing the metric of the pore system or by decorating a SBU (e.g. exchange of 1,4-benzene dicarboxylate by 2,6-naphthalene dicarboxylate). In the latter case the chemical nature of the MOF is (to some extent) maintained. To point out the differences of the two classes of variations in the parent MOF structure, the concept of **hard- and soft- modifications** is introduced. Changing the molecular structure of the framework significantly like in the case of metal exchange, is referred to as *hard-modifications*. In contrast to this the second type of modifications will be called *soft* (Fig. 9.1). Hard-modifications are known to have large impacts on the adsorption properties of MOFs. Thus a number of studies deal with this kind of pore tuning especially with respect to hydrogen storage [38] and selective adsorption of carbon dioxide. In contrast, few investigations are known, analyzing the influence of *soft-modifications* on host-guest systems. The reason for this is probably, due to the assumption that these variations of the framework, which do not affect the chemical properties, would

have less impact on the properties of the materials. To evaluate this hypothesis, this chapter focuses on how and to what extent soft-modifications can influence properties (e.g. mobility) of guest molecules within the matrix.

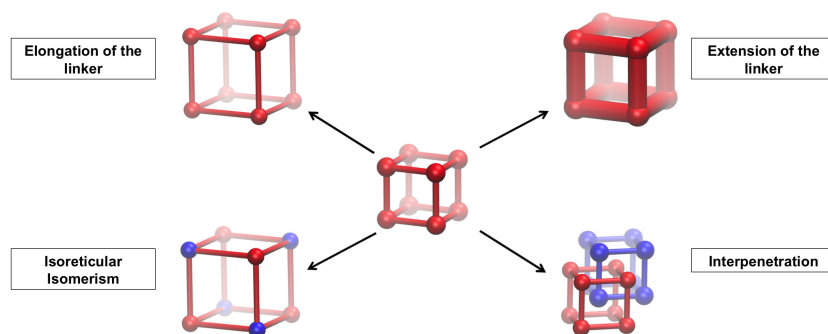


Figure 9.1: Some Examples of soft-modifications of Metal-Organic Frameworks

One class of porous coordination polymers, which includes derivatives of MOF-5 (IRMOF-1), is, as mentioned before, commonly entitled with the umbrella term isorecticular MOFs (IRMOF) [174]. Since they cover a wide range of possible soft-modifications, the examination of some representatives of these IRMOFs as host matrix is reasonable in terms of the intended study. Encouraged by the performance in terms of the description of both structural as well as dynamic properties of the MOF-5 system [98, 205] and its derivatives (Chapter 6), the previously *ab-initio* parametrized force field [98] was employed to enable an accurate description of the framework structure. The presented results, regarding the non-covalent interaction between benzene and the MOF-5 vertex, also reveal the power of the classical model to represent precisely all aspects of host-guest systems, based on the IRMOF family. Therefore, the host matrices, which are obtained by soft-modification of MOF-5, are loaded with benzene molecules and investigated by molecular dynamic simulations to evaluate the influence of various soft-modifications

9.1 Elongation of the linker

By replacing the terephthalic acid in IRMOF-1 with its biphenyl or triphenyl derivative, the matrices of IRMOF-10 and -16 are constructed. The cell dimension increases by 8.6 Å and 17.2 Å and simultaneously the pore opening scales by a factor of 1.35 and 1.86 going from IRMOF-1 to IRMOF-10 or IRMOF-16, respectively. A naive interpretation of the change in the metric would be that the mobility of a guest molecule within the pores should rise, since the hinderance by the framework would decrease. Further, due to the lower density of the guest molecules (same

number of molecules in a bigger cell) the collision with each other should be less and thus the mean free path longer. Both conclusions argue for an increase of the self-diffusion coefficient, which can be calculated according to Einstein's equation (Eq. 3.18) by analyzing the mean square displacements (MSDs) of the particles along the time. Although both the pore opening and the pore size of the MOFs exceed the size of the benzene molecule (distance between opposite hydrogen atoms is about 5 Å), the non-bonded interactions of the guest molecules with the matrix have to be taken into account. The strength of the host-guest interaction, however, vary within the pores, due to the structure of the framework.

The specific embedding of the inorganic cluster within the IRMOFs creates two types of cells [224]¹. In the vertices of the so-called A-cell the faces of the Zn_4O -tetrahedrons point into the pores, whereas the apex of them surround the B-cell. Further the relative orientation of the linkers differs. In the A-cell the planes of the aromatic linkers point into the center in contrast to the B-Cells where the edge face inwards.

9.1.1 Structure and mobility of the benzene molecules within the pores

The attractive interaction of the benzene molecules with the Zn_4O clusters in the A-cells initiates a well-ordered arrangement (Fig. 9.2). In previous experimental and theoretical works the preference of these adsorptions sites in IRMOF-1 was shown for other guest species [237, 240, 248]. The B-cell does not have this type of pocket and is significantly less preferred at a loading of 10 molecules per unit cell. Hence, the alternating arrangement of the two types of cells induce the formation of a checkerboard pattern for the adsorption of guest molecules. The elongation of the linkers does not change the chemical environment of the matrix, so that the primary adsorption pattern is unaltered for the IRMOF-10 and 16 (Fig. 9.2).

¹Note, that in this investigation the isorecticular isomer of the IRMOFs is considered, which has the lowest potential energy (see also Chapter 6) and is observed experimentally.

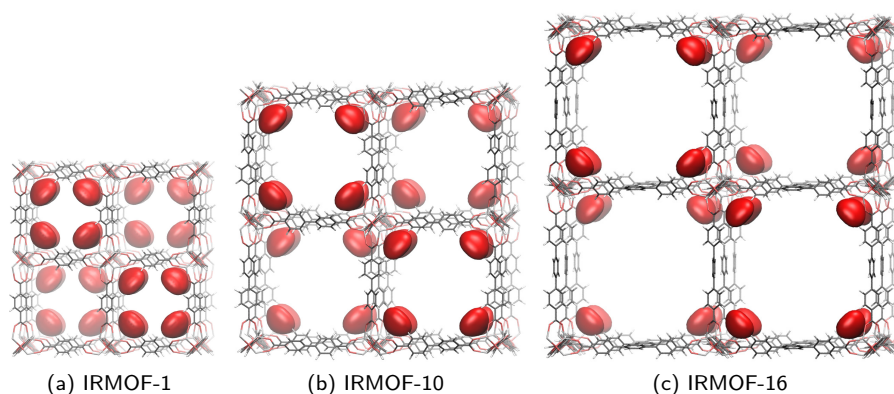


Figure 9.2: Probability distribution of the center of mass of benzene molecules at 300K within (a) IRMOF-1, (b) IRMOF-10 and (c) IRMOF-16 at a loading of 10 benzene molecules per unit cell and the same iso-value for the probability surfaces (red).

In addition the mobility of the guest molecules within the pores is influenced by the attractive host-guest interaction. Interestingly, the self-diffusion coefficient of benzene within the pores (Tab. 9.1) is in the range of liquid benzene ($2 - 3 \cdot 10^{-9} \text{m}^2/\text{s}$ [236]), although the density of benzene molecules within the pores of IRMOF-1, for instance, is at a loading of 10 bz/uc below 10% of liquid benzene ($\rho = 0.8765 \text{g/ml}$ [249]). Comparing the mobility of benzene in the presence and absence of the framework shows that the self-diffusion coefficient of the *free* benzene molecule is orders of magnitude higher². This indicates the strong influence of the host on the diffusion of the adsorbate and promotes the idea of using MOFs as *solid solvents*. This is reasonable, since the density of the benzene molecules in the framework is comparable with the gas phase, the mobility with the liquid state and the structure does not correlate with any pure phase of benzene. Consequently the framework *shapes* the relative orientation and the proximity of the guest molecules. In this regard, it should be pointed out that the center of mass (COM) of the phenyl rings in IRMOF-1 are almost in the same distance to the center of the α -sides (5.5 \AA) as the COM-COM distance in liquid benzene (ca. 5.5 \AA [250], ca. 5.4 \AA [251], ca. 5.2 \AA [252] for the first shell).

²Self-diffusion coefficient of Benzene calculated from a simulation of benzene molecules in a simulation box with the same size as IRMOF-1 ($D_{self} = 50 \cdot 10^{-9} \text{m}^2/\text{s}$) and IRMOF-10 ($D_{self} = 500 \cdot 10^{-9} \text{m}^2/\text{s}$)

Table 9.1: Self-Diffusion coefficient D_{self} of benzene in three IRMOFs at different temperatures and a loading of 10 benzene per unit cell.

	$D_{self} [10^{-9}m^2/s]$		
temperature	200	300	400
IRMOF-1	0.14 ± 0.06	2.00 ± 0.39	7.21 ± 1.64
IRMOF-10	0.06 ± 0.06	3.47 ± 0.84	16.95 ± 2.26
IRMOF-16	0.03 ± 0.02	2.56 ± 0.96	21.19 ± 2.46

Suprisingly, the elongation of the linkers influences the self-diffusion coefficient of benzene molecules at 300K only marginal (Tab. 9.1). The mobility of the guest molecules in IRMOF-16, which has the largest pores of three investigated system, is with $D_{self} = 2.55 \pm 0.96 \cdot 10^{-9}m^2/s$ almost in the same range as in the IRMOF-1 matrix ($D_{self} = 2.00 \pm 0.39 \cdot 10^{-9}m^2/s$), especially if the error bars are regarded. In the case of IRMOF-10 a slightly increase of the diffusivity is observed ($D_{self} = 3.47 \pm 0.86 \cdot 10^{-9}m^2/s$). As mentioned before, just for the loaded IRMOF-1 system, the benzene self-diffusion coefficient ($D_{self} = 2.00 \cdot 10^{-9}m^2/s$ ³) is measured [247], which is in good agreement with the calculated value from the simulation.

To understand the host-guest interaction in more detail, the free energy topology of the guest molecules within the frameworks is analyzed. Therefore the spatial probability density $q(r)$ for the finding of the center of mass of a benzene molecule at the point r is used to calculate a relative spatial free energy map by

$$\Delta G(r) = -RT \ln [q(r)],$$

with the global minimum (highest $q(r)$) taken as the zero of the free energy (with the gas constant R and the temperature T) [253]. The analysis of the obtained ΔG -topologies reveals that the adsorption pattern deviate as a function of the iso-value (Fig.9.3-9.5), indicating a different hierachy for the binding sites within the three matrices.

³This value was obtained for the fastest measured component.

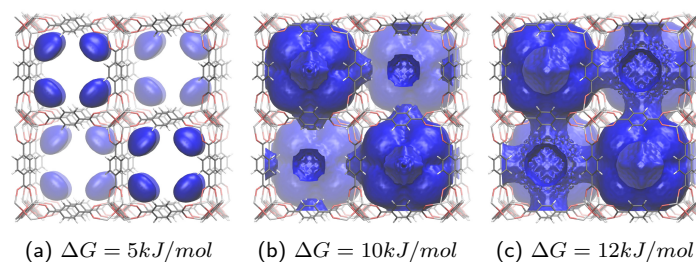


Figure 9.3: Free energy map of the benzene molecules in IRMOF-1 at a loading of 10bz/uc. Shown are the isosurfaces for the denoted ΔG -values.

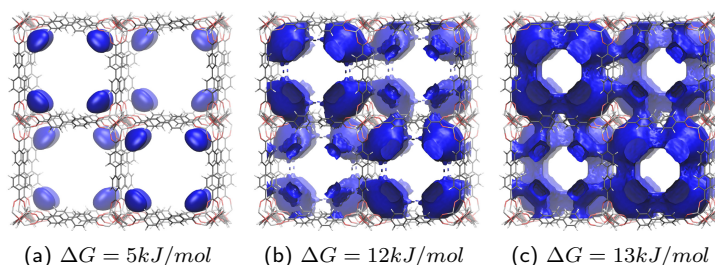


Figure 9.4: Free energy map of the benzene molecules in IRMOF-10 at a loading of 10bz/uc. Shown are the isosurfaces for the denoted ΔG -values.

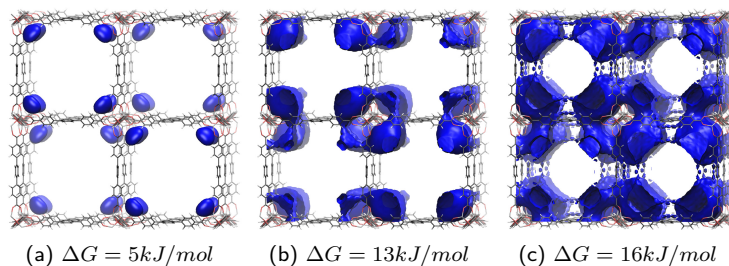


Figure 9.5: Free energy map of the benzene molecules in IRMOF-16 at a loading of 10bz/uc. Shown are the isosurfaces for the denoted ΔG -values.

The corners of the A-cells are the primary binding sites in all cases (α -site). For the IRMOF-1 system, additional adsorption takes place almost exclusively in the A-cell. In contrast to this, the β -sites, which are in the corners of the B-cell, are energetically more preferred with increasing linker size. The change in the metric of the framework causes that, for instance, guest molecules located at the pore windows are less stabilized. The phenylene groups located at a pore opening in IRMOF-1 are in an energetically favorable distance in terms of the host-guest

interaction, since all aromatic groups can interact simultaneously with the benzene molecule. In IRMOF-16 the pore dimension exceed the size of the guest molecule significantly, so that the beneficial arrangement is not possible.

In this regard it should be noted, that the distance dependency of the attractive interaction is one major challenge with respect to the efficient storage of guest molecules within MOFs. The modification of the framework often just increases the adsorption energy of single molecules with the inner surface, but once the preferred sites are occupied further adsorption is less favoured. Hence, beside the tuning of the host-guest interaction, the pore size has to be regulated to avoid volume elements, which are energetically less preferred. To circumvent to some extent the decrease of host-guest interaction within large pore systems, supporting molecules like fullerene can be embedded into the pore system, which introduce further adsorption sites [47, 254]. By this approach the adsorption process is promoted. However, by this approach both the gravimetric uptake and the storage capacity decrease, since some of the pore volume are blocked by the supporting molecules.

9.1.2 Benzene diffusion mechanism

The investigation of the free energy maps offer in addition to the thermodynamic properties (like adsorption sites) an insight into the diffusion mechanism of the guest molecules. In order to clarify the development of the self-diffusivity with respect to the linker size, the probability densities for the lower half of the unit cells (two A- and two B-cells) were integrated up along the z-coordinate, and the 2D free energy maps in the xy-plane were calculated using the same formalism as before. These contour plots are shown in Fig. 9.6 with isoline separations of 1 kJ/mol. Note, that these 2D maps are not slices of the 3D maps (Fig. 9.3-9.5). Because of the z-integration, each of the minima in the A-cell corresponds to two spatial sites seen in Fig. 9.2. Thus, the $\Delta G(x, y)$ value in this graph gives the free energy with respect to the α -site global minima for a guest molecule with its COM constrained to this particular x- and y-coordinate, sampling all other $3N - 2$ degrees of freedom. In addition, to simplify the comparison of the different networks the cell sizes were normalized.

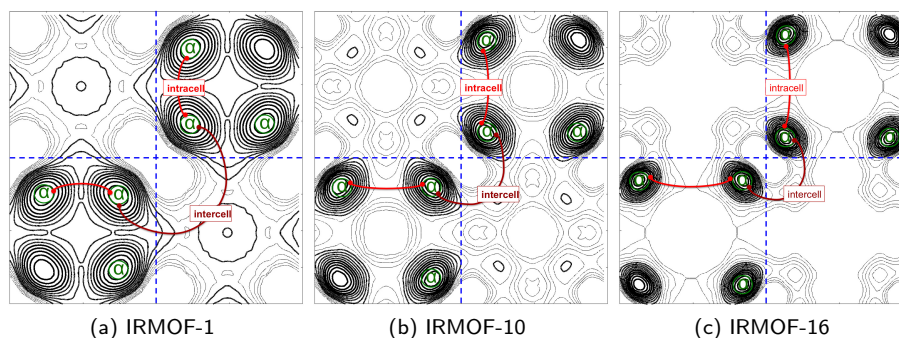


Figure 9.6: Contour plots of the free energy landscapes with isoline separations of 1 kJ/mol.

In agreement to previous results, the contour plots illustrate, that the IRMOF frameworks own two kind of cells, which are arranged in an alternating fashion and differ, due to the host-guest interaction, in the degree of accumulation of the guest molecules. Based on this, the long-range motion of the benzene molecules within the framework can be described in terms of an intra- or intercell process with the focus on the energetically preferred A-cell.

Considering the IRMOF-1 system, the free energy map reveals that the intracell diffusion has a free energy barrier of around 6 kJ/mol . The measured value for a rearrangement of benzene in IRMOF-1 of 6.14 kJ/mol [225] can be assigned to this intracell process. However, the long-range mobility of the guest molecules in IRMOF-1 is dominated, due to a higher free energy barrier, by the intercell motion, in which the guest molecules have to cross the pore opening and diffusion through the B-cell [224, 236]. The elongation of the linkers changes the topology of the free energy maps to some degree. The intercell process, which is primarily a motion around the corner of the cubic framework, is almost not affected if the linker is elongated. The free energy barrier for the intracell transition is increased compared to the IRMOF-1 system.

Despite the differences in the contour plots the overall diffusion mechanism is in all cases dominated by transitions between α -sites. Since the topology of the free energy surface correlates with the residence time of a benzene molecule, it can be assumed, that the guest molecules are located mainly in these pockets and that the transition occurs on a fast time scale. Based on this, the diffusion of the benzene molecules within the matrix will be described by a hopping model. The expression for the self-diffusion coefficient is in this case given by

$$D_{self} = \lambda^2 \cdot k_{eff},$$

where λ is the average step length of a benzene molecule and k_{eff} the corresponding effective rate constant. Corresponding to the previous classification,

two *jumps* can be distinguished. One is the intracell hopping and the other is the jump between α -sites in different A-cells (intercell). In this regard, the effective rate constant for the diffusion process can be subdivided into two elementary steps, which should occur sequentially for the long-range diffusion with the rate constants k_{intra} and k_{inter} for the two hopping steps, respectively. Both depend according to the transition state theory (TST) on the free energy topology. Therefore to study the change of the free energy barriers more quantitative the two-dimensional probability density $q(x, y)$ was further integrated along one axes and convert into an one-dimensional free energy plot (Fig. 9.7). At about the half of the cell length a barrier can be localized in the ΔG -plots, representing the transition from the A-cell to the B-cell. Since the free energy differences within the B-cell are less significant, the height of this free energy barrier can be assumed to be dominant for the intracell hopping. In agreement with the previous results, the plots show that the transition from one A-cell to an other is not affected by the elongation, since in all frameworks the motion is hindered by the same degree ($\Delta G_{inter} \approx 11.0 kJ/mol$; Tab. 9.2). For the intracell motion of the benzene molecules the plots offer a free energy barrier (ΔG_{intra}) at the middle of the A-cell, which has a strong dependency on the linker length (Tab. 9.2). In IRMOF-1 ΔG_{intra} is about the half of the value of ΔG_{inter} , which points out that the diffusion limiting step is the transition between different A-cells. Going to the system with the biphenyl-linkers the ratio between the two barriers is almost one. For the case of IRMOF-16 ΔG_{intra} is by about $2 kJ/mol$ higher compared to the ΔG_{inter} , so that the intracell hopping gets the rate determining process.

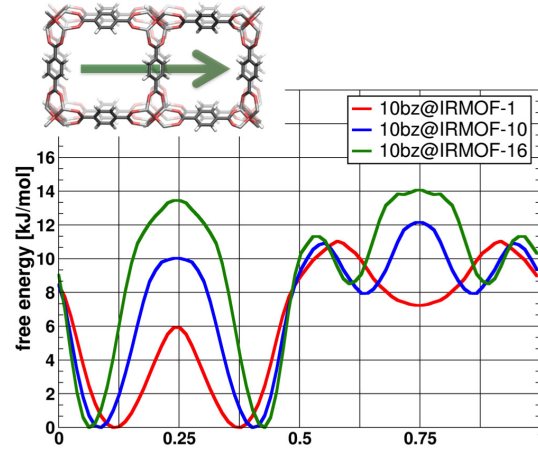


Figure 9.7: Free Energy curve along the diffusion path of a benzene molecule along the axis connecting an A-cell and a B-cell as illustration in the insert using the example of IRMOF-1. In order to simplify the comparison of the different networks the cell dimensions were normalized.

Table 9.2: Activation energy E_A of the diffusion process of benzene and the free energy barriers at 300K for the intracell (ΔG_{intra}) and intercell (ΔG_{inter}) hopping process in the three IRMOFs at a loading of 10 benzene per unit cell.

	E_A [kJ/mol]	ΔG_{intra} [kJ/mol]	ΔG_{inter} [kJ/mol]
IRMOF-1	55.35	5.92 ± 0.73	11.04 ± 0.61
IRMOF-10	78.99	10.03 ± 0.56	10.93 ± 0.79
IRMOF-16	93.35	13.46 ± 1.26	11.31 ± 1.41

The results from the investigations of the free energy data may seem to be contrary to the development of the self-diffusion coefficient, since a decrease of the mobility would be expected in case of IRMOF-16 due to the increase of the free energy barrier. But the conflict can be solved if the step length λ is taken into consideration. By elongating the linkers, the effective hopping rate k_{eff} decreases but at the same time λ increases due to the metric of the system. Thus in this particular case of the IRMOFs both factors probably compensate each other upon elongation of the linker, causing that the self-diffusion coefficient does not change significantly.

At elevated temperature the effect of the modified metric on the mobility becomes apparent (Tab 9.2). The self-diffusivity of benzene in IRMOF-16 rises by about an order of magnitude if the temperature is increased by 100K. For the case of IRMOF-1 the change is less distinct, just by a factor of 3.5 the mobility alters

going from 300K to 400K. Although the diffusion of the benzene molecules within all considered systems is an activated process, the temperature dependency is different for the three matrices. This is reflected by the activation energy E_A (Tab. 9.2), which is obtained by an Arrhenius plot of D_{self} . In accordance with the study of the free energy topology, the development of E_A with subject to the linker size points out that a higher kinetic energy is needed to initiate the diffusion process at elongated linkers. But once enough energy is available for the hopping between the α -sites (at elevated temperature), the larger step length λ in IRMOF-16 causes a significant difference of D_{self} in IRMOF-16 compared to IRMOF-1 (Tab. 9.1).

9.1.3 Monte-Carlo Hopping Model

In order to elaborate the hopping model, which was used so far qualitatively to analyze the diffusion of benzene within the IRMOFs, the TST formalism is used to obtain the rate constants k for the intra- and intercell hopping process by

$$k = \sqrt{\frac{k_B T}{2\pi m}} \frac{\exp\{\Delta G(q^*)\}}{\int_{q^*}^{\infty} dq \exp\{\Delta G(q)\}},$$

where k_B is the Boltzmann constant, m the mass of one benzene molecule, q the position and T the temperature. The asterisk marks the transition state of the corresponding process. The free energy barriers from the one-dimensional ΔG -plot (Tab. 9.1) are employed for the calculations. A first inspection of the rate constants, which are summarized in Tab. 9.3, reveals that in the case of IRMOF-1 the intracell motion is more than one order of magnitude faster compared to the intercell process, whereas in the IRMOF-16 matrix, k_{inter} is by a factor of 2 higher compared to k_{intra} .

Table 9.3: Calculated rate constants for the intracell (k_{intra}) and intercell (k_{inter}) hopping process of one benzene molecule in the three IRMOFs at a loading of 10 benzene per unit cell and a temperature of 300K.

	k_{intra} [1/s]	k_{inter} [1/s]
IRMOF-1	$4.82 \cdot 10^{10}$	$3.10 \cdot 10^9$
IRMOF-10	$4.60 \cdot 10^9$	$1.60 \cdot 10^9$
IRMOF-16	$2.48 \cdot 10^9$	$6.16 \cdot 10^9$

For the long-range diffusion of the benzene molecule within all frameworks both intra- and intercell hoppings have to occur, as mentioned before, sequentially. However, due to the arrangement of the adsorption sites, the step length describing this continuous process is not well defined. In contrast to this, the spatial evaluation of a benzene molecule leaving an α -pocket is known for a limited time scale. The host-guest interaction induces the transition to one of the adjacent primary binding site. Thus the number of possible pathways for a benzene molecule to escape from

one α -sites is limited in space (Fig. 9.8). If the benzene molecule performs one of these transitions it arrives in an environment, where the same steps are possible again. Consequently, the diffusion process can be describe in terms of this hopping events, which are repeated continuously.

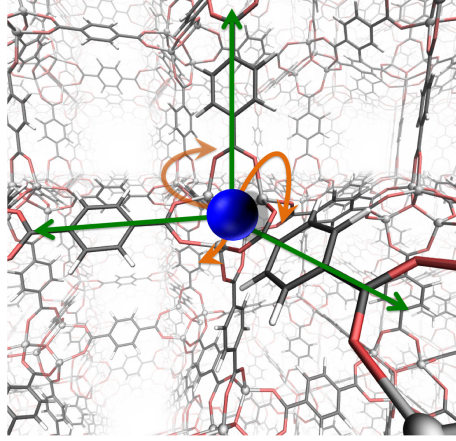


Figure 9.8: Different hopping event possible starting from α -site (green: intracell and orange:intercell transitions).

In this regard the rate constants k_{inter} and k_{intra} can be used to calculate the residence time for a benzene molecule in an α -site by⁴

$$t_{\alpha} = \frac{1}{3 \cdot k_{inter} + 3 \cdot k_{intra}}.$$

After a time t_{α} the molecule escapes the binding pocket and either an intra- or intercell hopping event takes place (Tab. 9.4). Using the ratio between k_{inter} and k_{intra} the probability for each step type can be written as

$$p_{inter} = \frac{k_{inter}}{k_{inter} + k_{intra}},$$

$$p_{intra} = \frac{k_{intra}}{k_{inter} + k_{intra}}.$$

Note that three different intracell steps are possible, whereas the transitions occur along one spatial direction (Fig. 9.8), respectively. Due to the isotropic nature of the network, the probability that a benzene molecule makes a motion in a direction i ($=x,y,z$ axis) is given by

$$p_{intra}^i = \frac{1}{3} \cdot p_{intra}.$$

The step length λ_{intra} in this case is simply the intracell distance between adjacent α -sites (Tab. 9.4).

⁴To consider the number of transition states present for the intra- and intercell steps, respectively, the prefactor three is used.

Table 9.4: Calculated rate constants for the intracell (k_{intra}) and intercell (k_{inter}) hopping process of one benzene molecule in the three IRMOFs at a loading of 10 benzene per unit cell and a temperature of 300K.

	$t_\alpha [ps]$	$\lambda_{intra} [\text{\AA}]$	$\lambda_{inter} [\text{\AA}]$	$D_{self} [10^{-9} m^2/s]$
IRMOF-1	6.5	6.5	6.5	5.90 ± 1.81
IRMOF-10	53.7	10.8	6.5	2.86 ± 0.73
IRMOF-16	38.6	14.9	6.4	4.63 ± 1.74

In contrast to this, an intercell hopping event always includes a motion into two directions in space (Fig. 9.9). The vector describing this process can be divided into two steps, which take place sequentially and along different spatial direction (Fig. 9.9). However, according to the structural properties of the network, a correlation between these partial steps exists. For instance, if a benzene molecule escapes the A-cell in x-direction, it has to perform a motion into the y- or z- direction to enter an A-cell again. Thus the probability for each of these six possible intercell steps is

$$p_{inter}^{i,j} = \frac{1}{3} \cdot \frac{1}{2} \cdot p_{inter} = \frac{1}{6} \cdot p_{inter},$$

where i gives the direction for the first partial move and j for the second. The step length λ_{inter} is in this case divided into the fractions along each spatial direction and can be obtained from the ΔG contour plots (Fig. 9.6; Tab. 9.4).

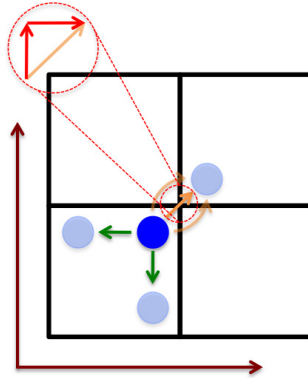


Figure 9.9: Schematic representation of the two hopping events in the IRMOF matrices. The intracell motions are illustrated by a green arrows, respectively. The intercell step is depicted in orange. The close-up (red dotted circle) describes the vector decomposition of the effective intercell transition according to the cell vectors.

The basic ideas of the derived hopping model is summarized in Figure 9.10. Based on this a Monte Carlo (MC) simulation is performed, which allows to calculate the trajectory of a single benzene molecule depending on the number of steps. Since the time for each step is given by t_α , the self-diffusion constant can be derived,

taking into account the mean square displacements of the molecule (from the MC simulation) and employing the Einstein-equation (Eq. 3.18).

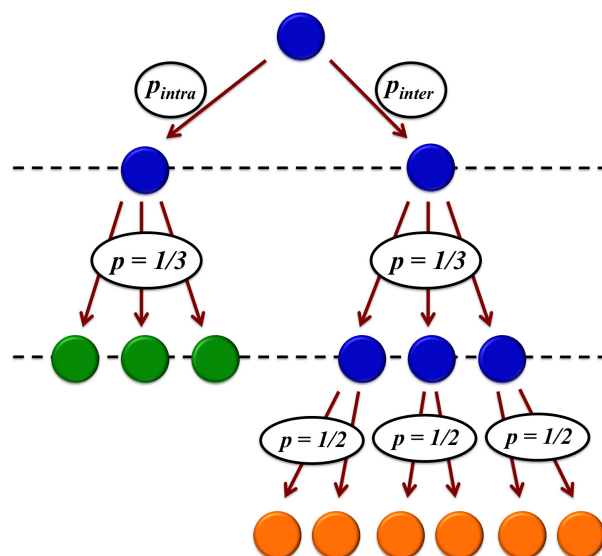


Figure 9.10: Hopping model, describing the diffusion process of a benzene molecule in the IRMOFs.

The self-diffusion constants obtained from the MD-simulations and the ones calculated based on the hopping model are in good agreement (Tab. 9.4). The small deviations are due to the approximations done within the latter⁵. In agreement with previous results, the data from the MC simulations show that the self-diffusion constant does not change significantly with increasing the linker length. To evaluate the hypothesis, that the decrease of the rate constant and the change of the linker size compensate each other in the IRMOF series, so that the self-diffusivity is unchanged, a fictitious system is considered. The system owns the free energy topology of the IRMOF-1 system, but the metric of IRMOF-10. In this case the self-diffusion coefficient rises to $1.1 \cdot 10^{-8} \text{ m}^2/\text{s}$. In contrast to this, the diffusion of benzene in a matrix with the free energy topology of IRMOF-16 and the metric of IRMOF-1 is significantly slower $1.7 \cdot 10^{-9} \text{ m}^2/\text{s}$. The results indicate the importance of both host-guest interaction, as well as metric for the guest molecule mobility.

Control of chemical reactions by diffusion

It should be kept in mind that the macroscopic observable D_{self} does not

⁵For example, just one benzene molecule is considered in the model. However, guest-guest interaction will influence the mobility. This is probably the reason for the higher D_{self} value in IRMOF-1. The effects of guest-guest interaction will be discussed later in more detail.

reflect the elementary phenomena rather gives an effective picture of the mobility. The detailed study of the diffusion mechanism, as presented, reveals an important phenomena of the systematically *soft-modification* of the host-guest systems. The elongation of the linkers can be used to separate adsorption sites by introducing a diffusion barrier. Thus the interaction between molecules adsorbed on the inner surface of the MOF is decreased. This feature can be used to control chemical reaction within the framework (Fig. 9.11).

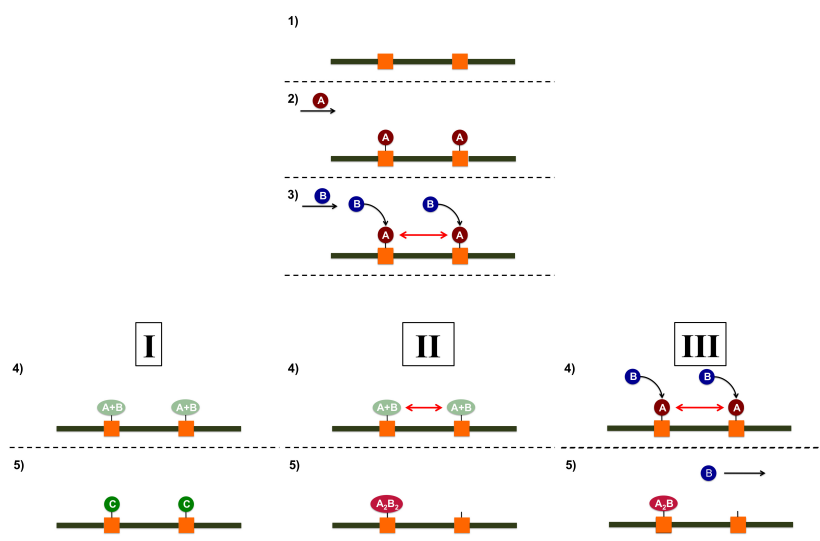


Figure 9.11: Control of reactions by varying the linker length. If the linker separating two sites is “small” the the adsorbed particle can interact with each other and rearrange. Consequently different reactions may occur. If the linker size is enlarged a diffusion barrier inhibit the mobility and the reaction is restricted to the catatlytic center as shown in I.

If the adsorption site is catalytically active such as an unsaturated metal center, the adsorbed molecules can undergo chemical reactions. In the case of small linkers between these reactive centers the adsorbed molecules can rearrange between different sites, which can cause undesirable side-reaction like dimerisation. Using large enough spacers the reactions at different centers can be decoupled from each other by diffusion barriers, which should increase the selectivity for a particular reaction. Since the tuning of the metric is in pinciple possible for porous coordination polymers, the presented results indicate the importance of these kind of soft-modifications with respect to MOF-based catalysis. However, the length of the linkers has to be tuned based on the host-guest interaction to improve rationally the performance for a particular system.

9.1.4 Influence of higher loadings on the host-guest interaction

The MOF has in the presented concept of diffusion controlled reactions two functions. Beside the catalytic property, the matrix controls due to its topology and metric the chronological and spatial arrangement of the reactive species. But the latter is just valid if the host-guest interaction is dominant and allows to guide the mobility of the adsorbates. Table 9.5 shows the diffusion coefficient of benzene in the IRMOFs at a loading of 32 molecules per unit cell. The increase of the guest molecule density within the pores promotes the mobility of benzene molecules. This can be explained by the development of the free energy topologies. In all cases the guest-guest interactions causes that the transition between the α -sites occur at lower free energy values (Fig. 9.12-9.13), which is in line with the decreases of the activation energy (IRMOF-1: 39.58 kJ/mol; IRMOF-10: 41.88 kJ/mol; IRMOF-16: 56.40 kJ/mol).

Table 9.5: Self-Diffusion coefficient D_{self} of benzene in three IRMOFs at different temperatures and a loading of 32 benzene per unit cell.

	$D_{self} [10^{-9}m^2/s]$		
temperature	200	300	400
IRMOF-1	0.44 ± 0.12	2.67 ± 0.37	7.65 ± 1.00
IRMOF-10	0.87 ± 0.23	6.62 ± 0.71	17.68 ± 1.64
IRMOF-16	0.40 ± 0.14	5.91 ± 0.55	22.84 ± 3.32

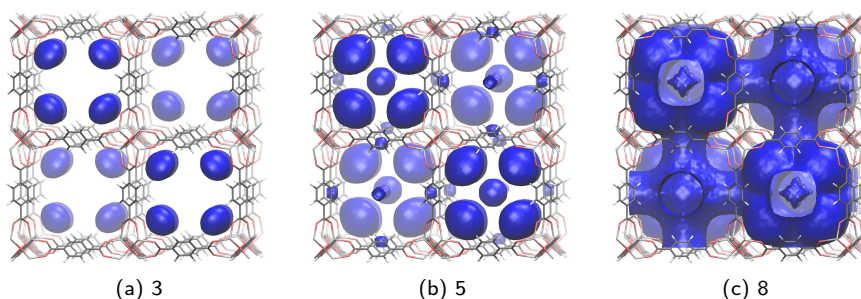


Figure 9.12: Free energy map of the benzene molecules in IRMOF-1 at a loading of 32bz/uc. Shown are the isosurfaces for the denoted ΔG -values.

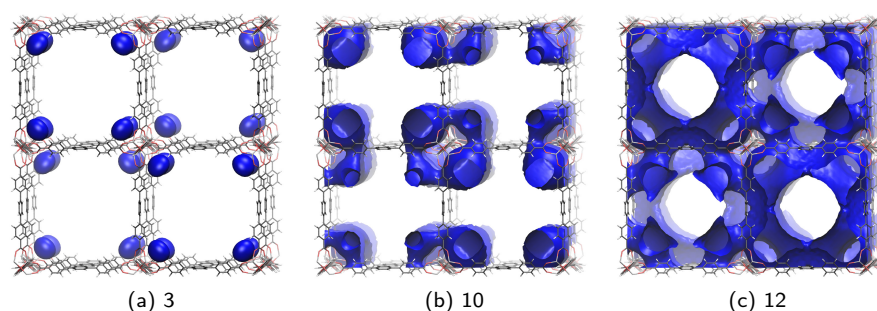


Figure 9.13: Free energy map of the benzene molecules in IRMOF-16 at a loading of 32bz/uc. Shown are the isosurfaces for the denoted ΔG -values.

A closer look at the free energy topology exhibits a differences between the three frameworks, which was already indicated at lower loading, but is more severe at higher loading. In the case of IRMOF-1 the metric of the framework favors in addition to the eight α -sites the development of a free energy minimum in the middle of the A-cell and pockets in the faces of the A-cell (Fig. 9.12). Note, that the benzene molecule located at the center of the A-cell is stabilized by other guest molecules adsorbed in the α -site. This is not the case in the larger pore system. Here, the guest-guest interaction favors the accumulation in the corners of the A-cell (Fig. 9.14).

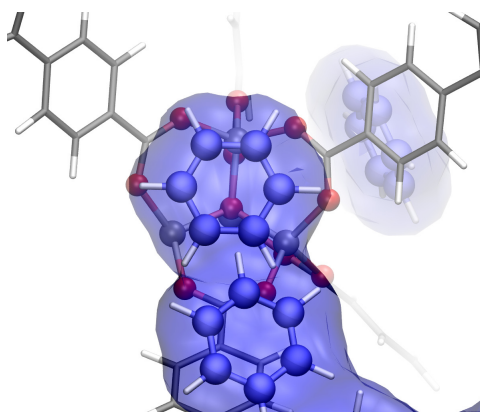


Figure 9.14: Accumulation of guest molecules in the α -site of IRMOF-10 and 16.

The interaction between the guest molecules decreases the barrier for the diffusion processes, consequently the mobility should increase. The increase of the diffusivity is in the IRMOF-10 and 16 pronounced (Tab. 9.5). Although the free energy topology of the guest molecules within the IRMOF-1 matrix is also leveled at higher loading, the mobility increases less significant. Within the scope of a hopping model, this can be explained by the fact, that with higher loading the probability that

nearby adsorption sites are blocked is raised. Therefore not every jump attempt is successful. Since the density of the benzene molecules in the elongated IRMOFs is less compared to IRMOF-1 this effect is not observed for these systems.

9.2 Isorecticular Isomers

Isorecticular Isomerism is one kind of soft-modification. The low-symmetry of the SBU and its rigid embedding within the matrix is used in this case to construct different isomeric forms of the same network topology (Fig. 9.15). This kind of variation of the framework does not modify the chemical nature rather the local structural environment within the MOF. In Chapter 6 isorecticular isomers were studied in terms of their structural and energetic properties. Here, the influence on the host-guest system is investigated. In this regard, simulations are performed for the benzene loaded regular and twisted isomer of IRMOF-1.

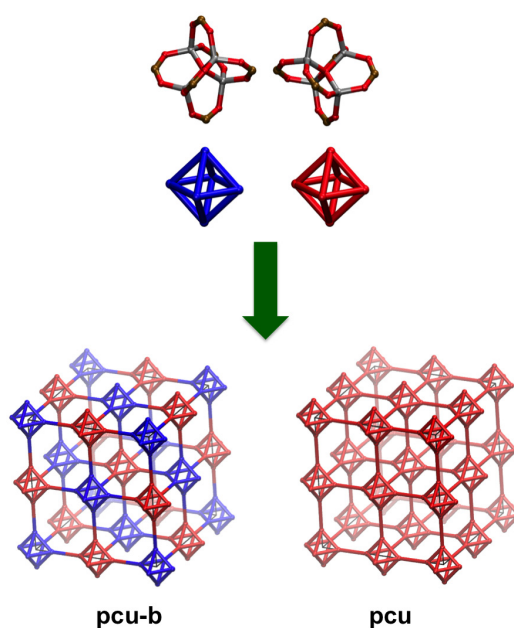


Figure 9.15: Representation of the regular and twisted isomer of IRMOF-1.

9.2.1 Structure and mobility of benzene in regular and twisted IRMOF-1

The primary adsorption sites remain above the faces of the Zn_4O -clusters (α -site) going from the regular to the twisted framework, since the chemical character of the framework is not affected by different orientation of the inorganic SBU. Nevertheless,

reveals the inspection of the spatial probability distribution of the center of mass of the benzene molecules within the two frameworks, a significant change of the known adsorption pattern of the IRMOF-1 by the soft-modification (Fig. 9.16). This can be explained by the structural features of the two isomers. The alternating arrangement of the tetrahedron within the *regular* IRMOF-1 framework force, as already mentionend before, the presence of two different cells. In the twisted MOF, this is not the case. The inorganic SBUs within the matrix are related just by a translational vector, which leads to the vanish of the two unequal cells. The only type of cell present in the twisted IRMOF-1 has four corners covered by the faces of the Zn_4O -tetrahedron and in the remaining corners the apex of the cluster points into the center of the cell. This change of the local structure is also reflected by the adsorption pattern of the benzene molecules (Fig. 9.16). In contrast to the regular framework, all cells are equally occupied in the twisted IRMOF-1 and the adsorption sites are no longer arranged in a cubic fashion rather form a tetrahedron within one pore.

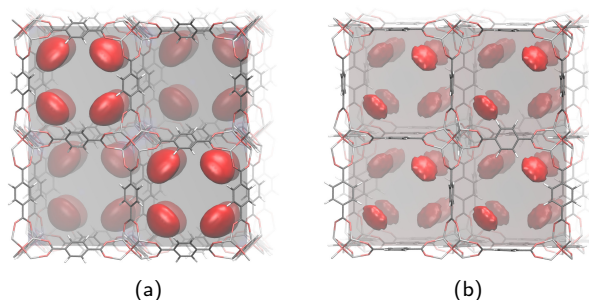


Figure 9.16: Probability distribution of the benzene molecules in (a) regular and (b) twisted IRMOF-1.

The transposition of the α -sites influences, beside the adsorption pattern of the guest molecules, their mobility. Fig. 9.17 shows the diffusion path of a single benzene molecule in the two frameworks. For the *regular* IRMOF-1 the presence of the A-cells, each with eight primary adsorption pockets, is evident along the trajectory. The retention time of a molecule within one site is larger compared to the transition between different sites. In comparison to this, the path of a benzene molecule within the twisted framework does not show well ordered sites, although the pockets over the Zn_4O -tetrahedron are maintained. The benzene molecule covers in this case a large distance in the same time compared to the regular IRMOF-1.

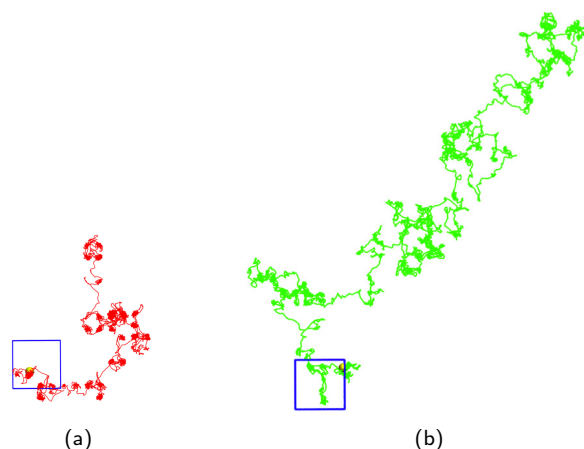


Figure 9.17: Diffusion path of a single benzene molecule within the (a) regular and (b) twisted IRMOF-1 at $T=300\text{K}$ and a trajectory length of 2.5 ns, respectively. Note, that the blue squares represent one unit cell and have almost the same size for the two frameworks. The view is along one cell vector.

Considering the self-diffusivity, as a global observable for the mobility of the guest molecules, reveals that D_{self} increases by a factor of 5 going from the regular to the twisted MOF at 300K and a loading of 10bz/uc (Tab. 9.6). The higher mobility of the guest molecules in the **pcu** framework becomes also apparent by the comparison of the self-diffusivity at different temperatures. The benzene molecules have at 200K in the twisted MOF the same mobility as the guest species in the *regular* framework at elevated temperature ($T=300\text{K}$) (Tab. 9.6). In agreement to this, the activation energy for the diffusion process in the pcu-b topology is about 20 kJ/mol higher compared to the value for the isomeric system (Tab. 9.6).

Table 9.6: Self-Diffusion coefficient D_{self} [$10^{-9}\text{m}^2/\text{s}$] of benzene in two isorecticular isomers of IRMOF-1 at different temperatures (values in brackets) and a loading of 10bz/uc. Further the corresponding activation energies for the diffusivity are given.

	$D_{self}(200\text{K})$	$D_{self}(300\text{K})$	$D_{self}(400\text{K})$	$E_A [\text{kJ/mol}]$
regular	0.14 ± 0.04	2.00 ± 0.39	7.21 ± 1.64	55.37
twisted	2.06 ± 0.71	10.04 ± 1.73	20.47 ± 4.55	32.14

To get an insight into the diffusion mechanism of the twisted framework, the spatial probability distribution of the center of mass (COM) of the guest molecules is converted into a three dimensional free energy map of the benzene molecules within the framework (Fig. 9.18). In comparison to the *regular* IRMOF-1 (Fig. 9.3), the free energy landscape of the guest molecules is smoother (Fig. 9.18). The analysis of the free energy topology alludes that the diffusion mechanism is different for the

two isorecticular isomers. The intracell diffusion of the guest molecules, within the *regular* framework is governed by an translation along an organic linker, which forms the edges of the cubic pores. Due to the tetrahedral arrangement of the α -sites in the twisted IRMOF-1, the benzene molecules have to go over the faces of the cubic pores to reach adjacent binding pocktes.

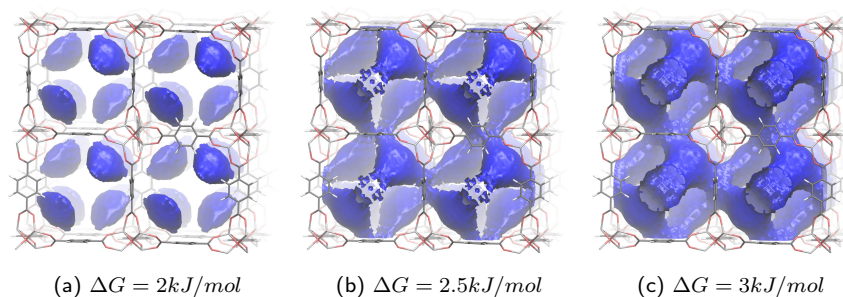


Figure 9.18: Free energy map of the benzene molecules in twisted IRMOF-1 at a loading of 10bz/uc. Schown are the isosurfaces for the denoted ΔG -values.

By integrating the probability density of the COM along one axis a contour plot of the free energy map can be calculated, which allows a more quantitative study of the diffusion mechanism.⁶ As discussed previously, the intercell diffusion in the regular IRMOF-1 implies the transition through an energetically unfavourable cell (Fig. 9.19), so that, in agreement to the observation from the diffusion path of a single benzene molecule (Fig. 9.17), the molecules remain mainly in the primary adsorption pocket and rearrange in the first instance within one cell. The intercell transition is hindered by a high free energy barrier. In the case of the twisted framework just one type of cell exists, which leads to a significant change in the diffusion mechanism (Fig. 9.19). Benzene molecules leaving one α -site just have to cross diagonally the pore opening to reach the adjacent cell, which offers again primary adsorption pockets. This kind of ordering of the α -site causes that both diffusion steps - intra- and intercell - have almost the same free energy barrier ($\Delta G \approx 3 \text{ kJ/mol}$), due to their similar transition states (faces of the cubic pores). Note, that this diffusion barrier is about the quarter of the value obtained for the intercell step in the *regular* MOF ($\Delta G \approx 11 \text{ kJ/mol}$), which is the diffusion determining step in that system. The low barriers present in the twisted IRMOF-1 leads to an almost free diffusion of the molecules within the matrix, so that the retention time in a pocket is decreased and a hopping between different sites is not observed (Fig. 9.17).

⁶Due to the symmetry of the two frameworks, this folding was done using the half (regular) or quarter (twist) of each simulation box to obtain the contour plots. The expression for the conversion of the probability density into the free energy is given in the previous chapter.

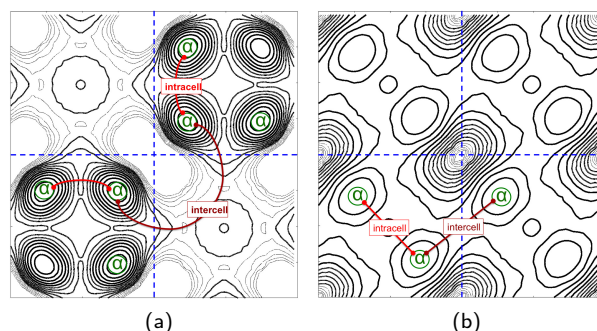


Figure 9.19: Diffusion mechanism in (a) regular and (b) twisted IRMOF-1

9.2.2 Defects in the network

Although the presented results point out the significant influence of isorecticular isomers on the adsorption and transport properties of guest molecules, previous studies on the IRMOFs pointed out that the energy difference between the twisted and regular IRMOF-1 is, with 17.9 kcal/mol per formula unit, quite high. However, other isorecticular isomers of IRMOF-1 are possible, which deviate energetically less from the parent framework. For example, to imbed one SBU of the considered unit cell in a different arrangement compared to the *regular* IRMOF-1 just 3.7 kcal/mol is needed (Isomer-1). Since the solvothermal synthesis of the IRMOFs occurs usually at elevated temperature ($T \approx 90 - 100^\circ\text{C}$) this energy amount is available during the self-assembling process of the building units. An other type of isorecticular isomers is thinkable, in which the inorganic SBUs along one plane are arranged alternating like in the *regular* IRMOF-1 and connectivity along the remaining axis is in a twisted fashion (Isomer-E). The energy difference between this isorecticular isomer and the **pcu-b** framework is with $\Delta E = 5.0 \text{ kcal/mol}$ still feasible. Nevertheless, whether these two isomeric forms of IRMOF-1 can be obtained in a pure fashion is questionable, but these structural motives could be present to some degree as “defects” within the *regular* framework.

In order to gain insight into the influence of structural defect on the mobility of the benzene molecules, MD simulations were performed for Isomer-1 and Isomer-E. Both isorecticular isomers of IRMOF-1 show an increase of the mobility compared to the regular framework ($D_{self}(\text{Isomer-1}) = 3.84 \pm 0.94 \cdot 10^{-9} \frac{\text{m}^2}{\text{s}}$; $D_{self}(\text{Isomer-E}) = 5.32 \pm 0.95 \cdot 10^{-9} \frac{\text{m}^2}{\text{s}}$). Taken the twisted framework as the system with the highest structural deviation compared to the parent structure, one can conclude that the change in the mobility correlates with the degree of defects.

9.2.3 Diffusion in twisted and regular IRMOF-7

The influence of the organic linker on the energetic of isorecticular isomers was shown in Chapter 6. For instance, decreases the energy gap between the twisted and regular framework if instead of the terephthalic acid linker a naphthalene derivative used ($\Delta E[\text{twist} - \text{regular}] = 2.0 \text{ kcal/mol}$). This decorated version of IRMOF-1 is IRMOF-7 and, as mentioned before, do experimental results allude the presence of mixtures of different isorecticular isomers. Based on this, the observations in terms of the mobility change in different isomers of IRMOF-1 gain in importance if the naphthalene system is considered..

First, the influence of the naphthalene linker itself on the diffusion of benzene is analyzed with respect to the regular IRMOF-1. The bulky organic linkers does not have an impact on the benzene self-diffusion constant at 300K compared to the terephthalic acid network (Tab. 9.7). However, the mobility of the guest species is less temperature dependent ($E_A = 48.15 \text{ kJ/mol}$; IRMOF-1: $E_A = 55.35 \text{ kJ/mol}$). In agreement to this, the free energy barriers for the diffusion process are smaller (Fig. 9.20). For instance, is the intercell transition hindered only by an energy barrier of about 8 kJ/mol (IRMOF-1: 11 kJ/mol), which would indicate an increase in the mobility of the benzene molecules. Nevertheless, the self-diffusivity is (almost) unchanged due to the interaction of the guest molecules with the bulky, aromatic groups of the framework. The phenomena is comparable with the situation at high loading in IRMOF-1 (Chapter 6), where the mobility of the benzene molecules is slowed by collision events.

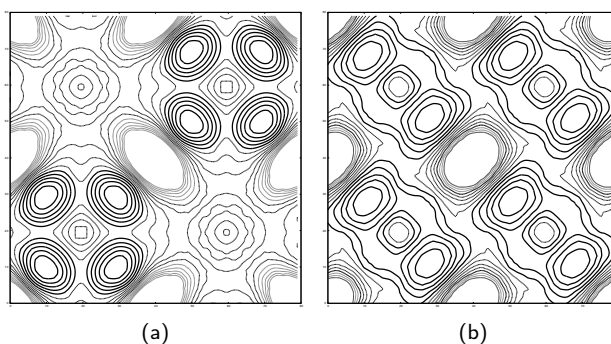


Figure 9.20: Contour plots of the free energy landscapes with isoline separations of 1 kJ/mol: (a) regular and (b) twisted IRMOF-7

Table 9.7: Self-Diffusion coefficient D_{self} [$10^{-9}m^2/s$] of benzene in two isorecticular isomers of IRMOF-7 at different temperatures (values in brackets) and a loading of 10bz/uc.

	$D_{self}(200K)$	$D_{self}(300K)$	$D_{self}(400K)$	$E_A[kJ/mol]$
regular	0.22 ± 0.12	2.25 ± 0.51	6.78 ± 1.80	48.15
twisted	0.77 ± 0.33	7.49 ± 1.49	13.08 ± 2.60	40.53

The mobility of the benzene molecules increase going from the regular framework to the twisted IRMOF-7. However, compared to the parent structure the change is distinctive. This can be explained by an analyzis of the free energy topology. Due to the steric interaction of the guest molecules and the bulky ligands, the free energy barriers increase slightly (about $1kJ/mol$) for the IRMOF-7 system.

9.3 Conclusion

In this chapter the influence of soft-modifications on host-guest interactions was studied using benzene as a probe molecule:

- The elongation of the linker was considered using the series: IRMOF-1, 10 and 16, which different just in the metric of the organic unit. By molecular dynamics simulation, it could be shown that the attractive interaction between the benzene molecules and the inner surface of the matrices induces in all cases the same primary adsorption pattern. Further the mobility of the benzene molecules is dominated by these host-guest interaction and not by steric strain effects. The self-diffusivity of benzene in the IRMOFs is almost equal for all systems and in the range of liquid benzene, which corroborates the view of MOFs as *solid solvent*. Due to the symmetry of the inorganic vertices of the cubic network, two different cell types can be distinguished, which are arranged in a checkerboard fashion. The free energy topologies of the benzene molecules reveal that the primary adsorption sites are in the corners of the A-cell (α -site). The other cell (B-cell) is significanty less populated. With increasing linker length the center and windows of the A-cell become less favoured. However, the α -sites determine in all cases the diffusion process within the pores, so that a hopping mechanism is used to describe the mobility of the guest molecules. Two hopping events can be discriminated. One is an intracell transition and one is a transition between different A-cell, which occurs via the less preferred B-cell. Using transition state theory and by analyzing the one dimensional free energy pathes of all systems, rate constants could be derived for both step, respectively. Based on this, a Monte Carlo simulation was performed, which pointed out that the diffusion within the MOF matrix is defined by the host-guest interaction and by the distance

between adsorption sites. This can be used to control chemical reactions, which take place at different sites within the framework by adjusting one of the two parameters. But at higher loading the attractive interaction between guest molecules gains in influence and the mobility increases. This is the case until the density of the guest species increases above a certain level. After a while the steric interaction of guest molecules hinder the diffusion process, so that the mobility decreases.

- For the first time, the influence of isorecticular isomerism on the interaction between guest molecules and MOF was studied. Although the framework is chemically unchanged, significant differences of the adsorption pattern are observed comparing the regular and twisted IRMOF-1 system. Due to the arrangement of the inorganic units, the twisted framework offers only one pore type, which owns four primary binding sites. As a consequence the mobility increases going from the **pcu** framework to the **pcu-b** by one order of magnitude. Based on these results, other isorecticular isomers were studied, which are energetically possible during the synthesis and can be seen as structural defects. In these cases the mobility increases compared to the parent structure, which indicates the experimental challenge to obtain systems with well defined transport properties. In addition the influence of more bulky ligands was analyzed. The exchange of the terephthalic acid by the naphthalene derivative, decreases the energy difference between the regular and twisted framework. The mobility increases in this case by a factor of 3.

Chapter 10

Conclusion

Atomistic modelling had and has a strong impact on the development of new porous materials. In particular, for the recently developed class of metal organic frameworks, very often experimental results are hard to interpret without resorting to theoretical models. Simulations allow to investigate individual processes of “*ideal*” systems, whereas under experimental conditions mostly integrated or global information of “*non-ideal*” systems can be gathered. Elucidating elementary phenomena is thus crucial in order to use the unique properties of MOFs in a rational way, which would advance the application of these compounds. In this regard two fundamental issues have to be tackled, in order to develop new functional materials based on MOFs: “*How can one obtain a designated structure and tune it on the atomistic level?*” and “*How does the molecular structure influence the host-guest interactions in a particular case?*”.

Considering the first question, MOFs allow in principle - based on their modular and hybrid assembling - to construct new structures with specific pore features. However, the range of possible elements, coordination modes and network topologies also poses a big challenge for the development of well definite synthetic strategies. Due to the diversity and complexity of these porous coordination polymers, a fundamental classification schema of the structure is indispensable for any systematic study. Therefore strategies like the topological approach have been developed to describe experimentally observed system in terms of their underlying network topology. However, further aspects have to be considered in the context of MOFs such as the molecular nature and the framework flexibility. For this reason the **reverse topological approach** was derived in this work, in which descriptors like the symmetry or the degrees of freedom of individual units of the matrix are used to evaluate the relationship between different networks. Based on this approach a hierarchy of structural complexity is derived, which allows to discriminate different structural phenomena.

The reverse topological approach, however, is not only an atomistic model to understand the individual structural phenomena, but it is rather a tool to highlight different aspect of the systems for further quantitative modelling. In this regard, molecular mechanics methods were employed to investigate individual aspect of different MOF structures in more detail. To treat structural issues of these soft materials, reliable atomistic models are need, which are able to reproduce both structural and dynamic properties. Since accurate quantum mechanical calculations are not feasible for these large porous materials, a “*bottom-up*” strategy, based on non-periodic model systems, was used throughout the work to parametrize a classical force field. The parametrization strategy focused on accuracy in reproducing the higher level of theory at the expense of transferability. This type of consistently first principles derived force fields for MOFs is unique.

Since theoretical methods allow to study even not yet synthesized structures, these kind of tools are predestined to explain experimental observations. In this regard, for the first time a detailed investigation of the molecular structure of copper paddle wheel MOFs was possible, which revealed the sterical preferences of certain topologies depending on the organic linker. In addition, even the corresponding interpenetrated systems were included into the study, so that a comprehensive picture of the intrinsic properties was obtained. The results enable the design of new MOFs with desired topologies.

How important extrinsic properties like solvent molecules and concentration might be, was shown by an analysis of the structure of another class of porous materials - covalent organic frameworks. In one case the theoretical preferred network topology does not match with the experimental finding, which indicates that other factors than steric effects can influence the obtained structure.

Furthermore the presence of isorecticular and conformational isomerism was analyzed using the example of the IRMOF family. As a results it could be conclude that the intramolecular interactions within the pores are important for the possibility to generate these kind of structural phenomena. Thus, isorecticular isomers are very likely to be present in real crystals as defects, which is an observation unnoted in current literature, yet.

In this regard the theoretical investigations reveal that the structure of MOF based materials can be tuned to some extent by using rationally the building block approach, since intrinsic effects of the system favor a certain network structure. This is definitely a partial success with respect to the initially quoted question of Richard P. Feynman. However, it was also shown that due to the molecular and soft nature of these compounds structural defects like isomerism is possible. In this regard the influence of extrinsic effects like solvation have to be taken into account in the future. Especially, since they might abolish the intrinsic preference in total

and cause other undesirable network structure.

In addition to a more sophisticated investigation of the bulk material by considering solvent effects for example, the growth mechanism of these compounds has to be studied. The tuning of the initial self-assembling process is pivotal for a control of the final structure. This aspect is closely related the question of how the conditions of the MOF surfaces are on a atomistic level. Motivated by this, the very first calculations on MOF surfaces were performed considering the molecular nature of these materials. The simulations allow to explain to some extent the preference of specific growth direction and consequently the crystal morphology.

However, as mentioned before, the understanding of the relationship between structural properties and their influence on the host-guest interaction is fundamental with respect to the development of new functional materials, since the majority of application fields of porous materials imply the presence of guest molecules within the pores. Thus, the second part of the work dealt with this issue. To allow reliable theoretical predictions the classical models were first validated based on high level quantum mechanical calculations. Then, the influence of **soft modifications** was studied in terms of adsorption and diffusion properties of guest molecules. The MD simulations allow a deep insight into the systems and help to understand macroscopic quantities like the self-diffusivity. In this context it was shown that the change of the pore metric has significant influence on the molecular level, which allows to tune different applications like catalysis or gas storage. Furthermore, as the results on the unloaded systems already indicated, are deviations from the *ideal* structure indeed possible under *real* conditions. Thus, the influence of isomerism and defects on the host-guest interaction was studied, which reveals that the quality of the material is crucial with respect to the performance of these materials. Note, that any other theoretical work performed up to now was constrained to experimentally determined framework structures. Due to the ability to predict unknown or energetically unfavourable isomeric structures via the reverse topological approach, it could for the first time be shown how large the impact of such soft modifications on for example transport properties can be.

Despite of the success of the employed theoretical strategy to describe and understand metal-organic frameworks on a molecular level, some aspects have to be mentioned, which need to be considered in the next steps to obtain a global picture of these materials. Considering the structural properties both for the bulk materials as well as the surface the effect of solvent molecules has to be elucidated more quantitatively. In this regard probably the extension of the classical model (e.g. polarization effects and reactive force field) and the inclusion of entropic effects is needed. In terms of the host-guest interactions the parameter set has to be extended to other guest molecules. A consistent schema has to be developed for

the parametrization of non-covalent interactions. Further the length and time scales of the simulations have to be increase to be able to cover all phenomena such as clustering of guest molecules.

Nevertheless the models used in this work are already well able to tackle some important issues with respect to the initial challenge by Richard P. Feynman in the case of metal organic frameworks and might be a starting point for further investigations, in which experimental and theoretical methods are employed complementary.

Chapter 11

Appendix

A1. Technical Details

All quantum mechanical calculations in Chapter 4, 6 and 7 were done using the *gaussian03* program package [94]. The TURBOMOLE 6.1 code [93] was used in case of the covalent organic frameworks. The program VMD [105] and molden [255] were used for pre- and post-processing of the outputs. For the force field calculations and the MD simulations the *tinker* program package [104] was used. Further a number of python scripts were employed, which were written by myself for the analysis of the different data.

B1. Parameter-set: Copper paddle wheel

Table 11.1: Force field parameters for the copper paddle-wheel core and carboxylate linker. Only parameters deviating from the original MM3 parameter set are given.

Bond stretch	reference dist. [Å]	force const. [mdyn/Å]	Morse pot. α [Å ⁻¹]
$Cu - Cu$	2.656	0.25	-
$Cu - O_{carb}$	1.976	1.27	2.5
$C_{carb} - O_{carb}$	1.262	9.71	-
$C_{carb} - C_{ph}$	1.503	4.445	-
$C_{ph} - C_{ph}$	1.38 ^a	6.56 ^a	-
In-plane angle bending	reference angle, [deg]	Force constant, [mdynÅ/rad ²]	
$O_{carb} - Cu - O_{carb}$	(90, 180) ^b	0.44 ^b	
$Cu - O_{carb} - C_{carb}$	118.71	0.26	
$O_{carb} - C_{carb} - O_{carb}$	126.84	1.61	
$O_{carb} - C_{carb} - C_{ph}$	117.52	0.999	
$C_{ph} - C_{ph} - C_{carb}$	115.31	0.723	
Out-of-plane bending (central-apex)	reference angle [deg]	Force constant, [mdynÅ/rad ²]	
$C_{carb} - O_{carb}$	0.0	1.313	
$C_{carb} - C_{ph}$	0.0	1.313	
Cross term ^c (stretch-stretch and stretch-bend)	stretch ₁ - bend, [mdyn/rad]	stretch ₂ -bend, [mdyn/rad]	stretch ₁ - stretch ₂ , [mdyn/Å]
$O_{carb} - C_{carb} - O_{carb}$	0.479	0.479	1.461
$O_{carb} - Cu - O_{carb}$	-	-	0.22
$Cu - O_{carb} - C_{carb}$	0.147	0.026	0.22
$O_{carb} - C_{carb} - C_{ph}$	0.5	0.4	0.6
$C_{ph} - C_{ph} - C_{ph}$	0.124	0.124	1.061
$C_{carb} - C_{ph} - C_{ph}$	0.353	0.092	0.293
Torsion	n	barrier height, [kcal/mol]	
$Cu - O_{carb} - C_{carb} - O_{carb}$	2	6.62	
$C_{ph} - C_{ph} - C_{carb} - O_{carb}$	2	1.75	
$C_{ph} - C_{ph} - C_{ph} - C_{carb}$	2	5.983 ^a	
$C_{carb} - C_{ph} - C_{ph} - H$	2	5.983 ^a	
$C_{ph} - C_{ph} - C_{ph} - C_{ph}$	2	5.983 ^a	
$C_{ph} - C_{ph} - C_{ph} - H$	2	5.385 ^a	
$H - C_{ph} - C_{ph} - H$	2	6.881 ^a	
Van der Waals term ^d	radius, Å	well depth, kcal/mol	bond length reduction factor
Cu	2.26	0.296	
O_{carb}	1.82	0.059	
C_{ph}	1.96	0.056	
C_{carb}	1.94	0.056	
H	1.62	0.020	0.923

^aThese values were adjusted by performing a SCF-MO calculation for the π -system.

^bSpecific bending potential for square planar conformation, see text.

^cThe reference distances and angles are identical to the regular bond stretch and angle bending parameters.

^dThe parameters are taken from ref. 163.

B2. a) Parameter-set: Covalent organic frameworks

B2. b) Validation of the force field

Table 11.2: Force field parameters for the Tetraphenyl-methane and -silane. Only parameters deviating from the original MM3 parameter set are given.

Bond stretch parameter		
bond type	reference distance [Å]	force constant, [mdyn/Å]
$C(sp^3) - C(sp^2)$	1.505	5.096
$C(sp^2) - C(sp^2)$	1.38 ^a	6.56 ^a
$Si - C(sp^2)$	1.262	9.71
In-plane angle bending parameter		
angle type	reference angle [deg]	force constant, [mdynÅ/rad ²]
$C(sp^2) - C(sp^3) - C(sp^2)$	100.140	1.512
$C(sp^2) - Si - C(sp^2)$	109.980	0.571
Out-of-plane angle bending parameter		
oop type: central-apex	reference angle [deg]	force constant, [mdynÅ/rad ²]
$C(sp^2) - C(sp^1)$	0.000	0.110
Combined stretch-stretch and stretch-bend cross term parameter ^c		
apex ₁ -central-apex ₂	stretch ₁ -bend, [mdyn/rad]	stretch ₁ -stretch ₂ , [mdyn/Å]
$C(sp^2) - C(sp^3) - C(sp^2)$	-0.176	0.862
Torsional parameter		
torsion type	<i>n</i>	barrier height, [kcal/mol]
$C(sp^3) - C(sp^2) - C(sp^2) - C(sp^2)$	2	4.049 ^a
$Si - C(sp^2) - C(sp^2) - C(sp^2)$	2	4.049 ^a
$C(sp^2) - C(sp^2) - C(sp^2) - C(sp^2)$	2	5.983 ^a
$C(sp^3) - C(sp^2) - C(sp^2) - H$	2	5.784 ^a
$Si - C(sp^2) - C(sp^2) - H$	2	5.784 ^a
$C(sp^2) - C(sp^2) - C(sp^2) - H$	2	6.881 ^a
$H - C(sp^2) - C(sp^2) - H$	2	5.385 ^a
$C(sp^2) - C(sp^3) - C(sp^2) - C(sp^2)$	6	0.000
$C(sp^2) - Si - C(sp^2) - C(sp^2)$	6	0.0512

^aThese values were adjusted by performing a SCF-MO calculation for the π -system.

^cThe reference distances and angles are identical to the regular bond stretch and angle bending parameters. In this case the stretch-bend parameters are equal.

Table 11.3: Force field parameters for the fragment **A**. Only parameters deviating from the original MM3 parameter set are given.

Bond stretch parameter		
bond type	reference distance [Å]	force constant [mdyn/Å]
$O - B$	1.400	4.940
$C(sp^2) - B$	1.539	4.670
In-plane angle bending parameter		
angle type	reference angle [deg]	Force constant, [mdynÅ/rad ²]
$C(sp^2) - C(sp^2) - B$	124.500	0.380
$B - O - B$	123.500	0.770
$C(sp^2) - B - O$	118.600	0.660
$O - B - O$	120.000	0.950
Out-of-plane angle bending parameter		
oop type: central-apex	reference angle [deg]	Force constant, [mdynÅ/rad ²]
$C(sp^2) - B$	0.000	0.060
$B - C(sp^2)$	0.000	1.880
$B - O$	0.000	0.850
Torsional parameter		
torsion type	n	barrier height, kcal/mol
$C(sp^2) - C(sp^2) - C(sp^2) - B$	2	6.040
$H - C(sp^2) - C(sp^2) - B$	2	5.390
$C(sp^2) - B - O - B$	2	1.440
$B - O - B - O$	2	3.940
$C(sp^2) - C(sp^2) - B - O$	2	1.760

Table 11.4: Additional Force field parameters for the fragment **B1**. Only parameters deviating from the original MM3 parameter set are given.

Bond stretch parameter		
bond type	reference distance [\AA]	force constant, [$\text{mdyn}/\text{\AA}$]
$C(sp^2) - C_{center}$	1.428	6.686
$C_{center} - C_{center}$	1.449	6.123
In-plane angle bending parameter		
angle type	reference angle, [deg]	Force constant, [$\text{mdyn}\text{\AA}/\text{rad}^2$]
$C_{center} - C_{center} - C_{center}$	126.816 / 121.700	0.505
$C_{center} - C_{center} - C(sp^2)$	123.024 / 121.700	0.940
Out-of-plane angle bending parameter		
oop type: central-apex	reference angle, [deg]	Force constant, [$\text{mdyn}\text{\AA}/\text{rad}^2$]
$C_{center} - C(sp^2)$	0.000	1.068
$C(sp^2) - C_{center}$	0.000	0.147
$C_{center} - C_{center}$	0.000	0.507
Torsional parameter		
torsion type	n	barrier height, [kcal/mol]
$C_{center} - C_{center} - C_{center} - C_{center}$	1/2/3	-1.837/8.372/-0.557
$C_{center} - C_{center} - C_{center} - C(sp^2)$	1/2/3	0.640/4.164/-1.720
$C_{center} - C_{center} - C(sp^2) - C(sp^2)$	1/2/3	-1.538/6.998/-1.894
$C(sp^2) - C_{center} - C_{center} - C(sp^2)$	1/2/3	-0.630/0.236/0.296
$C_{center} - C(sp^2) - C(sp^2) - C(sp^2)$	1/2/3	1.020/5.473/-1.348
$C_{center} - C_{center} - C(sp^2) - H$	1/2/3	0.276/4.911/0.520
$C_{center} - C(sp^2) - C(sp^2) - H$	1/2/3	2.016/5.909/1.896

Table 11.5: Additional Force field parameters for the fragment **B2**. Only parameters deviating from the original MM3 parameter set are given.

Bond stretch parameter		
bond type	reference distance, [\AA]	force constant, [$\text{mdyn}/\text{\AA}$]
$C(sp^2) - B$	1.528	4.79
$O - B$	1.389	4.94
In-plane angle bending parameter		
angle type	reference angle, [deg]	Force constant, [$\text{mdyn}\text{\AA}/\text{rad}^2$]
$C(sp^2) - O - B$	118.200	0.870
$O - B - O$	118.300	0.670
$C(sp^2) - B - O$	111.400	0.950
$C(sp^2) - C(sp^2) - B$	125.600	0.330
$C(sp^2) - C(sp^2) - O$	124.800	1.010
Out-of-plane angle bending parameter		
oop type: central-apex	reference angle, [deg]	Force constant, [$\text{mdyn}\text{\AA}/\text{rad}^2$]
$C(sp^2) - B$	0.000	0.050
$B - C(sp^2)$	0.000	0.970
$B - O$	0.000	0.990
$C(sp^2) - O$	0.000	0.540
Torsional parameter		
torsion type	n	barrier height, [kcal/mol]
$C(sp^2) - C(sp^2) - O - B$	2	0.960
$C(sp^2) - C(sp^2) - O - B$	2	3.890
$C(sp^2) - B - O - C(sp^2)$	2	1.120
$O - B - O - C(sp^2)$	2	8.570
$C(sp^2) - C(sp^2) - C(sp^2) - O$	2	0.000
$C(sp^2) - C(sp^2) - B - O$	2	1.500

Table 11.6: Additional Force field parameters for the fragment **C**. Only parameters deviating from the original MM3 parameter set are given.

Bond stretch parameter		
bond type	reference distance, [Å]	force constant, [mdyn/Å]
$B - O$	1.398	4.93
$C(sp^2) - B$	1.535	4.32
$C(sp^3) - Si$	1.706	2.92
$Si - O$	1.727	3.15
$C(sp^3) - H$	1.165	4.60

In-plane angle bending parameter		
angle type	reference angle, [deg]	Force constant, [mdynÅ/rad ²]
$O - B - O$	124.200	0.960
$C(sp^2) - C(sp^2) - B$	132.200	0.550
$C(sp^2) - B - O$	122.200	0.580
$C(sp^3) - Si - O$	110.200	0.680
$O - Si - O$	108.200	0.840
$Si - O - B$	137.200	0.300

Out-of-plane angle bending parameter		
oop type: central-apex	reference angle, [deg]	Force constant, [mdynÅ/rad ²]
$C(sp^2) - B$	0.000	0.350
$B - C(sp^2)$	0.000	1.330
$B - O$	0.000	1.180

Torsional parameter		
torsion type	n	barrier height, [kcal/mol]
$C(sp^2) - C(sp^2) - C(sp^2) - B$	2	8.850
$H - C(sp^2) - C(sp^2) - B$	2	5.400
$C(sp^2) - C(sp^2) - B - O$	2	2.140
$C(sp^2) - B - O - Si$	2	1.870
$O - B - O - Si$	2	0.700
$B - O - Si - C(sp^3)$	3	1.580
$B - O - Si - O$	3	0.240

Table 11.7: Van der Waals-parameters [163]

	radius, Å	well depth, [kcal/mol]	bond length reduction factor
$C(sp^3)$	2.040	0.027	
$C(sp^2)$	1.960	0.056	
B	2.150	0.140	
Si	2.290	0.140	
O	1.820	0.059	
H	1.620	0.020	0.923

Table 11.8: Point-Charges derived from the B3LYP/cc-pVDZ calculations

"general charges"	
atom	point-charge
$C(sp^2)$	-0.120
H	0.120
Tetraphenylmethane	
atom	point-charge
$C(sp^3)$	0.000
$C(sp^2)[-C(sp^3)]$	0.000
Tetraphenylsilane	
atom	point-charge
Si	-0.458
$C(sp^3)[-Si]$	0.1145
Borosil-Fragment	
atom	point-charge
Si	0.000
Center-Fragment	
atom	point-charge
C	0.000
Boroxin-Fragment	
atom	point-charge
O	-0.627
B	0.741
Borest-Fragment	
atom	point-charge
O	-0.358
B	0.449
$C[-O]$	0.195
$C[-B]$	-0.123

Table 11.9: Comparison of the force field results with the ab-initio data (B3PLYP/cc-pVDZ) for the non-periodic Fragments

mean deviation of the geometry in %		
	bond	angle
A	0.73	0.20
B1	1.11	0.63
B2	0.95	0.49
C	1.48	0.53
D[C]	0.88	0.28
D[Si]	0.87	0.42

Table 11.10: Normal modes in [cm^{-1}] below $400\text{ }cm^{-1}$ of the model system **C-Bu**

B3-LYP/cc-pVDZ	Force Field	deviation	overlap	mode degeneracy
14	13	-1	0.99	2
18	27	+9	0.83	1
38	28	-10	0.97	1
45	35	-10	0.84	1
32	38	+6	0.99	2
40	43	+3	0.91	2
55	57	+2	1.00	1
61	59	-2	0.97	1
65	74	+9	0.99	2
83	111	+28	0.99	1

Bibliography

- [1] Cronstedt, A. F. *Akad. Handl. Stockholm* **1756**, 18, 120.
- [2] Barrer, R. M. *J. Chem. Soc.* **1948**, 127.
- [3] Miton, R. M. *ACS Symposium Series (Zeolite Synth.)* **1989**, 398, 1.
- [4] Flanigen, E.; Bennett, J.; Grose, R.; Cohen, J.; Patton, R.; Kirchner, R.; Smith, J. *Nature* **1978**, 271, 512.
- [5] Bu, X.; Feng, P. *The Chemistry of Nanostructural Materials*; World Scientific, 2003; pp 1–37.
- [6] Stuart, L. J. *Chem. Soc. Review* **2003**, 32, 276.
- [7] Kresge, C. T.; Leonowicz, M. E.; Roth, W. J.; Vartuli, J. C.; Beck, J. S. *Nature* **1992**, 359, 710.
- [8] Bailar, J. C. *Jr. Prep. Inorg. React.* **1964**, 1.
- [9] Battern, R.; Suzanne, M.; Turner, D. *Coordination Polymers Design, Analysis and Application*; RCS Publishing, 2009.
- [10] Powell, H. M. *Nature* **1949**, 163, 566.
- [11] Schaeffer, W. D.; Dorsey, W. S.; Skinner, D. A.; Christian, C. J. *Am. Chem. Soc.* **1957**, 79, 5870.
- [12] Hofmann, K. Z. *anorg. Chem.* **1897**, 15, 204.
- [13] Soldatov, D. V.; Enright, G. D.; Ripmeester, J. A. *Cryst. Growth Des.* **2004**, 4, 1185.
- [14] Andreotti, G.; Bocelli, G.; Sgarabotto, P. *Cryst. Struct. Commun.* **1972**, 1, 51.
- [15] Robson, R. *Dalton Trans.* **2008**, 5113.
- [16] Hoskins, B.; Robson, R. *J. Am. Chem. Soc.* **1990**, 112, 1546.

- [17] Hoskins, B.; Robson, R. *J. Am. Chem. Soc.* **1989**, *111*, 5962.
- [18] Yaghi, O.; Li, G.; Li, H. *Nature* **1995**, *378*, 703.
- [19] Yaghi, O. M.; Davis, C. E.; Li, G.; Li, H. *J. Am. Chem. Soc.* **1997**, *119*, 2861.
- [20] Mitsuru, K.; Tomomichi, Y.; Hiroyuki, M.; Susumu, K.; Kenji, S. *Angew. Chem. Int. Ed. Engl.* **1997**, *36*, 1725.
- [21] Li, H.; Eddaoudi, M.; O'Keeffe, M.; Yaghi, O. *Nature* **1999**, *402*, 276.
- [22] Cavka, J.; Jakobsen, S.; Olsbye, U.; Guillou, N.; Lamberti, C.; Bordiga, S.; Lillerud, K. *J. Am. Chem. Soc.* **2008**, *130*, 13850.
- [23] Ferey, G. *Chem. Mater.* **2001**, *13*, 3084.
- [24] Park, K.; Nim, Z.; Côté, A.; Choi, J.; Huang, R.; Uribe-Romo, F.; Chae, H.; O'Keeffe, M.; Yaghi, O. *PNAS* **2006**, *103*, 10186.
- [25] Loiseau, T.; Serre, C.; Huguenard, C.; Fink, G.; Taulelle, F.; Henry, M.; Bataille, T.; Ferey, G. *Chem. Eur. J.* **2004**, *10*, 1373.
- [26] Chen, B.; Liang, C.; Yang, J.; Contreras, D. S.; Clancy, Y. L.; Lobkovsky, E. B.; Yaghi, O. M.; Dai, S. *Angew. Chem., Int. Ed.* **2006**, *45*, 1390.
- [27] Kitagawa, S.; Kitaura, R.; Noro, S. *Angew. Chem., Int. Ed.* **2004**, *43*, 2334.
- [28] Horike, S.; Shimomura, S.; Kitagawa, S. *Nat. Chem.* **2009**, *1*, 695.
- [29] Suib, S. *Annu. Rev. Mater. Sci.* **1996**, *26*, 135.
- [30] Ferey, G. *Chem. Soc. Rev.* **2008**, *37*, 191.
- [31] El-Kaderi, H. M.; Hunt, J. R.; Mendoza-Cortes, J. L.; Cote, A. P.; Taylor, R. E.; O'Keeffe, M.; Yaghi, O. M. *Science* **2007**, *316*, 268.
- [32] <http://www.basf.com/group/pressemitteilungen/P-10-428>.
- [33] <http://www.macademia-project.eu/>.
- [34] Vriezema, D. M.; Comellas Aragonès, M.; Elemans, J. A. A. W.; Cornelissen, J. J. L. M.; Rowan, A. E.; Nolte, R. J. M. *Chem. Rev.* **2005**, *105*, 1445.
- [35] O'Keeffe, M. *Chem. Soc. Rev.* **2009**, *38*, 1215.
- [36] Murray, L.; Dinca, M.; Long, J. *Chem. Soc. Rev.* **2009**, *38*, 1294.
- [37] Li, J.-R.; Kuppler, R. J.; Zhou, H. *Chem. Soc. Rev.* **2009**, *38*, 1477.

- [38] Han, S. S.; Mendoza-Cortes, J. L.; Goddard, W. A. *Chem. Soc. Rev.* **2009**, *38*, 1460.
- [39] Moon, H. R.; Kobayashi, N.; Suh, M. P. *Inorg. Chem.* **2006**, *45*, 8672.
- [40] Bae, Y.-S.; Farha, O. K.; Spokoyny, A. M.; Mirkin, C. A.; Hupp, J. T.; Snurr, R. Q. *Chem. Commun.* **2008**, 4135.
- [41] Chen, B.; Ockwig, N. W.; Millward, A. R.; Contreras, D. S.; Yaghi, O. M. *Angew. Chem., Int. Ed.* **2005**, *44*, 4745.
- [42] Dinca, M.; Dailly, A.; Liu, Y.; Brown, C. M.; Neumann, D. A.; Long, J. R. *J. Am. Chem. Soc.* **2006**, *128*, 16876.
- [43] Mavrandonakis, A.; Tylanakis, E.; Stubos, A. K.; Froudakis, G. E. *J. Phys. Chem. C* **2008**, *112*, 7290.
- [44] Han, S. S.; Goddard, W. A. *J. Am. Chem. Soc.* **2007**, *129*, 8422.
- [45] Mulfort, K. L.; Hupp, J. T. *J. Am. Chem. Soc.* **2007**, *129*, 9604.
- [46] Müller, M.; Devaux, A.; Yang, C.-H.; De Cola, L.; Fischer, R. A. *Photochem. Photobiol. Sci.* **2010**, *9*, 853.
- [47] Chae, H.; Siberio-Perez, D.; Kim, J.; Go, Y.-B.; Eddaoudi, M.; Matzger, A.; O'Keeffe, M.; Yaghi, O. *Nature* **2004**, *427*, 523.
- [48] McKinlay, A.; Morris, R.; Horcajada, P.; Férey, G.; Gref, R.; Couvreur, P.; Serre, C. *Angew. Chem.* **2010**, *49*, 6260.
- [49] Horcajada, P. et al. *Nat. Mater.* **2010**, *9*, 172.
- [50] Cychoz, K. A.; Wong-Foy, A. G.; Matzger, A. J. *J. Am. Chem. Soc.* **2008**, *130*, 6938.
- [51] Alaerts, L.; Maes, M.; Jacobs, P. A.; Denayer, J. F. M.; De Vos, D. E. *Phys. Chem. Chem. Phys.* **2008**, *10*, 2979.
- [52] Suslick, K. S.; Bhyrappa, P.; Chou, J.-H.; Kosal, M. E.; Nakagaki, S.; Smithenry, D. W.; Wilson, S. R. *Acc. Chem. Res.* **2005**, *38*, 283.
- [53] Wang, Q. M.; Shen, D.; Bülow, M.; Lau, M. L.; Deng, S.; Fitch, F. R.; Lemcoff, N. O.; Semanscin, J. *Micropor. Mesopor. Mater.* **2002**, *55*, 217.
- [54] Krungleviciute, V.; Lask, K.; Migone, A. D.; Lee, J.-Y.; Li, J. *AIChE J.* **2008**, *54*, 918.
- [55] Bastin, L.; Barcia, P. S.; Hurtado, E. J.; Silva, J. A. C.; Rodrigues, A. E.; Chen, B. *J. Phys. Chem. C* **2008**, *112*, 1575.

- [56] Guo, H.; Zhu, G.; Hewitt, I. J.; Qiu, S. *J. Am. Chem. Soc.* **2009**, *131*, 1646.
- [57] Keskin, S.; Sholl, D. S. *J. Phys. Chem. C* **2007**, *111*, 14055.
- [58] Car, A.; Stropnik, C.; Peinemann, K.-V. *Desalination* **2006**, *200*, 424.
- [59] Huang, A.; Bux, H.; Steinbach, F.; Caro, J. *Angew. Chem.* **2010**, *122*, 5078.
- [60] Castillo, J. M.; Vlugt, T. J. H.; Calero, S. *J. Phys. Chem. C* **2009**, *113*, 20869.
- [61] Alaerts, L.; Kirschhock, C.; Maes, M.; van der Veen, M.; Finsy, V.; Depla, A.; Martens, J.; Baron, G.; Jacobs, P.; Denayer, J.; de Vos, D. *Angew. Chem., Int. Ed.* **2007**, *46*, 4293.
- [62] Ahmad, R.; Wong-Foy, A. G.; Matzger, A. J. *Langmuir* **2009**, *25*, 11977.
- [63] Wang, Z.; Cohen, S. M. *Chem. Soc. Rev.* **2009**, *38*, 1315.
- [64] Tanabe, K. K.; Wang, Z.; Cohen, S. M. *J. Am. Chem. Soc.* **2008**, *130*, 8508.
- [65] Lee, J.; Farha, O. K.; Roberts, J.; Scheidt, K. A.; Nguyen, S. T.; Hupp, J. T. *Chem. Soc. Rev.* **2009**, *38*, 1450.
- [66] Cho, S.-H.; Ma, B.; Nguyen, S. T.; Hupp, J. T.; Albrecht-Schmitt, T. E. *Chem. Commun.* **2006**, 2563.
- [67] Hermes, S.; Schröter, M.-K.; Schmid, R.; Khodeir, L.; Muhler, M.; Tissler, A.; Fischer, R. W.; Fischer, R. A. *Angew. Chem., Int. Ed.* **2005**, *44*, 6237.
- [68] Müller, M.; Hermes, S.; Kahler, K.; van den Berg, M. W. E.; Muhler, M.; Fischer, R. A. *Chem. Mater.* **2008**, *20*, 4576.
- [69] Meilikhov, M.; Yussenko, K.; Esken, D.; Turner, S.; Van Tendeloo, G.; Fischer, R. A. *Eur. J. Inorg. Chem.* **2010**, *2010*, 3701.
- [70] Hermes, S.; Schroder, F.; Amirjalayer, S.; Schmid, R.; Fischer, R. A. *J. Mater. Chem.* **2006**, *16*, 2464.
- [71] Alkordi, M. H.; Liu, Y.; Larsen, R. W.; Eubank, J. F.; Eddaoudi, M. *J. Am. Chem. Soc.* **2008**, *130*, 12639.
- [72] Serre, C.; Millange, F.; Thouvenot, C.; Nogues, M.; Marsolier, G.; Louer, D.; Férey, G. *J. Am. Chem. Soc.* **2002**, *124*, 13519.
- [73] Serre, C.; Mellot-Draznieks, C.; Surblé, S.; Audebrand, N.; Filinchuk, Y.; Férey, G. *Science* **2007**, *315*, 1828.

- [74] Uemura, T.; Hiramatsu, D.; Kubota, Y.; Takata, M.; Kitagawa, S. *Angew. Chem., Int. Ed.* **2007**, *46*, 4987.
- [75] Winston, E. B.; Lowell, P. J.; Vacek, J.; Chocholousova, J.; Michl, J.; Price, J. C. *Phys. Chem. Chem. Phys.* **2008**, *10*, 5188.
- [76] Zhang, J.-P.; Chen, X.-M. *J. Am. Chem. Soc.* **2008**, *130*, 6010.
- [77] Gould, S. L.; Tranchemontagne, D.; Yaghi, O. M.; Garcia-Garibay, M. A. *J. Am. Chem. Soc.* **2008**, *130*, 3246.
- [78] Horike, S.; Matsuda, R.; Tanaka, D.; Matsubara, S.; Mizuno, M.; Endo, K.; Kitagawa, S. *Angew. Chem.* **2006**, *118*, 7384.
- [79] Zacher, D.; Shekhah, O.; Woll, C.; Fischer, R. A. *Chem. Soc. Rev.* **2009**, *38*, 1418.
- [80] Allendorf, M. D.; Houk, R. J. T.; Andruszkiewicz, L.; Talin, A. A.; Pikarsky, J.; Choudhury, A.; Gall, K. A.; Hesketh, P. J. *J. Am. Chem. Soc.* **2008**, *130*, 14404.
- [81] Brunauer, S.; Emmett, P. H.; Teller, E. *J. Am. Chem. Soc.* **1938**, *60*, 309.
- [82] Praprotnik, M.; Site, L. D.; Kremer, K. *Annu. Rev. Phys. Chem.* **2008**, *59*, 545.
- [83] Sutmann, G. *Classical Molecular Dynamics*; John von Neuman Institute for Computing, Jülich, NIC Series, 2002; Vol. 10, p 211.
- [84] Szabo, A.; Szabo, J.; Ostlund, N. *Modern Quantum Chemistry: Introduction to Advanced Electronic Structure Theory*, 3rd ed.; Dover Publ Inc, 2000.
- [85] Moller, C.; Plesset, M. S. *Phys. Rev.* **1934**, *46*, 618.
- [86] Grimme, S. *J. Chem. Phys.* **2003**, *118*, 9095.
- [87] Jensen, F. *Introduction to Computational Chemistry*; Wiley & Sons, 1998.
- [88] Koch, W.; Holthause, M. *A Chemist's Guide to Density Functional Theorey*; Wiley-V C H, 2000.
- [89] Becke, A. D. *Phys. Rev. A* **1988**, *38*, 3098.
- [90] Vosko, S.; Wilk, L.; Nusair, M. *Can. J. Phys./Rev. can. phys.* **1980**, *58*, 1200.
- [91] Stephens, P. J.; Devlin, F. J.; Chabalowski, C. F.; Frisch, M. J. *The Journal of Physical Chemistry* **1994**, *98*, 11623.
- [92] Lee, C.; Yang, W.; Parr, R. G. *Phys. Rev. B* **1988**, *37*, 785.

- [93] *TURBOMOLE V6.1 2009, a development of University of Karlsruhe and Forschungszentrum Karlsruhe GmbH, 1989-2007, TURBOMOLE GmbH, since 2007; available from*
<http://www.turbomole.com>.
- [94] Frisch, M. J.; Trucks, G. W.; Schlegel, H. B.; Scuseria, G. E.; Robb, M. A.; Cheeseman, J. R.; Montgomery, J. A. Jr.; Vreven, T.; Kudin, K. N.; Burant, J. C.; Millam, J. M.; Iyengar, S. S.; Tomasi, J.; Barone, V.; Mennucci, B.; Cossi, M.; Scalmani, G.; Rega, N.; Petersson, G. A.; Nakatsuji, H.; Hada, M.; Ehara, M.; Toyota, K.; Fukuda, R.; Hasegawa, J.; Ishida, M.; Nakajima, T.; Honda, Y.; Kitao, O.; Nakai, H.; Klene, M.; Li, X.; Knox, J. E.; Hratchian, H. P.; Cross, J. B.; Adamo, C.; Jaramillo, J.; Gomperts, R.; Stratmann, R. E.; Yazyev, O.; Austin, A. J.; Cammi, R.; Pomelli, C.; Ochterski, J. W.; Ayala, P. Y.; Morokuma, K.; Voth, G. A.; Salvador, P.; Dannenberg, J. J.; Zakrzewski, V. G.; Dapprich, S.; Daniels, A. D.; Strain, M. C.; Farkas, O.; Malick, D. K.; Rabuck, A. D.; Raghavachari, K.; Foresman, J. B.; Ortiz, J. V.; Cui, Q.; Baboul, A. G.; Clifford, S.; Cioslowski, J.; Stefanov, B. B.; Liu, G.; Liashenko, A.; Piskorz, P.; Komaromi, I.; Martin, R. L.; Fox, D. J.; Keith, T.; Al-Laham, M. A.; Peng, C. Y.; Nanayakkara, A.; Challacombe, M.; Gill, P. M. W.; Johnson, B.; Chen, W.; Wong, M. W.; Gonzalez, C.; Pople, J. A. *Gaussian 03, Revision B.04*; Gaussian, Inc.: Pittsburgh PA, 2003.
- [95] Grimme, S. *J. Chem. Phys.* **2006**, *124*, 034108.
- [96] Allinger, N. L.; Yuh, Y. H.; Lii, J.-H. *J. Am. Chem. Soc.* **1989**, *111*, 8551.
- [97] Essmann, U.; Perera, L.; Berkowitz, M. L.; Darden, T.; Lee, H.; Pedersen, L. G. *J. Chem. Phys.* **1995**, *103*, 8577.
- [98] Tafipolsky, M.; Schmid, R. *J. Phys. Chem. B* **2009**, *113*, 1341.
- [99] Maple, J. R.; Dinur, U.; Hagler, A. T. *Proc. Natl. Acad. Sci. U. S. A.* **1988**, *85*, 5350.
- [100] Goldberg, D. E. *Genetic Algorithms in Search, Optimization, and Machine Learning*; Addison-Wesley, 1989.
- [101] Sipachev, V. *J. Mol. Struct.-THEOCHEM* **1985**, *121*, 143.
- [102] Wilson, E. B.; Decius, J. C.; Cross, P. C. *Molecular Vibrations - The Theory of Infrared and Raman Vibrational Spectra*; Dover, NY, 1980.
- [103] Beeman, D. *J. Comput. Phys.* **1976**, *20*, 130.

- [104] Tinker software tools for molecular design. J. W. Ponder, P. Ren, R. V. Pappu, R. K. Hart, M. E. Hodgson, D. P. Cistola, C. E. Kundrot and F. M. Richards, Washington University School of Medicine, version 4.2, June 2004, 2004, at <http://dasher.wustl.edu/tinker/>.
- [105] Humphrey, W.; Dalke, A.; Schulten, K. *J. Mol. Graph. Model.* **1996**, *14*, 33.
- [106] Lewis, G. N. *J. Am. Chem. Soc.* **1916**, *38*, 762.
- [107] Gillespie, R. J.; Nyholm, R. S. *Q. Rev. Chem. Soc.* **1957**, *11*, 339–380.
- [108] Ramachandran, G.; Ramakrishnan, C.; Sasisekharan, V. *J. Mol. Biol.* **1963**, *7*, 95.
- [109] Ho, B.; Brasseur, R. *BMC Structural Biology* **2005**, *5*, 14.
- [110] Wells, A. *Further Studies of Three-Dimensional Nets*; Polycrystal Book Service, 1979; Vol. 9.
- [111] Wells, A. *Structural Inorganic Chemistry*; Oxford University Press, 1984.
- [112] Braga, D.; Grepioni, F. *Making Crystals by Design: Methods, Techniques and Applications*; Wiley-V C H, 2007.
- [113] Hill, R. J.; Long, D.-L.; Champness, N. R.; Hubberstey, P.; Schröder, M. *Acc. Chem. Res.* **2005**, *38*, 335.
- [114] Delgado-Friedrichs, O.; O'Keeffe, M.; Yaghi, O. M. *Phys. Chem. Chem. Phys.* **2007**, *9*, 1035.
- [115] Thomas, J.; Klinowski, J. *Angew. Chem.* **2007**, *119*, 7294.
- [116] Ockwig, N. W.; Delgado-Friedrichs, O.; O'Keeffe, M.; Yaghi, O. M. *Acc. Chem. Res.* **2005**, *38*, 176.
- [117] McCrone, W. *Polymorphism in Physics and Chemistry of the Organic Solid-State*; Interscience: New York, 1965.
- [118] Caskey, S. R.; Wong-Foy, A. G.; Matzger, A. J. *Inorg. Chem.* **2008**, *47*, 7751.
- [119] Hennigar, T. L.; MacQuarrie, D. C.; Losier, P.; Rogers, R. D.; Zaworotko, M. J. *Angew. Chem. Int. Ed. Engl.* **1997**, *36*, 972.
- [120] Moulton, B.; Zaworotko, M. J. *Chem. Rev.* **2001**, *101*, 1629.
- [121] Schröder, M.; Champness, N. R. *Encyclopedia of Supramolecular Chemistry* **2004**, *1*, 1420.

- [122] Blake, A.; Brooks, N. R.; Champness, N. R.; Crew, M.; Deveson, A.; Fenske, D.; Gregory, D. H.; Hanton, L. R.; Hubberstey, P.; Schröder, M. *Chem. Commun.* **2001**, 1432.
- [123] Barthelet, K.; Marrot, J.; Riou, D.; Ferey, G. *Angew. Chem., Int. Ed.* **2002**, *41*, 281.
- [124] Sun, D.; Ma, S.; Simmons, J. M.; Li, J.-R.; Yuan, D.; Zhou, H.-C. *Chem. Commun.* **2010**, *46*, 1329.
- [125] Schnobrich, J.; Lebel, O.; Cychosz, K.; Dailly, A.; Wong-Foy, A.; Matzger, A. *J. Am. Chem. Soc.* **2010**, *132*, 13941.
- [126] Chui, S. S. Y.; Lo, S. M. F.; Charmant, J. P. H.; Orpen, A. G.; Williams, I. D. *Science* **1999**, *283*, 1148.
- [127] Delgado-Friedrichs, O.; O'Keeffe, M.; Yaghi, O. M. *Acta Cryst. A* **2006**, *62*, 350.
- [128] Lin, X.; Telepeni, I.; Blake, A. J.; Dailly, A.; Brown, C. M.; Simmons, J. M.; Zoppi, M.; Walker, G. S.; Thomas, K. M.; Mays, T. J.; Hubberstey, P.; Champness, N. R.; Schroeder, M. *J. Am. Chem. Soc.* **2009**, *131*, 2159.
- [129] Ma, L.; Lin, W. *J. Am. Chem. Soc.* **2008**, *130*, 13834.
- [130] Horike, S.; Dinca, M.; Tamaki, K.; Long, J. *J. Am. Chem. Soc.* **2008**, *130*, 5854.
- [131] Collins, D.; Zhou, H.-C. *J. Mater. Chem.* **2007**, *17*, 3154.
- [132] Vagin, S. I.; Ott, A. K.; Rieger, B. *Chem. Ing. Tech.* **2007**, *79*, 767.
- [133] Vishnyakov, A.; Ravikovitch, P. I.; Neimark, A. V.; Bulow, M.; Wang, Q. M. *Nano Lett.* **2003**, *3*, 713.
- [134] Skoulidas, A. I. *J. Am. Chem. Soc.* **2004**, *126*, 1356.
- [135] Liu, B.; Smit, B. *Langmuir* **2009**, *25*, 5918.
- [136] Liu, J. C.; Rankin, R. B.; Johnson, J. K. *Mol. Simul.* **2009**, *35*, 60.
- [137] Yazaydin, A. O.; Benin, A. I.; Faheem, S. A.; Jakubczak, P.; Low, J. J.; Willis, R. R.; Snurr, R. Q. *Chem. Mater.* **2009**, *21*, 1425.
- [138] Babarao, R.; Jiang, J. W.; Sandler, S. I. *Langmuir* **2009**, *25*, 5239.
- [139] Castillo, J. M.; Vlugt, T. J. H.; Calero, S. *J. Phys. Chem. C* **2008**, *112*, 15934.

- [140] Chmelik, C.; Karger, J.; Wiebcke, M.; Caro, J.; van Baten, J. M.; Krishna, R. *Micropor. Mesopor. Mater.* **2009**, *117*, 22.
- [141] Garcia-Perez, E.; Gascon, J.; Morales-Florez, V.; Castillo, J. M.; Kapteijn, F.; Calero, S. *Langmuir* **2009**, *25*, 1725.
- [142] Yang, Q.-Y.; Zhong, C.-L. *J. Phys. Chem. B* **2006**, *110*, 17776.
- [143] Cotton, F. A.; Murillo, C. A.; Walton, R. A. *Multiple bonds between metal atoms*, 3rd ed.; Springer Science, New York, 2005.
- [144] Cotton, F. A.; Feng, X. J. *J. Am. Chem. Soc.* **1998**, *120*, 3387.
- [145] Melnik, M.; Kabesova, M.; Koman, M.; Macaskova, L.; Garaj, J.; Holloway, C. E.; Valent, A. *J. Coord. Chem.* **1998**, *45*, 147.
- [146] Bleaney, B.; Bowers, K. D. *Proc. R. Soc. London, Ser. A* **1952**, *214*, 451.
- [147] Van Niekerk, J. B.; Schoening, F. R. L. *Acta Crystallogr.* **1953**, *6*, 227.
- [148] Rivero, P.; Moreira, I. d. P. R.; Illas, F.; Scuseria, G. E. *J. Chem. Phys.* **2008**, *129*, 184110.
- [149] Rodriguez-Forteza, A.; Alemany, P.; Alvarez, S.; Ruiz, E. *Chem. Eur. J.* **2001**, *7*, 627.
- [150] Ukai, T.; Nakata, K.; Yamanaka, S.; Takada, T.; Yamaguchi, K. *Mol. Phys.* **2007**, *105*, 2667.
- [151] Ali, M. E.; Datta, S. N. *THEOCHEM* **2006**, *775*, 19.
- [152] Noodleman, L. *J. Chem. Phys.* **1981**, *74*, 5737.
- [153] Noodleman, L.; Case, D. A. *Adv. Inorg. Chem.* **1992**, *38*, 423.
- [154] Elmali, A. *Turk. J. Phys.* **2000**, *24*, 667.
- [155] Wilson, A. K.; Woon, D. E.; Peterson, K. A.; Dunning, T. H. *J. Chem. Phys.* **1999**, *110*, 7667.
- [156] Wilson, A. K.; Woon, D. E.; Peterson, K. A.; Dunning, T. H. *J. Chem. Phys.* **1999**, *110*, 7667.
- [157] Figgen, D.; Rauhut, G.; Dolg, M.; Stoll, H. *Chem. Phys.* **2005**, *311*, 227.
- [158] Brown, G. M.; Chidambaram, R. *Acta Cryst. B* **1973**, *29*, 2393.
- [159] Prestipino, C.; Regli, L.; Vitillo, J. G.; Bonino, F.; Damin, A.; Lamberti, C.; Zecchina, A.; Solari, P. L.; Kongshaug, K. O.; Bordiga, S. *Chem. Mater.* **2006**, *18*, 1337.

- [160] Wu, Y.; Kobayashi, A.; Halder, G. J.; Peterson, V. K.; Chapman, K. W.; Lock, N.; Southon, P. D.; Kepert, C. J. *Angew. Chem. Int. Ed.* **2008**, *47*, 8929.
- [161] Besler, B. H.; Merz, K. M.; Kollman, P. A. *J. Comput. Chem.* **1990**, *11*, 431.
- [162] Tafipolsky, M.; Amirjalayer, S.; Schmid, R. *Micropor. Mesopor. Mater.* **2010**, *129*, 304.
- [163] Allinger, N. L.; Zhou, X. F.; Bergsma, J. *THEOCHEM* **1994**, *118*, 69.
- [164] Tafipolsky, M.; Schmid, R. *J. Chem. Theory Comput.* **2009**, *5*, 2822.
- [165] Piquemal, J.-P.; Gresh, N.; Giessner-Prettre, C. *J. Phys. Chem. A* **2003**, *107*, 10353–10359.
- [166] Allured, V. S.; Kelly, C. M.; Landis, C. R. *J. Am. Chem. Soc.* **1991**, *113*, 1.
- [167] Rappe, A. K.; Bormann-Rochotte, L. M.; Wiser, D. C.; Hart, J. R.; Pietsch, M. A.; Casewit, C. J.; Skiff, W. M. *Mol. Phys.* **2007**, *105*, 301.
- [168] Allinger, N. L.; Li, F.; Yan, L. Q.; Tai, J. C. *J. Comput. Chem.* **1990**, *11*, 868.
- [169] Peterson, V. K.; Liu, Y.; Brown, C. M.; Kepert, C. J. *J. Am. Chem. Soc.* **2006**, *128*, 15578.
- [170] Dubbeldam, D.; Walton, K. S.; Ellis, D. E.; Snurr, R. Q. *Angew. Chem. Int. Edit.* **2007**, *46*, 4496.
- [171] Chapman, K. W.; Halder, G. J.; Chupas, P. J. *J. Am. Chem. Soc.* **2008**, *130*, 10524.
- [172] Bahr, D. F.; Reid, J. A.; Mook, W. M.; Bauer, C. A.; Stumpf, R.; Skulan, A. J.; Moody, N. R.; Simmons, B. A.; Shindel, M. M.; Allendorf, M. D. *Phys. Rev. B* **2007**, *76*, 184106.
- [173] O'Keeffe, M.; Peskov, M. A.; Ramsden, S. J.; Yaghi, O. M. *Acc. Chem. Res.* **2008**, *41*, 1782.
- [174] Eddaoudi, M.; Kim, J.; Rosi, N.; Vodak, D.; Wachter, J.; O'Keeffe, M.; Yaghi, O. M. *Science* **2002**, *295*, 469.
- [175] Chen, B.; Eddaoudi, M.; Hyde, S. T.; O'Keeffe, M.; Yaghi, O. M. *Science* **2001**, *291*, 1021.
- [176] Amirjalayer, S.; Schmid, R. *J. Phys. Chem. C* **2008**, *112*, 14980.

- [177] Li, Z.; Lazaridis, T. *Phys. Chem. Chem. Phys.* **2007**, *9*, 573.
- [178] Schellman, J. A. *Biophys. J.* **2003**, *85*, 108.
- [179] Duren, T.; Millange, F.; Ferey, G.; Walton, K. S.; Snurr, R. Q. *J. Phys. Chem. C* **2007**, *111*, 15350.
- [180] Furukawa, H.; Kim, J.; Ockwig, N. W.; O'Keeffe, M.; Yaghi, O. M. *J. Am. Chem. Soc.* **2008**, *130*, 11650.
- [181] Cote, A. P.; Benin, A. I.; Ockwig, N. W.; O'Keeffe, M.; Matzger, A. J.; Yaghi, O. M. *Science* **2005**, *310*, 1166.
- [182] Hunt, J. R.; Doonan, C. J.; LeVangie, J. D.; Côté, A. P.; Yaghi, O. M. *J. Am. Chem. Soc.* **2008**, *130*, 11872.
- [183] Mendoza-Cortés, J. L.; Han, S. S.; Furukawa, H.; Yaghi, O. M.; Goddard, W. A. *The Journal of Physical Chemistry A* **2010**, *114*, 10824.
- [184] Liu, Y.; Liu, D.; Yang, Q.; Zhong, C.; Mi, J. *Industrial & Engineering Chemistry Research* **2010**, *49*, 2902.
- [185] Klontzas, E.; Tylianakis, E.; Froudakis, G. E. *J. Phys. Chem. C* **2008**, *112*, 9095.
- [186] Cao, D.; Lan, J.; Wang, W.; Smit, B. *Angew. Chem., Int. Ed.* **2009**, *48*, 4730.
- [187] Lan, J.; Cao, D.; Wang, W. *J. Phys. Chem. C* **2010**, *114*, 3108.
- [188] Li, F.; Zhao, J.; Johansson, B.; Sun, L. *Int. J. Hydrogen Energy* **2010**, *35*, 266.
- [189] Klontzas, E.; Tylianakis, E.; Froudakis, G. E. *Nano Lett.* **2010**, *10*, 452.
- [190] Nevins, N.; Chen, K.; Allinger, N. L. *J. Comput. Chem.* **1996**, *17*, 669.
- [191] Halgren, T. A. *J. Comput. Chem.* **1996**, *17*, 490.
- [192] Rappe, A. K.; Casewit, C. J.; Colwell, K. S.; Goddard, W. A.; Skiff, W. M. *J. Am. Chem. Soc.* **1992**, *114*, 10024.
- [193] Yaghi, O. M.; O'Keeffe, M.; Ockwig, N. W.; Chae, H. K.; Eddaoudi, M.; Kim, J. *Nature* **2003**, *423*, 705.
- [194] Mintova, S.; Valtchev, V.; Kanev, I. *Molecular Engineering* **1995**, *4*, 369.
- [195] Furukawa, H.; Kim, J.; Ockwig, N. W.; O'Keeffe, M.; Yaghi, O. M. *J. Am. Chem. Soc.* **2008**, *130*, 11650.

- [196] Ockwig, N. W.; Delgado-Friedrichs, O.; O'Keeffe, M.; Yaghi, O. M. *Acc. Chem. Res.* **2005**, *38*, 176.
- [197] Férey, G. *J. Solid State Chem.* **2000**, *152*, 37.
- [198] Schmid, R.; Tafipolsky, M. *J. Am. Chem. Soc.* **2008**, *130*, 12600.
- [199] Holroyd, L. F.; van Mourik, T. *Chem. Phys. Lett.* **2007**, *442*, 42.
- [200] Grimme, S.; Diedrich, C.; Korth, M. *Angew. Chem., Int. Ed.* **2006**, *45*, 625.
- [201] Han, S. S.; Furukawa, H.; Yaghi, O. M.; Goddard, W. A. *J. Am. Chem. Soc.* **2008**, *130*, 11580.
- [202] Sillar, K.; Hofmann, A.; Sauer, J. *J. Am. Chem. Soc.* **2009**, *131*, 4143.
- [203] Tsuzuki, S.; Uchimaru, T.; Matsumura, K.; Mikami, M.; Tanabe, K. *Chem. Phys. Lett.* **2000**, *319*, 547.
- [204] Schwabe, T.; Grimme, S. *Acc. Chem. Res.* **2008**, *41*, 569.
- [205] Tafipolsky, M.; Amirjalayer, S.; Schmid, R. *J. Comput. Chem.* **2007**, *28*, 1169.
- [206] Manz, T. A.; Sholl, D. S. *J. Chem. Theory Comput.* **2010**, *6*, 2455.
- [207] Furukawa, H.; Yaghi, O. M. *J. Am. Chem. Soc.* **2009**, *131*, 8875.
- [208] Zhao, L.; Zhong, C. *J. Phys. Chem. C* **2009**, *113*, 16860.
- [209] Furukawa, H.; Ko, N.; Go, Y. B.; Aratani, N.; Choi, S. B.; Choi, E.; Yazaydin, A. O.; Snurr, R. Q.; O'Keeffe, M.; Kim, J.; Yaghi, O. M. *Science* **2010**, *329*, 424.
- [210] Zhou, W.; Wu, H.; Yildirim, T.; Simpson, J. R.; Walker, A. R. H. *Phys. Rev. B* **2008**, *78*, 054114.
- [211] Tafipolsky, M.; Amirjalayer, S.; Schmid, R. *J. Phys. Chem. C* **2010**, accepted with revisions.
- [212] Chapman, K. W.; Halder, G. J.; Chupas, P. J. *J. Am. Chem. Soc.* **2009**, *131*, 17546.
- [213] Düren, T.; Sarkisov, L.; Yaghi, O. M.; Snurr, R. Q. *Langmuir* **2004**, *20*, 2683.
- [214] Li, Q.; Zhang, W.; Miljanic, O.; Sue, C.-H.; Zhao, Y.-L.; Liu, L.; Knobler, C.; Stoddart, J.; Yaghi, O. *Science* **2009**, *325*, 855.
- [215] Sagara, T.; Ortony, J.; Ganz, E. *J. Chem. Phys.* **2005**, *123*, 214707.

- [216] Henke, S.; Schmid, R.; Grunwaldt, J.; Fischer, R. *Chem. Eur. J.* **2010**, *16*, 14296.
- [217] Sancho-Gracia, J. C.; Cornil, J. *J. Chem. Theory. Comput.* **2005**, *1*, 581.
- [218] Dolg, M.; Wedig, U.; Stoll, H.; Preuss, H. *J. Chem. Phys.* **1987**, *86*, 866–872.
- [219] Grimme, S. *J. Comput. Chem.* **2004**, *25*, 1463.
- [220] Gonzalez, C.; Lim, E. C. *J. Phys. Chem. A* **1999**, *103*, 1437.
- [221] Allinger, N. L.; Lii, J.-H. *J. Comput. Chem.* **1987**, *8*, 1146.
- [222] Mitchell, M. *An Introduction to Genetic Algorithms*; MIT Press; Cambridge, MA, 1996.
- [223] Tsuzuki, S.; Honda, K.; Uchimaru, T.; Mikami, M.; Tanabe, K. *J. Am. Chem. Soc.* **2002**, *124*, 104.
- [224] Amirjalayer, S.; Tafipolsky, M.; Schmid, R. *Angew. Chem.-Int. Edit.* **2007**, *46*, 463.
- [225] Gonzalez, J.; Devi, R. N.; Tunstall, D. P.; Cox, P. A.; Wright, P. A. *Micropor. Mesopor. Mater.* **2005**, *84*, 97.
- [226] Biemmi, E.; Scherb, C.; Bein, T. *J. Am. Chem. Soc.* **2007**, *129*, 8054.
- [227] Biemmi, E.; Darga, A.; Stock, N.; Bein, T. *Microp. Mesop. Mater.* **2008**, *114*, 380.
- [228] Shekhah, O.; Wang, H.; Kowarik, S.; Schreiber, F.; Paulus, M.; Tolan, M.; Sternemann, C.; Evers, F.; Zacher, D.; Fischer, R. A.; Wöll, C. *J. Am. Chem. Soc.* **2007**, *129*, 15118.
- [229] John, N. S.; Scherb, C.; Shoaee, M.; Anderson, M. W.; Attfield, M. P.; Bein, T. *Chem. Commun.* **2009**, 6294.
- [230] Shoaee, M.; Anderson, M.; Attfield, M. *Angew. Chem. Int. Ed.* **2008**, *47*, 8525.
- [231] Masri, P.; Tasker, P. *Surf. Sci.* **1985**, *149*, 209 – 225.
- [232] Chadi, D. J. *Phys. Rev. Lett.* **1979**, *43*, 43.
- [233] Srivastava, G. P. *Reports on Progress in Physics* **1997**, *60*, 561.
- [234] Odbadrakh, K.; Lewis, J. P.; Nicholson, D. M.; Petrova, T.; Michalkova, A.; Leszczynski, J. *J. Phys. Chem. C* **2010**, *114*, 3732.

- [235] Keskin, S.; Liu, J.; Rankin, R. B.; Johnson, J. K.; Sholl, D. S. *Ind. Eng. Chem. Res.* **2009**, *48*, 2355.
- [236] Amirjalayer, S.; Schmid, R. *Micropor. Mesopor. Mater.* **2009**, *125*, 90.
- [237] Yildirim, T.; Hartman, M. R. *Phys. Rev. Lett.* **2005**, *95*, 215504.
- [238] Dubbeldam, D.; Walton, K. S.; Ellis, D. E.; Snurr, R. Q. *Angew. Chem.-Int. Edit.* **2007**, *46*, 4496.
- [239] Rowsell, J. L. C.; Spencer, E. C.; Eckert, J.; Howard, J. A. K.; Yaghi, O. M. *Science* **2005**, *309*, 1350.
- [240] Spencer, E. C.; Howard, J. A. K.; McIntyre, G. J.; Rowsell, J. L. C.; Yaghi, O. M. *Chemical Communications* **2006**, 278.
- [241] Hobza, P.; Müller-Dethlefs, K. *Non-covalent interactions*; RSC Publishing, 2009.
- [242] Riley, K.; Pitonakk, M.; Jurecka, P.; Hobza, P. *Chem. Rev.* **2010**, *110*, 5023–5063.
- [243] Schwabe, T.; Grimme, S. *Phys. Chem. Chem. Phys.* **2007**, *9*, 3397.
- [244] Grimme, S. *J. Comput. Chem.* **2006**, *27*, 1787.
- [245] Ford, D.; Dubbeldam, D.; Snurr, Q. *diffusion-fundamentals.org* **2009**, *78*, 1–8.
- [246] Greathouse, J. A.; Allendorf, M. D. *J. Phys. Chem. C* **2008**, *112*, 5795.
- [247] Stallmach, F.; Gröger, S.; Künzel, V.; Kärger, J.; Yaghi, O. M.; Hesse, M.; Müller, U. *Angew. Chem. Int. Ed.* **2006**, *45*, 2123.
- [248] Rowsell, J. L. C.; Eckert, J.; Yaghi, O. M. *J. Am. Chem. Soc.* **2005**, *127*, 14904.
- [249] Del Campo, N.; Besnard, M. *Chem. Phys.* **1990**, 91.
- [250] Tassaing, T.; Cabaco, M.; Danten, Y.; Besnard, M. *J. Chem. Phys.* **2000**, *113*, 3758.
- [251] Cabaco, M.; Danten, Y.; Besnard, M.; Guissani, Y.; Guillot, B. *Chem. Phys. Lett.* **1996**, *262*, 120.
- [252] Nagy, J.; Smith, V.; Weaver, D. *J. Phys. Chem.* **1995**, *99*, 13868.
- [253] Dubbeldam, D.; Beerdsen, E.; Vlugt, T. J. H.; Smit, B. *J. Chem. Phys.* **2005**, *122*, 224712.

- [254] Thornton, A. W.; Nairn, K. M.; Hill, J. M.; Hill, A. J.; Hill, M. R. *J. Am. Chem. Soc.* **2009**, *131*, 10662.
- [255] Schaftenaar, G.; Noordik, J. H. *J Comput-Aided Mol Design* **2000**, *14*, 123.
Molden4.4, locally modified version.

List of Papers, Talks and Posters

List of Publications

- [1] "Loading of porous metal-organic open frameworks with organometallic CVD precursors: inclusion compounds of the type $[L_nM]_a@MOF-5$ ", S. Hermes, F. Schröder, S. Amirjalayer, R. Schmid, R. A. Fischer, J. Mater. Chem. **2006**, *16*, 2464-2472.
- [2] "Ab initio parametrized MM3 force field for the metal-organic framework MOF-5", M. Tafipolsky, S. Amirjalayer, R. Schmid, J. Comp. Chem. **2007**, *28*, 1169-1176.
- [3] "Molecular dynamics simulation of benzene diffusion in MOF-5: Importance of lattice dynamics", S. Amirjalayer, M. Tafipolsky, R. Schmid, Angew Chem. Int. Ed. **2007**, *46*, 463-466.
- [4] "Conformational Isomerism in the Isoreticular Metal Organic Framework Family: A Force Field Investigation", S. Amirjalayer, R. Schmid, J. Phys. Chem. C **2008**, *112*, 14980-14987.
- [5] "Mechanism of Benzene Diffusion in MOF-5: A Molecular Dynamics Investigation", S. Amirjalayer, R. Schmid, Micropor. Mesopor. Mater. **2009**, *125*, 90-96.
- [6] "Atomistic Theoretical Models for Nanoporous Hybrid Materials" (invited review), M. Tafipolsky, S. Amirjalayer, R. Schmid, Micropor. Mesopor. Mater. **2010**, *129*, 304-318.
- [7] "First-Principles-Derived Force Field for Copper Paddle-Wheel-Based Metal-Organic Frameworks", M. Tafipolsky, S. Amirjalayer, R. Schmid, J. Phys. Chem. C **2010**, *114*, 14402-14409.
- [8] "All-Nitrogen Coordinated Amidinato/Imido Complexes of Molybdenum and Tungsten: Syntheses and Characterization", V. Gwildies,

- T. Thiede, S. Amirjalayer, L. Alsamman, A. Devi, R. A. Fischer, *Inorg. Chem.* **2010**, 49, 8487-8494.
- [9] "Exploring Network Topologies of Copper Paddle-Wheel based Metal-Organic Frameworks with a First Principles Derived Force Field", S. Amirjalayer, M. Tafipolsky, R. Schmid, submitted.
- [10] "Understanding the Network Topologies of Covalent Organic Frameworks: Strain Analysis by a First Principles derived Force Field", S. Amirjalayer, R. Schmid, submitted.
- [11] "Surface Structures and Energies of a Metal-organic Framework: A first Theoretical Investigation", S. Amirjalayer, M. Tafipolsky, R. Schmid, submitted.
- [12] "Investigation of Non-covalent Host-Guest Interactions in Metal-Organic Framework", S. Amirjalayer, R. Schmid, in preparation.
- [13] "Diffusion in Isoreticular Isomers of the IRMOF Family", S. Amirjalayer, R. Schmid, in preparation.
- [14] "Benzene Diffusion in IRMOFs: Importance of pore dimension", S. Amirjalayer, R. Schmid, in preparation.
- [15] "Reverse Topological Approach: Exploring the molecular structure of hybrid porous materials", S. Amirjalayer, R. Schmid, in preparation.

List of Presentations

Oral Presentations:

- [OP1] "Investigation of static and dynamic properties of MOF-Systems", 6th Workshop of the IRTG "Diffusion in Porous Materials", Leipzig, February **2007**.
- [OP2] "Theoretical and experimental investigations on structural and dynamic properties of porous materials", Eitorf, September **2008**.
- [OP3] "Understanding the structure of Porous Coordination Polymers", Northwestern University, Evanston, August **2010**.
- [OP4] "Theoretical investigations of a MOF-surface: Understanding the surface termination by free energy calculations", International Chemical Congress of Pacific Basin Societies (Pacifichem), Hawaii, December **2010**.

Poster Presentations:

- [PP1] "Structural Isomers in the IRMOF-Series: A Force Field Investigation", CECAM-workshop "Simulation, Design and crystal engineering of metal-organic frameworks, Lyon (France), July **2007**.
- [PP2] "Investigation of metal containing guest molecules in Metal-Organic Frameworks", Zing Organometallics Conference, Cancun (Mexico), March **2008**.
- [PP3] "Conformational Isomerism in the IRMOF Family: A Force Field Investigation", International Center for Materials Research (ICMR) Summer School on Periodic Structures and Crystal Chemistry, Santa Barbara (USA), July-August **2008**.
- [PP4] "Conformational Isomerism in the IRMOF Family: A Force Field Investigation using a Genetic Algorithm Global Minimum Search Strategy", 1st International Conference on Metal-Organic Frameworks and Open Framework Compounds, Augsburg (Germany), October **2008**.
- [PP5] "Investigation of the Influence of Network Topology on the Diffusion of Guestmolecules in Metall-Organic Framework", MOFCAT-2009, Oslo (Norway), June **2009**.
- [PP6] "Supramolecular and Conformational Isomerism in Porous Hybrid Materials on the Example of a 3,6 Network[Zn_4OBTB_2]_n", CECAM-Workshop "Structural Transitions in Solids: Theory, Simulations, Experiments and Visualization Techniques", Lugano (Switzerland), July **2009**.
- [PP7] "Structural and Dynamic Properties of Porous Coordination Polymers: A Molecular Dynamics Investigation", Jülich (Germany), March **2009**.
- [PP8] "Understanding the Influence of the Network Topology of Porous Coordination Polymers on the Diffusion of Guest Molecules", Diffusion-Fundamentals III, Athens (Greece), August **2009**.
- [PP9] "Isorecticular Isomers of Porous Coordination Polymers", Diffusion-Fundamentals III, Athens (Greece), August **2009**.
- [PP10] "Investigation of the Influence of Network Topology on the Diffusion of Guestmolecules in Metal-Organic Frameworks", 2nd International Conference on Metal-Organic Frameworks and Open Framework Compounds MOF2010, Marseille (France), September **2010**.